PhD-FSTC-2015-03
The Faculty of Sciences, Technology and Communication

DISSERTATION

Defense held on 16/01/2015 in Luxembourg

to obtain the degree of

DOCTEUR DE L'UNIVERSITÉ DU LUXEMBOURG

EN SCIENCES DE L'INGENIEUR

by

Mike TIBOLT
Born on 4 January 1984 in Luxembourg, (Luxembourg)

DESIGN OF POINT FITTED INSULATING GLASS UNITS

Dissertation defense committee

Dr.-Ing. Christoph Odenbreit, dissertation supervisor
Professor, University of Luxembourg, Faculty of Sciences, Technology and Communication

Dr.-Ing. Stefan van Baars, Chairman
Professor, University of Luxembourg, Faculty of Sciences, Technology and Communication

Dr.-Ing. Andreas Zilian, Deputy Chairman
Professor, University of Luxembourg, Faculty of Sciences, Technology and Communication

Dr.-Ing. Oliver Hechler
ArcelorMittal, Luxembourg

Dr.-Ing. Olivier Vassart
ArcelorMittal, Luxembourg

Preface

The thesis was realized during my time as a research assistant at the *ArcelorMittal Chair of Steel and Façade Engineering* at the *University of Luxembourg*.

I would like to express my profound gratitude to my supervisor Prof. Dr.-Ing. Christoph Odenbreit who offered me the opportunity to realize the thesis at this chair. His expertise and his constructive criticism were a permanent motivation to successfully finish the thesis. Moreover I thank him for the pleasant working environment and an open ear for personal concerns.

I want to express my sincere thanks to Dr.-Ing. Oliver Hechler, former member of the *ArcelorMittal Chair of Steel and Façade Engineering*, for his scientific support in the development of the extended climate load model presented in this work and for his seminal input all over the period of the project. In addition, I appreciate his company during my participation in international conferences and congresses.

My thanks are also due to Dr.-Ing. Olivier Vassart, Visiting Professor at the *University of Ulster* and Head of Structural Long Products R&D at *ArcelorMittal*, for his willingness to participate as a member in my *Supervision committee* (CET). His suggestions were a precious contribution to the work.

I am deeply grateful to Prof. Dr.-Ing. Stefan van Baars, Professor in Foundation Engineering and Soil Mechanics at the *University of Luxembourg*, and Prof. Dr.-Ing. Andreas Zilian, Professor for Statics and Structural Analysis at the *University of Luxembourg,* for their participation as Chairman respectively Deputy Chairman in my dissertation defence committee.

The experimental part of this thesis would not have been possible without the marvellous support team in the laboratory of the *University of Luxembourg*. I am deeply grateful to the technicians Claude Collé, Ed Weyer, Logan Freitas and Vicente Adonis Reis for their tireless commitment. In this context, special thank is due to Logan Freitas for his extraordinary contribution to the assembling of the large scale tests. In addition, I would like to thank the engineers Marc Seil, Ralf Reiter, Gilbert Klein, Raphaël Hinger, Cédric Bruyère and Remi Radinovic for their experienced support in the matter of measurement equipment and software.

I thank all my colleagues at the *University of Luxembourg* who accompanied me during the research work. In particular, special thanks to my colleagues Vincent Dias, Sebastian Nellinger and Yves Staudt for their willingness to discuss and help. I express my gratitude to

the whole staff of the *University of Luxembourg* for their administrative support, especially Simone Drees, Rita Giannini and Virginie Mucciante.

I would like to thank Nicolas Hoffmann, Master student from the *ESSTIN*, for his assistance in the execution of the large scale tests and in the evaluation of the test results.

My profound gratitude is due to our partner *ArcelorMittal* for the global financing of this research work. Thanks are also due to *Guardian Luxembourg* and *Vitrumlux* for the supply and donation of glass material. Additionally, I thank the *Fischerwerke* for the free allocation of the Fischer undercut anchors and the mounting in the glass pane. My special thanks go to *Bischoff Glastechnik AG* for the production of the point fitted insulation glass units with the Fischer undercut anchors, *Dow Corning* for the supply with DC 993 silicone and *Kömmerling* for the provision with Ködiglaze S.

In the end, I thank my parents for their commendable support and patience.

Luxembourg, in January 2015 Mike Tibolt

Abstract

Today's building façades are not imaginable without the building material glass. Modern architects capitalise the transparency and the load carrying capacity of glass elements in the design of filigree and light-flooded structures. Priority is thereby given to the maximal transparency and the energy efficiency of the glass façade. In fact, the strategy paper "EU 2020" formulated by the European Union has an important impact on the design of glass façade and the energy efficiency will be a focal point in the design of glass façades in future. The optimal combination of transparency and energy efficiency is achieved by using point fitted insulation glass units. Their application in glass façades becomes therefore indispensable in the future.

Currently, three different point fitting systems for point fitted insulation glass units exist. They however present several disadvantages concerning their installation procedure and the tightness of the glazing cavity. Additionally, a general design concept for point fitted insulation glass does currently not exist. In consequence, point fitted insulation glass is a non-regulated construction product and requires an approval in individual cases from the national building authorities.

A model to proof the structural integrity of a developed point fitted insulation glass unit with a suitable point fitting system and edge seal system is proposed. A state of the art investigation reveals the Fischer undercut anchor to be the most suitable type for the application in insulation glass. A novel design concept for point fitted insulation glass with undercut anchors is developed. The concept considers the determination of the climate loads and proposes a verification procedure for each structural element of the insulation glass unit. For this purpose, an existing climate load model for linearly supported insulation glass is analytically extended to the static system of point fitted insulation glass units with undercut anchors. For the verification of the connection undercut anchor in glass, an existing design method for point fitted single and laminated glazing is extended to point fitted insulation glass. Component tests are conducted on the Fischer anchor and its ultimate load bearing capacity in glass is determined. A calibrated numerical model of the proposed point fitted insulation glass unit with the Fischer anchor is developed for parametric studies. Large scale tests on the proposed new point fitted insulation glass unit are run with the aim to verify the numerical model, the climate load model and the extended design method and to proof the structural integrity of the entire unit. Finally a new point fitted insulation glass unit with a suitable point fitting type and a corresponding novel design concept is developed.

Key-words: Insulation glass, undercut point fittings, design concept, climate load model

Table of content

1 Motivation

Glass has subsequently become an inherent part in the building industry. Nowadays, large glass canopies, balustrades, columns and fully glazed façades are nearly boundless applied in modern architecture. Spectacular designed glass façades have worldwide developed into a main element of townscapes.

The principle advantage of glass façades is their transparency whereas the degree of transparency strongly depends on the supporting structure of the glass panes. Point fittings are locally applied in the glass sheet and cover only a small part of the glass surface, whilst linearly supported glass is framed on its four sides and has therefore a reduced transparency.

In addition to the architectural aspect, glass façades have to ensure the proper thermal and energetic performance of the building. In 2010, the EU formulated the strategy paper “EU 2020” with the aim of a resource-gentle, ecological and competitive economy. Inter alia an increase in energy efficiency of 20% for the year 2020 has been postulated. In consequence, tight requirements on the heat insulation properties of glass façades (i.e. heat transfer coefficient) have been formulated in national standards. To comply with these norms, the application of insulation glass units in glass façades becomes indispensable in future.

A good ratio between transparency and thermal performance is achieved with point fitted **I**nsulation **G**lass **U**nits (**IGU**). Point fitted insulation glass combines the advantage of thermally efficient glass units with discrete glass connection systems, allowing highly transparent and energy efficient façades. Finally, under the aspect of the strategy EU2020, point fitted IGU presents an architecturally attractive alternative to linearly supported insulation glass.

The existing point fitting systems for insulation glass units are related to major disadvantages concerning their mounting procedure in the unit, the tightness of the glazing cavity and the transparency of the unit (section 2.4). In addition, a general design concept for point fitted insulation glass units does not exist. They are currently non-regulated construction products and their application glass in façades requires a time and cost-intensive single approval in each case. Consequently, glass façades are rarely made of point fitted insulation glass units.

This work is a contribution to simplify the application of point fitted insulation glass units in glass façades.

2 State of the art – Glass façades

2.1 Glass

Glass is a linear elastic, homogeneous and isotropic material. Important physical properties of soda-lime silicate and borosilicate glass according to [DIN 18008-1] are indicated in Table 2.1.

Table 2.1 Physical properties of selected glass types

Physical property	Soda-lime silicate glass	Borosilicate glass
Density	2500 kg/m^3	2200 - 2500 kg/m^3
Young's modulus	70 000 MPa	60 000 MPa
Poisson's ratio	0.23	0.2
Coefficient of expansion	$9 \cdot 10^{-6}$ K^{-1}	$6 \cdot 10^{-6}$ K^{-1}

The mechanical strength of glass is differentiated in a theoretical and practicable resistance. The theoretical resistance is the result of the bonding forces between the molecules of the components. The theoretical resistance is indicated in a range between 10 000 and 30 000 MPa (Siebert, 2004). However in practice, the theoretical resistance cannot be capitalised. Due to the absence of a plastic behaviour, stress peaks occurring at the tip of micro-flaws and scratches, which are located on the surface and edges, cannot be released and glass fails with a brittle fracture. The surface and the edges of a glass pane are covered with micro-flaws. The flaws are for instance caused by the production process and the later manipulation of the glass panes at the construction site. The loading of the glass pane generates stress peaks at the tip of the flaws and finally lead to premature failure. Consequently, the glass strength is not a material constant, but strongly depends on the distribution of the micro-flaws on the surface and the edge.

The characteristic values of the bending tensile strength of glass derived following DIN EN 1288-5 (without the influence of edge flaws) or DIN EN 1288-3 (with the influence of edge flaws) correspond to the 5% fractile value determined with a confidence level of 95%. The characteristic values of the bending tensile strength for different glass products are indicated in Table 2.2.

Table 2.2 Characteristic bending tensile strength values for different glass products

Glass product	$f_{y,k}$ [N/mm²]	Standard
Float glass	45	DIN 1249-10
Heat strenghthened glass (HSG)	70	DIN EN 1863
Fully tempered glass (FTG)	120	DIN 1249-10

The uniaxial compressive strength of glass is determined on glass cylinders with a height and diameter of 10 mm according to (DIN 1249-10). The characteristic values indicated in (DIN 1249-10) lie in range of 700 to 900 MPa. The compressive strength of glass is however rarely capitalised in practice, as the glass plates are slender and sensitive to instability effects like buckling and large out-of plane deformations.

2.2 Point fitted single glazing

2.2.1 Application field

In modern architecture the material glass is applied in the design of highly filigree, light-flooded and also “organic” structures. Point fitted glazing is the response to the architectural pursuit of further increasing the transparency of constructions (Figure 2.1). In fact, point fitted glazing represents currently less than 0.5% of the glass surface in building, compared to 8%-10% for linearly supported glazing (Albrecht, 2004) (Figure 2.2).

Figure 2.1 Point fitted single glazing façade, Auchan Kirchberg

Figure 2.2 Linearly supported glass façade, DEKA Kirchberg

The prototypes of point fitted glass façades were designed with the Planar^{TM}-System of Pilkington. The façade of the “Renault Centre” in Swindon (1982) by *Norman Foster* is

the first point fitted single glazing façade worldwide. The façade of the greenhouses in the “Parc La Villette” in Paris (1986) by *Peter Rice* is the first freely hanging glass wall suspended with steel cables.

Figure 2.3Renault Centre, Swindon, Source: Pilkington

Figure 2.4 Pilkington Planar™-System, Source: Pilkington

Figure 2.5 Greenhouse, Parc de la Villette, Paris, Source: R.F.R

Figure 2.6 Free hanging glass façade, Source: R.F.R

Nowadays, point fitted glazing features a widespread field of application. It is used as vertical glazing in glass façades, infill of balustrades (Figure 2.8) and as overhead glazing in glass roofs and canopies (walkable glazing) (Figure 2.7). Additionally, stairways (accessible glazing) are realized with point fitted glass.

Figure 2.7 Glass canopy, Airport Porto

Figure 2.8 Glass balustrade, Permasteelisa

Point fittings are predominantly drilled into the glass panes, creating a local stress peak at the borehole. In consequence, mainly laminated glass made of fully tempered or heat strengthened glass is applied in point fitted glass façades. For point fitted overhead glazing, laminated heat strengthened glass is used to assure its post breakage behaviour. In fact, the big glass fragments of laminated heat strengthened glass interlock via the interfoil in case of glass failure and avoid the disintegration of the glass pane.

2.2.2 Point fitting systems for single glazing

Respectively to their geometry and load bearing mechanism, point fittings can be generally classified into five categories:

1. Button fittings
2. Countersunk fittings
3. Undercut anchors
4. Clamped fittings
5. Adhesive point fittings

i. Button fittings

A button fitting consists of a steel bolt and two clamping disks (Figure 2.9).

Figure 2.9 Button point fitting, Source: Glas Trösch

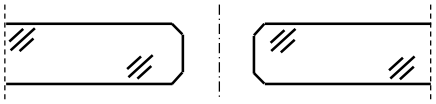

Figure 2.10 Cylindrical borehole

The steel bolt is inserted in a cylindrical through hole (Figure 2.10) and the glass pane is clamped between the two disks. The wind forces are transmitted by contact between the glass surface and the clamping disks. The dead load is carried by bearing pressure between the bolt and the borehole surface. A detailed investigation concerning the load bearing mechanism of button fixings is described in (Albrecht, 2004). Button fittings allow an easy compensation of dimension tolerances by oversized boreholes. The stress peaks due to the misalignment between the leaves of laminated glass are reduced. In addition, the post breakage behaviour is ensured by the clamping effect of the two disks. The disks however reduce the transparency of the glass panes and the outer disk is a possible location of dust accumulation.

ii. Countersunk fittings

The countersunk fitting (Figure 2.11) is composed of a countersunk bolt head flush-fitted in the glass surface and a clamping disk on the inner side.

Figure 2.11 Countersunk point fitting, Source: Glas Trösch

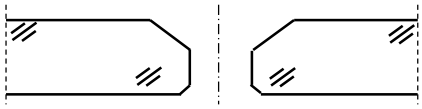

Figure 2.12 Countersunk borehole

Similar to button fixings, the dead load is transmitted by bearing pressure between the bolt and the borehole surface. The wind forces are transferred by contact between the clamping disk and/or the countersunk head and the glass surface. Since no disk is applied on the outer glass surface for countersunk fittings, the surface remains even without risk of dust entrapment or leakage. The cleaning process is facilitated. In addition, the dimensions of countersunk fixings are generally smaller compared to button fittings, leading to a higher transparency of the glass units. The small contact surface for the load transfer however induces high stress peaks at the borehole and leads to thick

glass panes. Additionally, the form closure has to be insured and size tolerances cannot be compensated in the borehole. As a result, countersunk point fittings generate higher stress peaks in laminated glass than button fittings and premature failure is possible. Finally the risk of fittings tearing out of the glass in case of failure is very high and the post breakage behaviour is consequently poor.

Direct contact between glass and steel is to be avoided by plastic or aluminium interlayers and bushes inserted between the glass surface and the steel elements. The interlayers differ in their material properties and thicknesses, influencing the rotation capacity of the point fitting. Depending on their rotation rigidity, point fittings are considered to be rigid or hinged. A regular hinged point fitting is realized with an embedded ball joint or plastic material. Hinged point fittings advantageously reduce restrain stress at the borehole. The position of the hinge influences the moment loading of the connection. An eccentric positioned hinge induces an additional moment in the point fitting and stresses in the glass. Hence, a constructively favourable position of the joint is exactly in the mid-section of the glass plate.

iii. Undercut anchors

The undercut anchor (Figure 2.13) is a special type of point fitting. An undercut borehole (Figure 2.14) is drilled in the glass by means of a special drill.

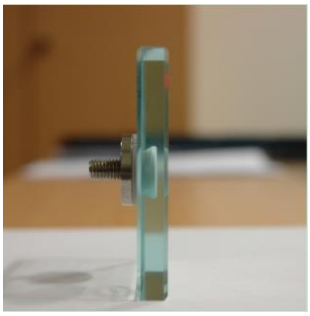

Figure 2.13 Fischer undercut anchor, FZP-G-Z

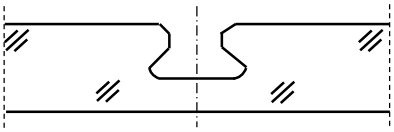

Figure 2.14 Undercut borehole

In a first step a cylindrical stud hole is drilled in the glass and finally the undercut is realized by inclining the cut head. The hole does not penetrate the whole thickness of the glass and leaves the outside glass surface undisturbed. The point fitting consists of a steel conical bolt with an expanding sleeve and a round nut. The anchor is mounted with a controlled moment of torque. The expanding slave opens and anchors the point fitting in the glass pane. The wind and dead loads are transferred by contact between the conical bolt and the sidewall. The direct contact between the glass and the conical bolt is avoided by a plastic plug surrounding the latter. The outer glass surface stays

totally even and tight against weather condition. Furthermore the steel bolt does not totally penetrate the glass pane and thus does not consist in a thermal bridge. Undercut anchors have smaller dimensions than button or countersunk fittings and allow the design of highly transparent glass panes. However, the post breakage behaviour is even less than with countersunk fittings and therefore undercut anchors are not used in overhead glazing. Existing undercut anchors on the market are e.g. the *Fischer FZP-G-Z* and the *Swissanchor*. For the *Fischer FZP-G-Z*, a general technical approval for single fully tempered glass of 10 mm and 12 mm thicknesses and laminated glass of 10 mm + 8 mm thick fully tempered glass exists (Z-70.2-122).

iv. Clamped fittings

Clamped fittings (Figure 2.15) are point supports located at the corner or the edges of the glass panes. The panes are clamped between two clamping plates and they are not drilled (Figure 2.16).

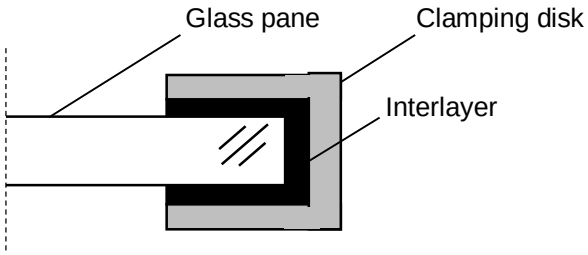

Figure 2.15 Clamped fitting, Source: INOVA **Figure 2.16 Principle of clamped fittings**

Out-of-plane loadings (e.g. wind) are transferred by mechanical interlock and in-plane loads (e.g. self-weight) by setting blocks and brackets (Wurm, 2007). Since no hole is drilled in clamped glass plates, the related stress peaks and tolerance problems are reduced. The location of the clamped fittings at the corner or the edge however leads to constructional expanded joints between two adjacent glass plates, limiting the transparency of the structure. Clamped fixings are often applied in anti-fall glass balustrades.

v. Adhesives point fittings

Adhesive point fittings (Figure 2.17) consist of glued steel disks on the glass surface and the glass is not weakened by drilled holes (Figure 2.18).

Figure 2.17 Adhesive point fitting, Source: Pilkington

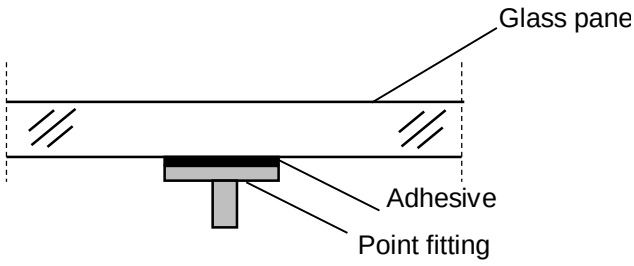

Figure 2.18 Principle of adhesive point fittings

The stress peak is reduced. The out-of-plane and in-plane loadings are exclusively carried by the adhesive. The ultimate load bearing resistance depends on the thickness and radius of the adhesives. Stiff pellucid adhesives, like acrylic or epoxy resin, are frequently applied. The transparency of the connection is comparable to undercut anchors and the outer glass surface remains even and tight. In addition, thermal bridges are reduced. The main concern is the durability of the adhesives. Temperature change, humidity and solar radiation reduce its stability and induce a yellowing of the adhesive (Wellershoff, 2005). Currently, adhesive point fittings are part of intensive scientific research.

Independent of the point fitting system, a low-restraint connexion between the glass panes and the substructure has to be ensured. In practice, an in-plane isostatic support is pursued. It is realized by long holes or slide blocks (Figure 2.19).

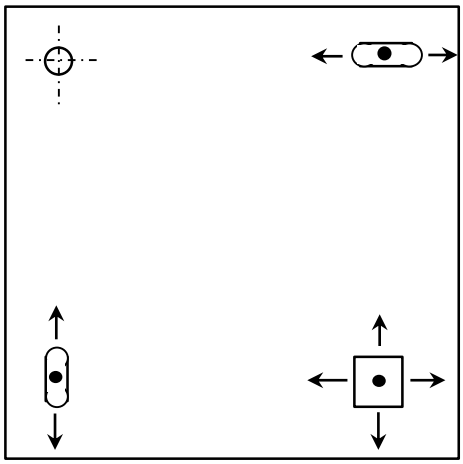

Figure 2.19 Isostatic support of a point fitted glass plane

Table 2.3 Advantages and disadvantages of the point fitting systems for single glazing

Point fitting	Figure	Advantages	Disadvanatges
Button fittings		- Compensation of tolerances - Low stress peak - High post breakage behaviour	- Reduced transparency - Additional thermal bridge
Countersunk fittings		- Even outer pane - High transparency	- Strict tolerances - High stress peak - Low post breakage behaviour - Additional thermal bridge
Undercut anchors	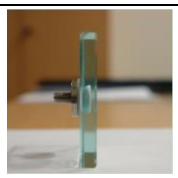	- Even outer pane - High transparency - Easy mounting in glass pane - Reduced thermal bridge	- Low post breakage behaviour
Clamped fittings		- Compensation of tolerances - No borehole - Low stress peak	- Reduced transparency
Adhesive fittings		- No borehole - Low stress peak - Easy application - Reduced thermal bridge - High transparency	- Long-term behaviour - Sensitive to UV and humidity - Yellowing of the adhesive

2.3 Insulation glass units

2.3.1 Application field

Insulating glass units are mostly linearly supported (Figure 2.20). Clamping strips are common embodiments for vertical and horizontal glazing. The insulation units are installed in a metallic, plastic or wooden frame and bear on setting blocks of neoprene, silicone or EPDM. The setting blocks allow an easy compensation of production tolerances and carry the in-plane loads (e.g. self-weight and thermal loading). The clamping strips apply a linear pressure load on the glass units and transfer the out-of-plane loads (e.g. wind and climate loads). The direct contact between the clamping strips and the glass is avoided by an elastic joint. The joint also ensures the tightness and the elasticity of the connection.

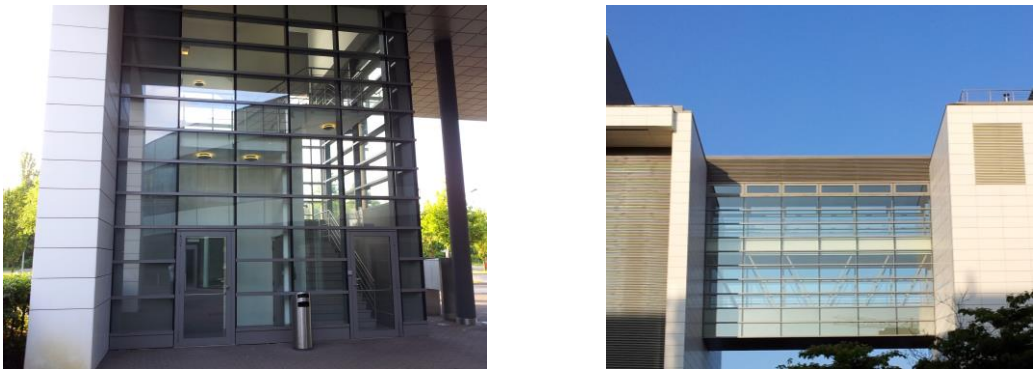

Figure 2.20 Linearly supported IGU in vertical glazing application, K2-Building, Kirchberg

Structural sealant glazing (SSG) (Figure 2.21) builds a second method for the design of a linear supported connection.

Figure 2.21 IGU in structural sealant application (SSG), K2-Building, Kirchberg

The insulation glass units are glued on an adapter frame ex-factory and integrated in the primary structure on the construction site. The adapter frame is made of aluminium or steel and the primary structure consists in a metallic mullion-transom system. Structural

silicone is mainly used in structural sealant application. It tightens the connection and transmits the out-of pane loads like wind or climate loads. Requirements concerning its tightness and structural properties are given in (ETAG 002). According to (ETAG 002), insulating glass units are only applicable in combination with ETAG type I and type II. For these types, the in-plane loads are carried by elastic setting blocs, which are fixed on mechanical devices.

2.3.2 Manufacturing process of insulation glass

According to (DIN EN 1279-1), an insulation glass unit consists of at least two glass panes which are linearly connected over their edges to seal a gas filling in the gap (glazing cavity) between them (Figure 2.22 to Figure 2.24).

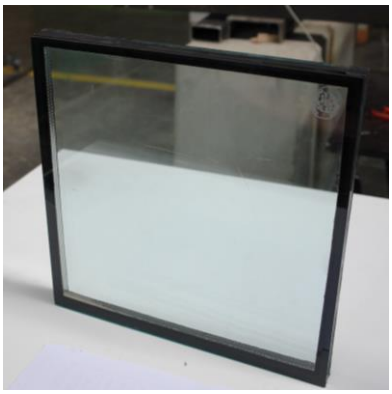

Figure 2.22 Insulation glass unit

Figure 2.23 Corner of an insulation glass unit

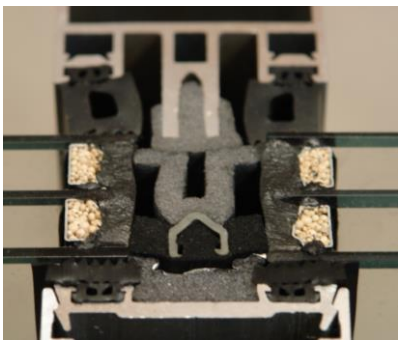

Figure 2.24 Edge seal system of an insulation glass unit

The two glass panes are predominantly made of fully tempered glass, where the outer pane is laminated fully tempered glass to offer protection against wind loads and hail. In addition, the outer laminated glass pane avoids fragments to drop from the façade in case of failure. The inner pane is made of laminated glass in cases fall protection is decisive (DIN 18008-4). The glazing cavity in standard insulation glass has a thickness of 12 to 18 mm and is filled with gas to minimize thermal conductivity. In individual cases, the size of the cavity is increased up to 40 mm to install light deflecting structures. The

edge seal of common insulation glass units has a width of 12 mm and its key-function is to provide a gas-and moisture barrier and to structurally bond the glass panes together. Different edge seal systems exist on the market (see section 2.3.3). The choice for a particular system complies with the functionality of the insulation glass unit (for example thermal insulation and solar control). Standard edge seal systems are composed of a metallic spacer and two sealant materials.

Two different manufacturing procedures for insulation glass exist. They differ in the gas filling process.

The traditional method consists in primarily assembling the unit with air, trapped in the cavity. Secondly the air is replaced by inert gas with two needles introduced into the cavity at two opposite corners of the unit and a vacuum pump. The air is evacuated and the gas is introduced. Finally the remaining hole in the sealant is closed.

The modern method is an automatic production line. The assembling of the insulation glass unit is located in a chamber, directly containing the inert gas. No hole needs to be drilled through the edge sealant to fill the cavity with gas and a better sealant tightness is achieved.

The automatic assembling of an insulation glass unit with a standard edge seal system consists in four steps. First of all the glass panes are cut to the specific size and cleaned with solvents. Secondly the metallic spacer is machined cold-formed and glued with the primary sealant (i.e. butyl) to the first glass pane. Thirdly the glass pane with the spacer is placed in a chamber filled with inert gas and the second glass plane is glued on the spacer of the first pane with butyl. Finally the unit is sealed by machinable application of the secondary sealant (i.e. silicone, polyurethane or polysulfide) over the edges of the glass plates. For both manufacturing methods, each glass pane has to be mechanically processed (e.g. cut, drilled, grounded) and tempered before the assembling to insulation glass.

2.3.3 Edge seal systems

In the framework of increasing requirements on the thermal and structural performance of insulation glass, the edge seal systems play an important role. Edge seals can be classified into three categories:

- Dual-sealed systems
- Thermoplastic edge seal systems (Thermoplastic spacers, TPS)
- Structural edge seal systems

i. Dual edge-seal system

Dual-sealed systems (Figure 2.25) account for about 2/3 of the edge seal systems worldwide (Wolf, 2005).

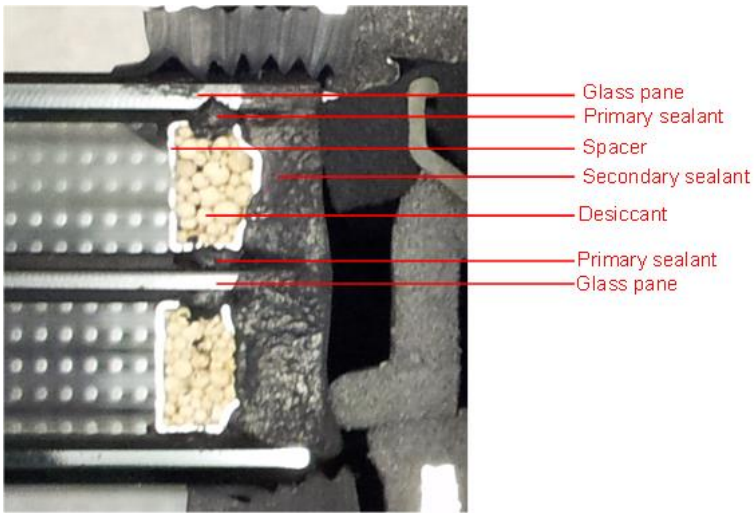

Figure 2.25 Dual edge seal system

The system is composed of a spacer and two different sealants as to know the primary and the secondary sealant. The primary sealant is exclusively made of polyisobutylene (PIB, butyl) and is inserted in a hot application process between the spacer and the glass panes. The thickness of the primary sealant is generally about 0.25 mm. It has a high gas and diffusion tightness and its main function is the provision of a moisture and gas barrier. PIB adheres only mechanically to the glass and the bond is highly sensitive to atmospheric exposure like humidity and solar radiation. PIB has a breaking elongation of 700% and a Young's modulus in a range of $0.7 \cdot 10^{-6}$ – $1.5 \cdot 10^{-6}$ N/m^2 (Schäfer, 2002). Therefore PIB is supposed to have no structural function (Besserud, 2012).

The secondary sealant materials are predominantly polysulfide (PS), polyurethane (PU) and silicone (Si). The key-function of the secondary sealant is the preservation of the structural integrity of the insulation unit and the protection of the primary sealant against atmospheric exposure and mechanical loading. Polysulfide and polyurethane are strongly sensitive to UV-radiation and heat impact. That means, edge seals made of these two elastomers must be additionally protected (e.g. cover bars). Silicone sealants are poorly affected by UV-radiation, heat and humidity. However it has a high gas diffusion permeability and damage of the primary sealant leads to a quick gas leakage. Intensive testing on the durability of edge sealants according to (DIN 1286-1) has revealed that the combination of PIB and silicone has the best overall performance (Wolf, 2005). Today, silicone sealed insulation glass units represent 12% of all units

manufactured globally (Wolf, 2005). The hollow spacer establishes the precise distance between the glass panes, transmits pressure loads (i.e. wind, snow and climate loads) and reduces the effective diffusion cross-section of the primary seal. It is mainly made of aluminium, stainless steel or plastics. The advantage of plastic spacers is their lower thermal conductivity compared to metal spacers. The spacer is filled with a desiccant to totally dry the content of the unit and to avoid formation of condensation inside the unit. The desiccant consists of silicate gel, calcium sulphate or calcium chloride.

ii. Thermoplastic edge seal systems

Thermoplastic edge seal systems (TPS) present a new generation of edge seal systems (Figure 2.26).

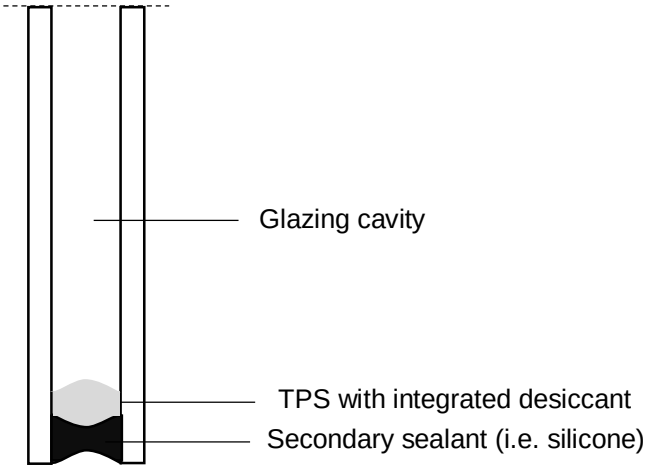

Figure 2.26 Thermoplastic edge seal system (TPS)

Compared to the dual-sealed systems, the rigid spacer, the desiccant and the primary sealant are replaced by only one single thermoplastic butyl sealant, already containing the desiccant. Only two elements are left, the butyl sealant and the outer secondary elastomeric sealant. The reduced number of components facilitates and accelerates the production. Thermoplastic spacers are highly flexible and limit the mechanical loading of the butyl sealant, increasing its tightness. Additionally, the absence of a metallic spacer reduces the thermal conductivity of the edge sealant system of a factor thousand compared to dual-sealed systems (“Warm edge systems”) (Wurm, 2007). Due to the missing rigid spacer, the thermoplastic edge sealant itself cannot transmit pressure loads. The outer secondary sealant takes this function over and its loading is consequently higher than in dual-sealed systems.

iii. Structural edge seal systems

Structural edge seal systems are applied in insulation glass units where the outer glass pane is statically connected to the inner pane via the edge seal. This is for instance the case for structural sealant glazing (SSG) with only the inner pane glued to an adapter frame (Type IV of SSG according to (ETAG 002)). The edge sealant acts as a statically active bonded joint and the secondary sealant has to comply with the standards for structural glazing (ETAG 002) as well as with the standards for the long term performance of insulation glass units, [DIN 1286] or [EN 1279]. Currently only structural silicone fulfils these requirements. Dual-sealed and thermoplastic sealant systems can be used in structural edge seal applications. For TPS, the pressure loads are transmitted by the secondary sealant and the entire systems undergoes higher deformations than dual edge-seal systems. Hence, more restrictive limits for the minimum covering thickness of the secondary sealant of TPS are required by (ETAG 002), limiting its in structural applications.

2.3.4 Functionality of insulation glass units

Primarily insulation glass has been developed to comply with two functional requirements on glass façades, namely the protection against atmospheric exposure and the thermal insulation of the building. Over the last four decades insulation glass units have been developed to a multifunctional and structural façade element with sound insulation, sun and intruder protections.

The main functions of insulation glass units are the following:

- Thermal insulation
- Solar control
- Sound insulation
- Intrusion protection

The properties of insulation glass units are determined by the coatings, the gas filling, the glass leaves composition and the edge bond systems.

The thermal insulation performance is improved by the application of special coatings (low e-coating) on the glass surface. The coatings reduce the heat emission through the corresponding glass. The application of a tin oxide layer reduces for example the emissivity of the glass from 90% to 15% (Wurm, 2007). Various coating types exist on the market. They are classified as hard or soft coatings depending on their mechanical and heat resistance. The magnetron sputtering procedure is mostly applied by industry to apply a coating on a glass surface (Wurm, 2007). The gas filling also increases the

thermal insulation capacity of insulation glass. Former units were filled with dry air to limit the thermal conduction between the inner and outer panes. Modern insulation glass units are filled with inert gas like argon (Ag) or rarely the more expensive gases krypton (Kr) and xenon (Xe) with lower thermal conductivities than dry air. The use of inert gases decreases the thermal transmittance coefficient of the glazing of about 0.3 W/m^2K. The edge seal system is a further element enhancing the thermal insulation properties of insulation glass (see section 2.3.3).

An effective reduction of solar heat is achieved with reflecting solar control coatings on one pane of insulation glass. Double silver coating systems for instance offer a light transmittance of 70% with a limited solar energy transmittance of only 35% (Wurm, 2007). Alternatively, fixed prismatic panels are integrated in the glazing cavity. The shape of these elements reflects the sunlight from certain angles and a seasonable solar control is enabled with this measure.

The acoustic insulation properties are increased by employing laminated glass. In combination with the natural frequency of the mass-spring-mass system of insulation glass, the high mass of laminated glass considerably improves the sound damping properties of insulation glass units. Since the formerly used sulphur hexafluoride (SF_6) has a high global warming potential it is not used anymore as gas.

The intrusion protection is realized by laminated glass. In case of a smashed outer glass sheet, the interlayer (e.g. PVB or SGP) assures the overall shape of the insulation glass unit and the passage is blocked.

2.4 Point fitted insulation glass units

As outlined in section 2.3.1, insulating glass units in façades are predominantly linear supported. The advantages of this connection type are an easy installation, compensation of construction tolerances and straightforward design, i.e. [DIN-18008-2]. But insulation glass units can also be connected to the substructure with point fittings (Figure 2.27).

Figure 2.27 Point fitted insulation glass façade, The Cube, Madrid, Source: AGC

Currently three different point fitting systems are commonly used in glass façades:

- Drilled through fittings (Button and countersunk fittings)
- Planar point fittings
- Embedded point fittings

i. Drilled through fittings

Button and countersunk fittings are drilled through the whole insulation glass unit (Figure 2.28 and Figure 2.29). A hole is drilled in the inner and outer glass pane and a stainless steel bolt perforates the unit in its entire extent. The tightness of the cavity at the level of the borehole is assured by a circular sealant system lagging the bolt. For the button fitting, two steel disks press the inner and outer glass panes together. The countersunk fitting consists of an inner steel disk and an outer countersunk head. The head is flush mounted with the outer glass pane and offers an even glass surface. The head and the inner disk are tightened and press the glass panes against each other. The composition of the circular sealant system is generally the same as for the edge sealant. A circular spacer profile is glued with butyl on the glass and covered with silicone, polysulfide or polyurethane. The gap between the glass panel and the disks are filled with interlayers and a bush is slipped over the bolt to avoid contact between steel and glass. Commonly used materials for the interlayers and bushes are EPDM, polyamide, aluminium or polyurethane. The out-of-plane loads are transferred via contact between the disks and the glass surface. The in-plane loads are transmitted by bearing pressure between the bolt and the borehole wall. The edge sealant does not transfer loads.

Figure 2.28 Countersunk point fitting for IGU, Source: Glas Trösch

Figure 2.29 Button point fitting for IGU, Source: Glas Trösch

The manufacturing and mounting process of point fitted insulating glass units with drilled through fittings is complex. In a first step, the two glass plates are drilled and subsequently tempered. Secondly they are assembled to an insulation glass unit, where the circular sealant around the point fitting is manually applied. On the construction site, the point fittings are connected to the substructure and the insulation glass unit is installed by sticking the bolts of the point fittings through the holes of the insulation glass unit and tightening the clamping disks.

ii. Planar point fittings

The company Pilkington markets a planar point fitting system, the so called “Pilkington Planar^{TM} Intrafix” (Figure 2.30 and Figure 2.31).

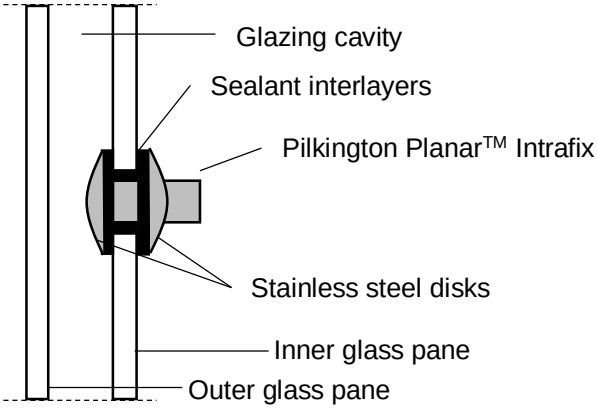

Figure 2.30 Principle of the Pilkington Planar™ Intrafix System

Figure 2.31 Pilkington Planar™ Intrafix System, Source: Pilkington

The system captures the tempered or laminated inner glass leaf with two stainless steel disks. The steel bolt does not penetrate the outer glass pane. The tightness of the cavity is assured by the sealant materials of the interlayers and the bush. The out-of- and in-pane loads acting on the external glass pane are transferred by the edge bond to the inner pane and by the point fittings to the substructure. In consequence, the planar point fitting requires a structural edge sealant system. The outer pane stays even and is easier to clean. In addition, a coating can be applied on the external lite to improve solar control and the insulation capacity of the unit.

The fitting is mounted in the inner glass pane before the pane is assembled to an insulating glass unit. Beforehand, the inner and outer lite have been drilled, tempered and eventually laminated. On the construction site, the unit is finally connected with the point fittings to the substructure.

iii. Embedded point fittings

Embedded point fittings (Figure 2.32) are a hybrid form of mechanical and adhesive point fittings. The conical head is concealed within the lamination interfoil of the inner lite and does not perforate the inner glass pane in its entire extent.

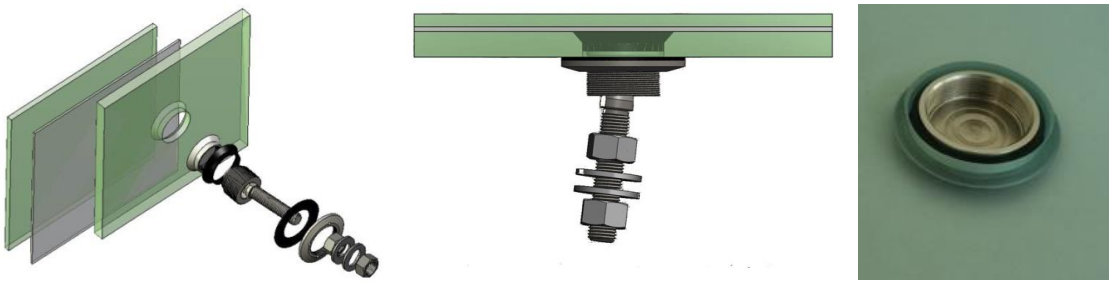

Figure 2.32 Embedded point fitting system, Source: VICER

As for the planar point fittings, the surface of the external glass pane is even. The cavity remains fully undisturbed and no gas leakage due to boreholes occurs. Out-of- pane and in-pane loads acting on the external glass pane are transmitted by the structural edge bond to the inner pane and via the point fitting to the load bearing structure. The load transfer from the inner glass pane to the point fitting is a combination of a mechanical and adhesive load transfer mechanism. A part of the load is directly transmitted by the laminated interfoil to the embedded point fitting head and the other part is transferred mechanically by contact between the glass and the countersunk head. In this way, the stress peak at the borehole is reduced compared to other point fitting systems. Common interlayer materials used in combination with embedded point fittings are PVB and SentryGlas®. An embedded point fitting applied in glass structures is provided by the company VICER (Cruz, 2014).

The point fitting is connected to the interfoil during the industrial lamination process “line and autoclave” (Cruz, 2014). The laminated inner lite with the mounted embedded point fitting is subsequently assembled to an insulation glass unit and fixed to the substructure on the construction site.

2.5 Design concepts for point fitted single glazing

Point fittings are mainly drilled into the glass panes (see section 2.2.2). The loads are exclusively transmitted by the point fitting and stress peaks occur at the boreholes. These stress peaks are decisive for the design of the glazing. Since no analytical solution for the determination of the stresses in point fitted glazing exists, numerical software based on finite elements (FE) is used to quantify the stress peaks (Beyer, 2007). The results delivered by the software however strongly depend on the knowledge of the user and the implemented point fitting model. The mesh, the type of elements, the contact definition and the material properties for the different point fitting components influence the results and could lead to wrong stress values (Siebert, 2004). Three different methods have been developed which allow the designing engineer to verify and calibrate

his own numerical model for a safe design: (Brendler, 2004), (Kasper, 2006) and (Siebert, 2006). In addition, an adequate design concept for point fitted single glazing has been developed and first established in the general technical approval of the Fischer FZP-G-Z (Z-70.2-122), (Beyer, 2007). The so called SLG-method only needs a simple FE-model of the glass pane which facilitates the whole designing process. Further design rules and recommendations are provided in (DIN 18008-3).

The following sections shortly resume the different design concepts:

2.5.1 Method of *Brendler* (Brendler, 2004)

For the verification of the point fitting according to (Brendler, 2004), preliminary small scale static and cyclic tests are conducted for different temperature levels. The point fittings are mounted in a steel plate and subjected to compression, tension and shear forces in order to determine their longitudinal and lateral stiffness values.

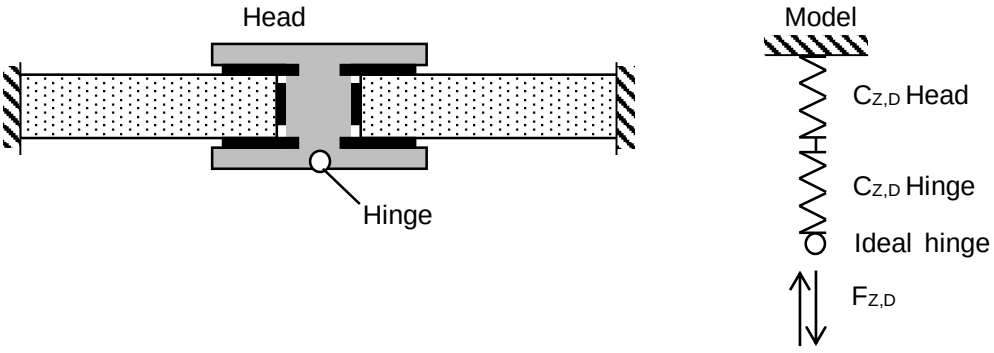

Figure 2.33 Longitudinal stiffness of a point fitting according to [Brendler-2007], from [Brendler-2007]

The longitudinal stiffness of the point fitting consists in the flexibility of the interlayers and an eventual hinge (Figure 2.33). The lateral stiffness is composed of the flexibility of the bush or the filling material and the rotation of the fitting head due to the elastic deformation of the interlayers (Brendler, 2004). The interval limits for the point fitting stiffness in longitudinal and lateral direction are implemented in the general technical approval of the corresponding point fitting. A numerical model of the fitting respecting the stiffness values within these limits is able to correctly determine the stress state at the borehole.

The verification process of the numerical model consists in simulating the small scale tests and verifying the longitudinal and transversal stiffness values of the point fitting (Figure 2.34). The verification process is executed in four steps: In a first step the Young's Modulus of the interlayer material is varied in order to comply with the longitudinal stiffness limits of the point fitting. Secondly, the stiffness of an eventual hinge is verified. The hinge is numerically modelled with a spring element and its stiffness is

trimmed to the stiffness range in the general technical approval. Thirdly, the Young's Modulus of the bush or the filling material is varied to lie within the given lateral stiffness range. In fact, the variation of the Young's Modulus for the interlayers and bushes considers the scattering of the point fitting stiffness.

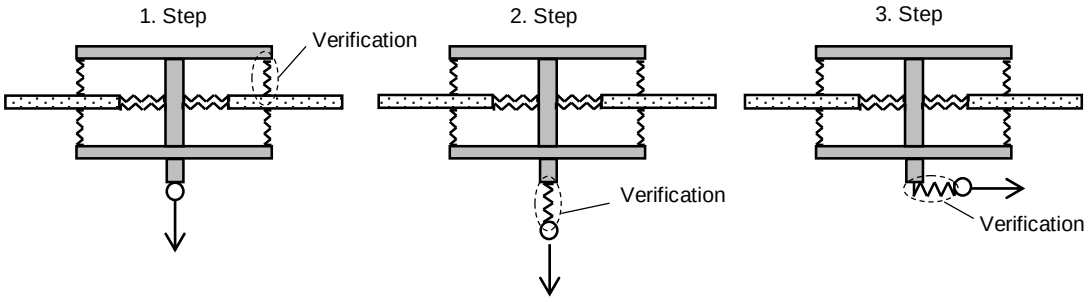

Figure 2.34 Verification steps for a point fitting according to (Brendler, 2004) and [Brendler-2007]

The verification process is finally concluded with the calculation of a reference glass plate described in the corresponding approval (Figure 2.35). The plate is modelled with the point fitting model of the first three steps and subjected to a surface load, which corresponds to the average value of the expected wind loads in practice. The determined support forces, stresses and deformations have to comply with the values given in the approval.

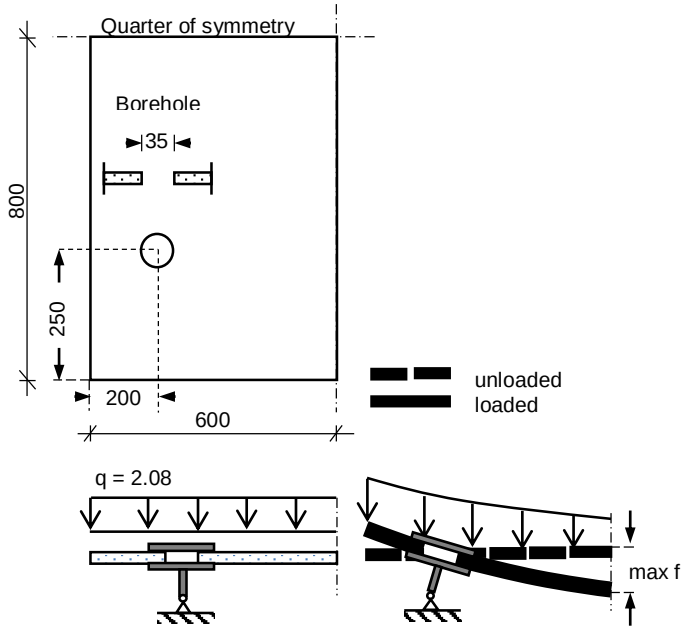

Figure 2.35 Reference glass plate, from (Z-70.2-99)

The design of the point-fitting glazing is performed by adoption of this model to the geometry to be designed and subsequent checking of the results against the design values.

The method according to (Brendler, 2004) has been implemented in the approval of several point fitting systems, e.g. (Z-70.2-99).

2.5.2 Method of *Kasper* (Kasper, 2006)

According to (Kasper, 2006), preliminary small scale static tests are conducted. The point fittings are drilled in a glass pane and subjected to different load configurations. The load is directly introduced at the point fitting under the angles of 0°, 22.5°, 45° and 90° (Figure 2.36). The strains along defined paths on the glass surface are measured during the tests (Figure 2.37).

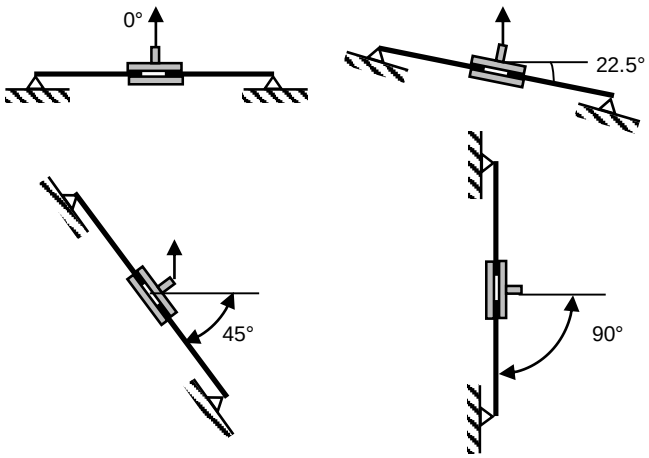

Figure 2.36 Small scale test, from (Kasper, 2006)

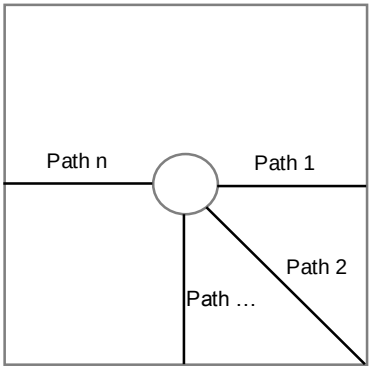

Figure 2.37 Path definition, from (Kasper, 2006)

The small scale tests are subsequently simulated numerically in order to determine the value and location of the main tensile stresses. Only numerical models able to reflect the measured strains are retained for the stress determination. The measured strains and the calculated maximum main tensile stresses are finally implemented in data sheets for the different load configurations.

The numerical model of the point fitting for design is verified by simulating the small scale tests. Thereby the strains and maximum main tensile stresses in the data sheets have to be determined conservatively for all load configurations (Kasper, 2006). The varying parameters for the calibration of the model are the Young's Moduli of the interlayers and bushes.

The verified numerical model of the point fitting is finally implemented in the glass pane to be designed.

2.5.3 Method of *Siebert* (Siebert, 2006)

Similar to the method described in (Kasper, 2006), small scale tests on the point fittings are conducted. The point fitting is centrally mounted in the glass sample and subjected to tension and compression for a symmetrical and eccentric support configuration (Figure 2.38).

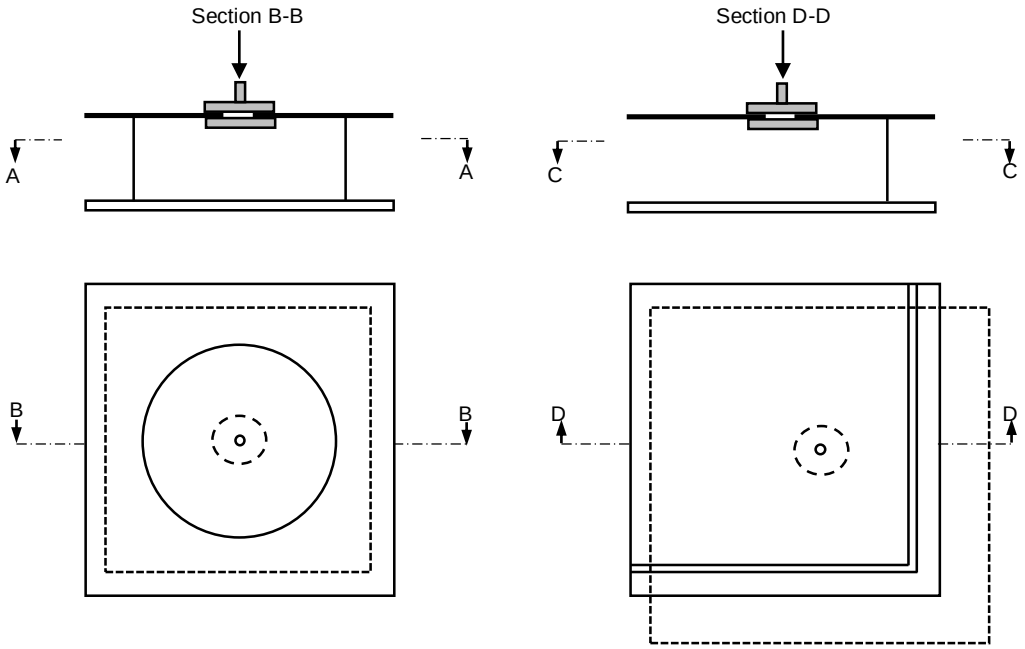

Figure 2.38 Small scale tests with symmetrical and eccentric support of the glass samples, from [Seibert-2006]

Each test is repeated twice: once with aluminium as interlayer material and once with the real interlayer materials. During the tests, strains are measured with linear gauges and rosettes along defined paths (Figure 2.39 and Figure 2.40). The gauges are applied along the paths till the borehole edge.

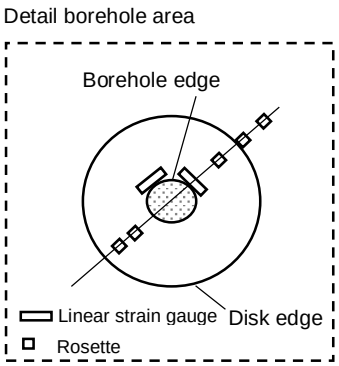

Figure 2.39 Example of strain positions, from (Siebert, 2006)

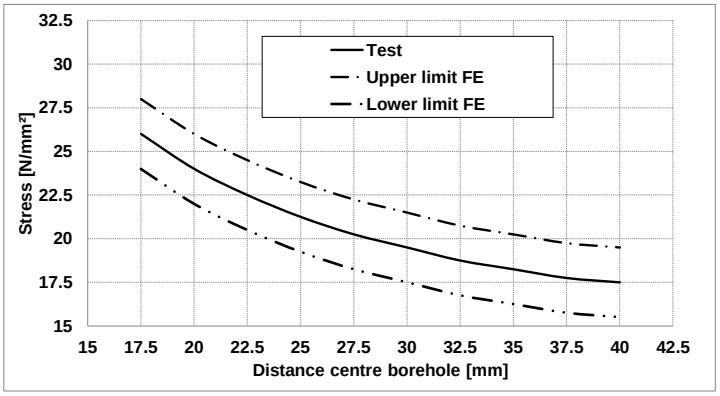

Figure 2.40 Example of stress distribution to be verified, from (Siebert, 2006)

Finally the stresses are calculated by means of the measured strains and implemented in data sheets for both interlayer materials.

The verification of the numerical model is done in three steps: First of all a die plate is modelled and subjected to tension. The stress peak occurring at the borehole is compared to the analytical solution (Young, 1989) to proof the mesh quality of the glass plate. In a second step, the small scale tests with aluminium as interlayers are simulated. The model has to determine the stresses in the data sheets on the safer side. Aluminium is used as interlayer material because of its well-known material properties. In this way, the contact definitions between the point fitting and the glass are verified. Finally the small scale tests with the real interlayer materials are simulated. The Young's Moduli of the interlayer materials are varied till the numerical model determines the stresses in the data sheet conservatively.

The calibrated model is subsequently implemented in the glass pane for design.

2.5.4 SLG-method (Beyer, 2007)

The SLG-method (**S**uperposition of **L**ocal and **G**lobal components) consists in the separation of the global behaviour of the glass pane from the local stress concentration in the borehole area. According to the principle of *Saint-Venant*, the stress concentration at the borehole decays at a distance of at least three times the borehole's diameter. From this distance on, the stress states in a plate with a hole and in a plate without a hole are identical. This leads to the definition of the local area which is a circular area around the borehole (Figure 2.41).

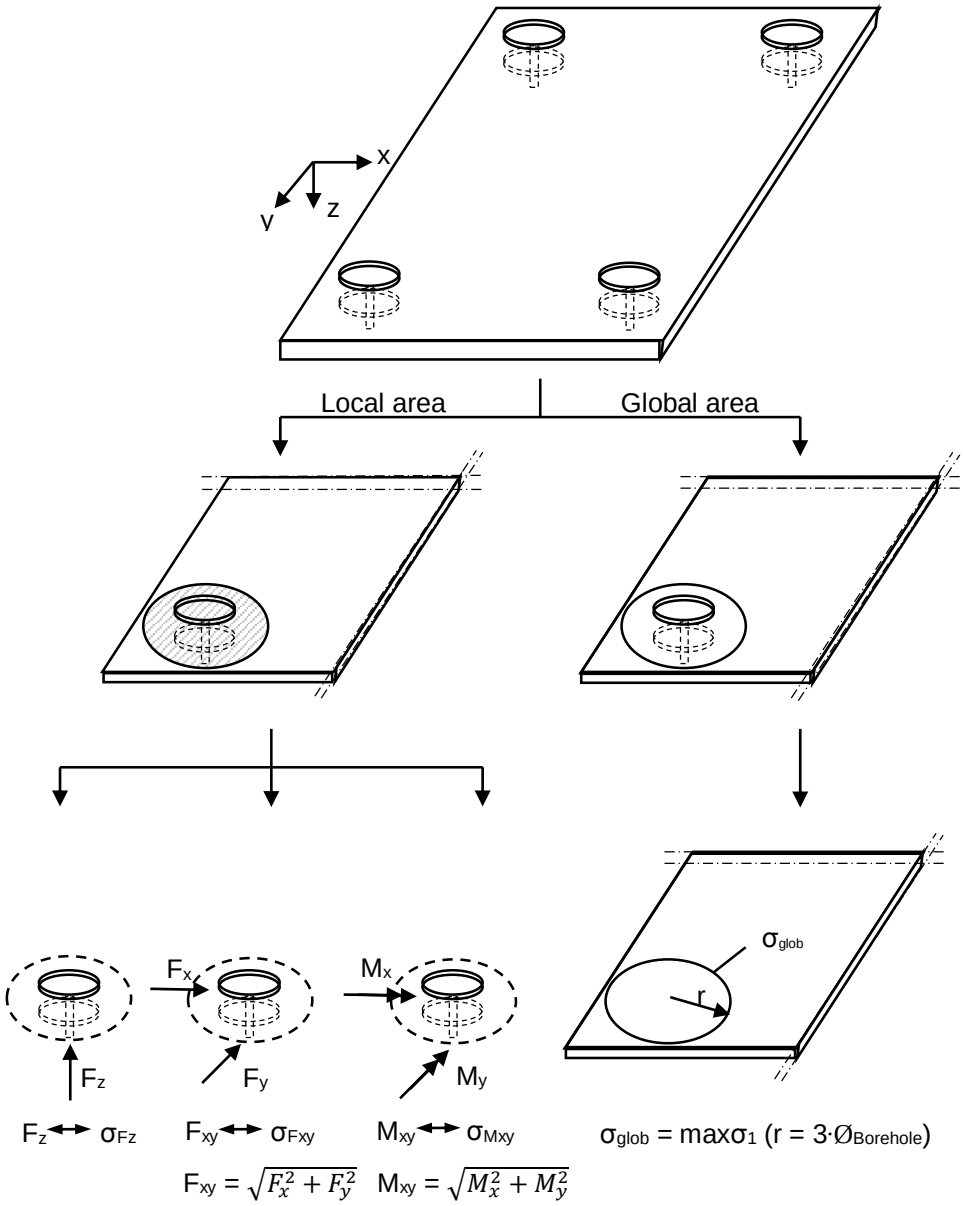

Figure 2.41 Concept of the SLG-method according to (Beyer, 2007)

The SLG-method capitalises the principle of *Saint-Venant* and proposes a simple two-dimensional FE-model of the glass plate for the design. The glass pane is modelled with shell-elements and the point fittings with springs of corresponding stiffness values. There is no need to model neither the borehole nor the complex three dimensional geometry of the point fitting. The stiffness values of the point fitting are experimentally determined in small scale tests by mounting the fittings in steel plates and subjecting them to tension, compression, shear and bending. The single support of the glass plate produces an infinite stress peak at this node and consequently the stress concentration at the borehole (local area) cannot be determined directly with the simple numerical model. According to the SLG-method, the stress concentration inside the local area is separated

into components assigned to the corresponding support reactions and linearly superimposed with the global component, represented by the main tensile stress at the rim of the local area (Beyer, 2009).

$$\sigma_{max} = \sigma_{F_z} + \sigma_{M_{xy}} + \sigma_{F_{xy}} + k \cdot \sigma_{glob} \quad \textbf{(2-1)}$$

The global component σ_{glob} is amplified by a stress concentration factor k, which considers the stress-increase at the borehole due to the flexion of the plate. The factor depends on the glass thickness, the borehole geometry and the position of the point fitting (e.g. edge distance). It is defined as the quotient between the stress peak at the borehole and the global component at the borderline of the local area.

The local stress components σ_N, σ_M, and σ_Q are determined by so called transfer functions (Beyer, 2007). The functions allow the conversion of the point fitting load to the corresponding stress peak occurring at the borehole. Alternatively, the stress components can be calculated by stress component factors (Beyer, 2009). The factors depend on the plate thickness, the stiffness of the interlayer, the point fitting and the borehole geometry. They are established for a reference plate thickness of 10mm and can be converted to any other glass thickness. The stress components are determined by multiplying the support reactions by the stress component factors (Beyer, 2009):

$$\sigma_{F_z/F_{xy}} = b_{F_z/F_{xy}} \cdot F \quad \textbf{(2-2)}$$

$$\sigma_{M_{xy}} = b_{M_{xy}} \cdot M \quad \textbf{(2-3)}$$

In preparation of a general technical approval, the stress concentration and component factors or the transfer functions are uniquely determined by a calibrated FE-model of the related point fitting and provided to the designing engineer.

The design according to the SLG-method is done in two parts: the global and local verification of the glass pane. For the global verification, the maximum tensile stresses and deformations at the mid-span or at the edge of the glass pane are determined with the simple two-dimensional FE-model and compared to the maximum permissible values:

$$\sigma_{vorh} \leq \sigma_{zul} \quad \textbf{(2-4)}$$

$$f_{vorh} \leq f_{zul} \quad \textbf{(2-5)}$$

The local verification consists in limiting the stress concentration at the borehole:

$$\sigma_{max} = \sigma_{F_z} + \sigma_{M_{xy}} + \sigma_{F_{xy}} + k \cdot \sigma_{glob} \leq \sigma_{zul} \quad \textbf{(2-6)}$$

The reaction forces in the point fittings are determined with the two-dimensional FE-model of the glass plate and converted to stress components by means of the transfer functions. The global stress component is also calculated with the simple FE-model and corresponds to the maximum tensile stress value at the rim of the local area. It is multiplied with the stress concentration factor to account for the stress-increase due to the flexion of the glass plate.

The permissible values for the stresses and the deformations are given by the valid general technical approval of the point fitting.

The SLG-method has been successfully implemented in the general technical approval of the Fischer FZP-G-Z (Z-70.2-122).

2.5.5 Discussion on the design methods

Strictly speaking, among the four design concepts presented in the previous sections, only the method according to *Brendler* (Brendler, 2004) and the SLG-method (Beyer, 2007) can be considered as state of the art. In fact, the methods according to *Kasper* (Kasper, 2006) and *Siebert* (Siebert, 2006) have not been implemented in any technical approval or standard yet.

In this section, the advantages and disadvantages of the different design methods are discussed:

The method according to *Brendler* is based on a mechanical model of the point fitting. Only numerical models able to realistically simulating the deformability of the point fitting are retained. The dependency of the interlayer stiffness on the temperature and on the loading type (static or dynamic) is considered by the stiffness range indicated in the general technical approval. Physically meaningless stiffness values for the interlayers are consequently avoided. Additionally, the numerical model of the point fitting is verified with a reference geometry described in the approval. In this way the non-sensitivity of the model against changing boundary conditions is proofed. The disadvantage of the method is its “trial and error” character. The material properties (Young’s modulus) of the interlayers have to be varied till accordance with the approval. With regard to the complex three-dimensional FE-model of the point fitting, the verification process may be time and cost consuming.

According to the method of *Kasper*, the numerical model of the point fitting is verified for different load introduction angles. The model is subsequent able to correctly simulate tension, compression, shear, moments and the different load interactions in the point

fitting. In addition, the compliance between the calculated and measured strains is verified for different paths and an accidental accordance is excluded. Furthermore, the calibration process proposed by *Kasper* has been verified on large scale tests and the insensitivity of the numerical model against changes of boundary conditions has been proofed (Kasper, 2006). However, no limits for the Young's modulus of the interlayer materials are indicated in the approval. In consequence, physical meaningless interlayer material properties can be chosen for the calibration of the numerical point fitting model. Furthermore, high demands are made on the measurement technique. The calibration is done with strain measurements and small deviations in the position of the strain gauges lead to high differences between the measured and calculated values.

The advantage of the method according to *Siebert* is the "step by step" calibration process to reduce error sources to a minimum. The mesh quality of the glass plate is individually verified and it can be optimized apart from other parameter influences. Moreover, the contact definition between the point fitting components and the glass is verified in a designated step. Only if the mesh quality and the contact definition are adequate, the stresses are numerically calculated and compared to the measured values in order to calibrate the model. By this "step by step" procedure, the risk of retaining a wrong FE-model for verification is minimized. The preliminary determination of input parameters for an approval is however time and cost intensive. Two different tests series have to be conducted: One with aluminium as material interlayer and a second with the real material. Additionally, strains are measured during the tests with specific gauges and rosettes and compared to the calculated values. As for the method of *Kasper*, measurement failures could lead to high deviation between the numerical and measured strains and to wrongly reject a specific model of the point fitting. Only compression tests are conducted for the calibration and the quality of the model under tension, shear and moments is not assured. Finally, the adaption of the calibrated model to the geometry to be design is not covered by large scale tests and its sensitivity to changing boundary conditions is not verified.

The SLG-method is the only design concept among the four methods, which is based on an engineering model. The behaviour of the glass plate is separated in a global and local area. A simplified two dimensional FE-model of the plate is sufficient to simulate the plate's global behaviour. The local stress concentration at the borehole is determined with so called load-stress diagrams by knowing the support reaction in the point fittings. The boreholes as well as the complex point fitting systems do not need to be simulated and modelling become easy. The risk of inaccurate simulation is reduced and the whole designing process is quick and straight forward. However, the maximum tensile stress

at the borehole is calculated by linear superposition of the stress components and the method is therefore highly conservative: between 15% and 56% for given glass pane geometries (Beyer, 2007).

2.6 DIN 18008-3

(DIN 18008-3) was published in 2013 and covers the design of point fitted glazing. In Germany, it will replace the (TRPV, 2006).

In the main part of (DIN 18008-3), the authorised construction elements, the application limits of point fitted glazing and additional regulations for vertical and horizontal point fitted glazing are described. It is important to notice that (DIN 18008-3) only covers two types of point fittings: button fittings with cylindrical boreholes and clamping disks without boreholes.

In general, the minimal number of point fittings is fixed to three and the minimal edge distance of the boreholes is limited to 80 mm. For horizontal glazing, only laminated glass made of heat strengthened glass leaves of the same thickness is allowed. Additionally, only button fittings or alternatively clamping disks are applicable for horizontal glazing and the post breakage behaviour has to be assured according to (DIN 18008-1). Only laminated glass made of fully tempered or heat strengthened glass is prescribed for the use of point fitted vertical glazing. If the glass is exclusively clamped, single fully tempered glass, laminated float glass and insulation glass can be applied. The ultimate and the serviceability limit state are verified according to [DIN 18008-1]. The maximum deflection of the glass pane is limited to 1/100 of the decisive span. FE-modelling is proposed as an adequate instrument for the design of point fitted glazing.

In annexe A of (DIN 18008-3), guide values for the different material properties of the interlayers are given.

A calibration method for the FE-model of the glass pane is described in annexe B of (DIN 18008-3). A die plate is subjected to pure bending and the stress peak at the borehole is calculated and compared to an analytical solution.

Annexe C delivers a design method for point fitted single glazing with button fittings exclusively. In fact, it is the SLG-method developed in (Beyer, 2007). The stress concentration and component factors are tabulated for different disk and borehole diameters. The local area corresponds to a circle with a radius of three times the borehole diameter.

In annexe D, ultimate load bearing tests for the point fittings are generally described. A methodology for the determination of the design value for the resistance of the connection point fitting-glass is proposed. Additionally, general information about the experimental determination of the point fitting stiffness values is indicated.

Essential content of (TRPV, 2006) has been adopted by the main part of (DIN 18008-3). Only minor changes have been made, for instance the minimal edge distance of the borehole and the maximal dimension of the glass plates. The annexes are however new and are based on the latest scientific outcome.

Compared to current regulations for point fitted glass (e.g. (TRPV, 2006)), (DIN 18008-3) is based on the partial safety concept. The glass plates are accordingly verified in the ultimate and serviceability limit state. The verification for both states consists in proofing that the design value of the impact does not exceed the design value of the resistance. The design value of the impact is determined according to (DIN 1055-100). All possible load combinations have to be analysed and the most unfavourable load case is finally retained for design. The design value of the resistance is calculated according to [DIN 18008-1].

2.7 Design of structural edge seal systems

Structural edge seal systems are applied in insulation glass units with the outer pane statically connected to the inner lite via the sealant. This is the case for point fitted insulation glass with the fittings only mounted in the inner pane and for structural sealant glazing.

In structural edge seal systems, the secondary sealant plays a load-bearing role and has to comply with the requirements on structural sealant applications. In Europe, the secondary sealant has to be designed according to (ETAG 002). (ETAG 002) only allows silicone as material for the secondary sealant and specifies the static design of the sealant. The calculation method is based on 7 years of experience with silicone and consists in determining the minimum covering thickness of the spacer with the secondary silicone sealant. The following three design steps are regulated in (ETAG 002):

- Transfer of permanent shear loading
- Transfer of permanent tension or compression loading
- Transfer of dynamic loading

The minimum covering thickness is determined for a permanent load acting in the glass pane and subjecting the edge seal to shear. This is for instance the case for the self-weight of a point fitted insulation glass unit with undercut anchors.

$$r > \frac{P}{2 \cdot b \cdot \Gamma_{\infty}} \quad \textbf{(2-7)}$$

r = minimum covering thickness [mm]

P = permanent shear load [N/mm^2]

b = long edge of glass pane [mm]

Γ_{∞} = permissible shear stress under permanent load [N/mm^2]

For horizontal glazing, self-weight subjects the edge sealant to permanent tension loads. In this case, the minimum covering thickness is determined as follows:

$$r > \frac{P}{2 \cdot (a + b) \cdot \sigma_{stat,rec}} \quad \textbf{(2-8)}$$

r = minimum covering thickness [mm]

P = permanent tension load [N/mm^2]

a = short edge of glass pane [mm]

b = long edge of glass pane [mm]

$\sigma_{stat,rec}$ = permissible static tension stress under permanent load [N/mm^2]

Finally the minimum covering thickness is determined for the transfer of dynamic loads. Dynamic loads for insulation glass units are wind loads, climate loads and live loads. The load combination which leads to the maximal overpressure in the cavity is decisive. In fact, the overpressure creates tension stresses in the secondary sealant and the minimum thickness is determined accordingly:

$$r > \frac{a \cdot P}{2 \cdot \sigma_{dyn,rec}} \quad \textbf{(2-9)}$$

r = minimum covering thickness [mm]

P = overpressure in the glazing cavity [N/mm^2]

a = short edge of glass pane [mm]

$\sigma_{dyn,rec}$ = permissible dynamic tension stress under dynamic load [N/mm^2]

In all cases, the lower limit for the minimum covering thickness is fixed to 6 mm by (ETAG 002).

The different permissible stresses for the silicone material of the secondary sealant are generally specified by the manufacturers, e.g. (Dow Corning, 2004). The values are experimentally determined and are based on 5%-fractile values derived from tension and shear tests conducted on samples conditioned at 23°C during 29 days according to (ETAG 002). The characteristic dynamic tension stress value is reduced with a factor of 6 (Dow Corning, 2004), (ETAG 002). In addition to the factor of 6, the characteristic shear and tension stress values under permanent load are divided by a safety factor of 10 to account for the creeping of the silicone (Dow Corning, 2004), [ETAG-002]. The safety factors on the material resistance are based on a global safety concept.

Beyond their mechanical resistance, structural edge seal systems have to comply with several quality requirements concerning the durability of insulation glass units. The edge seal configuration has to reduce the absorption of humidity and the gas loss rate of the insulation glass unit during its lifetime. Additionally, the adhesion of the secondary silicone sealant on the glass plates and on the spacer has to be assured. Corresponding test procedures are described for instance in (DIN EN 1279-2), (DIN EN 1279-3) and (DIN EN 1279-4).

2.8 Climate load models for insulation glass

The glass plates of insulation glass units are mechanically coupled via the gas in the glazing cavity. The outer glass pane deforms when subjecting to an external load (e.g. wind load) and the volume of the cavity changes. The volume change induces an over- or underpressure in the cavity, which finally acts on both glass panes. In addition, a change in temperature or barometric pressure creates a pressure difference between the cavity and the environment and consequently leads to a surface load on each glass pane. These are the so called “climate loads” (Feldmeier, 2006). Each glass pane deform under the effect of the climate loads. These deformations are the source of the distorted reflections of glass façades with insulation glass units (Figure 2.42).

Figure 2.42 Effect of climate loads on the aspect of a glass façade, Office building, Kirchberg

The design of insulation glass units requires the determination of the climate loads (Figure 2.43).

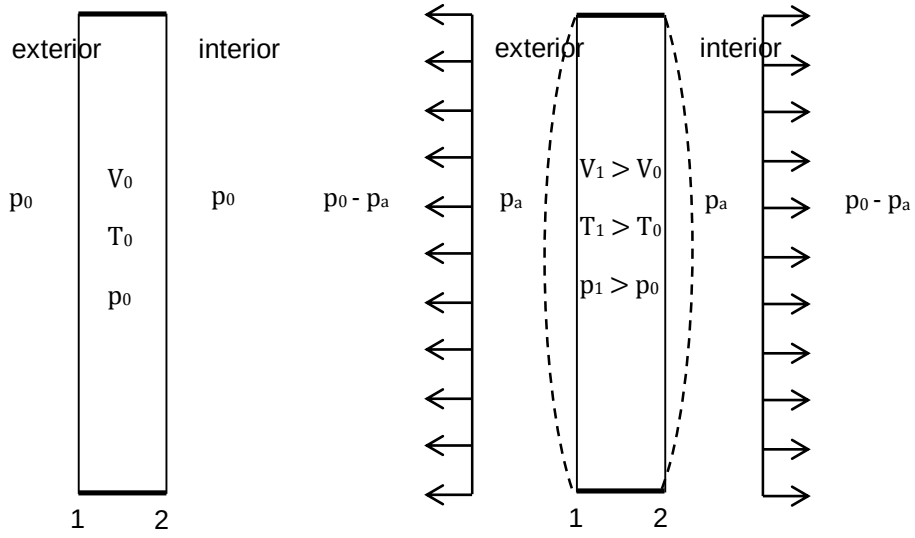

Figure 2.43 Climate loads of a linearly supported IGU for an overpressure in the cavity

Two different climate load models have been developed for linearly supported insulation glass: (Feldmeier, 2006) and (Schaller, 2013). For point fitted insulating glass, a practicable approach exists (Beyer, 2007).

2.8.1 Climate load model of *Feldmeier* (Feldmeier, 2006)

The climate load model developed in (Feldmeier, 2006) is valid for multiple insulation glass units linearly supported on its four edges. The model accounts for external surface, linear and point loads.

The method consists in analytically determining the gas pressure in the glazing cavity for given climatic conditions. Knowing the ambient pressure at the installation location, the pressure difference between the cavity and the ambiance is calculated and applied as surface loads on each glass pane of the insulation glass unit. The surface loads are finally superimposed with the external loads, like i.e. wind- and snow loads.

The edge bond is assumed to be a freely rotating but rigid line support for the edge of each single glass plate (Feldmeier, 2006). Each single glass pane is thus *Navier*-supported.

The deformation of the glass plates is assumed to be small and the volume spanned by the glass plates is consequently proportional to the loading:

$$\Delta V = \vartheta \cdot p \qquad \textbf{(2-10)}$$

The volume coefficient ϑ corresponds to the volume spanned by the glass pane under the unit load [$m^3/(kN/m^2)$]. It is analytically or numerically (FE) determined and only depends on the span relation of the pane.

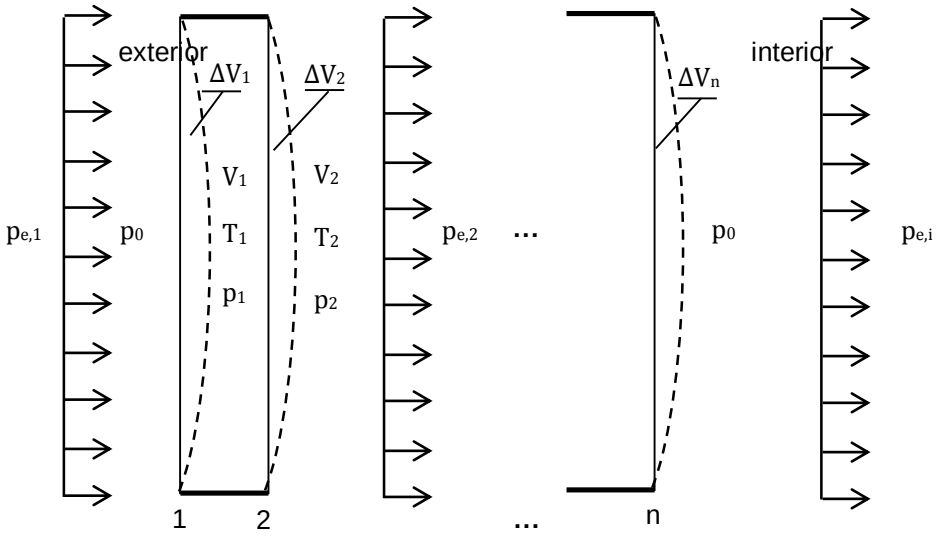

Figure 2.44 Notations for a linearly supported IGU, from (Feldmeier, 2006)

The volume of the cavity V_i (Figure 2.44) due to the deformation of the single glass panes is given by equation (2-11):

$$V_i = V_{pr,i} - \Delta V_i + \Delta V_{i+1} \qquad \textbf{(2-11)}$$

$V_{pr,i}$ = volume of the cavity at production location

ΔV_i = volume change of the cavity due to the deformation of plate i

ΔV_{i+1} = volume change of the cavity due to the deformation of plate i+1

Since the cavity is hermetically sealed, the gas quantity remains constant and the gas behaviour can be described by the ideal gas law:

$$\frac{p_i \cdot V_i}{T_i} = \frac{p_{pr} \cdot V_{pr,i}}{T_{pr}} \quad \textbf{(2-12)}$$

p_i = pressure in cavity i

V_i = volume of cavity i

T_i = temperature in cavity i

p_{pr} = pressure in cavity at production location

V_{pr} = volume of cavity i at production location

T_{pr} = temperature in cavity at production location

The equations (2-10) and (2-11) are placed into equation (2-12). Solving equation (2-12) for p_i delivers a system of coupled quadratic equations:

$$p_i \cdot \left(V_{pr,i} - \vartheta_{p,i} \cdot p_{i-1} + \left(\vartheta_{p,i} - \vartheta_{p,i+1}\right) \cdot p_i - \vartheta_{p,i+1} \cdot p_{i+1} - \Delta V_{ex,i}\right) = \frac{T_i}{T_{pr}} \cdot p_{pr} \cdot V_{pr,i} \quad \textbf{(2-13)}$$

Equation (2-13) is linearised under the assumption of small pressure variances between the production and installation location of the insulation glass unit and small volume changes compared to the volume of the cavity (Feldmeier, 2006). After mathematical transformation (Feldmeier, 2006), the term of the linearised system is expressed for doubled insulation glass unit with equation (2-14):

$$\begin{pmatrix} p_{res,e} \\ p_{res,i} \end{pmatrix} = \begin{pmatrix} -\varphi & 1 - \varphi \cdot \alpha & \varphi\alpha^+ \\ \varphi & \varphi \cdot \alpha & 1 - \varphi\alpha^+ \end{pmatrix} \cdot \begin{pmatrix} \Delta p_c \\ p_{ex,e} \\ p_{ex,i} \end{pmatrix} \quad \textbf{(2-14)}$$

$p_{res,e}$ = resulting surface loads on the external glass pane

$p_{res,i}$ = resulting surface loads on the internal glass pane

Δp_c = pressure difference in cavity due to climate loading

$p_{ex,e}$ = external surface load on external pane

$p_{ex,i}$ = external surface load on internal pane

φ = insulating glass factor

α = relative volume change of the external pane

α^+ = relative volume change of the internal pane

Finally, the resulting surface loads acting on each glass pane can be analytically determined with equation (2-14).

The climate load model according to (Feldmeier, 2006) has been implemented in the (TRLV, 2006) and in (DIN 18008-2).

2.8.2 Climate load model of *Schaller* (Schaller, 2013)

In linearly supported insulation glass, the characteristic of a line or point load acting for instance on the outer glass pane is lost for the indirectly charged inner glass pane. In fact, the inner glass pane is subjected to a surface load due to the coupling of the two glass panes via the gas in the glazing cavity. This surface load is proportional to the displaced volume of the outer glass pane.

Accordingly to (Schaller, 2013), the displaced volume can be defined as the product of the mean deflection with the pane surface. Since the mean deflection is proportional to the loading, the gas filling in the cavity can be replaced by coupled springs (Figure 2.45). Consequently, the determination of the resulting cavity pressure can be determined by means of the force method (Schaller, 2013).

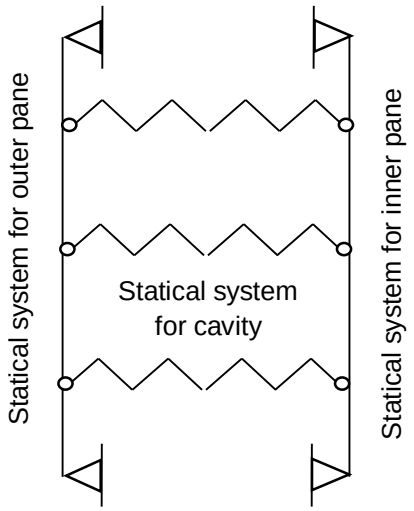

Figure 2.45 Replacement systems according to (Schaller, 2013), from (Schaller, 2013)

The “0-plan” consists in the outer glass pane, which is charged and decoupled from the inner glass pane (Figure 2.46).

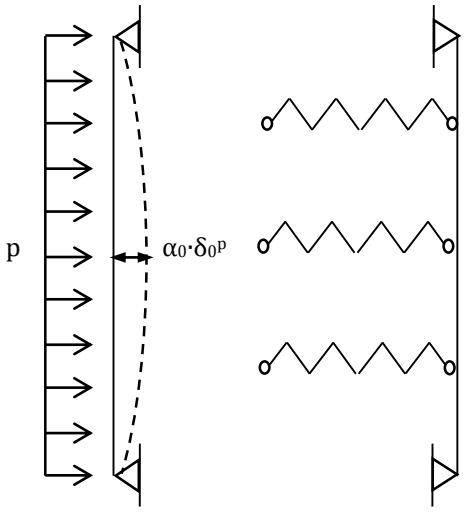

Figure 2.46 0-plan according to (Schaller, 2013), from (Schaller, 2013)

Its mean deflection is determined with equation (2-15):

$$\delta_0^P = \alpha_0 \cdot \max\delta^P \qquad \textbf{(2-15)}$$

δ_0^P = mean deflection of glass pane under the load p

α_0 = correction value

$\max\delta^P$ = maximal deflection of glass pane under the load p

The maximal deflection $\max\delta^P$ is numerically determined and the correction value α_0 is tabulated in (Schaller, 2013).

The “1-plan” is composed of the decoupled glass pane and springs under unit load 1 (Figure 2.47).

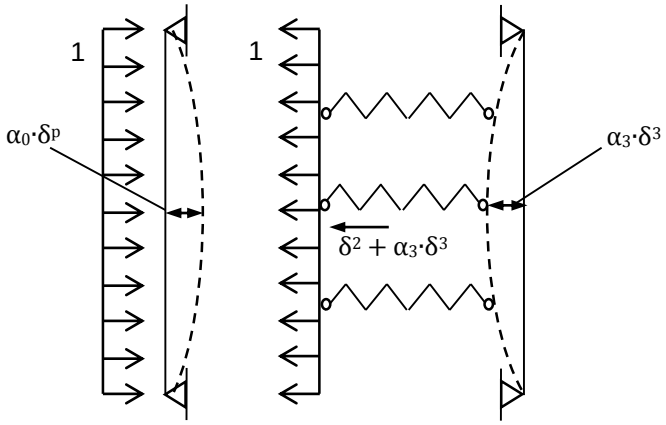

Figure 2.47 1-plan according to (Schaller, 2013), from (Schaller, 2013)

The displaced volume corresponding to the unit load 1 is given by equation (2-16):

$$V_1 = V_1^1 + V_1^2 + V_1^3 \quad \textbf{(2-16)}$$

V_1 = displaced volume under unit load 1

V_1^1 = displaced volume of the outer glass pane under unit load 1

V_1^2 = volume change in the cavity due to the gas rearrangement

V_1^3 = displaced volume of the inner glass pane under unit load 1

The volume change V_1^2 is determined with equation (2-17):

$$V_1^2 \approx V_{LZR} \cdot \frac{1}{p^0} \quad \textbf{(2-17)}$$

V_{LZR} = initial volume of the glazing cavity at production

p^0 = initial pressure in glazing cavity at production

Due to the inverse proportion between the volume and the pressure, equation (2-17) is an approximation with an error of less than 1% (Schaller, 2013).

With the two equations (2-16) and (2-17), the mean deflection of the outer glass pane can be calculated:

$$\delta_1 = \frac{V_1^1+V_1^2+V_1^3}{l_x \cdot l_y} = \delta_1^1 + \delta_1^2 + \delta_1^3 \quad \textbf{(2-18)}$$

$l_x \cdot l_y$ = pane surface

δ_1 = total mean deflection

δ_1^1 = mean deflection of the outer glass pane under unit load 1

δ_1^2 = elongation or contraction of the cavity under unit load 1 kN/m^2

δ_1^3 = mean deflection of the inner glass pane under unit load 1

The mean deflections of the outer and inner glass pane are determined with the equations (2-19) and (2-20):

$$\delta_1^1 = \alpha_1 \cdot \max\delta^1 \quad \textbf{(2-19)}$$

$$\delta_1^3 = \alpha_3 \cdot \max\delta^3 \quad \textbf{(2-20)}$$

δ_1^1 = mean deflection of the outer glass pane under unit load 1

δ_1^3 = mean deflection of the inner glass pane under unit load 1

α_1, α_3 = correction values

$\max\delta^1$ = maximal deflection of the outer glass pane under unit load

$\max\delta^3$ = maximal deflection of the inner glass pane under unit load

The maximal deflections are numerically determined and the correction values are tabulated in (Schaller, 2013).

Accordingly to the force method, the mean deflection δ_0^P under the load p and the total mean deflection δ_1 cancel each other. The pressure difference Δp between the glazing cavity and the ambiance can finally be determined with equation (2-21):

$$\Delta p = \frac{-\delta_0^P}{\delta_1} \quad \textbf{(2-21)}$$

In summary, the method according to (Schaller, 2013) allows the determination of the pressure difference by means of the force method. The maximal deflections of the glass panes have to be numerically determined with a corresponding FE-software. They are subsequently transferred to mean deflections by tabulated correction values and the pressure difference between the cavity and the ambiance can be calculated with the relations of the force method. The method is only valid for linearly supported insulation glass units.

2.8.3 Practicable approach for point fitted insulation glass units

A practicable approach for the determination of the climate loads for point fitted insulation glass units is described in (Beyer, 2007). It is called “inscribed rectangle” and consists in inscribing a rectangle in the point fitted insulation glass unit (Figure 2.48). The dimensions of the rectangle are defined by the positions of the point fittings. The climate loads are determined, assuming the point fitted insulation glass unit to be a linearly supported unit with the dimensions of the rectangle.

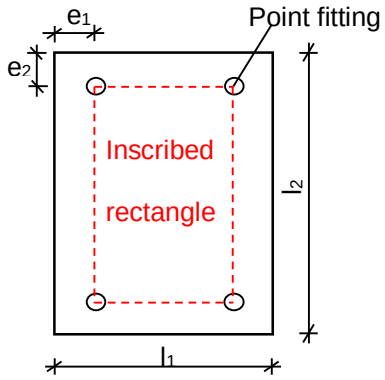

Figure 2.48 Inscribed rectangle

The approach however only roughly approximates the climate loads. In fact, a certain area of the glass surface is neglected according to the position of the point fittings. This surface nevertheless contributes to the volume change of the cavity and reduces the pressure change in the cavity. In conclusion, the approach overestimates the real climate loads and delivers improvident results and hence a conservative solution. Additionally, it is exclusively applicable to drilled through point fittings and cannot be used for undercut anchors.

3 Objectives and methodology

The objective of this work has been to propose a point fitted insulation glass unit with an appropriate point fitting type for vertical application in glass façade and to develop a corresponding design concept.

To achieve the objective, the research work proceeds in four parallel processes:

1. The “conceptual” process

In the conceptual process, the state of the art concerning point fitted glazing and insulation glass units in the building sector is recapitulated. The most suitable point fitting and seal system for point fitted insulation glass are chosen and a new point fitted insulation glass unit is proposed.

In a first step, the different point fitting systems on the market for single and insulation glazing are shorty presented in chapter 2. Their advantages and disadvantages are outlined in order to choose the optimal point fitting type for the application in insulation glass.

In a second step, the functionality and the assembling process of insulation glass units are presented and the most commonly applied edge seal systems for insulation glass are described in chapter 2. The edge seal systems are reviewed and their properties are assessed. The most appropriate system with regard to its application in point fitted insulation glass units with the chosen point fitting type is identified.

In a third step, a new point fitted insulation glass unit is derived in chapter 4. The novelty consists in the application of undercut anchors in an insulation glass unit with a structural dual-sealed edge system.

2. The “design” process

The application of undercut anchors in insulation glass raises the question of how to design the novel unit. The design concept has to include a model for the determination of the climate loads and engineering design checks for each structural element of the insulation glass unit. The existing design concepts are however only applicable to point fitted single glazing (section 2.5). In the design process, a novel design concept for point fitted insulation glass units with undercut anchors is therefore developed.

The requirements on the design concept for point fitted insulation glass units with undercut anchors and a structural edge seal system are defined in chapter 4. Based on the load transfer mechanism of the unit, the different structural elements to be verified are identified. An engineering design check for ech structural element is provided. A

comparison between the requirements on the novel design concept and the state of the art reveals the missing climate load model for point fitted insulation glass units with undercut anchors, i.e. a model which takes into account the distribution of an external load to the inner and outer glass pane of the insulation glass unit and which enables the determination of the surface load acting on the inner and outer glass pane due to pressure change of the gas inside the glazing cavity (Figure 3.1).

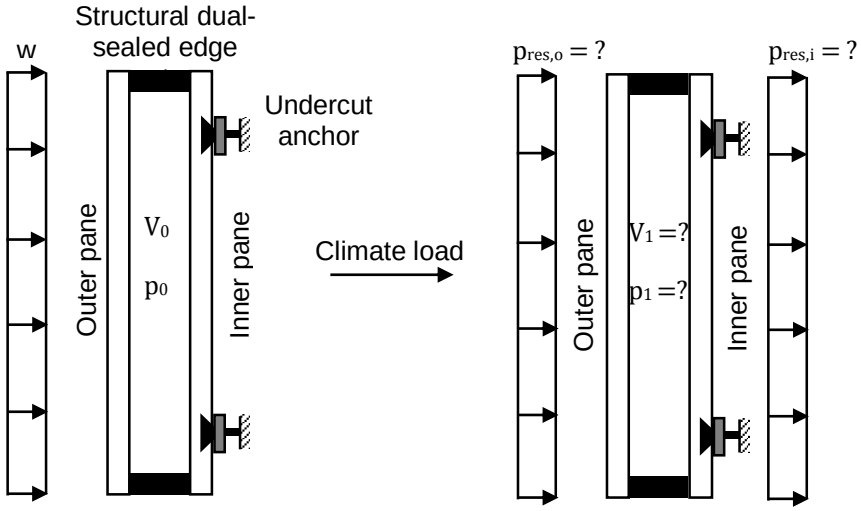

Figure 3.1 Climate load model for point fitted IGU with undercut anchors

In addition, an engineering design check for the inner glass pane of point fitted insulation glass units with undercut anchors is lacking, i.e. a method for the determination of the maximal tensile stress peak at the borehole and the maximal tensile stresses and maximal deformations in the field range of the inner glass pane (Figure 3.2).

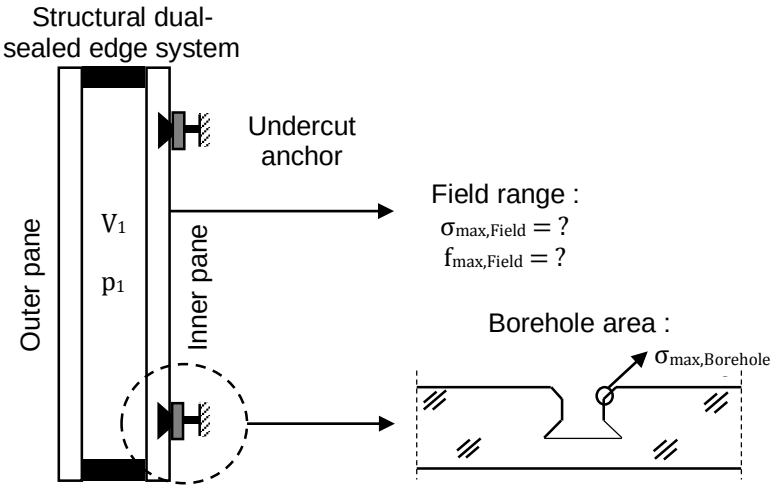

Figure 3.2 Engineering design check for the inner glass pane of point fitted IGU with undercut anchors

In consequence, a climate load model and a verification method for the inner glass pane of point fitted insulation glass units with undercut anchors need to be developed.

Therefore, the existing climate load model derived in (Feldmeier, 2006) for linearly supported insulation glass (section 2.8.1) is analytically extended to the static system of point fitted insulation glass units with undercut anchors in chapter 7. The so called “extended climate load model” is a novel climate load model which allows the determination of the load distribution on the inner and outer glass pane of a point fitted insulation glass unit with underuct anchors due to the external loads and climate loads. The extended climate load model is numerically and experimentally verified in chapter 7 respectively in chapter 9.

Additionally, the SLG-method developed in (Beyer, 2007) for the verification of point fitted single and laminated glazing (section 2.5.4) is extended to the use for point fitted insulation glass unit with undercut anchors in chapter 8. A general procedure for the extension of the SLG-method is developed and applied to the specific case of the point fitted insulation glass unit with the Fischer undercut anchor FZP-G-Z. Based on parameter studys, the three key parameters of the SLG-method (i.e. the size of the local area, the transfer functions and the stress concentration factors) are subsequently adapted to the static system of point fitted insulation glass units with the Fischer undercut anchors. In addition, the verification inequalities for the stresses and deformations in the field range and the stress peak at the borehole of the inner glass pane are derived. Finally the general application procedure of the extended SLG-method is presented in form of a flow-chart. The so called “extended SLG-method” allows the verification of the inner glass pane of point fitted insulation glass unit with undercut anchors. The accuracy of the exteneded SLG-method is experimentally proofen in chapter 9.

3. The “experimental investigations” process

The “experimental investigations” process includes small scale tests on the different components of the proposed point fitted insulation glass unit and large scale tests on the entire insulation glass unit.

Component tests on the chosen undercut anchor in monolithic glass are conducted in chapter 6. The anchor is subjected to tension, shear and bending in order to determine the ultimate service load of the connection point fitting - glass. Additionally, strains are measured along defined paths during the tests and a data set is created for later calibration of a corresponding numerical model.

Finally, the overall load bearing behaviour of the proposed point fitted insulation glass unit is investigated in large scale tests in chapter 9. The climate loads, wind loads and

the self-weight are applied on the unit and the deformations and strains of the glass panes are measured. The values are compared to the numerical values to verify the numerical model of the point fitted insulation glass unit. Additionally, the test results allow the experimental validation of the extended climate load model.

4. The “numerical simulation” process

The process implies the numerical simulations of the component and the large scale tests of the “experimental investigation” process.

A numerical model of the selected undercut anchor is developed in chapter 6. The model is calibrated by comparison of the numerical values to the results of the component tests conducted on the undercut anchor.

Additionally, two different numerical models of the derived point fitted insulation glass unit are implemented in FE software. The first model is a complex volume model with 3D-solid elements and it is developed in chapter 9. It takes into account the exact geometry of the borehole, the point fitting and the edge bond system. The second model is a simplified model with 2D-shell elements for the glass panes and it is developed in chapter 5. The undercut anchors are replaced by springs of corresponding stiffness values and hence the borehole is not modelled. The second model considers the exact edge bond geometry with 3D solid elements. The first model is used for the planning of the large scale tests and is finally calibrated by means of the test results. It is used for the experimental verification of the extended climate load model in chapter 9 and a parametric study concerning the influence of the edge bond configurations on the stress peak at the borehole in chapter 8. The second simplified model is used for the numerical verification of the extended climate load model in chapter 7 and for the extension of the SLG-method for the verification of point fitted single glazing to point fitted insulation glass units with undercut anchors in chapter 8.

The outline of the research work is shown in Figure 3.3:

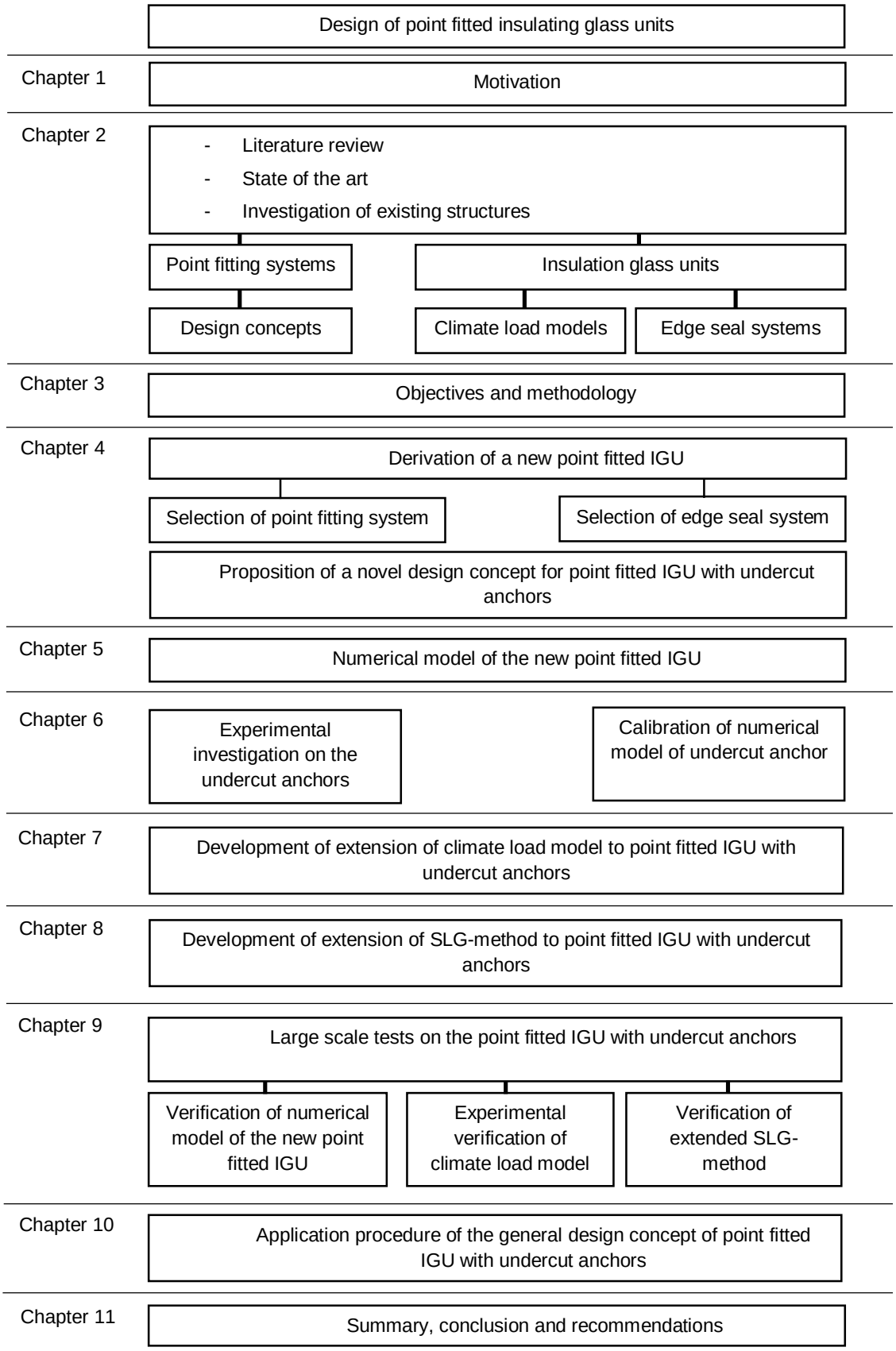

Figure 3.3 Outline of the research work

4 Derivation of a new insulation glass unit with point fittings

4.1 Background

A state of the art investigation concerning the existing point fitting systems for insulation glass reveals the complexity of their mounting procedure in insulation glass. In addition, any general design concept for point fitted insulation glass units exists and point fitted insulation glass units are currently non-regulated construction elements. Therefore a new point fitted insulation glass unit with an appropriate point fitting system and the need of a design concept (section 4.5) is given in this chapter.

4.2 Judgement and selection of a suitable point fitting type

A suitable point fitting system for insulation glass has to assure a technical easy and quick mounting procedure. Additionally, its realisation must not compromise the tightness of the glazing cavity and must not reduce the thermal performance of the overall glass unit.

As outlined in section 2.4, three different point fitting systems for insulation glass unit are currently applied in glass façades. They are however complex connection systems with high requirements on the mounting procedure. Minor deviations from the tolerances lead to initial failure of the connection or potentially cause leakage of the glazing cavity under long-term loading. In consequence, the application of point fitted insulation glass units in façades by means of the three existing systems requires the support of specialised manufacturers and designers and is expensive. In addition, a service life of 20-30 years, as presumed for linearly supported insulation glass, cannot be achieved. In the following, a detailed judgements on the existing point fitting systems for insulation glass is done:

The main concerns for drilled through point fittings are the construction tolerances and the tightness of the glazing cavity at the boreholes. A misalignment of the boreholes in the inner and outer glass panes in the assembling process of the insulation glass unit generates high stresses at the borehole and a premature failure of the unit. This especially applies for countersunk fittings and laminated glazing. Countersunk fittings do not allow the compensation of construction tolerances and in the lamination process a further misalignment between the glass leaves occurs (Siebert, 2004). In addition, the tightness of the cavity under long-term loading is hard to assure. The circular edge seal around the point fittings is permanently compressed by the clamping disks of the point fitting and subjected to cyclic loading by the climate loads. The sealant materials

consequently creep. The tightness of the sealant materials also strongly depends on the manufacturing quality of the connection. Ignoring mounting tolerances induces constraining forces in the sealants and gradually weakens the materials. Moreover, the steel bolt penetrates the unit in its entire extend and creates a direct link between the outside and the inside of the building. Consequently the point fitting consists in an additional thermal bridge. Finally, the outer clamping disk or countersunk head disrupt the transparency of the unit.

As for the drilled through fittings, the construction tolerances and the tightness of the cavity are the main issues for planar point fittings. Due to its conical section, the borehole cannot be oversized and tolerances cannot be compensated accordingly. In consequence, a precise mounting of the point fitting is indispensable to avoid high stress peaks in the glass. Under cyclic and long-term loading, the sealant materials for the interlayers are likely to lose their tightness and gas leakage at the borehole occurs (Panait, 2007). Additionally, the deformation of the inner and outer glass panes have to be reduced to avoid contact between the outer glass pane and the clamping disk of the point fitting in the glazing cavity.

The ultimate load bearing resistance of embedded point fittings strongly depends on the properties of the interlayer materials (Cruz, 2014). These materials are affected by environmental factors, such as temperature, humidity and radiation. Temperature has been revealed as the most influencing parameter. For high temperatures beyond the glass transition temperature, the shear stiffness significantly decreases and air bubbles occur, indicating the delamination of the interlayer. (Serafinavicius, 2014). Additionally, the adhesion properties of the interlayer depend on the production process (Froli, 2012). The storage humidity for instance has a high influence on the adhesion property of PIB. As a consequence, the load bearing resistance of embedded point fittings depends on atmospheric exposure and the manufacturing quality of the laminated glass.

In Table 4.1, the advantaged and disadvantages of the existing point fitting systems for insulation glass are condensed.

Table 4.1 Advantages and disadvantages of point fitting systems for IGU

Point fitting	Figure	Advantages	Disadvanatges
Button fittings		- Compensation of tolerances - Low stress peak - High post breakage behaviour	- Production procedure - Mounting procedure - Reduced transparency - Additional thermal bridge - Tightness of the cavity
Countersunk fittings		- Even outer pane - High transparency	- Production procedure - Mounting procedure - Reduced transparency - Additional thermal bridge - Tightness of the cavity - High stress peak
Planar fitting		- Even outer pane - High transparency - Reduced thermal bridge	- Production procedure - Mounting procedure - Low post breakage behaviour - Tightness of the cavity
Embedded fitting		- Even outer pane - High transparency - Reduced thermal bridge - No tightness problem for cavity	- Sensitive to UV and humidity - Long-term behaviour

Undercut anchors are described in section 2.2.2. Currently, they are exclusively used in single and laminated glazing. In this research work, the potential of undercut anchors in insulation glass is elaborated:

First of all, the production and installation of an insulation glass unit with undercut anchors is straightforward. The boreholes are drilled in the inner glass pane. The inner and outer glass panes are tempered and assembled to an insulation glass unit. In a last step, the anchors are mounted. On the construction site, the unit is directly installed with the anchors to the substructure.

Secondly, the anchors are only partially drilled in the inner glass pane and do not penetrate the glazing cavity, which remains intact (Figure 4.1). In consequence, its tightness in the anchor area is assured without any additional sealant system, e.g. sealant ring around the steel bolt as for drilled through fittings. Additionally, the anchor does not create a direct link between the outside and the inside of the building and the thermal bridge due to the anchor is marginal compared to the currently applied point fitting systems.

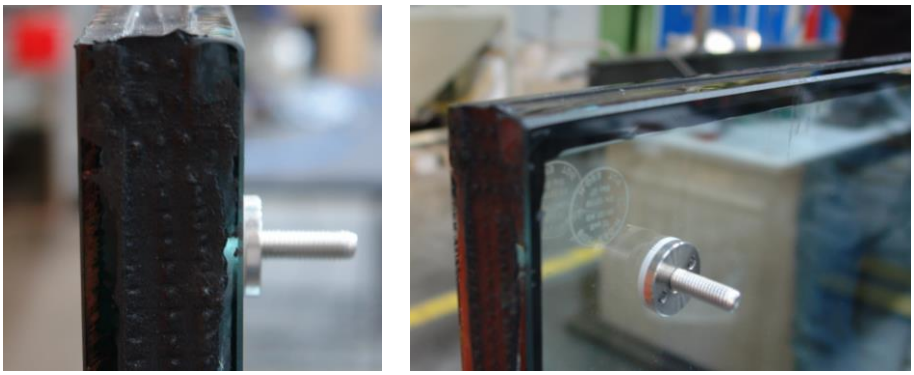

Figure 4.1 The Fischer undercut anchor FZP-G-Z in IGU

Thirdly, the application of undercut anchors in laminated glass with two plies is possible. Laminated glass offers additional safety in case of glass breakage and undercut anchors in laminated glass have a higher load bearing resistance than in single glazing. Compared to embedded point fittings (section 2.4), the undercut fittings are anchored in the second ply and not directly in the interlayer. Consequently, the load bearing resistance of the connection is independent from the property change of the interlayer materials.

Finally, the outer glass pane remains flat and visually masks the anchor in the inner pane. In combination with the small size of the undercut anchors (section 2.2.2), the transparency of the insulation glass unit is higher than with any other point fitting system.

As a result, the application of undercut anchors in insulation glass requires less steps than for the currently applied three point fitting systems and permits a time- and cost reduced production. Moreover, the risk of leakage of the glazing cavity is limited to a minimum and leads to a potential higher service life of the insulation unit. In addition, the thermal performance of insulation glass with undercut anchors is improved, since the thermal bridge due to the anchors is only marginal. Finally, undercut anchors are only of small size and the transparency of the insulation unit is increased.

Undercut anchors combine an adequate service life and thermal performance with high transparency and a simple production process of insulation glass units.

In consequence, the application of the Fischer FZP-G-Z in insulation glass units is proposed in this research work. More precisely, the Fischer undercut anchor FZP-G-Z is chosen (Figure 4.1). In fact the Fischer anchor has a general technical approval for single and laminated glazing (Z-70.2-122). Important properties like its geometry, stiffness and the material properties of its components are well known. In addition, the SLG- design method (Beyer, 2007) on which is based the design concept in the approval is potentially

extendable to point fitted insulation glass unit. Finally, the potential of undercut anchors in insulation glass justifies the choice of the Fischer undercut anchor.

4.3 Judgement and selection of a suitable edge bond system

In point fitted insulation glass units with undercut anchors, the edge bond transfers the loads from the outer to the inner pane (section 4.5.2). In consequence, it has to meet the requirements set on a structural edge seal system. Despite of their good thermal insulation performance, thermoplastic spacers have been rejected, as they are unable to carry any compressive loads (section 2.3.3).

Consequently, a structural dual-sealed edge system is proposed for the insulation glass unit. The primary sealant is made of PIB and solely tightens the glazing cavity. It has no structural function. For the secondary sealant, the thermally and mechanically stable Dow Corning DC 993 structural silicone is chosen. It transfers the traction loads and the self-weight from the outer to the inner pane. The spacer transmits the compression loads. Since the compression loads in the edge seal of point fitted insulation glass units with undercut anchors can reach high values (i.e. winter climate loads), a metallic spacer made of aluminium is chosen. Plastic spacers have a lower thermal conductivity than metallic spacers, but they have a lower stiffness (E = 1000 N/mm^2 for PP and E = 2000 N/mm^2 for PC) and are not able to transfer the compressive loads occurring in the edge seal of point fitted insulation glass units with undercut anchors.

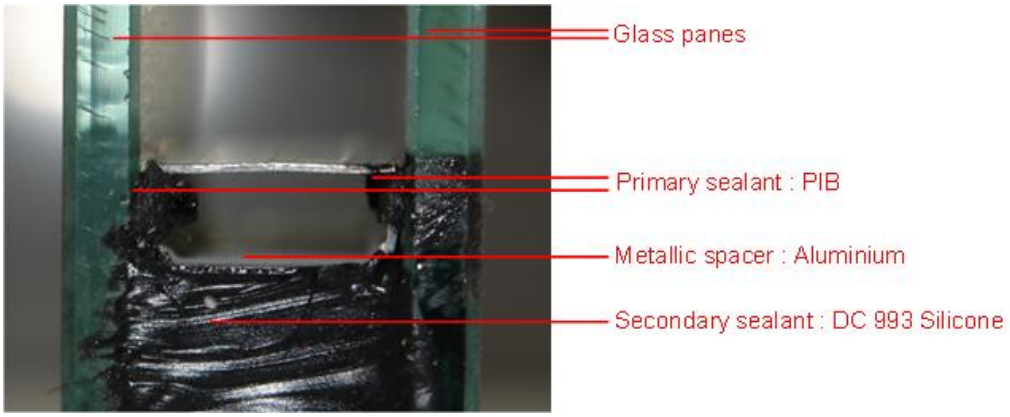

Figure 4.2 Proposed edge seal system

4.4 Proposed point fitted insulation glass unit with undercut anchors

An insulation glass unit with the Fischer undercut anchor FZP-G-Z and the dual edge-seal system as described in the sections 4.2 and 4.3 is proposed in this research work.

Figure 4.3 Proposed IGU with the Fischer undercut anchor FZP-G-Z

The proposed unit is a double insulation glass unit made of fully tempered glass panes. Technically, the Fischer undercut anchor can be drilled in single glass panes of thicknesses in the range of 8 mm to 15 mm and in laminated glass of 10 mm + 8 mm thick fully tempered glass panes [Z-70.12-122]. For the outer glass pane, there are any restrictions.

Generally, at least one glass pane of insulation glass is made of laminated glass to improve its post breakage behaviour and shock resistance. The load bearing behaviour of laminated glass panes however changes with the properties of the interlayer foil. Additional investigations on the different interlayer materials are necessary to cover the behaviour of point fitted insulation glass units with laminated panes. This research work deals with the basic principle of the load bearing behaviour of undercut point fitted insulation glass and therefore laminated glass is not considered.

Consequently, the point fitted insulation glass units with the Fischer undercut anchor experimentally investigated in this research work are made of two fully tempered single glass panes.

4.5 A novel design concept for point fitted IGU with undercut anchors

4.5.1 Background

The design of point fitted glazing is a complex task. For single glazing, the main concern consists in the determination of the stress peak occurring at the borehole. In consideration of a missing analytical solution, several methods have been developed for the numerical determination of the stress concentration (section 2.5). The SLG-method has been revealed to be the most appropriate design method. It is based on an engineering model, it only requires a simple 2D FE-model of the glass plate and the point fittings are replaced by springs with corresponding stiffness.

Compared to single glazing, the design of point fitted insulation glass units is related to further challenges. In insulation glass, the compression or expansion of the encapsulated gas in the glazing cavity additional loads the glass panes (section 2.8). A climate load model for undercut point fitted insulation glass does currently however not exist. Additionally, the stress peak at the borehole in IGU cannot be determined with the methods in section 2.5, as they are only applicable to single glazing. Finally, a design concept for point fitted IGU with undercut anchors, which gives a general procedure for the design of the different structural elements, is currently inexistent. In consequence, individual case approvals with involved time-consuming numerical simulations and expensive test campaigns are mandatory for the application of point fitted insulation glass in façades.

The missing design concept restricts the practicable application of the point fitted insulation glass unit with the Fischer anchor proposed in chapter 3. The procedure to get an individual case approval is too inefficient for most designing offices. Accordingly, the thermal potential and further advantages of point fitted insulation glass units with undercut anchors are currently not capitalised in glass façades.

In this work, a general design concept for undercut point fitted insulation glass units is proposed. It considers the determination of the climate loads and the verification of each structural element of the unit.

4.5.2 Requirements on a design concept

To define the requirements on a design concept, the structural elements of point fitted insulation glass with undercut anchors have to be determined. Therefore, the loads acting on the IGU and its load bearing behaviour are investigated (Figure 4.4).

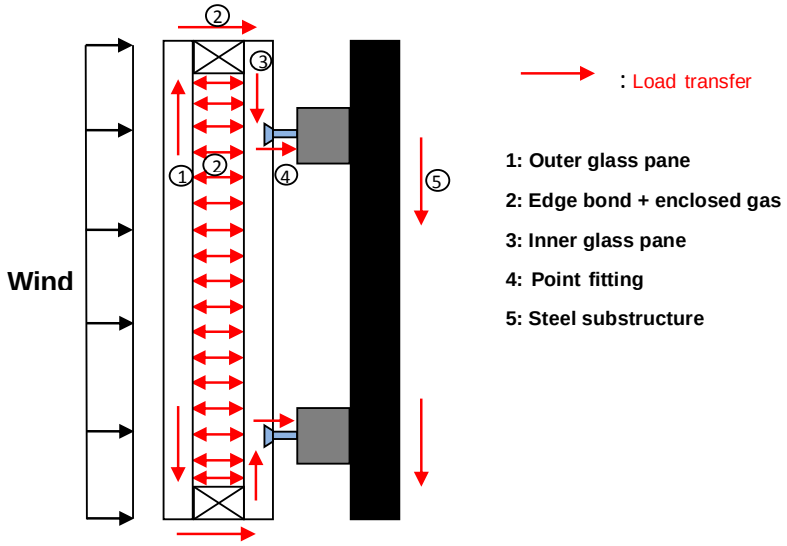

Figure 4.4 Load transfer of point fitted IGU with undercut anchors in vertical glazing application

In vertical glazing applications, point fitted insulation glass units are subjected to the in-pane acting self-weight and the out-of-pane acting wind and climate loads (section 2.8). The self-weight of the outer pane is transferred to the inner pane via the edge seal system exclusively. The wind loads on the outer glass pane are transferred to the inner pane via the edge seal system and with the gas in the glazing cavity via its compression or expansion. From the inner glass pane the loads are transferred to the substructure via the point fittings.

In conclusion, the development of a design concept for point fitted IGU with undercut anchors requires a corresponding climate load model and a method for the determination of the stress peak at the borehole. Therefore, the climate load model of (Feldmeier, 2006) for linearly supported IGU and the SLG-method for single glazing are extended to point fitted IGU with undercut anchors (chapter 7 and chapter 8).

4.5.3 Proposed design concept for point fitted IGU with undercut anchors

A general design concept for point fitted insulation glass units with undercut anchors for vertical glazing applications (max. inclination 10%) is proposed in the following.

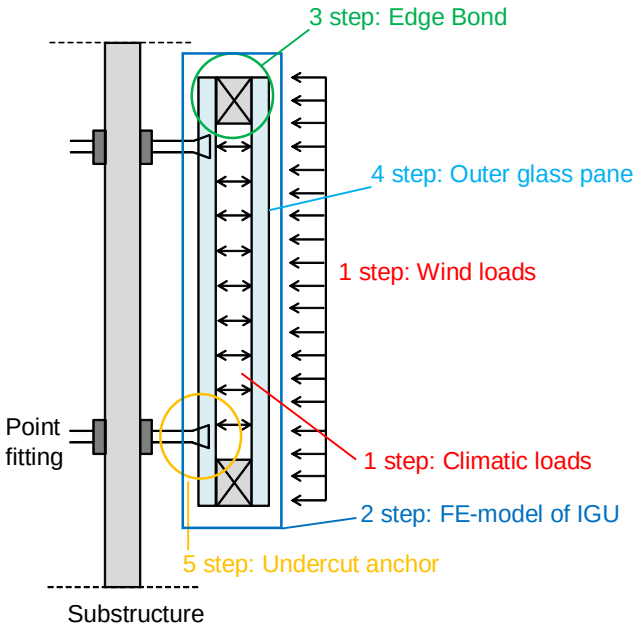

Figure 4.5 Elements of the point fitted IGU to be verified

The design procedure proceeds in 5 steps (Figure 4.5) (Hechler et al., 2012):

Loadings:

1. In a first step, the outer and inner loads acting on each glass pane are determined. The outer loads, e.g. wind, are determined according to the respective standard (DIN 1055-4) or (DIN EN 1991-4). The inner climate loads are calculated with a climate load model developed in chapter 7.

FE-model:

2. In a second step, a numerical model of the insulation glass units is implemented in an appropriate FE-software. Due to the coupling of the two glass panes via the edge bond system, it is not possible to study them independently and the two glass panes with the edge bond system have to be numerically modelled. The point fittings are represented by springs with corresponding stiffness values and the glass panes are modelled with 2D-shell elements. The edge bond is represented with 3D-solid elements, taking into account its detailed geometry and the material laws for the different components.

Design of edge bond:

3. In a third step, the structural edge bond is verified according to (ETAG 002). The minimal covering thickness of the secondary sealant is determined in dependency of the stress state in the silicone and its ultimate design strength (ETAG 002) (section 2.7).

Design of outer glass pane:

4. Fourthly, the outer glass pane is verified. The maximal tensile stresses and deformations are numerically determined with the simple 2D-FE model and checked against the ultimate glass strength respectively deformations given in (TRLV, 2006) or (DIN 18008-1).

Design of inner glass pane and point fitting:

5. In a last step, the inner pane is verified according to the extended SLG-method (chapter 8). The stress peak at the borehole is determined and limited to the ultimate glass strength. In parallel, the maximal tensile stresses and deformations at mid-span or the edges of the glass pane are numerically determined and compared to the permissible values in (TRPV, 2006) or in (DIN 18008-3)

The structural design of a point fitted IGU with undercut anchors according to the proposed design concept is based on simple numerical modelling (chapter 5) and is done without testing. In addition, the design concept can be applied to any undercut anchor and edge seal system. The stiffness values of the point fitting in question are previously determined by testing and delivered in data sheets provided by the producers. The user adapts the stiffness values of the springs and the geometry and material properties in the numerical model to the corresponding anchor respectively edge seal system.

4.6 Conclusion

A general design concept for point fitted IGU with undercut anchors for vertical glazing application is proposed. The concept is based on the load bearing mechanism of the unit and is structured in 5 steps. The climate loads are determined with an appropriate climate load model adapted to the static system of point fitted insulation glass units with undercut anchors (chapter 7). The elements to be verified are the outer glass pane, the edge seal system and the inner glass pane. The edge bond is verified according to the method described in (ETAG 002). The glass panes are verified numerically and the insulation glass unit is implemented in a FE-software. Since the stress peak at the borehole of the inner glass pane is determined with an extended SLG-method (chapter 8) for point fitted IGU with undercut anchors, a simple FE-model of the unit is sufficient. The modelling of the borehole and point fitting geometries as well as the definition of contact elements do not apply.

The general design concept can be applied to any undercut anchor type and edge bond geometry. The stiffness values of the springs have to be adapted to the point fittings in question and the edge bond has to be modelled with the corresponding geometry and material properties. The stiffness values of the point fittings are experimentally determined beforehand and delivered in data sheets of the anchors. The concept is based on an engineering logic for the determination of the climate loads and the stress peak at the borehole of the inner pane. In conclusion, the proposed concept allows a test-free design of point fitted insulation glass units with undercut anchors and rigorously simplifies the numerical modelling.

5 Numerical model of the point fitted IGU with undercut anchors

A numerical model of the point fitted insulation glass unit with undercut anchors is needed for the design. In this section, the requirements on the model are described.

Since the glass panes of point fitted insulating glass units with undercut anchors are coupled via the edge bond system, it is impossible to study them independently and the numerical model consists of the two glass panes which are linked at their edge by the edge bond system.

The edge bond is modelled with its true geometry and material properties. For the dual-sealed edge bond system as described in section 4.3 for instance, 3D solid elements are used for the secondary sealant and the metal spacer (Figure 5.1). The primary sealant is not modelled, since it has no structural function. The metal spacer is numerically tied to the silicone sealant. This means, that the nodes of the spacer and the sealant experience the same deformations and that the secondary sealant cannot detach from the spacer. The hyper-elastic material law developed in (Dias, 2013) is applied to simulate the behaviour of the secondary silicone sealant. A linear elastic material law with a Young's Modulus of E = 70000 N/mm² and a Poisson's ratio of ϑ = 0.3 is assessed for the aluminium spacer.

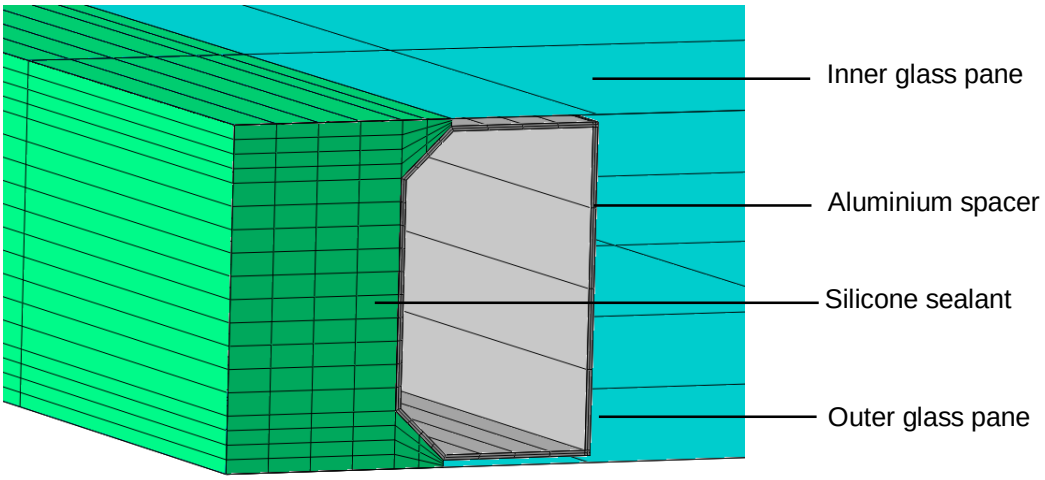

Figure 5.1 FE-model of the dual-sealed edge bond system

As the inner glass pane is verified according to the extended SLG-method (section 4.5.3 and chapter 8), the undercut anchors and the complex borehole geometries (Figure 5.2) do not need to be modelled. The longitudinal, lateral and rotational stiffness of the undercut anchor are represented by springs. In this way, the inner and outer glass plates

can be modelled with 2D shell elements (Figure 5.3) and the complex contact definitions (section 6.3.1) between the undercut anchor and the inner glass pane are omitted. The nodes on the four edges of the glass plates and the corresponding nodes of the secondary sealant are numerically coupled and undergo the same deformations. The glass plates cannot detach from the edge seal system consequently. The material glass is implemented in the FE-software with a Young's Modulus of E = 70000 N/mm² and a Poisson's ratio of ϑ = 0.23.

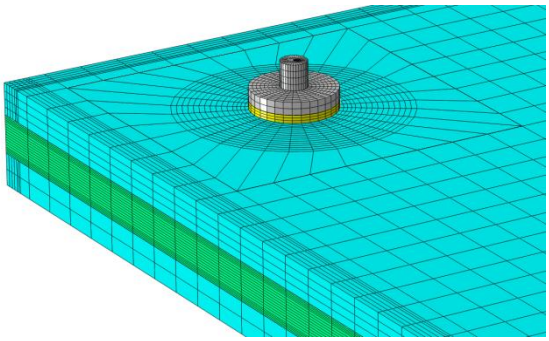

Figure 5.2 Complex 3D FE-model with the exact geometry of the borehole and the undercut anchor (here: FZP-G-Z)

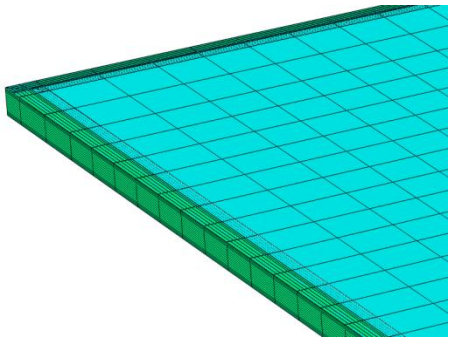

Figure 5.3 Simple 2D FE-model without the borehole and the undercut anchor modelled with springs

Due to the fact that the inner and outer glass pane are modelled with 2D-shell elements and that the undercut anchors are replaced by springs, the numerical model is also referred to as a simple 2D-FE model (Figure 5.4).

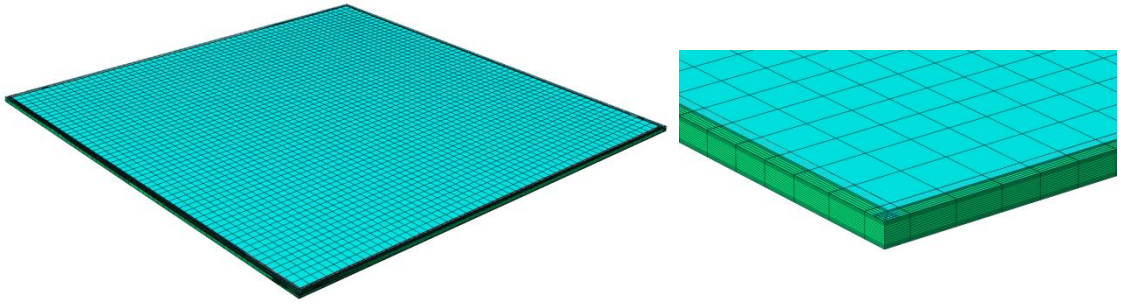

Figure 5.4 Simple 2D FE-model of the point fitted IGU with undercut anchors

The numerical model of the IGU (Figure 5.4) is verified in chapter 9 by comparing the numerically determined glass strains and deformations to the experimental values of the large scale tests. By this way, the approach of replacing the complex numerical model reflecting the detailed borehole and point fitting geometry with a simple model without any holes, point fittings and contact definitions is experimentally approved.

6 Investigations of the Fischer undercut anchor in monolithic glass

6.1 Objectives

In a test campaign, component tests have been conducted on the Fischer undercut anchor in fully tempered monolithic glass and the test results are validated with the resistance values given in the German technical approval (Z-70.2-122). In this way, the reliability and reproducibility of our own test results for a changed environment are also confirmed and the values in the technical approval are solidified. Additionally, a data set is created with the test results in order to calibrate and verify our own FE-analyses of the Fischer anchor.

6.2 Component tests of the Fischer undercut anchor in monolithic glass

6.2.1 Test description

The “Institut für Konstruktiven Ingenieurbau (IKI) der Universität für Bodenkultur in Wien” has already conducted for the establishment of the general technical approval [Z-70.2.122] the accordant tests (Tibolt, 2013).

The test set-up developed at the University of Luxembourg (Figure 6.1) is similar to the test configuration at the IKI. The glass samples are positioned on a polyamide (PA6) ring with a diameter of 145 mm to avoid glass to steel contact. The ring is glued to a steel plate welded on two U-profiles, which can be positioned at different inclination angles (Tibolt, 2013). In this vein, the set-up allows the load introduction at the Fischer anchor under different angles: 0° (pure tension) (Figure 6.2), 45° (diagonal pull) (Figure 6.3) and 90° (shear) (Figure 6.4). The load is introduced by draw shackles directly into the point fitting (Tibolt, 2013).

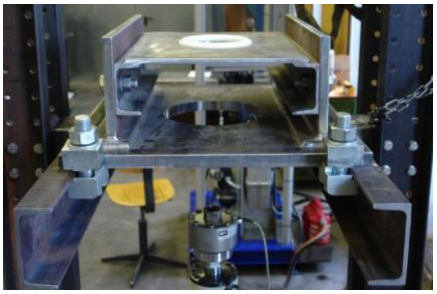

Figure 6.1 Test set-up designed at the University of Luxembourg

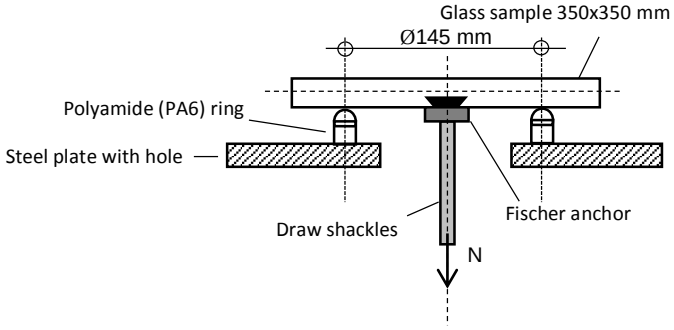

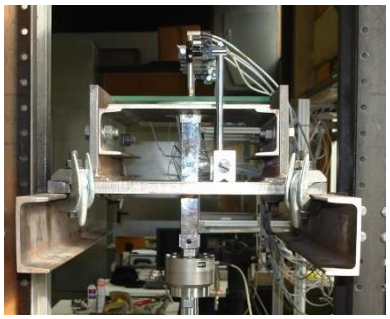

Figure 6.2 Tension test

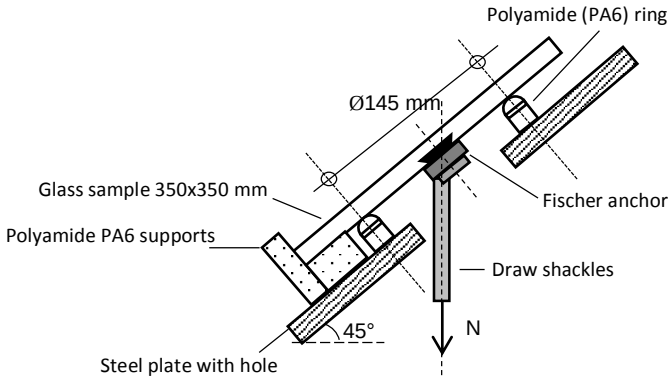

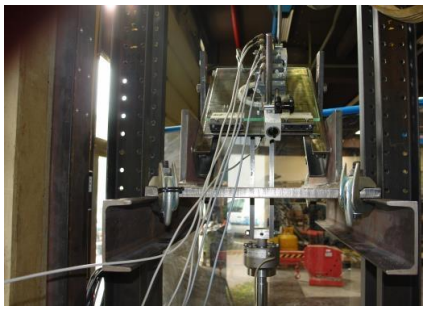

Figure 6.3 Diagonal pull test

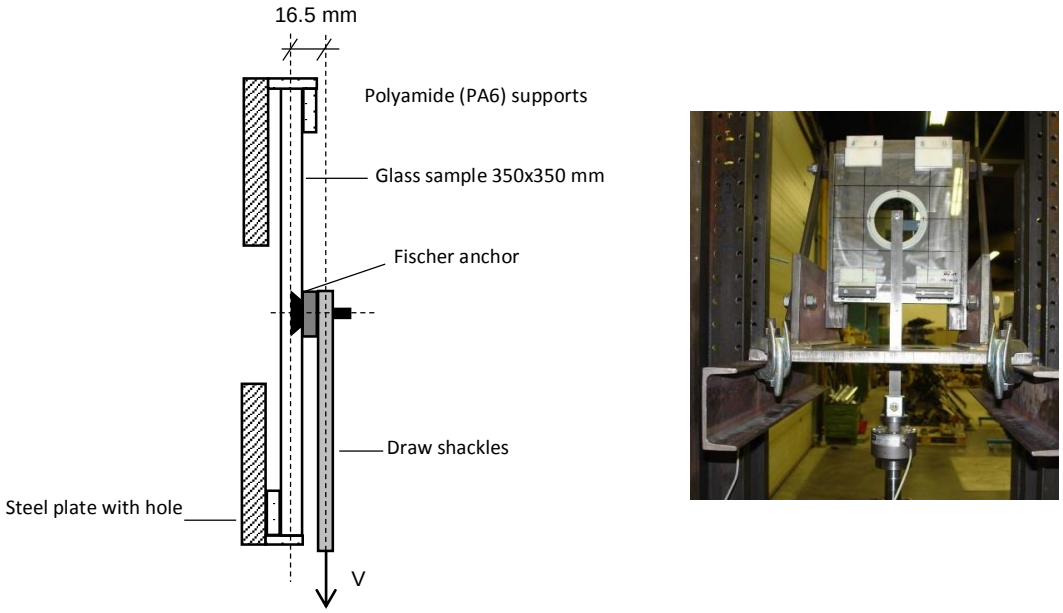

Figure 6.4 Shear test

It is not possible to subject the Fischer anchor to “pure” shear, because a lever arm between the centre line of the glass pane and the steel profile for the load introduction will always be present. The measured lever arm in the tests is 16.5mm (Figure 6.4).

The tested, fully tempered monolithic glass panes have the dimensions of 350x350 mm and a thickness of 10 mm respectively 12 mm (Figure 6.6). For each sample, one Fischer anchor FZP-G-Z is mounted in the centre of the glass pane. The thermal prestress is measured at four points on the upper and lower surface of each glass pane with the Scattered Light Polariscope *SCALP-04* (Figure 6.5). The measurement points are located in the middle points of the plate quadrants.

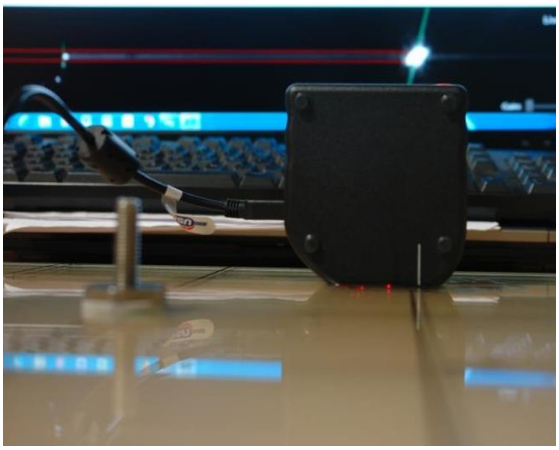

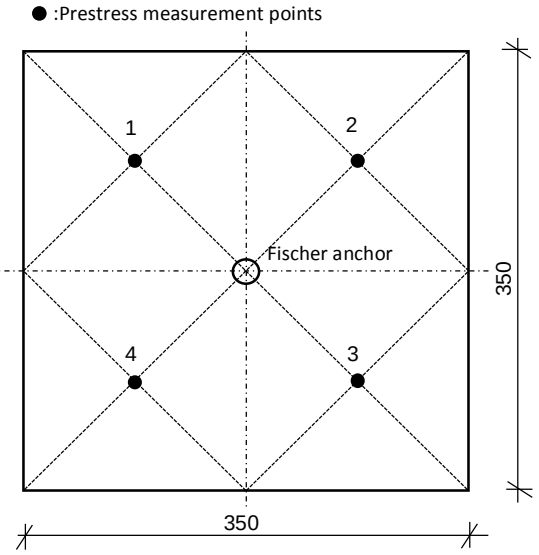

Figure 6.5 Scattered Light Polariscope (SCALP)

Figure 6.6 Test specimen

The arithmetic average of the four measurement points delivers a thermal prestress value of about σ_V = 100 N/mm² on both glass surfaces. The glass plates tested at the IKI also show a thermal prestress of circa σ_V = 100 N/mm² and permit a direct comparison between the results of the test campaigns at the University of Luxembourg and the IKI.

The tests are conducted displacement controlled with a speed at the hydraulic jack of 0.4 mm/min at room temperature (circa. 20°C) until failure of the connection and hence glass breakage. Up to six samples are tested for each test series (Table 6.1).

Table 6.1 Test series of component tests

Test	Parameter	t_{pane}	Series	No.of samples
[-]	[-]	[mm]	[-]	[-]
Tension	N	10	N10	5
		12	N12	6
Shear	Q	10	Q10	5
		12	Q12	5
Diagonal Pull	N+Q	10	NQ10	5
		12	NQ12	5

In order to calibrate a finite element model of the anchor, the strains of two samples of each test series are measured during the tests along defined paths with linear strain gauges (Figure 6.7 to Figure 6.9). The values of each test series are evaluated and averaged, to exclude measurement errors. The positions of the strain gauges were preliminary determined by FE-calculation.

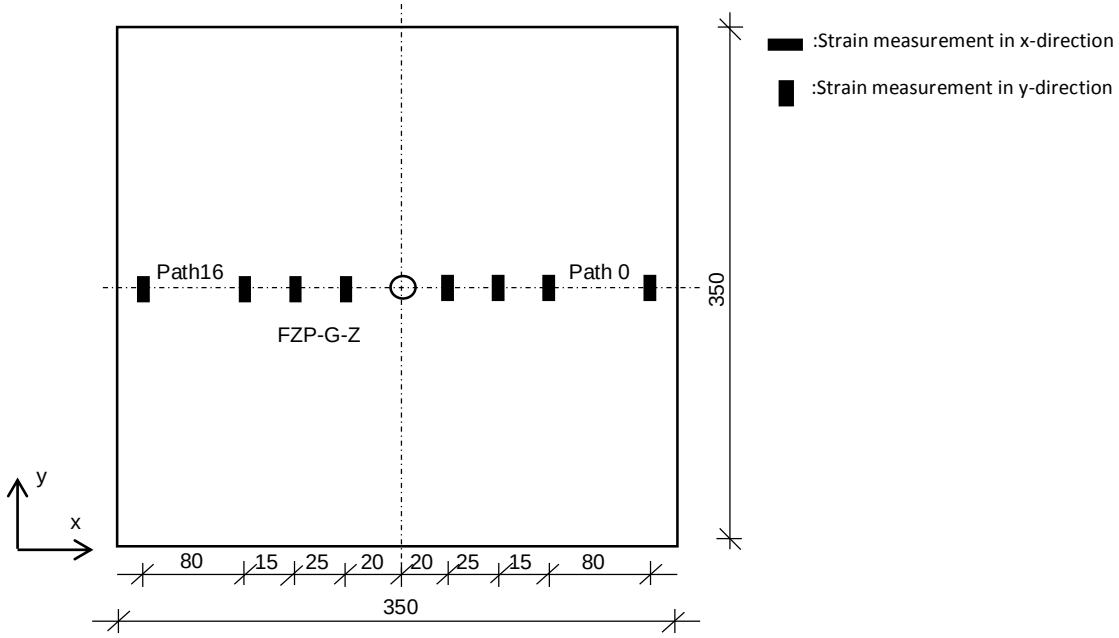

Figure 6.7 Strain gauge positions for the tension test specimens

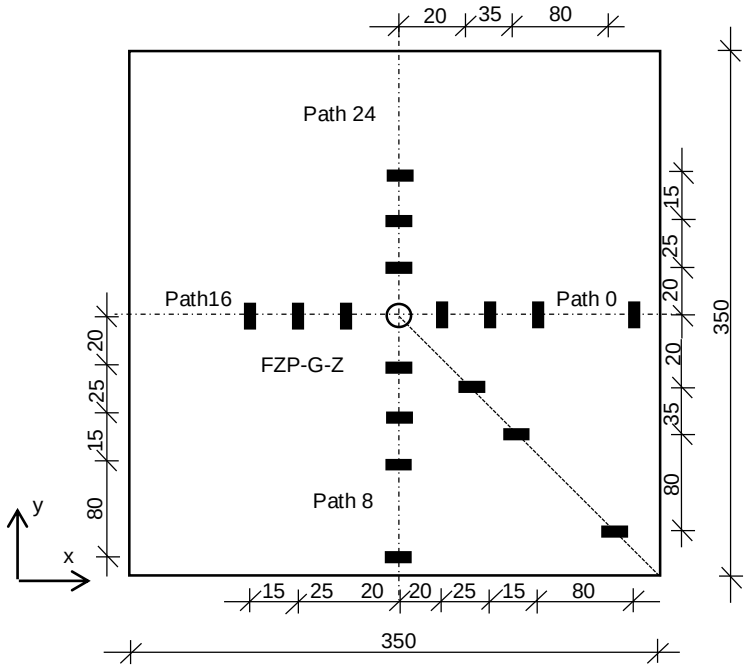

Figure 6.8 Strain gauge positions for the diagonal pull test specimens

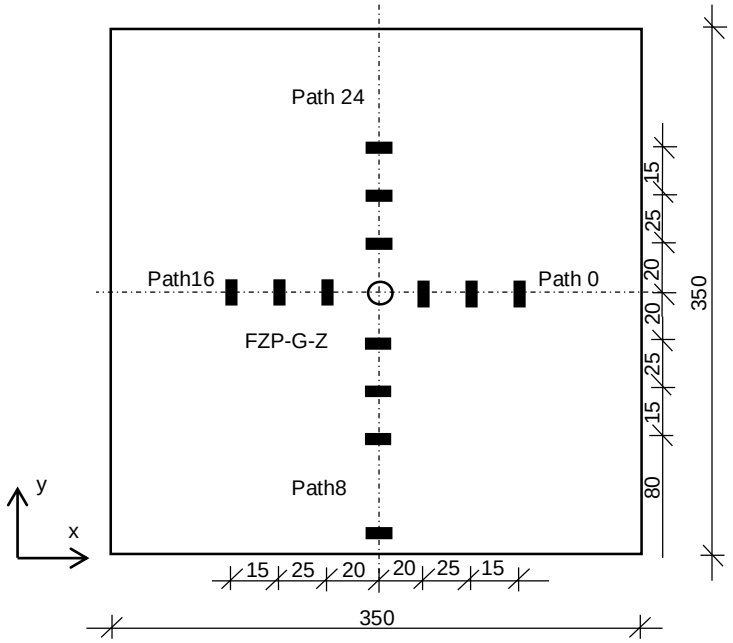

Figure 6.9 Strain gauge positions for the diagonal pull test specimens

6.2.2 Evaluation methodology and test results

The tests are conducted until failure of the connection. The maximum bearing force is recorded for each test sample. The data is statistically evaluated and the characteristic connection resistance and a corresponding partial safety factor is derived (Tibolt, 2013). The mean values of the connection resistance (Table 6.2) are compared to the mean values of the test campaign at the IKI (Beyer, 2007).

Table 6.2 Mean values of load at failure

Series	$F_{max,mean,test}$	$F_{max,mean,IKI}$	ΔF
[-]	[kN]	[kN]	[%]
N10	4.45	4.54	2
N12	5.27	5.75	9
Q10	4.37	5.34	22
Q12	6.67	7.84	18
NQ10	4.57	4.56	< 1
NQ12	5.59	-	-

For the tension and diagonal pull test series, a good correspondence between the mean values of the connection resistance and the results of the test campaign at the “IKI” is noticed. For the 10 mm and 12 mm glass plates, the difference is on average lower than 10%. No indication about the results for the diagonal pull tests of the 12 mm plates has been found for (Beyer, 2007). A high deviation is however observed between the test results and the values of the “IKI” for the shear tests (Q10 and Q12). The mean values found in the tests for the 10 mm and 12 mm plates are about 20% lower than the values of the “IKI”. This can be explained by the longer lever arm in our own tests (16.5 mm), compared to the lever arm in the test campaign at the “IKI” (14.5 mm). With regard to the sensitivity of the Fischer undercut anchor to bending moments, the higher lever arm explains the lower values in the shear tests.

The interaction rule between the tension and shear forces is derived from the results of the diagonal pull test series (Figure 6.10).

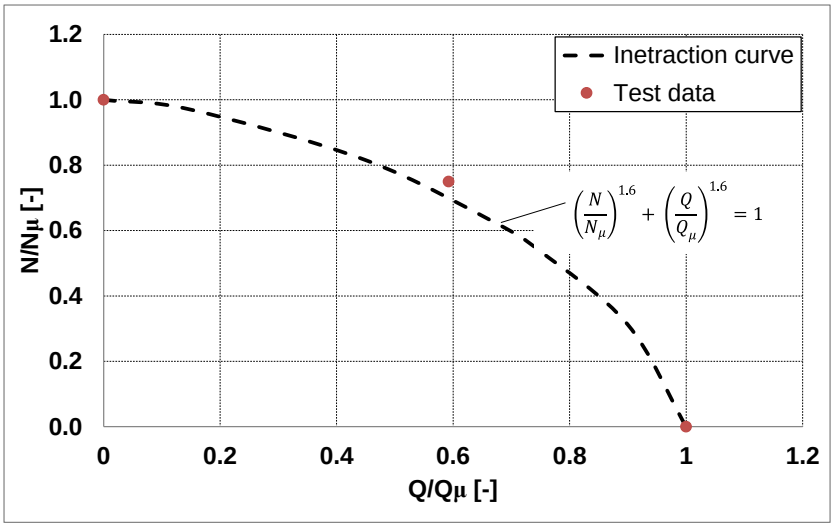

Figure 6.10 Normalised N-Q curve, Glass sample t = 12 mm

The mean values of the breaking loads from the series “Tension”, “Shear” and “Diagonal pull” are normalised and can be approximated with the curve described with equation (5-1):

$$\left(\frac{N}{N_\mu}\right)^{1.6} + \left(\frac{Q}{Q_\mu}\right)^{1.6} = 1 \qquad \textbf{(6-1)}$$

The same interaction rule is found for the test data from IKI (Beyer, 2007).

In the framework of the component tests, the *Lilliefors* hypothesis testing (Kühlmeyer, 2001) is applied to check if the log-normal distribution potentially describes the test data.

The log-normal distribution is assumed because it cannot reach negative values, which is consistent with the test data (Tibolt, 2013). In addition, the derivation procedure for the characteristic values of the connection resistance described in DIN EN 1990, Annexe D7 (DIN EN 1990) is based on the normal respectively the log-normal distribution function. The density function of the log-normal distribution is given by equation (5-2):

$$f(x) = \frac{1}{\sigma \cdot \sqrt{2 \cdot \pi}} \cdot \frac{1}{x} \cdot e^{\left[\frac{(\ln x - \mu)^2}{2 \cdot \sigma^2}\right]} \quad \textbf{(6-2)}$$

The parameters mean value μ, standard deviation σ and coefficient of variation ν are determined with the equations (5-3) to (5-5):

$$\mu = \ln\left(\frac{\bar{x}}{\sqrt{1+\nu^2}}\right) \quad \textbf{(6-3)}$$

$$\sigma = \sqrt{\ln(1+\nu^2)} \quad \textbf{(6-4)}$$

$$\nu = \frac{\bar{x}}{s} \quad \textbf{(6-5)}$$

The evaluation of the test of goodness of fit according to *Lilliefors* is given in Annexe A.

The characteristic values of the connection resistance are determined according to the simplified method of DIN EN 1990, Annexe D7 (DIN EN 1990). It is based on the *Bayes'* method and delivers nearly the same results as standard stochastic procedures with a confidence coefficient of 75 %. A detailed description of the method is given in Annexe A.

The characteristic values of the connection resistance and the corresponding standard deviation of each test series are shown in Table 6.3.

Table 6.3 Comparison of characteristic values of the breaking loads

Series	5%-$F_{max,test}$	σ_{test}	5%-$F_{Z\text{-}70.2\text{-}122}$	ΔF
[-]	[kN]	[kN]	[kN]	[%]
N10	4.20	0.113	3.89	8
N12	4.70	0.259	4.60	3
Q10	3.48	0.450	3.50	-1
Q12	5.97	0.314	6.50	-8
NQ10	4.32	0.104	3.90	11
NQ12	5.32	0.119	-	-

As expected, the characteristic values for the ultimate force are higher for the 12 mm than for the 10 mm glass plates. The biggest difference is observed for the shear test series (about 70%). Additionally, a low standard deviation has been identified pointing out the small scattering of the values and underlining the high reproducibility of the test results.

A comparison to the values in the general technical approval (Z-70.2-122) reveals the good accordance between the values. The highest deviation of 11% is observed for the diagonal pull test series. The small deviations could result from different test set-ups and differing statistical evaluation methods. The characteristic shear resistance values are lower than indicated in the approval (Z-70.2-122). The reason is the larger lever arm in the tests that are conducted in the framework of this research work. As a conclusion, the values in the approval are confirmed and the designed test-set up allows to simulate the load bearing behaviour of the Fischer undercut anchor FZP-G-Z with a good reproducibility and accuracy.

Based on the test results, the partial safety factors γ_R for the connection resistance is derived for each test series according to (DIN EN 1990):

$$\gamma_R = e^{[\vartheta \cdot (\alpha_R \cdot \beta - k_n)]} \quad \textbf{(6-6)}$$

here

ϑ = variation coefficient

α_R = sensivity factor

β = reliability index

k_n = k_n-factor

For the ultimate limit state and a service life of 50 years, Table C.2 in (DIN EN 1990) indicates a target value of $\beta = 3.8$. The sensitivity factor α_R is assumed to 0.8.

The determination of the partial safety factor γ_R is illustrated in Annexe A.

The safety concept in (DIN EN 1990) is the partial safety concept, while the concept in (Z-70.2-122) is based on the global safety concept. To allow a comparison to the defined safety level of (Z-70.2-122), a global safety factor γ^* is determined according to (Schneider, 2001):

$$\gamma^* = \gamma_S \cdot \gamma_R \quad \textbf{(6-7)}$$

γ_S = Partial safety factor for the loading

γ_R = Partial safety factor for the resistance

γ_S = 1.5 is assumed for the external loading.

Table 6.4 Global safety factor

Series	γ_R	γ^*
[-]	[-]	[-]
N10	1.1	1.7
N12	1.1	1.7
Q10	1.1	1.7
Q12	1.1	1.7
NQ10	1.1	1.7
NQ12	1.1	1.7

The global safety factors γ^* derived from the test campaign can be indicated with $\gamma^* = 1.7$ for each test series (Table 6.4). The global safety in (Z-70.2-122) is given with $\gamma^* = 2.4$. As a result, the global safety concept in (Z-70.2-122) is conservative.

However, the global safety factors γ^* derived from the different test series are based on a small number of test samples and cannot be directly used in the design of the connection. Further all glass samples have been produced by only one manufacturer and the prestress of the glass was performed always by the same refiner in one production shift. Though, the influence of production and refining on the glass strength is known (Beyer, 2007). The influence is not included in the partial safety factors derived

from the test campaign and therefore the factors are only valid for samples tested with the test set-up in section 6.2.1.

6.3 Calibration of the 3D FE-model for the Fischer undercut anchor

6.3.1 General FE-model

A detailed numerical model of the Fischer undercut anchor is implemented in the FE-software ABAQUS® (Figure 6.11). The model accounts for the exact geometry of the borehole and the point fitting (Tibolt, 2013).

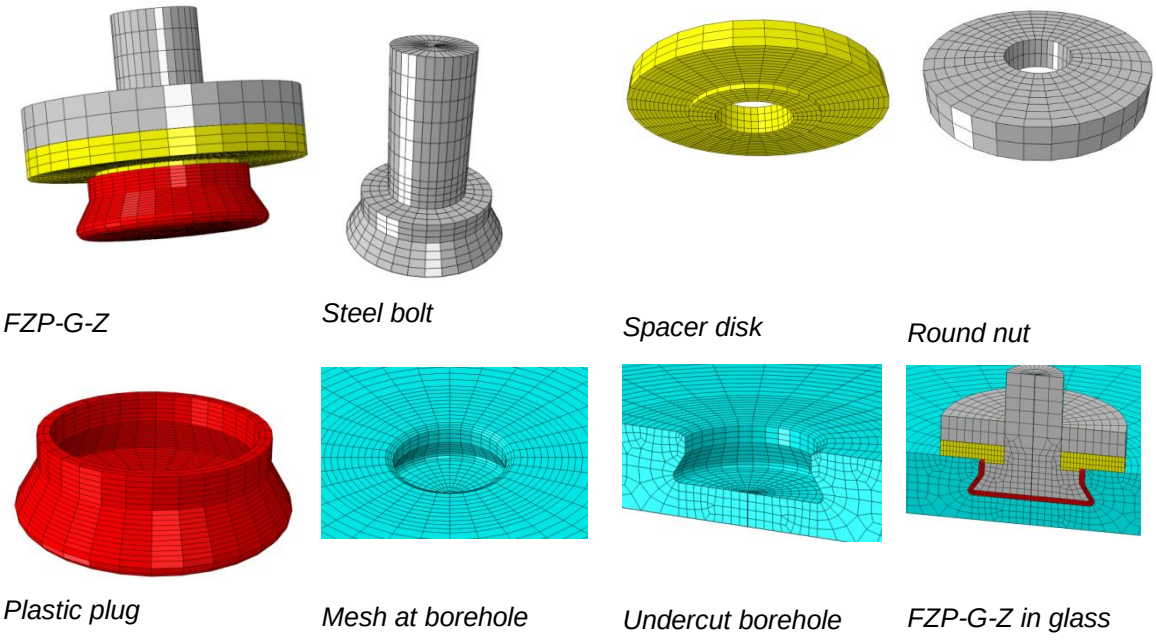

Figure 6.11 FE-model of the Fischer anchor FZP-G-Z with solid elements

The glass pane and the different components of the anchor are modelled with solid elements which are described in section 6.3.2. Contact properties are defined between the glass pane and the point fitting to simulate the decoupling between anchor and glass. The material properties of the components and interlayers are shown in Table 6.5.

Table 6.5 Material properties of the components, Source: (Beyer, 2007)

Component	Material	E-modulus	Poisson's ratio	Density
[-]	[-]	[N/mm²]	[-]	[kg/m³]
Anchor	Stainless steel	190000	0.3	7850
Spacer disk	Polyamide	1000	0.4	1100
Round nut	Stainless steel	190000	0.3	7850
Plastic plug	Polyurethane	80	0.4	1080

6.3.2 Calibration process

The calibration of the numerical model contains four steps (Tibolt, 2013):

- Verification of the FEM element type and mesh quality of the glass pane
- Verification of the contact definitions between the glass and the point fitting
- Verification of the rotational stiffness of the point fitting in the glass pane
- Calibration of the overall numerical model with comparison of the numerical strains to the experimental determined strains.

For the verification of the type of element and the quality of the mesh of the glass pane, the stress concentration factor k is calculated with the numerical model and compared to the values given in (Z-70.2-122). Two glass panes with the dimensions of 3000x750x10 mm and 3000x750x12 mm with the exact undercut borehole are modelled and subjected to pure bending (Figure 6.12).

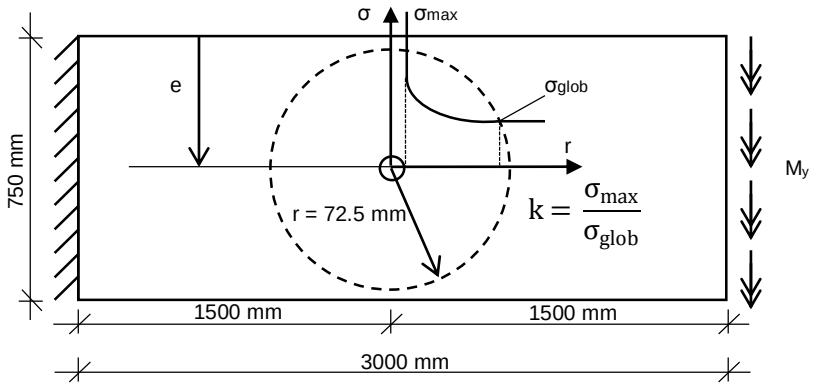

Figure 6.12 The stress concentration factor k

The stress concentration factor k, defined as the quotient of the maximal tensile stress at the borehole and the maximal global stress at the rim of the local area (r = 72.5 mm), is numerically determined for two different edge distances of the borehole (Table 6.6).

Table 6.6 Comparison of stress concentration factors

t_{pane}	e	σ_{max}	$\sigma_{72.5}$	k_{num}	$k_{Z\text{-}70.2\text{-}122}$	Δk
[mm]	[mm]	[N/mm²]	[N/mm²]	[-]	[-]	[%]
10	60	7.02	3.66	1.92	1.9	1
	90	5.83	3.72	1.57	1.6	-2
12	60	9.94	5	1.99	1.9	4.7
	90	8.28	5.08	1.63	1.6	1.8

A good correspondence between the values is observed for the element type C3D8I (an 8-node linear brick with incompatible nodes to overcome shear locking problems) and the following mesh configuration in the borehole area (Figure 6.13):

- 32 elements in tangential direction.
- 39 elements in radial direction.
- 8 elements over the pane thickness.

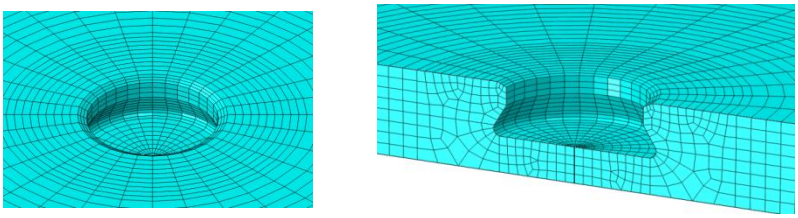

Figure 6.13 Mesh in borehole area

In consequence, the C3D8I elements and the generation of the mesh are appropriate for the FE-model of the connection.

To verify the contact definitions between the glass and the Fischer FZP-G-Z, the so called “transfer functions” (section 2.5.4) are generated with the numerical model and compared with the diagrams in (Beyer, 2007). The transfer functions relate the forces or moments in the point fitting to the corresponding maximal tensile stress peak occurring at the borehole (Beyer, 2007). The 10 mm thick glass pane samples of the component tests are numerically modelled and the point fitting was subjected to tension, shear and bending. The load-stress-diagrams are generated and compared with the results in (Beyer, 2007). For a hard and frictionless contact definition between the Fischer undercut anchor and the glass, the functions perfectly match with a maximum deviation of only 2% (Figure 6.14 to Figure 6.16).

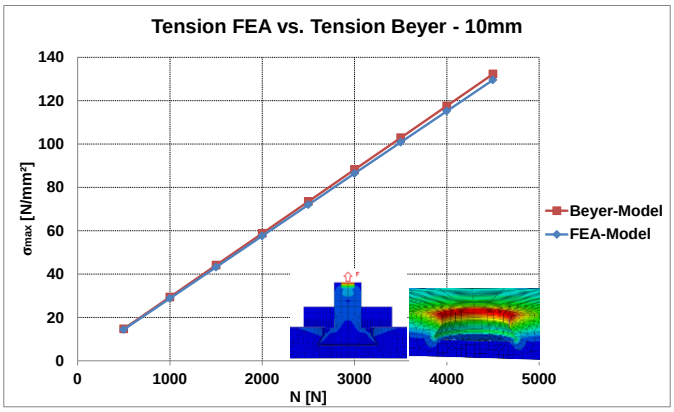

Figure 6.14 Transfer function for load case “Tension”

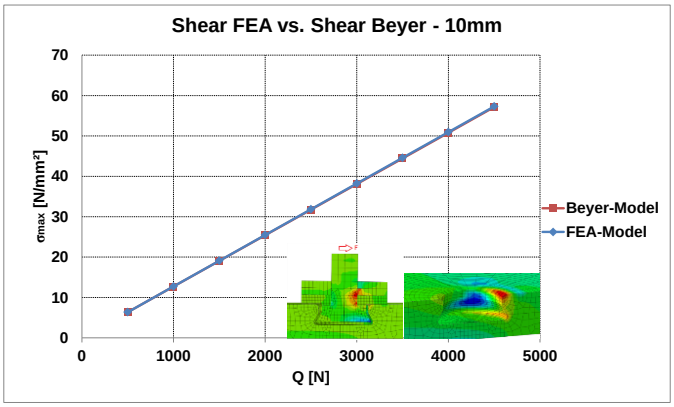

Figure 6.15 Transfer function for load case "Shear"

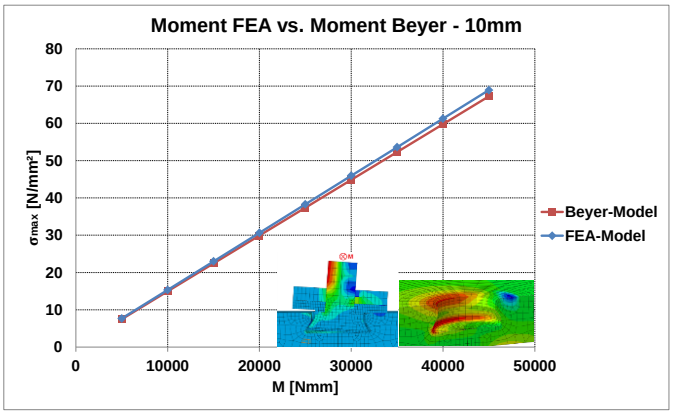

Figure 6.16 Transfer function for load case "Diagonal pull"

A comparison with the transfer functions for the 12 mm thick glass panes is not possible, because the corresponding diagrams are not indicated in (Beyer, 2007). It is however assumed, that the contact definitions are independent from the glass pane thickness. As a conclusion, the contact definitions are verified.

The rotational stiffness of the Fischer anchor in the glass pane is verified by comparing the numerical results of the stiffness values to the experimental values given in (Z-70.2-122) for the 10 mm and 12 mm thick glass panes. A moment of M_y = 45 000 Nmm is applied to the point fitting in the FE-model and the rotation angle φ is measured (Figure 6.17). A linear stiffness $k_{d,num}$ is calculated and compared to the values given in (Z-70.2-122).

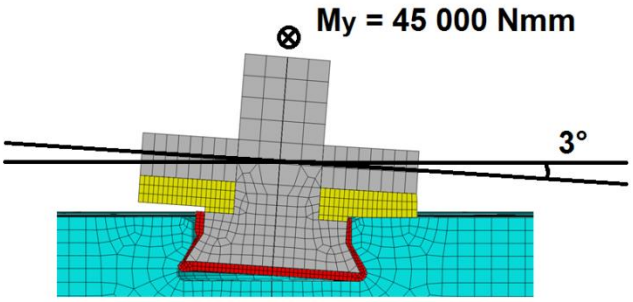

Figure 6.17 Rotation angle of Fischer undercut anchor FZP-G-Z

$$k_{d,num} = \frac{M_y}{\varphi} \qquad \textbf{(6-8)}$$

Table 6.7 Comparison of numerical and experimental rotation stiffness of the Fischer anchor FZP-G-Z

t_{pane}	$k_{d,num}$	$k_{d,exp}$	Δk
[mm]	[Nm/°]	[Nm/°]	[%]
10	14.52	15	-3.2
12	15	15	0

A good correlation between the numerical and experimental values is observed (Table 6.7). Thus, the numerical model with the specified element types, mesh generation and contact definitions correctly takes into account the deformation behaviour of the Fischer undercut anchor FZP-G-Z in 10 mm and 12 mm thick glass panes.

The FE-model is finally calibrated by simulating the component tests and comparing the numerical with the measured strains. The comparison of the strains is shown in Figure 6.18 and Figure 6.19 for the test series N10 and N12 and a force of N = 2500 N in the point fitting. Further results are presented in Annexe A.

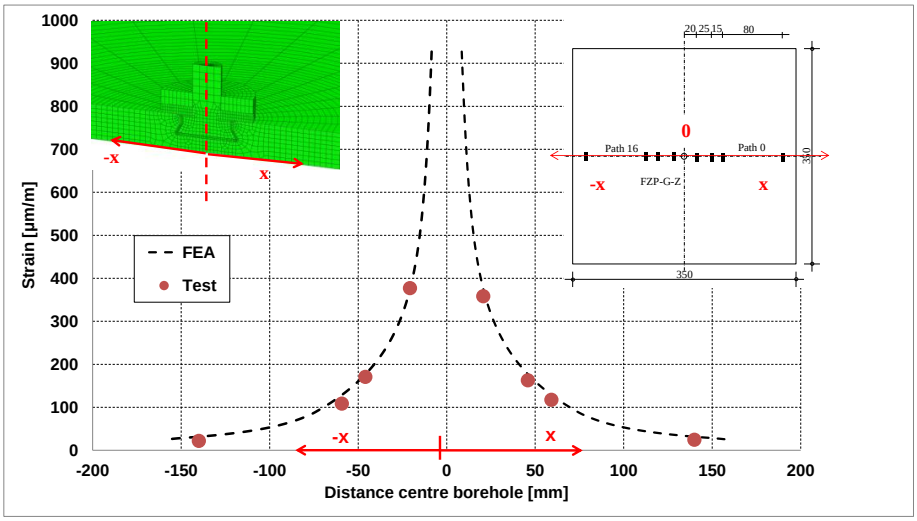

Figure 6.18 Measured vs. calculated strains, Test series N10, N = 2500 N

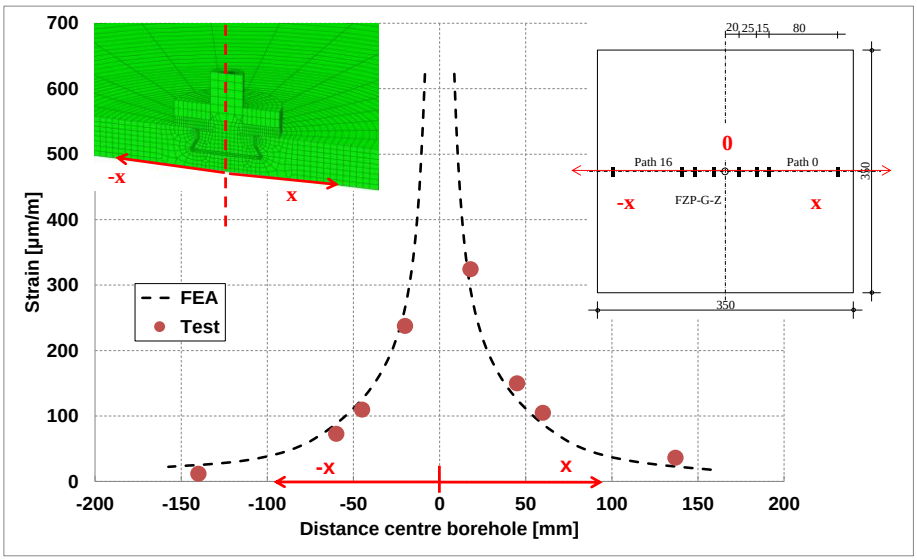

Figure 6.19 Measured vs. calculated strains, Test series N12, N = 2500 N

The good correspondence between the calculated and the measured strains proofs the validity of the FE-model.

6.4 Conclusion

Component tests are conducted on the Fischer undercut anchor in a fully tempered monolithic glass. The point fitting is subjected to tension, shear and diagonal pull. For each test series, the ultimate load bearing force of the point fitting in a fully tempered monolithic glass is determined. The test results are statistically evaluated and the characteristic values of the connection resistance are derived. Further, a corresponding partial and global safety factor is determined for each test series.

A comparison of the test results to the values in the German technical approval (Z-70.2-122) reveals a good correspondence between the approval and the test results. Moreover, the interaction rule for the tension and the shear forces given in (Z-70.2-122) and (Beyer, 2007) is verified by the test results. Thus, the accuracy and the reproducibility of the test data are confirmed and the values in the technical approval are solidified. As a result, the data can be used for the calibration of a FE-model of the Fischer undercut anchor FZP-G-Z.

A numerical model of the Fischer point fitting is introduced. The element and mesh quality of the glass pane, the contact definitions and the rotational stiffness of the point fitting are verified by comparing the FE results with the results of (Beyer, 2007) and (Z-70.2-122). Finally the overall FE-model is calibrated by checking the measured strains in the test against the numerically calculated strains. In this way, the numerical model of the Fischer undercut anchor is validated.

7 Development of an extended climate load model for point fitted IGU with undercut anchors

7.1 Objectives

A practicable approach for the determination of the climate loads of point fitted insulation glass units is described in section 2.8.3. The method however consists in a rough approximation of the climate loads and results in an inefficient design of point fitted insulation glass (Beyer, 2007). Additionally, the method is only applicable to point fittings which are drilled through the cavity and does consequently not comply to the static system of point fitted IGU with undercut anchors.

In this research work, the climate load model of *Feldmeier* for linearly supported insulation glass is therefore analytically extended to the static system of point fitted insulation glass with undercut anchors. The model allows the determination of the resulting surface loads acting on each glass pane of the insulation glass unit. In addition, the model is numerically verified by comparing the resulting surface loads to the loads delivered by a FE-model which considers the behaviour and redistribution of the gas inside the cavity with high accuracy. Finally the parameters influencing the climate loads are identified and their influence is investigated in a parameter study.

7.2 Extension procedure

7.2.1 Development of a static system for the determination of the climate loads

In linearly supported insulation glass units, the glass panes are only coupled via the gas inside the glazing cavity. The coupling effect of the gas is described by the ideal gas law and it is possible to consider the static system of each glass pane separately. The edge bond is considered as a rotating and rigid support along the edges of the glass panes [Klochinski-2004], (Feldmeier, 2006). Thus, each glass pane is *Navier*-supported (Figure 7.1).

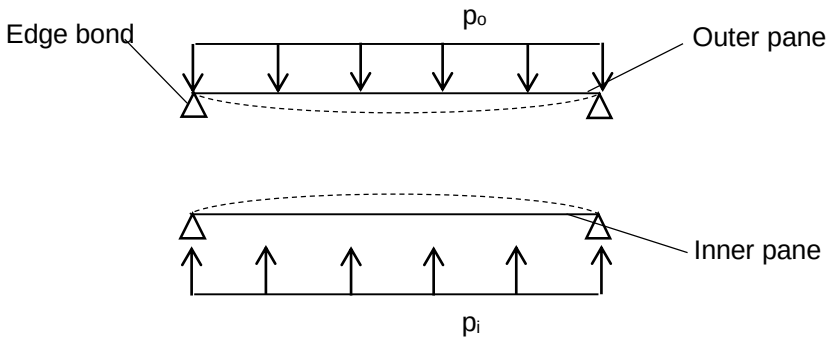

Figure 7.1 Static system and deformed shape of a linearly supported IGU according to (Feldmeier, 2006)

The static system has to be adopted for the extension of the climate load model of *Feldmeier* to point fitted insulation glass units with undercut anchors.

The static system of a point fitted insulation glass unit with undercut anchors, which is assumed for the determination of the climate loads, is shown in Figure 7.2.

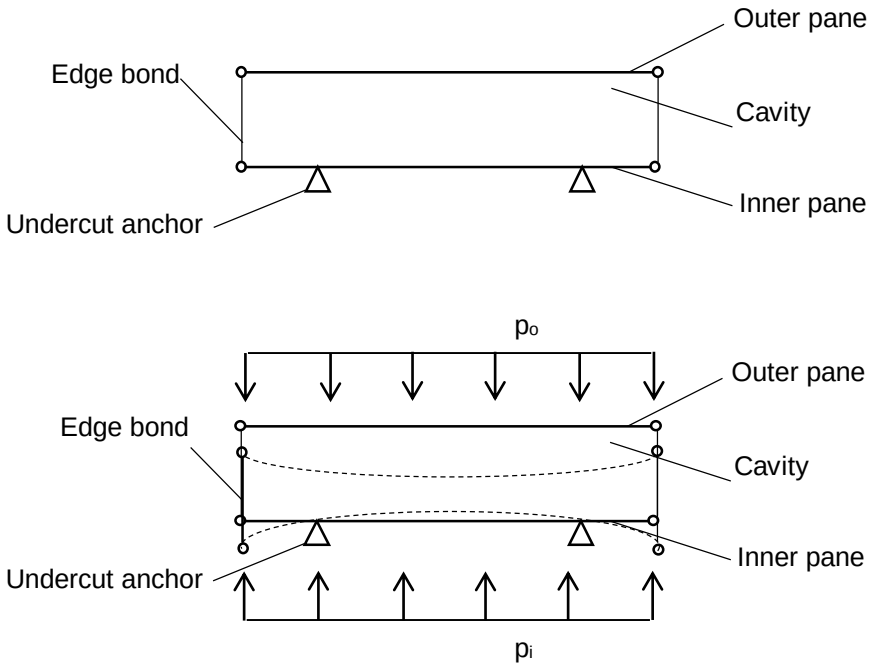

Figure 7.2 Static system and deformed shape of a point fitted IGU with undercut anchors

In point fitted insulation glass with undercut anchors, the glass panes are coupled via the edge bond in addition to the gas coupling. Thus, a loading acting on the outer pane is partially transmitted to the inner pane by the gas inside the cavity and by the edge bond. As for linearly supported IGU, the coupling of the panes via the gas is specified by the ideal gas law. Additionally, the glass panes are statically coupled by the edge bond. In

consequence, the panes cannot be considered separately as *Navier*-supported, (Hechler et al., 2012). In the static system of point fitted IGU with undercut anchors, the edge bond hence is considered as a pinned ended column between the glass panes. This means, that the gap between the edges of the glass panes remains constant and that the glass panes can freely rotate at their edges. The panes are not coupled in pane direction and the transition of shear forces is consequently not considered, which is not allowed by the standards to set into account. The undercut anchors are represented by pinned supports. Thus, at the position of the anchors, the glass pane can freely rotate and cannot deform perpendicularly to its plane. The accuracy of the static system is verified in section 7.6.

7.2.2 Analytical extension of the climate load model to point fitted IGU

In the following section, the climate load model of *Feldmeier* for linearly supported insulation glass is analytically extended to comply with the static system of point fitted IGU with undercut anchors (Hechler et al, 2012). The extended model is developed for multiple point fitted IGU under consideration of external surface loads. External line and point loads are not comprised.

Figure 7.3 shows the deformed shape of a multiple insulation glass unit with undercut anchors and the corresponding notations. The index k = 1 to n indicates the panes and the index i = 1 to n-1 identifies the cavities. The temperatures $(T_i)_{i=1\ldots n-1}$ of the gas in the cavities are given by the climate conditions at the point of installation. The volume $(V_i)_{i=1\ldots n-1}$ and pressure $(p_i)_{i=1\ldots n-1}$ of the gas are determined as follows. The pressure p_0 is the ambient pressure at the installation location of the IGU. The external surface loads acting on each glass pane are denoted with $(p_e)_{i=1\ldots n}$.

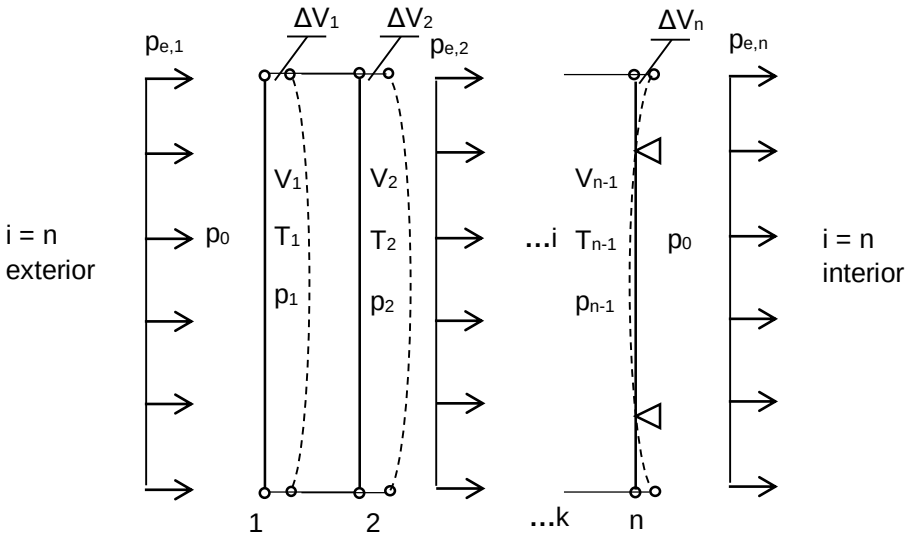

Figure 7.3 Notation and deformed shape of a point fitted IGU with undercut anchors

For the analytical extension of the climate load model, the following sign convention for the loads is applied:

- A load which deforms the outer pane towards the cavity is positive and vice versa (Figure 7.4).
- A load which deforms the inner pane towards the cavity is negative and vice versa (Figure 7.5).

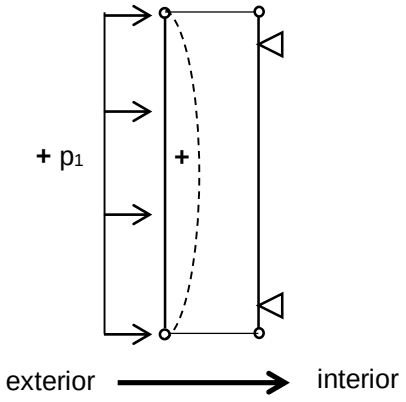

Figure 7.4 The sign convention for the outer pane

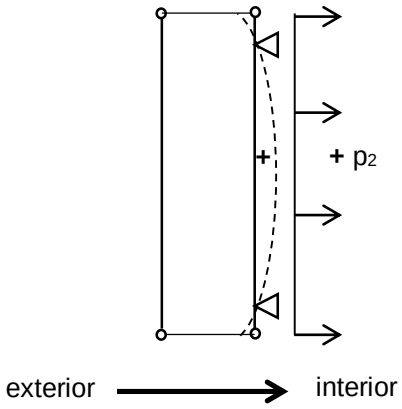

Figure 7.5 The sign convention for the inner pane

As for the model of *Feldmeier*, the deformations of the glass panes are assumed to be small and hence proportional to the loading:

$$\Delta V = \vartheta \cdot p \qquad \textbf{(7-1)}$$

ϑ = Volume coefficient for a surface load (pressure) [m^3/kPa]

p = surface load [kN/m^2]

The volume coefficient ϑ is the enclosed volume of the deformed pane due to a surface load or pressure “1” [kN/m^2].

Consequently, the extended climate load model does not account for non-linear effects, e.g. membrane effects.

The volume V_i of cavity i is calculated with equation (7-2):

$$i = 1, \dots, n-1$$

$$V_i = V_{pr,i} - \Delta V_i + \Delta V_{i+1} \qquad \textbf{(7-2)}$$

V_i = The volume of cavity i at the installation location of the unit [mm^3]

$V_{pr,i}$ = The volume of cavity i at the production location of the unit [mm^3]

ΔV_i = The volume change of cavity i due to the deformation of pane i [mm^3]

ΔV_{i+1} = The volume change of cavity i due to the deformation of pane $i+1$ [mm^3]

The volume change ΔV_i depends on the deflection of the glass pane i. Due to the coupling of the glass panes via the edge bond however, this deflection also depends on the external loading on each pane and the pressure within each cavity i. The volume change ΔV_i is given by equation (7-3):

$$i = 1, \dots, n-1$$

$$\Delta V_i = \sum_{k=1}^{n} \vartheta_{i,k} \cdot (p_{k-1} - p_k) + \sum_{k=1}^{n} \vartheta_{pe,i,k} \cdot p_{e,k} \quad \textbf{(7-3)}$$

$\vartheta_{i,k}$ = The enclosed volume of pane i due to a pressure "1" on pane k [$m^3/(kN/m^2)$]

$\vartheta_{pe,i,k}$ = The enclosed volume of pane i due to an external surface load "1" on pane k [$m^3/(kN/m^2)$]

p_k = The pressure acting on pane k [kN/m^2]

p_{k-1} = The pressure acting on pane k-1 [kN/m^2]

$p_{e,k}$ = The external surface load acting on pane k [kN/m^2]

The volume change ΔV_{i+1} is calculated analogue to ΔV_i:

$$i = 1, \dots, n-1$$

$$\Delta V_{i+1} = \sum_{k=1}^{n} \vartheta_{i+1,k} \cdot (p_{k-1} - p_k) + \sum_{k=1}^{n} \vartheta_{pe,i+1,k} \cdot p_{e,k} \quad \textbf{(7-4)}$$

$\vartheta_{i+1,k}$ = The enclosed volume of pane i+1 due to a pressure "1" on pane k [$m^3/(kN/m^2)$]

$\vartheta_{pe,i+1,k}$ = The enclosed volume of pane i+1 due to an external surface load "1" on pane k [$m^3/(kN/m^2)$]

Insertion of the equations (7-3) and (7-4) in equation (7-2) delivers V_i:

$$i = 1, \dots, n-1$$

$$V_i = V_{pr,i} + \sum_{k=1}^{n} \left\{ -(\vartheta_{i,k} - \vartheta_{i+1,k}) \cdot p_{k-1} + (\vartheta_{i,k} - \vartheta_{i+1,k}) \cdot p_k \right\} - \Delta V_{ex,i} \quad \textbf{(7-5)}$$

With:

$$\Delta V_{ex,i} = V_{ex,i} - V_{ex,i+1} \quad \textbf{(7-6)}$$

$$V_{ex,i} = \sum_{k=1}^{n} \vartheta_{pe,i,k} \cdot p_{e,k} \quad \textbf{(7-7)}$$

$$V_{ex,i+1} = \sum_{k=1}^{n} \vartheta_{pe,i+1,k} \cdot p_{e,k} \quad \textbf{(7-8)}$$

As introduced in section 7.2.1, the glass panes are coupled by the encapsulated gas in the cavity. The quantity of each gas in the cavity has been fixed during production (index pr) and rests constant. Consequently, the pressure change of the gas due to the variation of its volume and temperature can be described by the ideal gas law:

$$i = 1, \dots, n-1$$

$$\frac{p_i \cdot V_i}{T_i} = \frac{p_{pr,i} \cdot V_{pr,i}}{T_{pr,i}} \quad \textbf{(7-9)}$$

p_i = The pressure of the gas in cavity i at the installation location [kN/m²]

V_i = The volume of the gas in cavity i at the installation location [mm³]

T_i = The temperature of the gas in cavity i at the installation location [K]

$p_{pr,i}$ = The pressure of the gas in cavity i at the production location [kN/m²]

$V_{pr,i}$ = The volume of the gas in cavity i at the production location [mm³]

$T_{pr,i}$ = The temperature of the gas in cavity i at the production location [K]

The ideal gas law assumes that the pressure, the volume and the temperature are the same in each cavity at production.

Insertion of equation (7-5) in (7-9) delivers equation (7-10):

$$i = 1, \dots, n-1$$

$$p_i \cdot \left[1 + \sum_{k=1}^{n} \left\{ -\frac{(\vartheta_{i,k} - \vartheta_{i+1,k})}{V_{pr,i}} \cdot p_{k-1} + \frac{(\vartheta_{i,k} - \vartheta_{i+1,k})}{V_{pr,i}} \cdot p_k \right\} - \frac{\Delta V_{ex,i}}{V_{pr,i}} \right] = \frac{T_i \cdot p_{pr,i}}{T_{pr,i}} \quad \textbf{(7-10)}$$

With the definition of the under- respectively overpressure in the cavities to the ambient pressure

$$\Delta p_i = p_i - p_a \quad \textbf{(7-11)}$$

p_a = The barometric pressure at the installation location of the IGU.

With the introduction of the dimensionless factors $\alpha_{i,k}$ and $\alpha^{+}_{i,k}$ in equation (7-12) and equation (7-13):

$$\alpha_{i,k} = \frac{\vartheta_{i,k}}{V_{pr,i}} \cdot p_a \quad \textbf{(7-12)}$$

$$\alpha^{+}_{i,k} = \frac{\vartheta_{i+1,k}}{V_{pr,i}} \cdot p_a \quad \textbf{(7-13)}$$

and

$\alpha_{i,k}$ = The relative volume change of pane i due to a loading on pane k

$\alpha^{+}_{i,k}$ = The relative volume change of pane $i+1$ due to a loading on pane k

equation (7-10) is reformulated to equation (7-14)

$$1 + \sum_{k=1}^{n} \left\{ \left(\alpha_{i,k}^{+} - \alpha_{i,k} \right) \cdot \frac{\Delta p_{k-1}}{p_a} + \left(\alpha_{i,k} - \alpha_{i,k}^{+} \right) \cdot \frac{\Delta p_k}{p_a} \right\} - \frac{\Delta V_{ex,i}}{V_{pr,i}} + \frac{\Delta p_i}{p_a} + \sum_{k=1}^{n} \left\{ \left(\alpha_{i,k}^{+} - \alpha_{i,k} \right) \cdot \right.$$

$$\left. \cdot \frac{\Delta p_{k-1} \cdot \Delta p_i}{p_a^2} + \left(\alpha_{i,k} - \alpha_{i,k}^{+} \right) \cdot \frac{\Delta p_k \cdot \Delta p_i}{p_a^2} \right\} - \frac{\Delta p_i}{p_a} \cdot \frac{\Delta V_{ex,i}}{V_{pr,i}} = \frac{T_i \cdot p_{pr,i}}{T_{pr,i} \cdot p_a} \qquad \textbf{(7-14)}$$

(7-14) is a system of coupled quadratic equations. The system can be solved for the pressure difference Δp_i in each cavity by means of mathematical software. The pressure difference finally delivers the loading of each glass pane. With the aim to deliver an analytical logic, feasible by hand, the system (7-15) is linearised according to (Feldmeier, 2006) with the following assumptions:

- The pressures p_i in the cavities are in the range of the barometric pressure p_a at the installation location.

  $$\left| \frac{\Delta p_i}{p_a} \right| \ll 1$$

- The volume changes $\Delta V_{ex,i}$ due to the external loads are small compared to the volumes $V_{pr,i}$ of the cavities.

  $$\left| \frac{\Delta V_{ex,i}}{V_{pr,i}} \right| \ll 1$$

The assumptions allow the linearization of the system (7-14) and leads to the linearised system (7-15):

$$\sum_{k=1}^{n} \left\{ \left(\alpha_{i,k}^{+} - \alpha_{i,k} \right) \cdot \Delta p_{k-1} + \left(\alpha_{i,k} - \alpha_{i,k}^{+} \right) \cdot \Delta p_k \right\} + \Delta p_i = \frac{\Delta V_{ex,i}}{V_{pr,i}} \cdot p_a +$$

$$+ \left(\frac{T_i \cdot p_{pr,i}}{T_{pr,i} \cdot p_a} - 1 \right) \cdot p_a \qquad \textbf{(7-15)}$$

The term on the right of equation (7-15) comprehends the external loading and climatic conditions. Similar to (Feldmeier, 2006), pressure differences are introduced respectively:

- The pressure difference in cavity i due to the external loads:

  $$\Delta p_{ex,i} = \frac{\Delta V_{ex,i}}{V_{pr,i}} \cdot p_a \qquad \textbf{(7-16)}$$

and

- The pressure difference in cavity i due to the climatic changes:

$$\Delta p_{c,i} = \left(\frac{T_i \cdot p_{pr,i}}{T_{pr,i} \cdot p_a} - 1\right) \cdot p_a \tag{7-17}$$

Similar to the insulation glass factor in (Feldmeier, 2006), a coupling factor $\varphi_{i,k}$ is defined:

$$\varphi_{i,k} = \alpha_{i,k}^{+} - \alpha_{i,k} \tag{7-18}$$

The factor $\varphi_{i,k}$ considers the coupling of the glass panes via the edge bond system. It indicates the contribution of an external load acting on pane k to the pressure difference in cavity i.

The equations (7-16) to (7-28) are inserted in equation (7-15), which can finally be written as a matrix:

$$\begin{pmatrix} 1+\varphi_{1,2}-\varphi_{1,1} & \varphi_{1,3}-\varphi_{1,2} & \cdots & \varphi_{1,n}-\varphi_{1,n-1} \\ \varphi_{2,2}-\varphi_{2,1} & 1+\varphi_{2,3}-\varphi_{2,2} & \cdots & \varphi_{2,n}-\varphi_{2,n-1} \\ \cdots & \cdots & \cdots & \cdots \\ \varphi_{n-1,2}-\varphi_{n-1,1} & \varphi_{n-1,3}-\varphi_{n-1,2} & \cdots & 1+\varphi_{n-1,n}-\varphi_{n-1,n-1} \end{pmatrix} \cdot \begin{pmatrix} \Delta p_1 \\ \Delta p_2 \\ \cdots \\ \Delta p_{n-1} \end{pmatrix} = \begin{pmatrix} \Delta p_{ex,1} + \Delta p_{c,1} \\ \Delta p_{ex,2} + \Delta p_{c,2} \\ \cdots \\ \Delta p_{ex,n-1} + \Delta p_{c,n-1} \end{pmatrix} \tag{7-19}$$

The solution of the matrix delivers the over- respectively the underpressure in each cavity. The pressure is applied as a surface load on each glass pane and can be superimposed with the external surface loads, e.g. wind.

The matrix (7-19) can be applied to double insulation glass with undercut anchors:

$$\begin{pmatrix} p_{res,1} \\ p_{res,2} \end{pmatrix} = \frac{1}{(1+\varphi_{1,2}-\varphi_{1,1})} \cdot \begin{pmatrix} -1 & 1+\varphi_{1,2} & \varphi_{1,2} \\ 1 & -\varphi_{1,1} & 1-\varphi_{1,1} \end{pmatrix} \cdot \begin{pmatrix} \Delta p_{c,1} \\ p_{e,1} \\ p_{e,2} \end{pmatrix} \tag{7-20}$$

With the definition of the resulting surface loads acting on the outer (index 1) respectively the inner pane (index 2)

$$\begin{cases} p_{res,1} = p_{e,1} - \Delta p_1 \\ p_{res,2} = p_{e,2} + \Delta p_1 \end{cases} \tag{7-21}$$

The matrix (7-20) allows the determination of the resulting surface load acting on each glass pane under consideration of the climate loads $\Delta p_{c,1}$ and the external surface loads on the outer pane $p_{e,1}$ and the inner pane $p_{e,2}$. The coupling factors $\varphi_{1,1}$ and $\varphi_{1,2}$ depends on the four volume coefficients $\vartheta_{1,1}$, $\vartheta_{1,2}$, $\vartheta_{2,1}$, $\vartheta_{2,2}$ (see equations (7-12), (7-13) and (7-18)). For point fitted insulation glass units with undercut anchors, an analytical solution for the

determination of the volume coefficients does not exist. Hence, the user determines the coefficients numerically.

A detailed description of the analytical extension of the climate load model and the application to point fitted triple insulation glass units with undercut anchors are given in annexe B.

7.3 Application procedure of the extended climate load model

In this section, the application procedure of the extended climate load model is exemplarily presented for point fitted double insulation glass with undercut anchors (Figure 7.6). The application of the procedure to point fitted triple insulation glass is analogue.

In a first step, the user determines the volume coefficients $\vartheta_{1,1}$, $\vartheta_{1,2}$, $\vartheta_{2,1}$, and $\vartheta_{2,2}$ for the given IGU geometry and assembly. Therefore, the static system of point fitted insulation glass with undercut anchors (section 7.2.1) is implemented in a FE-software and the inner and outer glass pane are consecutively charged with a unit load of 1 kN/m^2. The volume spanned by each glass pane is calculated and corresponds to the volume coefficients.

In a second step, the coupling factors $\varphi_{1,1}$ and $\varphi_{1,2}$ are calculated by means of the volume coefficients according to the equations (7-12), (7-13) and (7-18).

Finally the coupling factors are inserted in the matrix (7-20) and the resulting surface loads acting on each glass pane are calculated.

For quick calculation, the matrix (7-20) can be implemented in a spreadsheet application tool.

The application procedure is resumed in Figure 7.6:

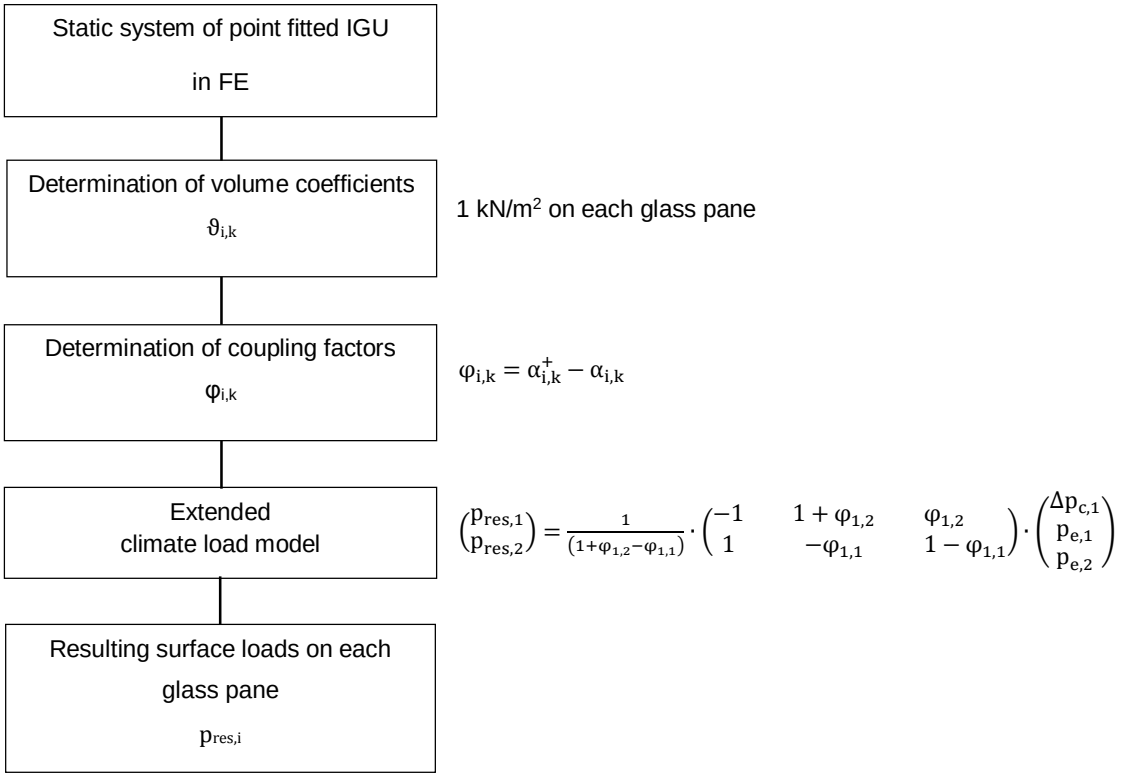

Figure 7.6 Application procedure of the extended climate load model

7.4 The volume coefficients

The volume coefficients $\vartheta_{i,k}$ describe the volume spanned by glass pane i due to the unique loading 1 kN/m² on pane k.

Currently, an analytical solution for the determination of the volume coefficient does not exist for point fitted insulation glass. Consequently, the coefficients have to be determined numerically by the user.

Each coefficient depends on several parameters:

- The thickness of the inner glass pane
- The thickness of the outer glass pane
- The thickness of the cavity
- The edge distance of the point fittings
- The dimensions of the IGU

The huge amount of parameters makes a general tabulation or formula for the calculation of the volume coefficients impossible. The volume coefficient can however be tabulated

for given standard geometries of point fitted insulation glass. The tables are presented in annexe B.

7.5 Numerical verification of the extended climate load model

7.5.1 Verification procedure and investigated point fitted IGU geometries

For the numerical verification of the extended climate load model developed in this research work, the resulting surface loads acting on each glass pane of different common double insulation glass geometries are determined by means of the extended climate load model and compared to values delivered by commercial multi-layered element theory software (Tibolt, 2014).

In detail this means:

In a first step, the static system as described in section 7.2.1 is implemented in the FE-software ABAQUS® for each IGU geometry. A unit load is consecutively applied on the inner and outer glass pane and the deformations of each node of the glass panes are determined. The spanned volume of each glass pane and hence the volume coefficients are calculated by multiplication of the element surface with the deformation at each node and summed over the plate surface. The four volume coefficients are inserted in the matrix (7-20) and the resulting surface loads acting on each glass pane are determined.

In a second step, the resulting surface loads are numerically determined with multi-layered element theory software. The software allows the modelling of the gas and its behaviour in the cavity for given external loads and climate conditions. As a result, the over- or underpressure in the glazing cavity is numerically calculated and the resulting surface loads can be derived.

Finally the values are compared in order to proof the accuracy of the extended climate load model.

The investigated undercut point fitted double insulation glass geometries are indicated in Figure 7.7 and Table 7.1.

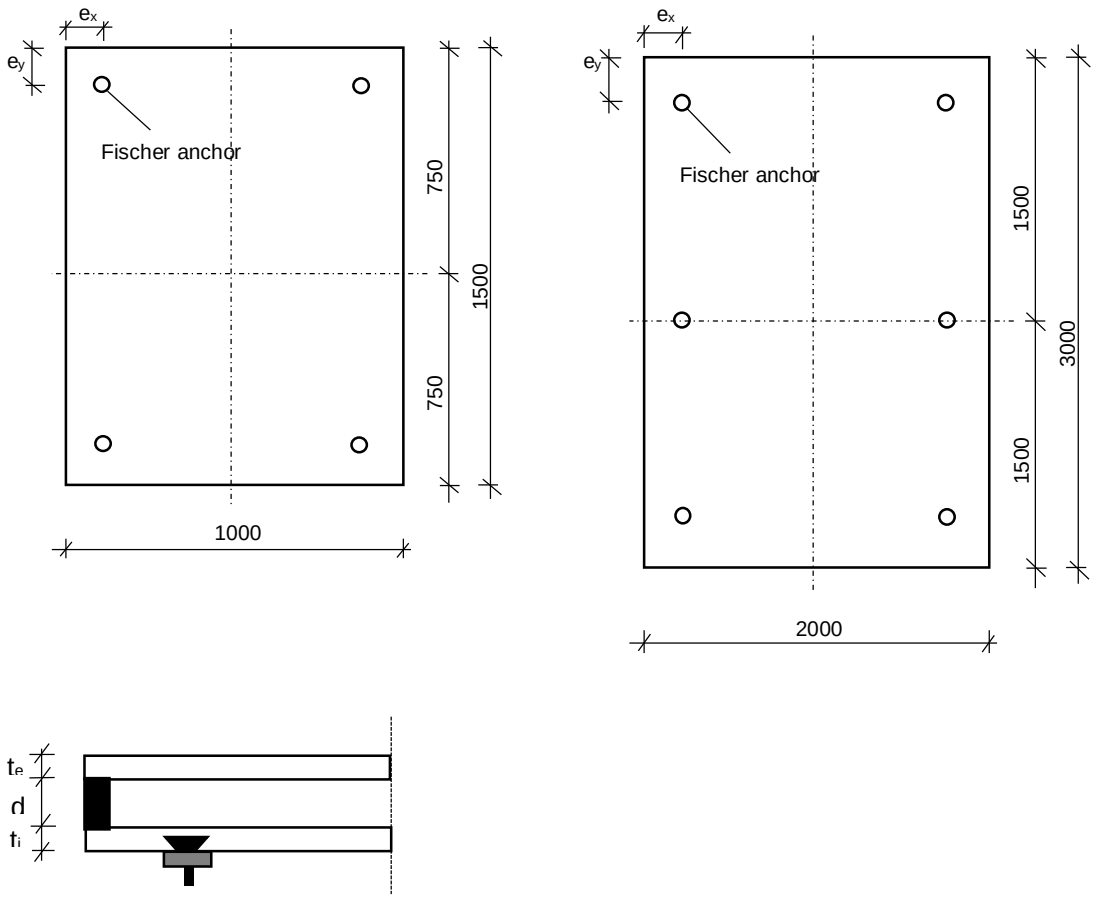

Figure 7.7 Investigated point fitted IGU geometries with undercut anchors

Table 7.1 Dimensions of point fitted IGU

Format	d [mm]	Lx x Ly [mm]	ex x ey [mm]	te [mm]	ti [mm]
M1	12	1500 x 1000	100 x 100	10	10
M2				10	20
M3				20	10
M4				16	20
L1	12	3000 x 2000	300 x 300	10	10
L2				10	20
L3				20	10
L4				16	20

Two different common glass pane formats with four and six point fittings are investigated: 1500 mm x 1000 mm (M) and 3000 mm x 2000 mm (L) (Table 6.1). By this way, the applicability of the extended climate load model to common IGU geometries with varying number of point fittings is verified. Four different glass thicknesses for the outer and inner glass panes configurations are investigated in order to proof the ability of the extended

climate load model to cover the load distribution on the panes in dependency of their stiffness. For each IGU format, the glazing cavity has a thickness of 12 mm.

For each format, the two extreme climate loads (winter and summer) (Table 7.2) according to the (DIN 18008-2) are considered and in parallel a wind pressure load of 2,0 kN/m^2 is applied on the outer pane.

Table 7.2 The extreme climate loads according to (DIN 18008-2)

Climate load	ΔT [K]	Δp_{met} [kN/m²]	ΔH [m]	p_0 [kN/m²]
Summer	20	-2	600	16
Winter	-25	4	-300	-16

7.5.2 Calculation with multi-layered element theory (*MEPLA*®)

The multi-layered element theory software *MEPLA*® is based on an isoparametric 9-node multi-layered element (Figure 7.8).

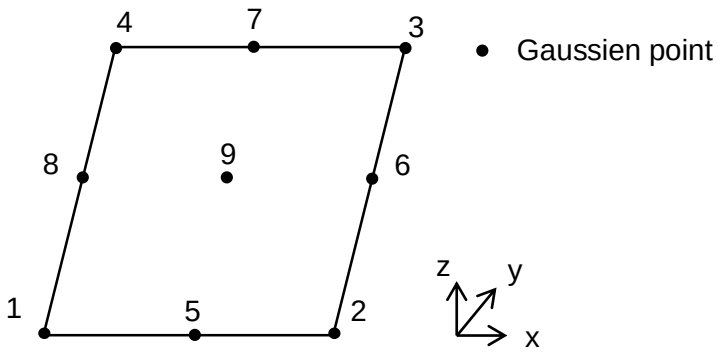

Figure 7.8 Isoparametric 9-node multi-layered element according to [MEPLA]

The multi-layered elements allow the calculation of the change of gas pressure by the gas-equation. Due to the same topology of the mesh for each layer, the gas stiffness can be correctly integrated at the Gaussian points. As the gas law is highly non-linear, the equilibrium equation is solved through iterations with consideration of the rearrangement of the gas volume, caused by the deformations of the glass panes [MEPLA]. In consequence, the climate loads can be determined with the multi-layered element theory software *MEPLA*® and compared to the results of the analytically derived extended climate load model.

The different IGU geometries are implemented *MEPLA*®. The glass plates are modelled with the 9 nodes isoparametric multi-layered elements and the corresponding thickness of the plate (Figure 7.9). The point fixations are represented by pinned supports (Case 1

in Table 7.3) and the edge bond is modelled as a pinned ended column between the edge nodes of the glass panes (section 7.2.1).

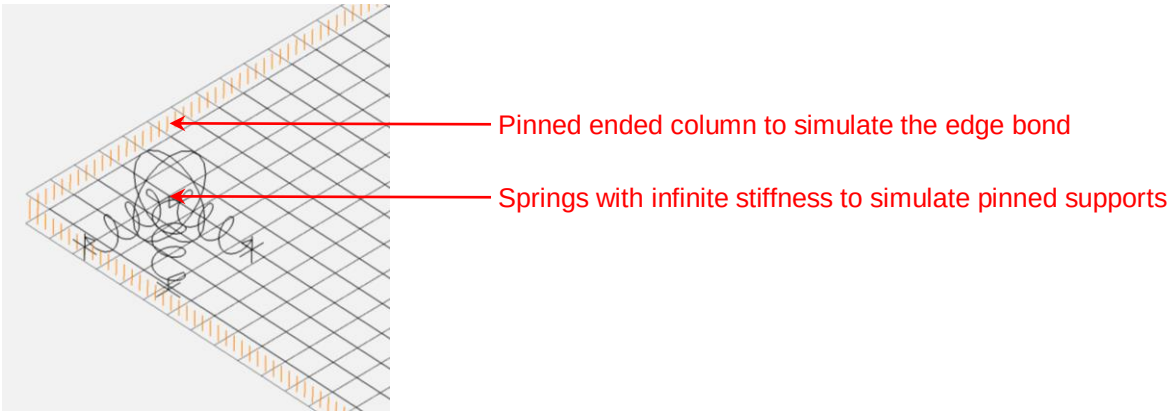

Figure 7.9 FE-model of the point fitted IGU with undercut anchors in *MEPLA*

7.5.3 Results and comparison

The resulting surface loads acting on each glass pane are determined with the extended climate load model and compared to the values given by *MEPLA*® (Figure 7.10 to Figure 7.13). The comparison is made for each format in Table 7.1 and for both load cases in Table 7.2.

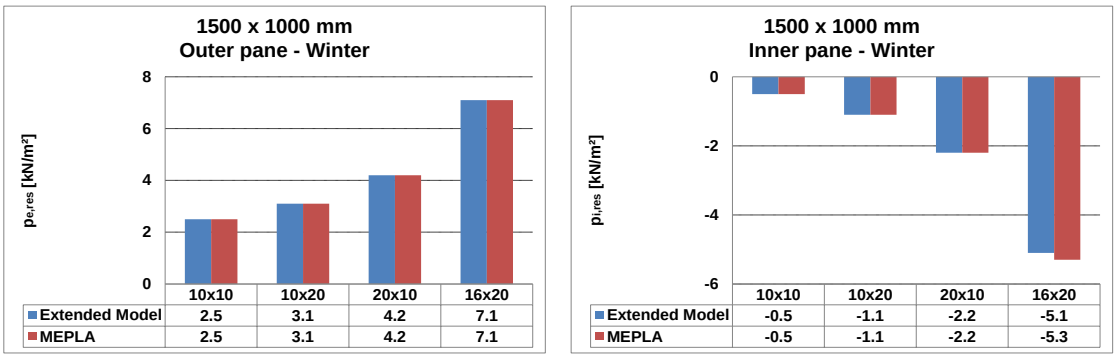

Figure 7.10 Resulting surface loads on inner and outer pane for the formats M1-M4 and load case winter

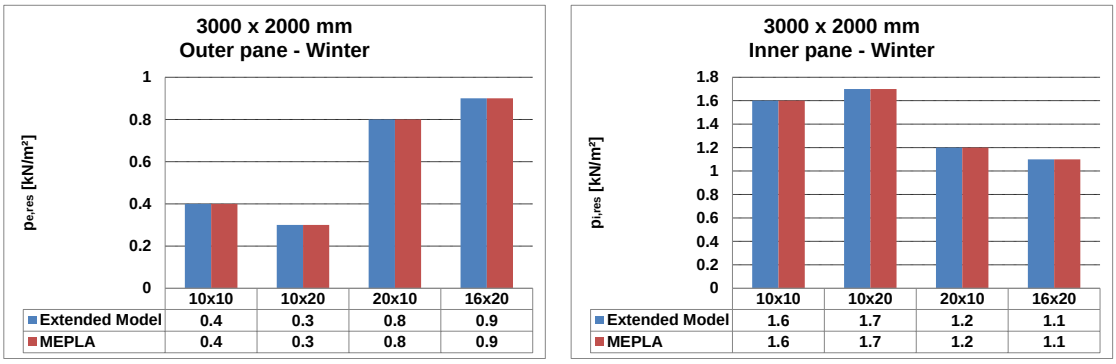

Figure 7.11 Resulting surface loads on inner and outer pane for the formats L1-L4 and load case winter

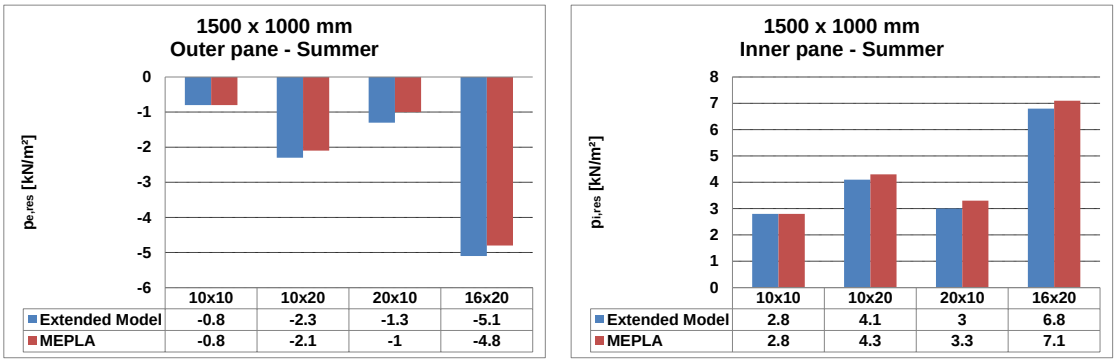

Figure 7.12 Resulting surface loads on inner and outer pane for the formats M1-M4 and load case summer

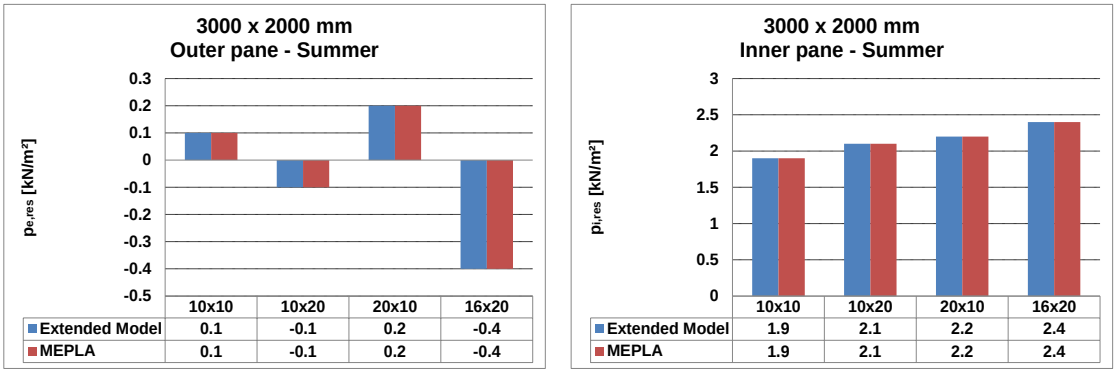

Figure 7.13 Resulting surface loads on inner and outer pane for the formats L1-L4 and load case summer

A good accordance between the resulting surface loads determined with the climate load model and the values delivered by the software MEPLA® is observed. The small deviations (< 4%) are due to rounding errors in the calculation process. In conclusion, the extended climate load model is able to determine the climate loads with high accuracy and to cover the distribution of an external load on the glass panes according to their stiffness.

7.6 Parameter study on the climate loads

7.6.1 Parameter definition

In this section, the influence of defined parameters on the climate loads is investigated. In fact, different assumptions are made for the static system which is used for the determination of the climate loads. For instance, the undercut point fittings are modelled as pinned supports and the edge bond is considered as rigid link between the edges of the glass plate. The parameter study is done to proof the accuracy of the assumptions made in section 7.2.1 and to quantify the influence of each parameter on the climate loads. Therefore, the following parameters are investigated:

- The stiffness of the undercut point fittings and of the substructure
- The stiffness of the edge bond
- The edge distance of the point fittings

7.6.2 The stiffness of the undercut point fittings and the substructure

For the static system of point fitted insulation glass described in section 7.2.1, the point fittings are assumed to be pinned supports. Thus, at the position of the anchors, the glass pane can freely rotate but cannot deform perpendicularly to its plane. In practice, the point fittings however present a finite stiffness in pane direction and they are elastically spanned in the glass pane, which influences the deformation of the glass panes. In addition, the stiffness of the substructure also impacts the deformed shape of the glass panes and thus the volume change of the cavity. In order to verify the accuracy of the assumption, the climate loads are determined with the extended climate load model. By doing so, the support conditions in Table 7.3 and in Figure 7.14 are applied in the numerical model for the determination of the volume coefficients. In all cases, the edge bond is assumed to be a rigid link.

Table 7.3 The support conditions applied in the numerical model

Case	Description	Point fitting stiffness / Substructure stiffness				
		k_x / $k_{x,Sub}$ [N/mm]	k_y / $k_{y,Sub}$ [N/mm]	k_z / $k_{z,Sub}$ [N/mm]	k_{mx} / $k_{mx,Sub}$ [Nmm/rad]	k_{my} / $k_{my,Sub}$ [Nmm/rad]
1	Pinned supports	∞ / ∞	∞ / ∞	∞ / ∞	0 / 0	0 / 0
2	FZP-G-Z + rigid substructure	4600 / ∞	4600 / ∞	1E+07 / ∞	8.59E+05 / ∞	8.59E+05 / ∞
3	Fictive point fitting + rigid substructure	100 / ∞	100 / ∞	100 / ∞	100 / ∞	100 / ∞
4	FZP-G-Z + "SystemOne"	4600 / 1111	4600 / 1111	1E+07 / 625	8.59E+05 / 9.50E05	8.59E+05 / 7.96E+05

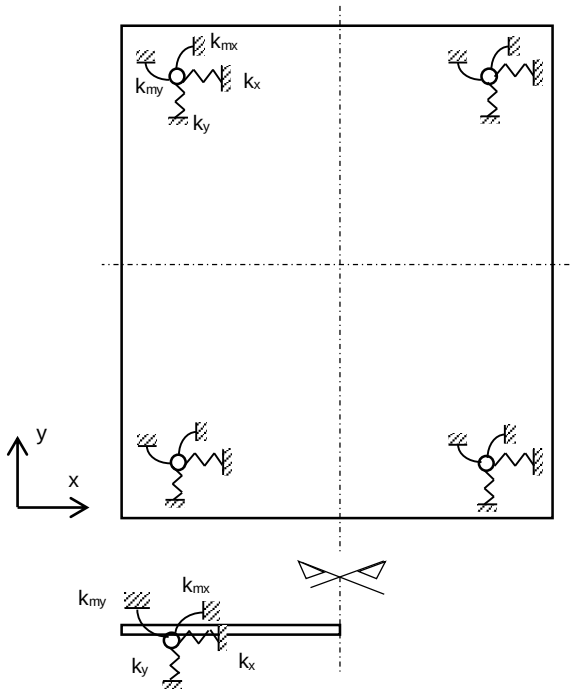

Figure 7.14 Spring stiffness definition

For condition 3, a fictive point fitting is applied in the numerical model in order to investigate the influence of a point fitting with low stiffness values on the climate loads. The substructure “SystemOne” of case 4 is a standardized substructure system

developed by the company Fischer for the Fischer undercut anchor. The stiffness values are delivered by the company (Fischer, 2007).

For the four support conditions, the resulting surface loads acting on each glass pane are determined with the extended climate load model for the formats M3 and L3 (Table 7.1) and for the load cases “winter” and “summer” with in parallel a wind pressure load of p_{ex} = 2 kN/m² on the outer pane (Table 7.2).

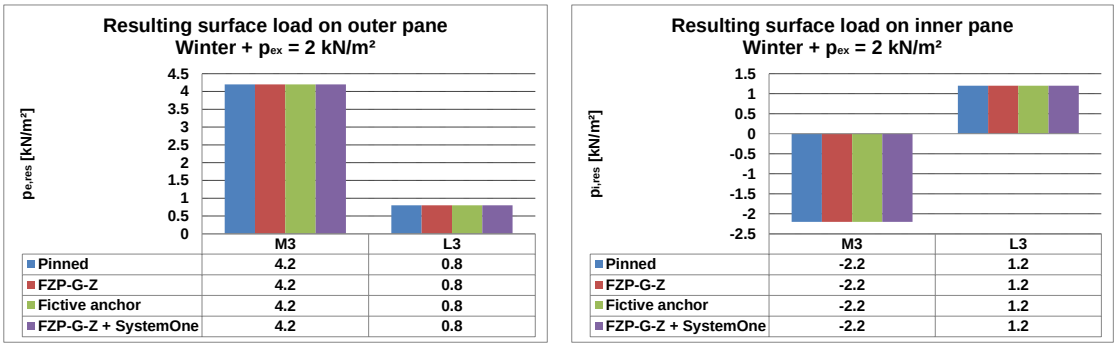

Figure 7.15 Resulting surface loads on inner and outer pane for the formats M3 + L3 and load case winter

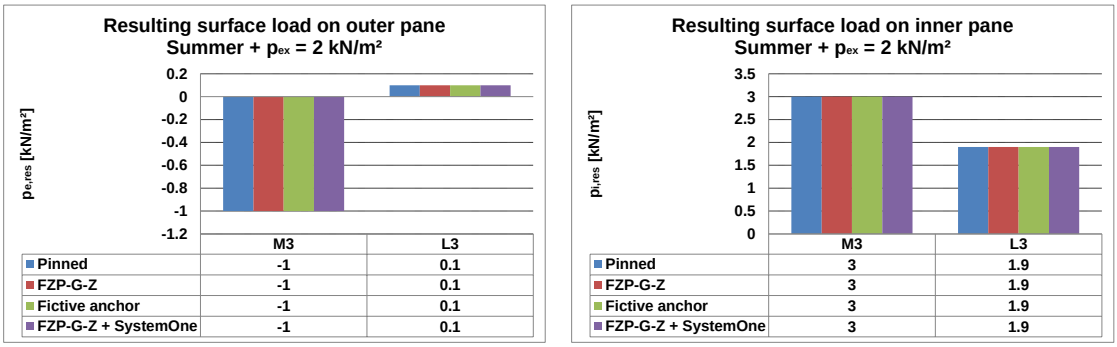

Figure 7.16 Resulting surface loads on inner and outer pane for the formats M3 + L3 and load case summer

The same climate loads are found independently from the support conditions (Figure 7.15 to **Error! Reference source not found.**).

Hence, the stiffness of the point fitting and the substructure obviously has no influence on the climate loads. In conclusion, the assumption that the point fittings can be replaced by pinned supports is verified.

7.6.3 The stiffness of the edge bond

For the determination of the climate loads, the edge bond is assumed to act as rigid link (pinned columns) along the edges of the glass pane. This assumption neglects the bending stiffness and the local sandwich element behaviour (shear transmission) of the

edge bond. Additionally, the assumption of a rigid link implies a constant gap between the edges of the glass panes. In practice, the edge bond can however expand or compress under loading, which influences the deformations of the glass panes and thus the climate loads.

In this section, the assumption that the edge bond can be modelled with rigid links is verified. The climate loads are determined with the extended climate load model. The edge bond is thereby modelled in FE once as a rigid link and another time with a current edge bond geometry with different material laws for the secondary sealant.

The dimensions of the edge bond and the corresponding FE-model are indicated in Figure 7.17.

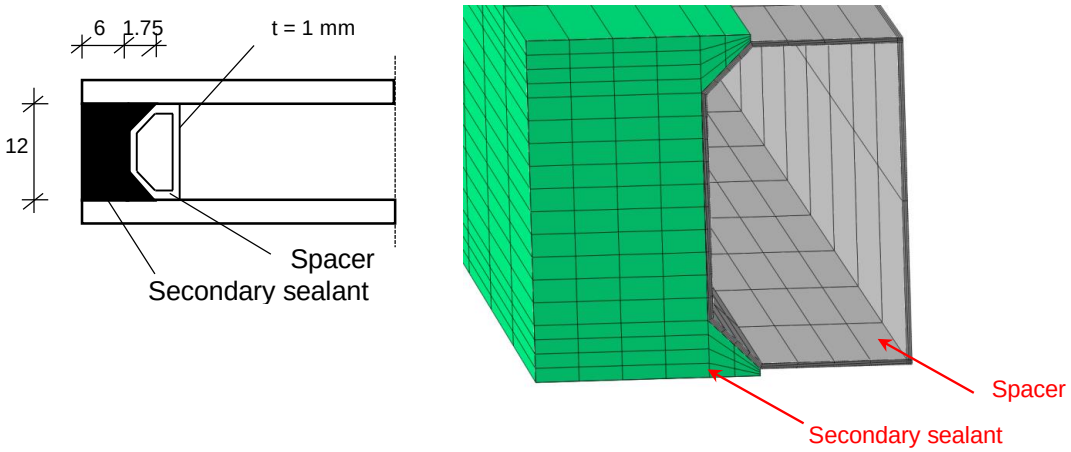

Figure 7.17 Edge bond geometry and the corresponding FE-model in ABAQUS®

The primary sealant PIB is not modelled, as it is assumed to have no structural function (section 2.3.3). Contact is defined between the glass panes and the spacer to account for the load transfer between both elements and the related stiffening effect of the edge bond, once the glass get in touch with the spacer.

The investigated cases with the different material laws for the components of the edge bond are presented in Table 7.4.

Table 7.4 Investigated cases with the corresponding material laws for the edge bond components

Case	Component	Material	Material law
1	Spacer	Aluminium	E = 70 000 N/mm²
	Secondary sealant	Structural silicone DC 993	E = 1 N/mm²
2	Spacer	Aluminium	E = 70 000 N/mm²
	Secondary sealant	Structural silicone DC 993	E = 2.4 N/mm²
3	Spacer	Aluminium	E = 70 000 N/mm²
	Secondary sealant	Structural silicone DC 993	Dias
4	Spacer	No spacer	-
	Secondary sealant	Structural silicone DC 993	Dias

For the cases 1 to 3, the spacer is made of aluminium with a linear elastic material law and the secondary sealant is made of structural silicone DC 993 for which a linear elastic material law is assumed. The Young's moduli for the silicone are derived from pure tension test (E = 1 N/mm^2) (Dias, 2013) or delivered by the producer (E = 2.4 N/mm^2) (Dow Corning, 2004). The material law called "Dias" corresponds to a hyperelastic material law for the structural silicone DC 993, which is derived in (Dias, 2013) based on tension, compression, shear and oedometric tests. It consequently reflects the real material behaviour of the silicone. For case 4, the spacer is removed in order to investigate the influence of the stiffness of the spacer on the climate loads. In all cases, the point fittings are modelled as pinned supports.

For the cases 1 to 4 and the formats M3 and L3, the resulting surface loads acting on each glass pane are determined with the extended climate load model for the two extreme climate load cases "winter" and "summer" and a wind pressure load of 2 kN/m^2 on the outer pane. In addition, the resulting surface load is determined for the assumption of a rigid link (Figure 7.18 and Figure 7.19).

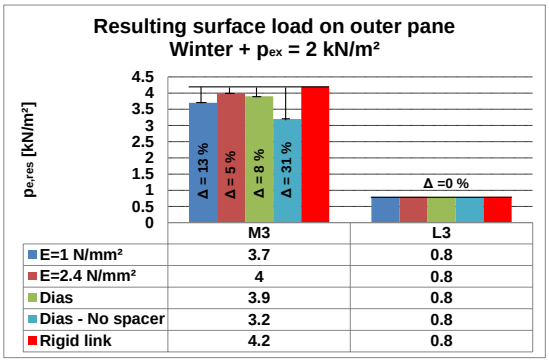

	M3	L3
E=1 N/mm²	3.7	0.8
E=2.4 N/mm²	4	0.8
Dias	3.9	0.8
Dias - No spacer	3.2	0.8
Rigid link	4.2	0.8

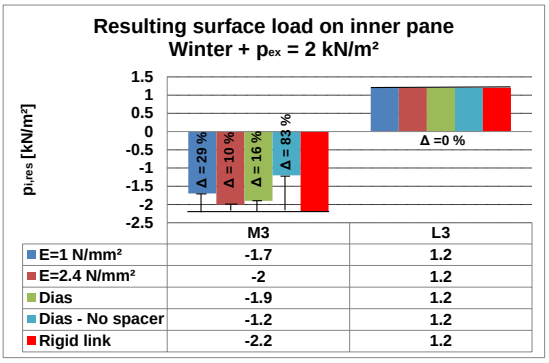

	M3	L3
E=1 N/mm²	-1.7	1.2
E=2.4 N/mm²	-2	1.2
Dias	-1.9	1.2
Dias - No spacer	-1.2	1.2
Rigid link	-2.2	1.2

Figure 7.18 Climate loads versus edge bond stiffness for the formats M3 + L3 and load case winter

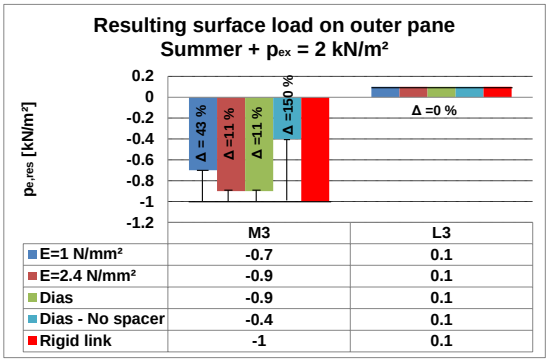

	M3	L3
E=1 N/mm²	-0.7	0.1
E=2.4 N/mm²	-0.9	0.1
Dias	-0.9	0.1
Dias - No spacer	-0.4	0.1
Rigid link	-1	0.1

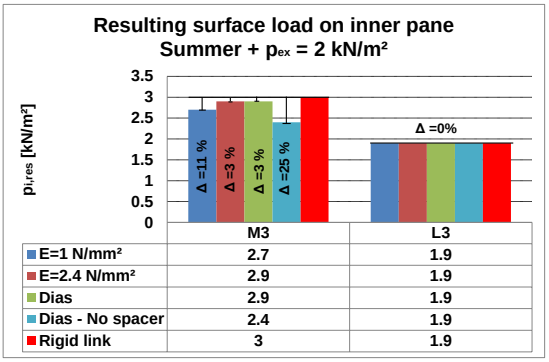

	M3	L3
E=1 N/mm²	2.7	1.9
E=2.4 N/mm²	2.9	1.9
Dias	2.9	1.9
Dias - No spacer	2.4	1.9
Rigid link	3	1.9

Figure 7.19 Climate loads versus edge bond stiffness for the formats M3 + L3 and load case summer

For the format M3, a high influence of the silicone stiffness on the climate loads is observed. The resulting surface loads decrease with decreasing stiffness values of the silicone and vice versa. The edge bond configuration without the spacer leads to the lowest loads. The loads are up to 150 % (Figure 7.19) lower than for the case, where the edge bond is modelled with rigid links. In fact, a low stiffness of the edge bond, induced whether by a low silicone stiffness or spacer stiffness, implies higher deformations of the glass panes and thus bigger volume changes of the cavity. Larger volume changes involve a decrease of the overpressure (load case summer) respectively underpressure (load case winter) in the cavity and hence lower resulting surface loads.

For the format L3, neither an influence of the silicone secondary sealant nor an influence of the spacer is set. This is due to the fact, that the format L3 presents a high initial volume of the cavity and that the volume changes caused by the external loading and the pressure change are small compared to the initial volume. In consequence, the influence of the stiffness of the edge bond on the climate loads is not visible for large IGU formats.

The modelling of the edge bond as a rigid link delivers the highest resulting surface loads for format M3 and the same resulting surface loads than every other case for format L3.

In consequence, the assumption that the edge bond acts like a rigid link is conservative and hence it is justified.

The high influence of the edge bond stiffness on the climate loads for format M3 raises the question in how far the differences in the climate loads are reflected in the deformations and stresses of each glass pane of the IGU. Therefore, the maximal deformations and stresses at the mid-span of the inner and outer glass panes are numerically determined for each case of format M3 (Table 7.4) with the corresponding resulting surface loads and edge bond configurations (Figure 7.18 to Figure 7.19). For comparison, the deformations and the stresses are additionally calculated for each case of format M3 with the resulting surface loads determined with help of the numerical model, where the edge bond is considered as a rigid link. For the calculation, the point fittings are represented by springs with the stiffness values of the Fischer undercut anchor FZP-G-Z.

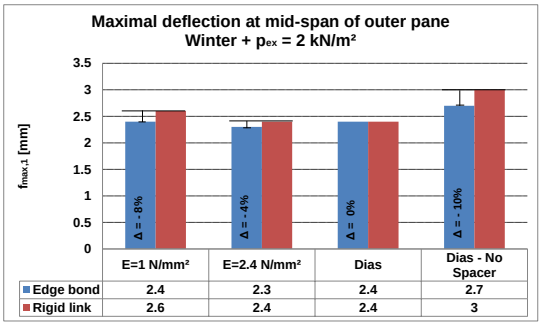

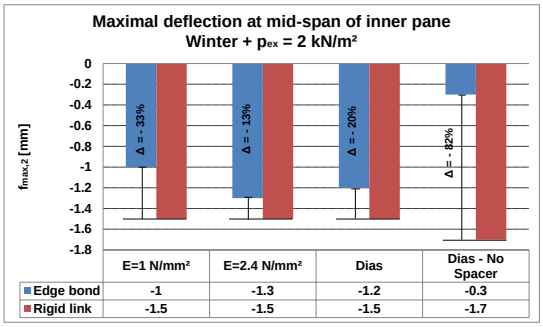

Figure 7.20 Maximal deflection at mid-span of outer pane for format M3 and load case winter

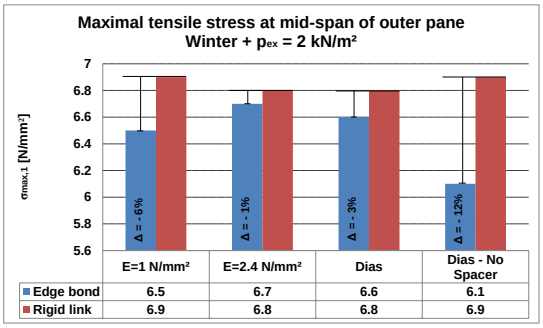

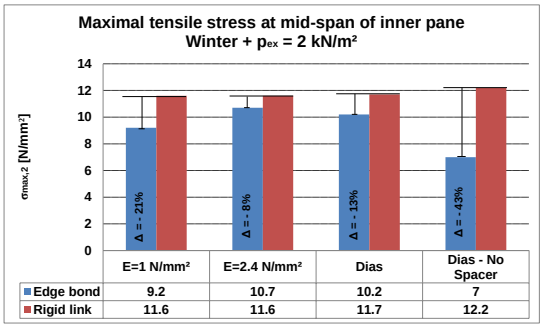

Figure 7.21 Maximal tensile stress at mid-span of outer pane for format M3 and load case winter

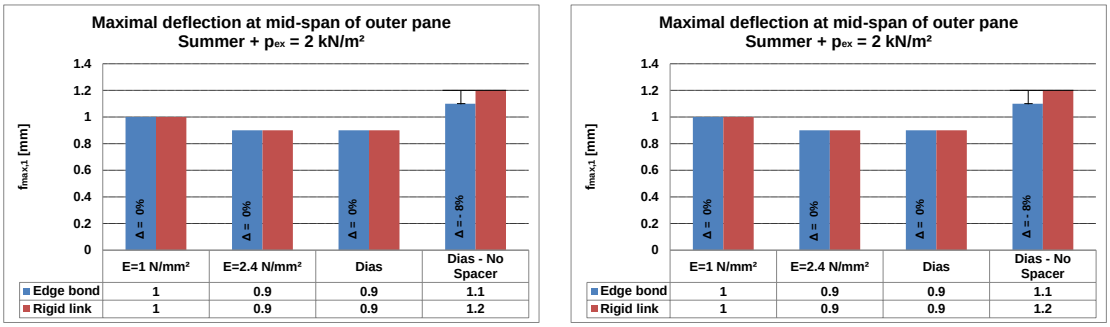

Figure 7.22 Maximal deflection at mid-span of outer pane for format M3 and load case summer

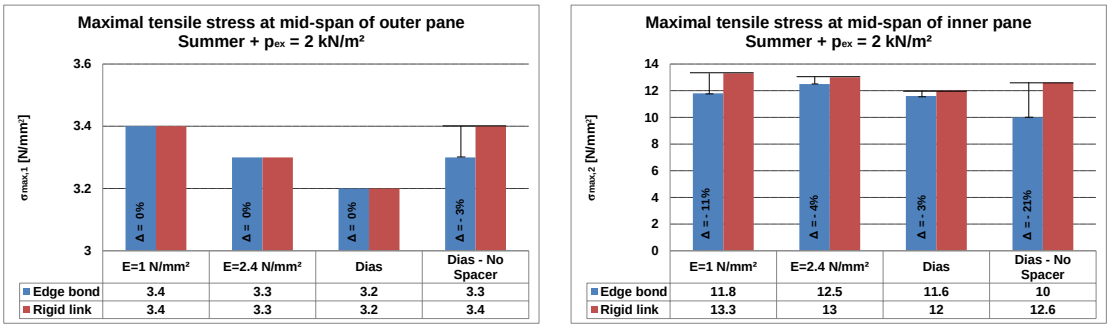

Figure 7.23 Maximal tensile stress at mid-span of outer pane for format M3 and load case summer

In all cases, the deformations and stresses calculated with the resulting surface loads, which are determined with help of the numerical model, where the edge bond is replaced by a rigid link, are higher than the values obtained for the resulting surface loads, which are determined with assistance of the numerical models taking into account the exact edge bond geometry and the different material laws for the secondary sealant and the spacer.

The maximal differences (82 %) are noticed for the edge bond configuration without the spacer. This result coincides with observation done for the climate loads. The differences for the deformations and stresses are however lower than for the climate loads. For instance, a difference of 150 % for the climate loads (Figure 7.19) on the outer pane implies a difference of only 8 % and 3 % for the deformations respectively the stresses of the pane (Figure 7.22 and Figure 7.23). This observation apparently does not correspond to the expectation, that higher loads induce higher deformations and stresses. Nevertheless an explanation for the observation can be given: In double insulation glass, the inner and outer glass panes are coupled and an increase of the climate loads implies an increase of the resulting surface loads on both panes. As the surface loads on the panes are oriented in opposite directions, they partially compensate each other and as the result, the deformations and the stresses only vary slightly.

For all cases, the assumption of a rigid link delivers conservative values for the deformations and stresses. In consequence, it is justified to replace the edge bond in the numerical model for the determination of the volume coefficients by a rigid link.

7.6.4 The edge distance of the point fitting

In order to quantify the influence of the edge distance of the point fittings on the climate loads, the resulting surface loads are determined for the formats M3 and L3 for different edge distances of the point fittings (Figure 7.24). For the calculation, the point fittings are represented by pinned supports and the edge bond is modelled with rigid links.

The different edge distances are shown in Table 6.5.

Table 7.5 Edge distances of the point fittings

Format	e_x x e_y [mm]
M3	60 x 60
	100 x 100
	150 x 150
	200 x 200
	300 x 300
L3	60 x 60
	100 x 100
	150 x 150
	200 x 200
	300 x 300

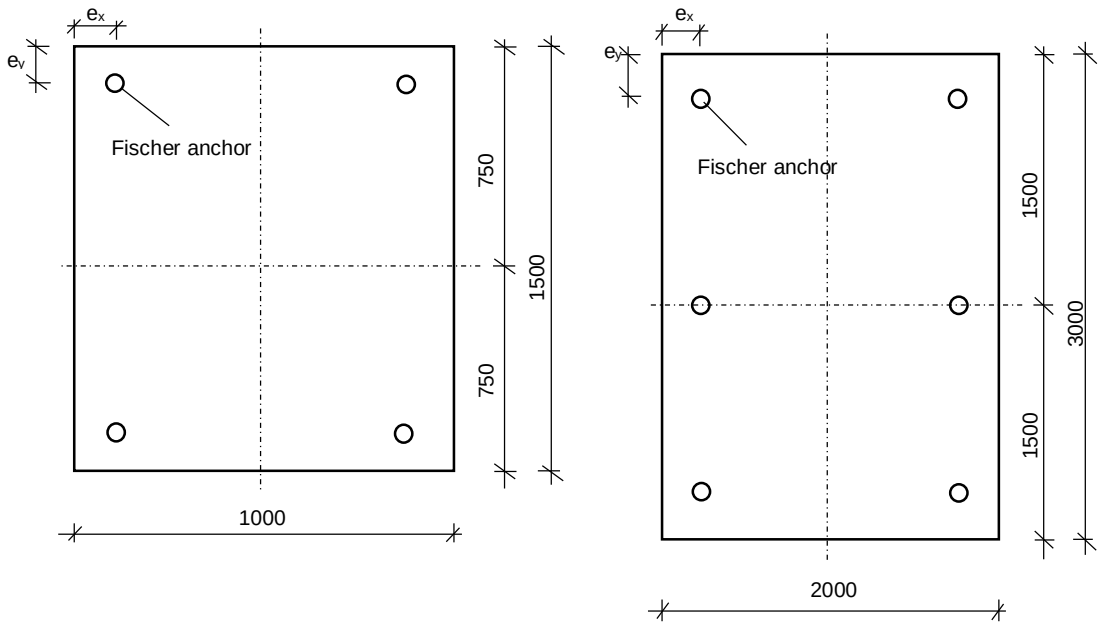

Figure 7.24 Investigated point fitted IGU geometries with undercut anchors

The edge distances of 60x60 mm correspond to the minimal allowable distance for the Fischer undercut anchor FZP-G-Z in single glazing (Z-70.2-122) and the distances of 300x300 mm are the maximal allowable distances according to (Z-70.2-122).

First of all, the resulting surface loads are determined for each format defined in and for the two extreme climate conditions “winter” and “summer”. No external load is applied.

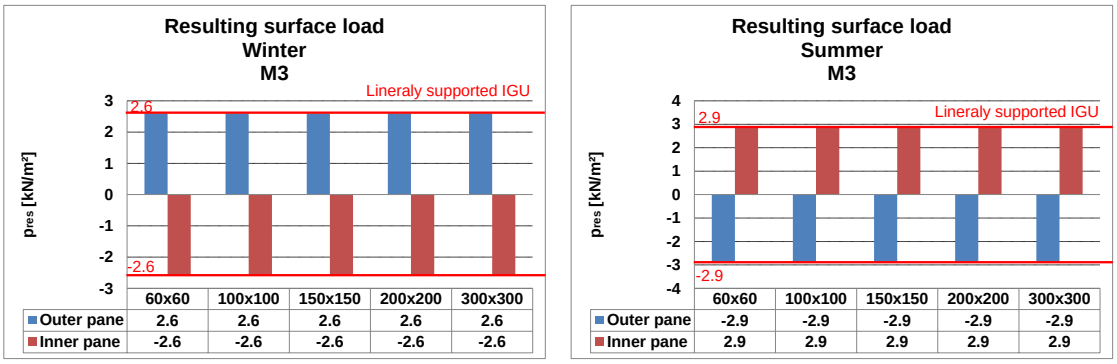

Figure 7.25 Climate loads versus edge distance for the format M3 and the load cases winter and summer

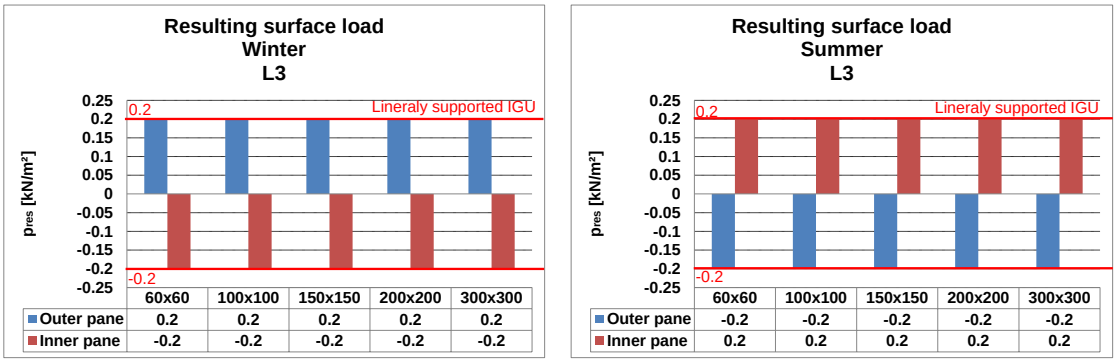

Figure 7.26 Climate loads versus edge distance for the format L3 and the load cases winter and summer

No difference in the resulting surface loads acting on the inner and outer pane is observed for the different edge distances of the point fittings (Figure 7.25 and Figure 7.26). In addition, the loads are identic to the climate loads of linearly supported IGU. In fact, the two extreme climate conditions “winter” and “summer” create an under- respectively overpressure in the cavity and thus resulting surface loads acting on the inner and outer pane. These loads equilibrate each other and the resulting forces in the point fittings (pinned supports) and the edge bond are consequently null. As a result, the coupling effect of the inner and outer glass pane via the edge bond is not activated. In this case, the climate loads of point fitted IGU with undercut anchors are identic to those of linearly supported IGU and the edge distance of the point fitting does not influence the climate loads.

Secondly, the resulting surface loads are determined for each format defined in and for the two extreme climate conditions “winter” and “summer” with in parallel a wind pressure load of p_{ex} = 2 kN/m^2.

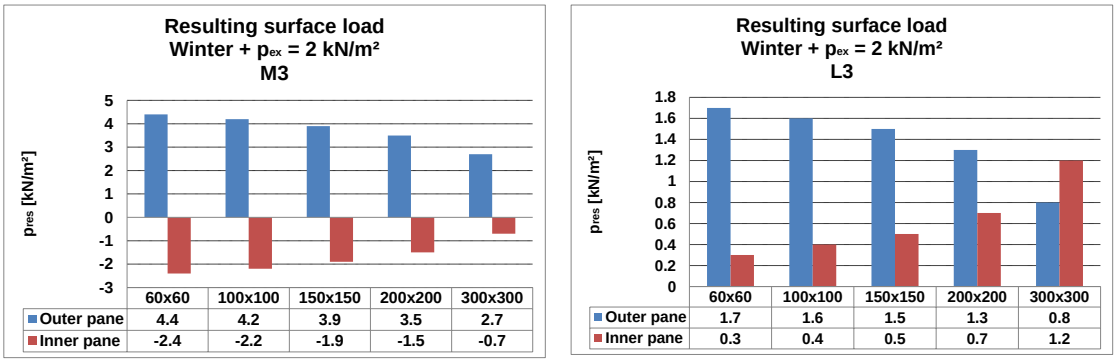

Figure 7.27 Climate loads versus edge distance for the formats M3 + L3 and load case winter + wind load

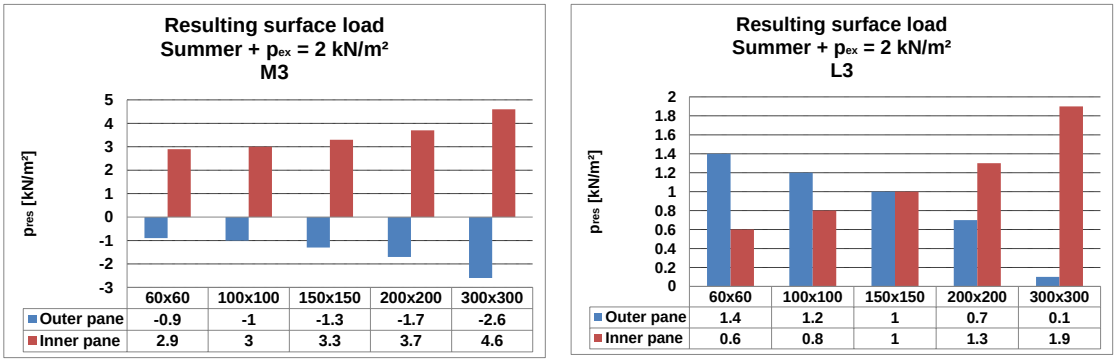

Figure 7.28 Climate loads versus edge distance for the formats M3 + L3 and load case summer + wind load

Due to the external wind pressure load, the point fittings are under load and their positions influence the climate loads.

For format M3 and the load case “winter” with a wind pressure load (Figure 7.27), the pressure in the cavity increases with increasing edge distances. As a result, the underpressure in the cavity is reduced and the resulting surface loads acting on the inner and outer glass pane decrease. The same effect is noticed for the load case “summer” with a wind pressure load for format M3 (Figure 7.28).

For format L3 and the load case “winter” with a wind pressure load (Figure 7.27), the wind pressure load on the outer pane is so high that despite of the load case “winter”, an overpressure acts in the cavity. This is the reason why the resulting surface loads acting on the inner pane is positive according to the sign convention defined in Figure 7.5. As for the format M3, the pressure in the cavity increases with increasing edge distances of the point fittings. In consequence, the resulting surface load on the outer pane decreases and the surface load on the inner pane increases with higher edge distances. The same observation is done for the “summer” climate load with in parallel a wind pressure load on the outer pane (Figure 7.28).

7.7 Summary and conclusion

The climate load model of *Feldmeier* for linearly supported IGU is analytically extended to the static system of point fitted IGU with undercut anchors. The glass panes are coupled via the edge bond in addition to gas in the glazing cavity. An adequate static system for point fitted IGU with undercut anchors is developed for this purpose. In the static model, the point fittings are modelled as pinned supports and the edge bond is represented by pinned ended columns. The principle of the extended model consists in the determination of the pressure in the cavity for given climate conditions. The pressure difference between the cavity and the environment delivers the resulting surface load acting on each glass pane.

For the calculation of the climate loads, the user has to numerically determine different volume coefficients $\vartheta_{i,k}$. $\vartheta_{i,k}$ corresponds to the enclosed volume of a pane “i" due the loading of pane “k” with a load “1”. For the determination of the volume coefficients, the static system of the IGU is implemented in commercial FE-software (MEPLA®) and each pane is subsequently loaded with a unit load. The volume coefficients depend on several parameters and a general tabulation is therefore not possible. They are however tabulated for some common IGU geometries.

The extended climate load model is numerically verified by comparing the resulting surface loads on each glass pane to the equivalent values delivered by commercial multi-layered element theory software. The comparison is done for different IGU dimensions and pane thicknesses. By this way, the validity of the extended climate load model for different numbers of point fittings and its capacity to cover the load distribution on the glass panes according to their stiffness is proofed. Good accordance between the climate loads is noticed and in consequence, the extended climate load model is numerically verified.

The influence of different parameters of the point fitted insulation glass unit on the climate loads is investigated. The objective is to quantify the influence and to verify the assumptions made for the static system of point fitted IGU, which is used for the determination of the climate loads.

The stiffness of the point fittings and of the substructure is found to have no influence on the climate loads. Consequently, the point fittings can be replaced by pinned supports in the static system.

The influence of the stiffness of the edge bond system strongly depends on the dimensions of the point fitted IGU. For large dimensions, the volume change of the cavity

due to the extension or compression of the edge bond is small compared due the initial volume of the cavity and the influence is not detectable. For smaller dimensions of the IGU, the stiffness of the edge bond has a high influence on the climate loads and the loads increase with increasing stiffness values. The highest climate loads and the corresponding deformations and stresses are obtained for the assumption that the edge bond behaves like a rigid link. In conclusion, the assumption is conservative and the edge bond geometry can be replaced by a rigid link in the static system for the determination of the climate loads.

For the pure “winter” and “summer” loads according to (TRLV, 2006), no influence of the edge distance of the point fittings on the climate loads is noticed. In these cases, the climate loads of point fitted insulation glass units with undercut anchors are identic to those of linearly supported IGU. This can be explained by the non-activated coupling effect of the glass panes via the edge bond and the load-free point fittings (section 7.6.4). If an external load is applied on the inner or outer pane, the influence of the edge distance becomes detectable. The pressure of the gas inside the glazing cavity increases with increasing edge distances of the point fittings and the climate loads vary accordingly.

In conclusion, the developed extended climate load model for point fitted IGU with undercut anchors allows the determination of the resulting surface loads acting on each glass pane. The climate model and the assumptions made for the static system, on which it is based, are numerically verified. The experimental verification of the model is presented in chapter 9.

8 Extension of the SLG-method to point fitted IGU with undercut anchors

8.1 Objectives

For the application of the SLG-method (Beyer, 2007), an extension to the use for point fitted IGU with undercut anchors is needed. First, a general procedure for the extension of the SLG-method to point fitted IGU with undercut anchors is proposed. Secondly, the general procedure is applied for the extension of the SLG-method to the specific case of the proposed point fitted IGU with the Fischer undercut anchor FZP-G-Z and the dual-sealed edge bond system in section 4.4. Thirdly, the verification inequalities for the extended SLG-method are derived for the proposed point fitted IGU in section 4.4 and the general application procedure of the method is resumed in a flow-chart. Finally, a parameter study concerning the influence of the edge bond stiffness on the stress concentration in the borehole area is presented.

8.2 General procedure for the extension of the SLG-method

The general procedure for the extension of the SLG-method to point fitted IGU with undercut anchors is subdivided into three steps:

i. Identification of the influencing parameters

The application of the SLG-method requires the preliminary knowledge of three key parameters: the size of the local area, the stress concentration factor and the transfer functions (see also section 2.5.4). They are developed in (Beyer, 2007) and are delivered to the user in form of data sheets for the corresponding point fitting type. For single glazing and for a given point fitting system, they depend on the following parameters: the size of the local area depends on the run-out length of the stress concentration and its location at the borehole. The stress concentration factor is a function of the size of the local area, the edge distance of the point fitting, the thickness of the glass plate and the geometry of the borehole. The transfer functions only depend on the plate thickness and the borehole geometry. The extension of the SLG-method to point fitted IGU with undercut anchors necessitates the adaption of the key parameters (size of local area, stress concentration factor and transfer functions), which now depend on the system parameters of the point fitted IGU with undercut anchors. In a first step, these parameters are identified by elaborating the differences between point fitted single glazing and point fitted IGU.

ii. Extension of the SLG-method

In the second step, the existing SLG-method for point fitted single and laminated glazing is finally extended to point fitted IGU by adapting gradually the size of the local area, the stress concentration factor and the transfer functions.

iii. Derivation of the verification inequalities

In a third step, the verification inequalities for the field range and the borehole area of the inner glass pane are derived. For the verification in the borehole area, component tests of the undercut anchors in single glazing are conducted until failure of the connection (Chapter 6). The positions of the break inducing stress peaks at the borehole are determined by numerically simulating the component tests. Finally the verification inequalities are derived for each position.

8.3 Definition of the parameters for the extension of the SLG-method

A comparison between point fitted single glazing and point fitted IGU identifies the potential parameters to be investigated.

The presence of the edge bond system in insulation glass is the first significant difference in comparison to single glazing. The edge bond statically couples the two glass panes of double insulation glass units and the edges of the inner and outer glass pane cannot freely deform as it is the case for the point fitted single glazing. Thus, the stiffness of the edge bond system and its geometry influence the deformation behaviour of the IGU and hence the key parameters of the SLG-method (The size of the local area, the stress concentration factor and the transfer functions). The stiffness of the edge bond system depends on the stiffness of each of its components. Consequently, the influence of the stiffness of each component on the key parameters has to be investigated.

The second difference between single glazing and insulation glass is the presence of the second glass pane in the IGU. In fact, the coupling of the two glass panes via the edge seal system also engenders the stiffness of the outer glass pane to have an influence on the deformations of the whole unit and thus on the key parameters of the SLG-method.

Finally, a last difference between point fitted single glazing and point fitted IGU consists in the gas entrapped in the glazing cavity of the IGU. The gas extends or contracts in dependency of the external loads acting on the glass panes, the temperature differences in the cavity and the barometric pressure changes. This behaviour of the gas creates additionally loads that act on the inner and outer glass panes of the IGU, the so called climate loads (Chapter 7). The climate loads are calculated with the extended climate

load model developed in chapter 7 and are superimposed with the external surface loads. In this way, the gas in the cavity is decoupled from the static system of point fitted IGU and the climate loads consequently do not influence the key parameters of the SLG-method.

In conclusion, the following parameters have to be investigated for the extension of the SLG-method to point fitted IGU with undercut anchors:

- The edge distance of the point fitting
- The stiffness of the edge bond system
- The geometry of the borehole
- The geometry of the edge bond system
- The thickness of the inner pane of the IGU
- The thickness of the outer pane of the IGU

8.4 Application of the general procedure to the IGU with the Fischer undercut anchor

The main aim of this chapter is the adaption of the key parameters of the SLG-method for point fitted single glazing to point fitted IGU with undercut anchors. The key parameters potentially depend on the parameters identified in section 8.3. These parameters are strongly related to the selected edge seal and point fitting systems for the point fitted IGU. With regards to the various existing point fitting and edge bond systems on the market, the expenditure of time for the investigation of the influence of each of these systems on the key parameters is too big. In this chapter, the general procedure in section 8.2 is therefore applied to the point fitted IGU with the Fischer undercut anchors and the dual-sealed edge system as proposed in section 4.4. In this way the influence of the parameter “geometry of the borehole” on the key parameters is omitted.

The different edge bond geometries, glass pane thicknesses as well as the stiffness values for the silicone and the spacer that are investigated and implemented in the FE-software for the adaption of the key parameters of the SLG-method are given in Figure 8.1 and Table 8.1.

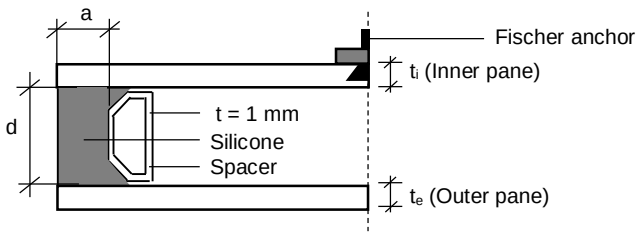

Figure 8.1 The dual-sealed edge bond system for the point fitted IGU with the Fischer undercut anchor

Table 8.1 Investigated pane thicknesses and edge bond geometries

t_i [mm]	t_e [mm]	a [mm]	d [mm]
10	10	6	12
			16
		16	12
			16
	24	6	12
			16
		16	12
			16
12	10	6	12
			16
		16	12
			16
	24	6	12
			16
		16	12
			16

From point fitted single glazing it is preliminary known, that the thickness of the glass pane with the Fischer undercut anchor significantly influences the key parameters of the SLG-method (Beyer, 2007). Therefore, the two approved thicknesses (10 mm and 12 mm) for the mounting of the Fischer undercut anchor in a monolithic glass pane are investigated for the inner pane of the point fitted IGU. For the outer pane, two different thicknesses are investigated (10 mm and 24 mm) to analyse the influence of a thin and thick outer glass pane on the transfer functions. Concerning the dual-sealed edge

system, four different geometries which are commonly applied in practice are investigated.

Table 8.2 Investigated stiffness values for the silicone sealant and the spacer

Component	Material	Material law		
		Type	E [N/mm²]	ϑ [-]
Glass pane	Glass	Linear elastic	70 000	0.23
Silicone sealant	Structural silicone	Linear elastic	1 2.4 4.8	0.48
		Hyper-elastic - Dias	-	-
Spacer	Stainless steel	Linear elastic	210 000	0.3
	Aluminium		70 000	
	Polypropylene (PP)		1000	

For the inner and outer glass pane, the linear elastic properties of the material glass are chosen (section 2.1).

Three different linear elastic material laws for the silicone sealant are investigated. They are given in the data sheets of the producers (Dow Corning, 2004), (Sika, 2012) and (Bostik, 2008). The values for the Young's modulus are experimentally determined by the producers according to (ETAG 002). The values correspond to the chord modulus based on the two specific strain values ε_1 = 0.05 % and ε_2 = 0.25 %. In this case, the time dependency of the silicone is not considered. A value of 0.48 is used for the Poisson's ratio of the silicone sealant. According to the producers, the Poisson's ratio of silicone should be ϑ = 0.5 to reproduce its isochoric behaviour. However, the numerical calculation does not converge with a value of 0.5. Furthermore, in (O'Hara, 1983) Poisson's ratio in the range of 0.48 to 0.49 are found for small strains by using the hydrostatic method. In consequence, a value of 0.48 for the Poisson's ratio of silicone is justified. Additionally to the three linear elastic material laws for the silicone sealant, a hyper elastic material law is considered. The law is developed in (Dias, 2013) for the silicone DC 993 and is based on the change of the energy potential in tension, compression, shear and oedometric tests. The material law takes into account: the continuous and discontinuous (*Mullin's* effect) damage of the silicone under cyclic loading, the influence of the loading rate on the initial stiffness of the silicone and the stress softening of the silicone under long-term loading. The influence of these

parameters is considered in the material constants of the law (Dias, 2013). Thus, the material law allows the realistic simulation of the behaviour of the structural silicone DC 993 under quasi-static loading or cyclic loading.

For the spacer, three different in practice commonly applied materials are investigated: Stainless steel and aluminium with a relative high stiffness and PP, a plastic material with a low stiffness. For each of the three materials, a linear elastic material law from literature is chosen. In this way, the influence of different spacer materials on the key parameters of the SLG-method is investigated.

8.5 Extension of the SLG-method

The development of the extended SLG-method consists in the adaption of the size of the local area, the stress concentration factor and the transfer functions to the point fitted insulation glass unit with the Fischer undercut anchors and the dual-sealed edge system.

8.5.1 Adaption of the size of the local area to undercut point fitted IGU

The SLG-method was originally developed for the design of point fitted single and laminated glazing. It allows the determination of the stress peak at the borehole by means of a simple 2D FE-model of the glass pane. In the numerical model, the point fittings are simulated by springs which are locally defined in single nodes. The elastic clamping of a single node leads to stress singularities which, according to the principle of *Saint-Venant*, decline at a certain distance away from the borehole. From up this distance, the stress distributions in a plate with a borehole and a plate without a borehole are identic. For point fitted single and laminated glazing with the Fischer undercut anchor, it is shown in (Beyer, 2007) that this distance corresponds to three times the diameter of the borehole. In consequence, the minimal radius of the local area is fixed to $r = 3 \cdot Ø_{Borehole}$. Additionally, it is proofed in (Beyer, 2007) that the stress peak in single and laminated glazing always occurs at the inner surface of the borehole, which is oriented towards the pane surface. Thus, a maximal allowable size for the local area does not exist. Finally its radius for point fitted single and laminated glazing with the Fischer undercut anchor is fixed to r = 72.5 mm (Beyer, 2007).

For point fitted insulation glass units with the Fischer undercut anchor, the limits for the size of the local area have to be checked and if necessary, they have to be adapted.

This is done in three steps:

In a first step, the minimal size of the local area is defined. The distribution of the maximal tensile stresses along a path from the middle of a circular IGU without a borehole and a

circular IGU with the Fischer undercut borehole to the edge are numerically determined and compared. The distance wherefrom a coincidence between the two stress distributions is noticed, corresponds to the minimal allowable radius of the local area. The geometries of the circular insulation glass units are indicated in Figure 8.2.

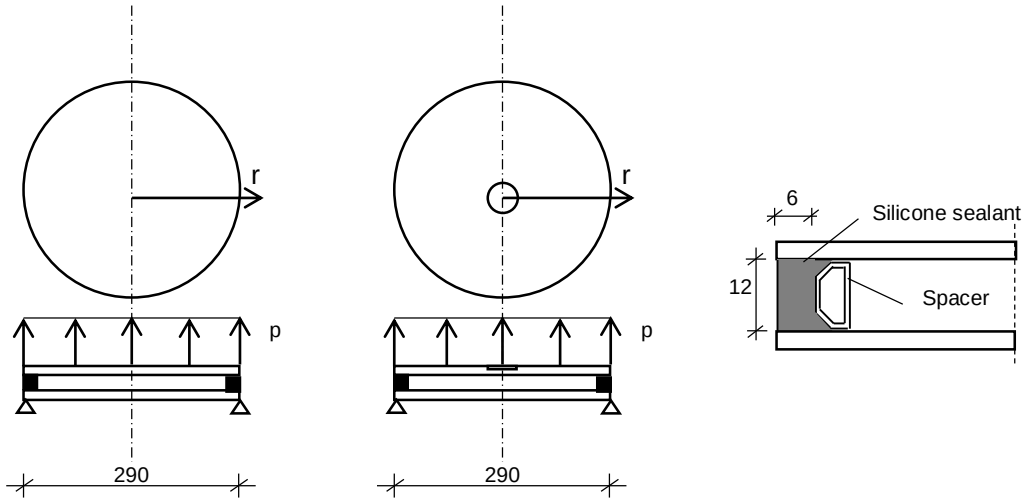

Figure 8.2 Geometry, static system and loading of the circular insulation glass units

In Figure 8.3, the stress distributions are exemplarily shown for the silicone sealant described with the hyperelastic material law of Dias (Dias, 2013) and an aluminium spacer (E = 70 000 N/mm², ϑ = 0.3). Both stress distributions coincide from up a distance of r = 45 mm, which exactly corresponds to three times the diameter of the borehole of the Fischer undercut anchor. Further numerical simulations show, that this observation is independent from the stiffness and geometry of the edge bond, the material of the spacer as well as of the thicknesses of the inner and outer glass panes. In conclusion, the minimal allowable radius of the local area for point fitted insulation glass with the Fischer undercut anchor corresponds to r_{min} = 45 mm.

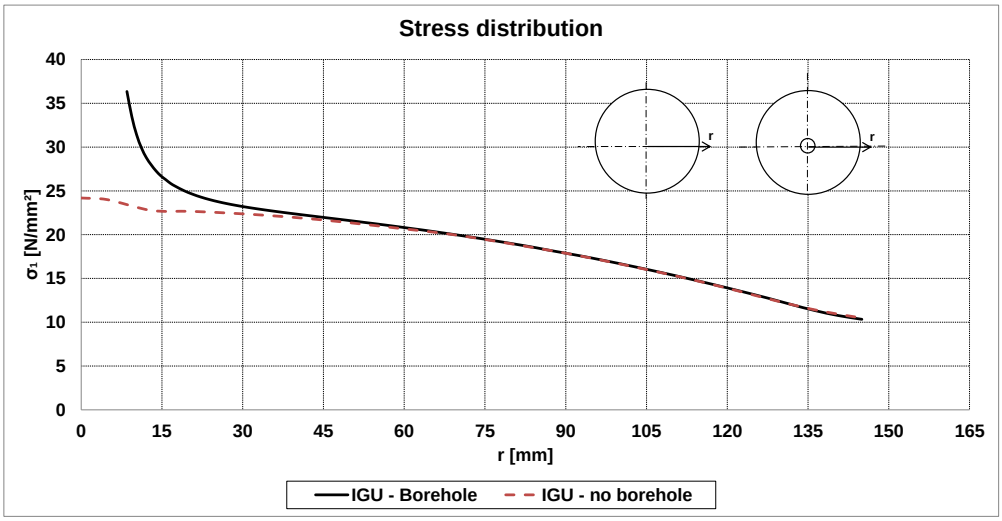

Figure 8.3 Stress distribution from the middle of the circular IGU to the edge, hyperelastic material law for the silicone sealant, aluminium spacer, no PIB

In a second step, the maximal size of the local area is defined. The location of the stress peak at the borehole is investigated for different load configurations and edge bond stiffness values. In dependency of the position of the stress peak, the maximal allowable radius of the local area is defined. For the proposed point fitted IGU with the Fischer undercut anchor, the location of stress peak at the borehole strongly depends on the loading level and on the edge bond stiffness. The stress peak can occur at the surface wall of the borehole which is oriented towards the free edge of the IGU (Figure 8.5).

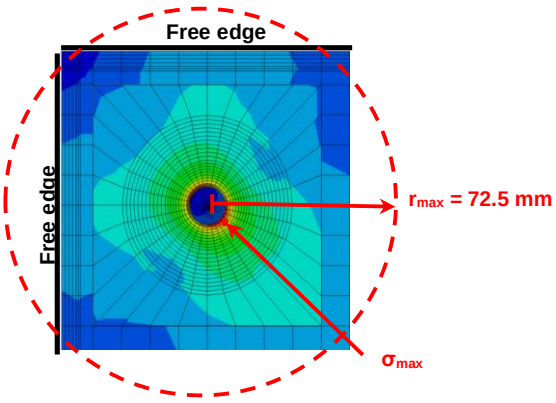

Figure 8.4 Stress peak in single glazing

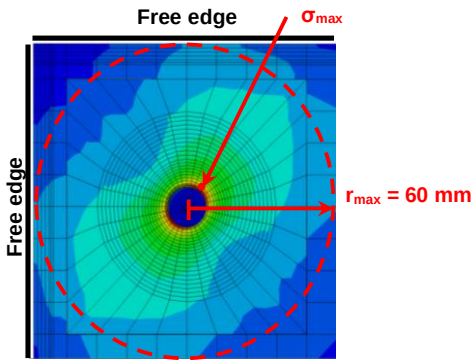

Figure 8.5 Stress peak in IGU

To avoid the local area to overlap the glass pane, the maximal allowable size of the local area is defined as the minimal possible edge distance of the Fischer anchor, as to know r_{max} = 60 mm.

Finally, it is verified that the 2D FE-model in chapter 5 is able to find the same stress distribution within the limits for the size of the local area than an equivalent 3D FE-model

which considers the exact geometry of the borehole and of the Fischer undercut anchor. Figure 8.6 shows the comparison of the maximal tensile stress distribution between the 2D and the 3D FE-model of a point fitted IGU with 4 Fischer undercut anchors and a full surface loading.

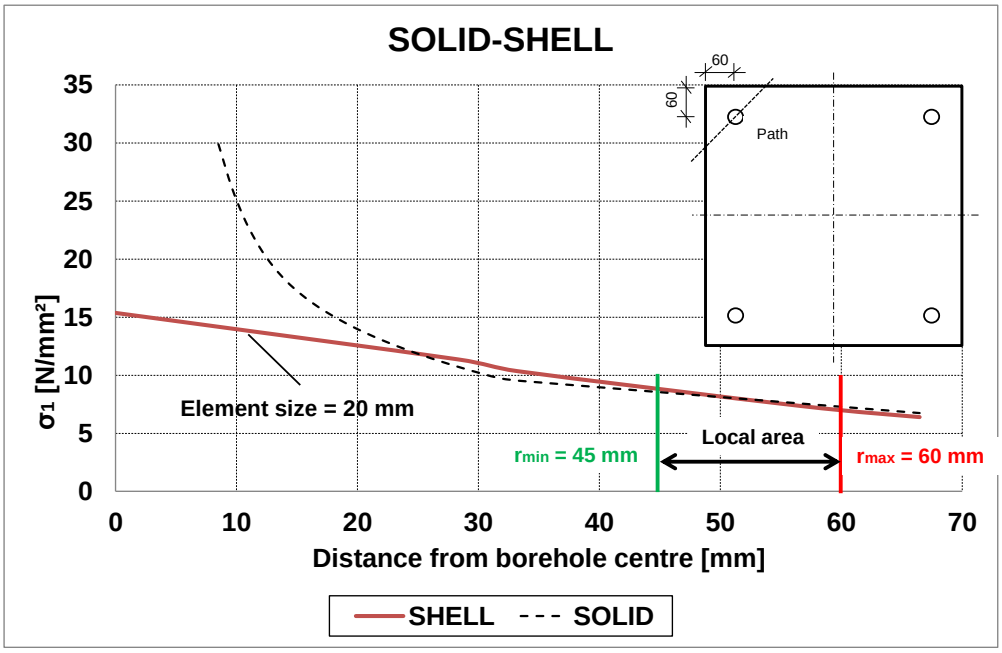

Figure 8.6 Comparison of the stress distribution

For an element size of 20 mm for the shell-elements in the 2D FE-model, a good correspondence with the 3D FE-model is noticed from up a distance of 45 mm away from the borehole. The same observation is done for the different edge bond stiffness values and geometries, different edge distances of the point fittings and different plate thicknesses. In consequence, the 2D FE-model described in section 4.4 is able to correctly simulate the stress distribution within the limits of the local area. In conclusion, the definitions of the minimal (r_{min} = 45 mm) and maximal (r_{max} = 60 mm) allowable sizes for the local area are justified and the size has to be fixed within these limits. It is proposed to fix the size of the local area for the point fitted IGU with the Fischer undercut anchor described in section 4.4 to r = 60 mm.

8.5.2 Adaption of the transfer functions

The transfer functions, also called load-stress diagrams, assign the support reactions in the point fitting (Tension, shear and moments) to the associated local component of the stress peak at the borehole (see also section 2.5.4). For the derivation of the transfer functions, the components of the stress peak at the borehole are numerically determined with an adequate FE-model for each case: tension force, shear force and the moment in

the point fitting. The drawing of the stress components against the corresponding forces respectively moments delivers the transfer functions.

In this section, the influence of the different system parameters of the point fitted IGU with the Fischer undercut anchor on the transfer functions is numerically investigated. Additionally, the transfer functions are adapted to the system of the point fitted IGU with the Fischer undercut anchors.

The transfer functions for the point fitted IGU with the Fischer undercut anchor are redefined for the following three load cases:

- Tension force in the point fitting
- Shear force in the point fitting
- Moment in the point fitting

The ultimate compression load for the connection “Fischer anchor– glass” is about 4 times higher than the ultimate tension load. Thus, to induce a failure of the connection under compression, a surface load that exceeds the range of wind loads occurring in practice would be necessary. For instance a wind load of 14 kN/m^2 is necessary to induce a compression failure at the connection in an IGU with the dimension 1200 mm x1200 mm, four Fischer undercut anchors and with an inner pane thickness of 10 mm. Therefore, the compression forces in the point fitting are not considered for the extension of the SLG-method.

The dimensions of the numerical models of the point fitted insulation glass units are resumed in Figure 8.7 to Figure 8.9.

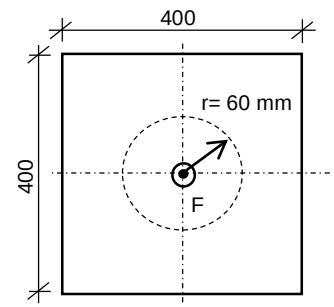

Figure 8.7 Tension in the anchor

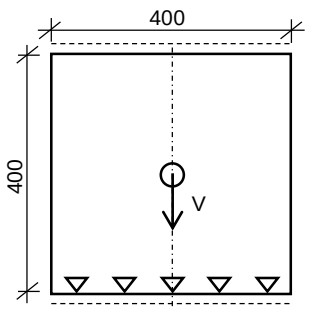

Figure 8.8 Shear in the anchor

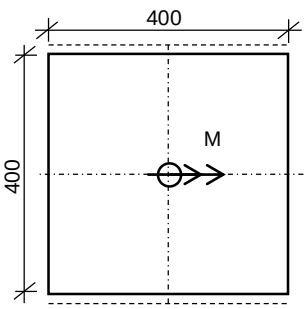

Figure 8.9 Moment in the anchor

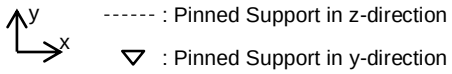

For the load case “tension in the Fischer anchor”, the support conditions consist in a circular pinned support with a radius of r = 60 mm, which corresponds to the size of the local area. For the load case “shear in the Fischer anchor”, the shear load is applied in the centre line of the connection Fischer anchor – glass to avoid eccentric moments and to assure a pure shear loading in the point fitting.

In fact the FE-models for the determination of the transfer functions consist in the calibrated and verified numerical model of the monolithic glass pane with the Fischer undercut anchor from section 6.3.1, which is implemented in a corresponding IGU geometry (Figure 8.10). The PIB is not modelled as it has no structural function (section 9.6.1).

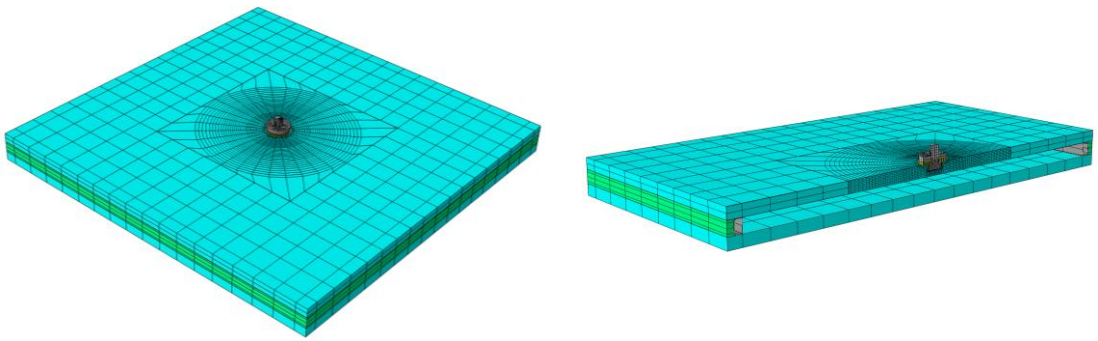

Figure 8.10 FE-model of the point fitted IGU for the determination of the transfer functions

For the determination of the transfer functions, a defined range of tension forces, shear forces and moments are applied at the point fitting in the FE-models (Figure 8.7 to Figure 8.9) and the corresponding stress concentration components at the borehole are

numerically determined. The drawing of the applied forces and moments against the stress components finally delivers the transfer functions.

A parameter study is conducted to reveal the parameters (section 8.4) which influence the transfer functions. The study is resumed in annex C.

It is found that the thickness of the inner glass pane of the point fitted IGU with the Fischer undercut anchor is the only parameter which influences the transfer functions. Consequently, the transfer functions for 10 mm and 12 mm thick inner glass panes are numerically determined with the FE-model in Figure 8.10. The transfer functions for the 10 mm thick inner glass pane are shown in Figure 8.11 to Figure 8.13 and the transfer functions for the 12 mm thick inner glass pane are indicated in annexe C.

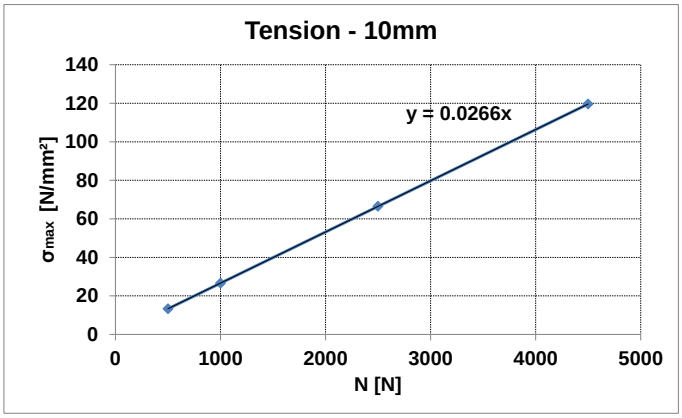

Figure 8.11 The transfer function for the tension force in the Fischer undercut anchor, t_i = 10 mm

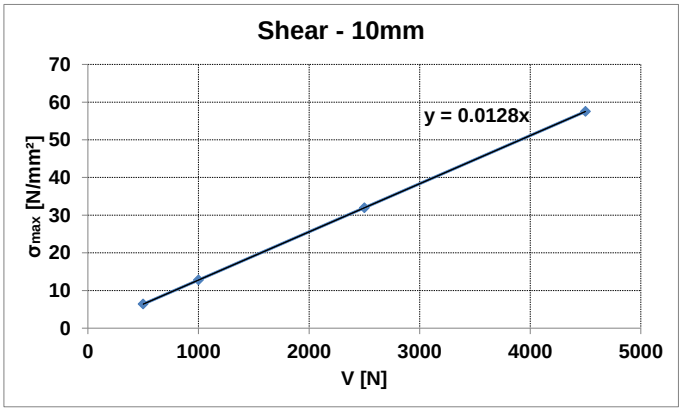

Figure 8.12 The transfer function for the shear force in the Fischer undercut anchor, t_i = 10 mm

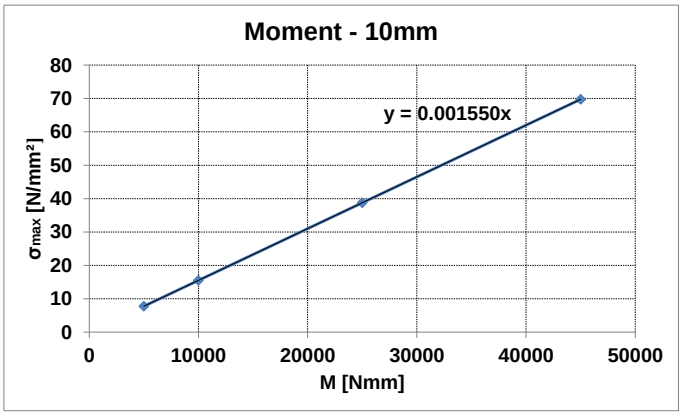

Figure 8.13 The transfer function for the moment in the Fischer undercut anchor, t_i = 10 mm

8.5.3 Adaption of the stress concentration factors

The stress concentration factors (k-factors) consider the amplification of the stress peak at the borehole due to the pure bending of the glass pane. In (Beyer, 2007) the factor is defined as the quotient of the stress peak at the borehole and the global stress component at the rim of the local area in glass pane under pure bending. As the size of the local area is redefined for the point fitted IGU with the Fischer undercut anchor (section 8.5.1), the stress concentration factors have to be adapted. In this section, the influence of the different parameters on the k-factors are investigated and the factors are redefined to comply with the system of the point fitted IGU with the Fischer undercut anchor, which is proposed in this research work.

Depending on the position of the point fittings in the glass panes, they are categorized into two groups (Figure 8.14) (Beyer, 2007):

- Corner point fittings
- Edge point fittings

The corner point fittings are located at the corner of the glass pane. The point fittings in glass panes with four fittings are generally corner point fittings.

The edge point fittings are positioned at the edge of glass panes. In glass panes with at least 6 point fittings, the fittings in the centre lines are edge point fittings.

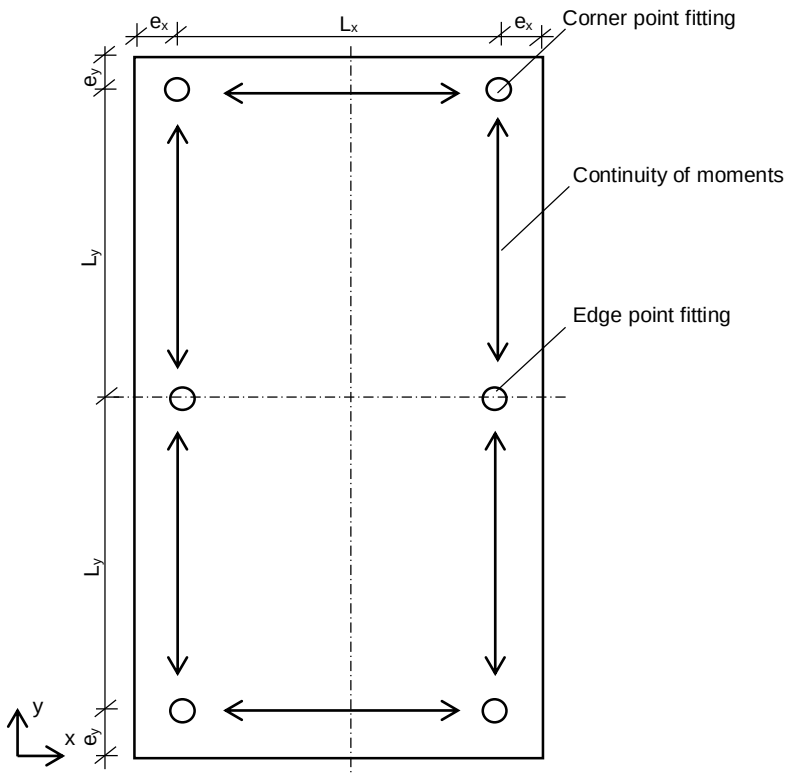

Figure 8.14 Definition of point fittings and continuity of moments in the glass pane

In dependency of the continuity of moments in the glass pane, the k-factors have to be determined separately for the corner and for the edge point fittings.

Edge point fittings:

In point fitted single glazing, the k-factors for the edge point fittings are numerically determined by means of a glass plate with the borehole which is subjected to uniaxial bending. The stress peak at the borehole and the global stress component at the rim of the local area are determined for different edge distances and pane thicknesses. The quotient of both stress values finally delivers the k-factors (Beyer, 2007). For the point fitted IGU with the Fischer undercut anchor, the procedure is the same. The only difference consists in the additional investigation of the influence of the different edge bond stiffness values and geometries and the different outer glass pane thicknesses on the k-factors. The geometry of the FE-model of the IGU is shown in Figure 8.15 and Table 8.3. The glass pane with the undercut borehole and the verified mesh and element quality of chapter 6 is implemented in the IGU and the IGU is subjected to pure bending.

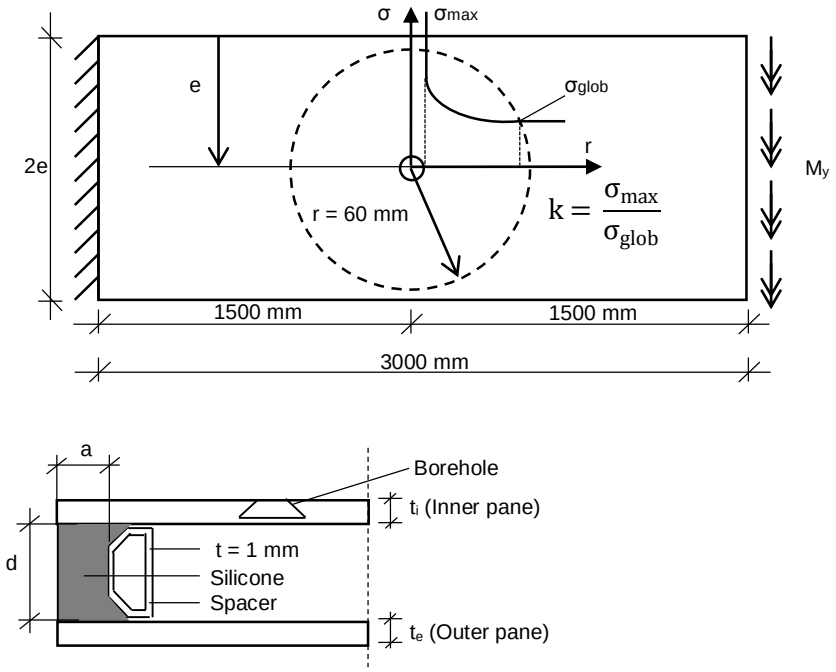

Figure 8.15 Geometry of the FE-model of the point fitted IGU

Table 8.3 Outer and inner pane thicknesses and thickness ratio

t_i [mm]	t_e [mm]	t_e/t_i [-]
10	6	0.6
	10	1
	16	1.6
	24	2.4
12	6	0.5
	12	1
	16	1.3
	24	2

The selected pane thicknesses correspond to the values which are commonly applied in insulation glass for façade applications. The values also cover the effective thicknesses of laminated glass according to (Z-70.2-122).

The investigated edge seal geometries and the different material laws for the edge bond components are listed in Table 8.1 and Table 8.2. The different edge distances of the edge point fitting are shown in Table 8.4. The edge distances of 60 mm and 300 mm correspond to the lower respectively the upper acceptable limit for the edge distances of the Fischer undercut anchor according to (Z-70.2-122).

Table 8.4 Edge distances of the edge point fittings

e [mm]
60
90
150
200
300

Similar to the procedure for the adaption of the transfer functions, a parameter study detects the influencing parameters. The parameter study is described in annex C.

The stiffness of the silicone, the thickness ratio of the glass panes and the edge distance of the undercut anchors are the parameters which influence the k-factor. Concerning the influence of the silicone stiffness, the highest values for the k-factors are observed for the hyperelastic material law of *Dias* (annexe C). As this law accurately describes the silicone behaviour (Dias, 2013) and delivers the stress concentration factors on the conservative side, the k-factors are exclusively derived for the hyperelastic material law of *Dias*.

The deviation procedure of the stress concentration factors is exemplarily explained for a 10 mm thick inner glass pane and an edge distance of the Fischer undercut anchor of 60 mm. In Figure 8.16, the k-factors are drawn against the different thickness ratios.

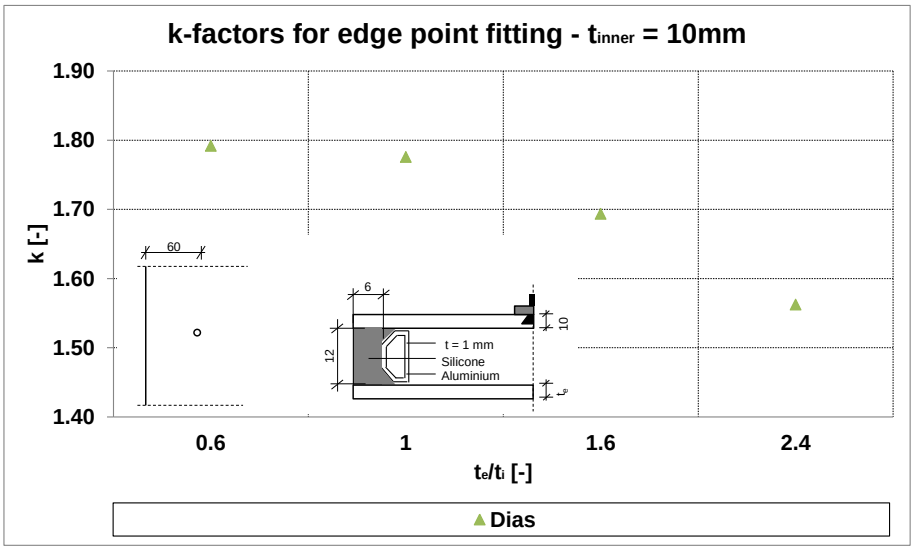

Figure 8.16 k-factors for the different thickness ratios of the inner and outer glass pane, t_i = 10 mm, e =60 mm

For the thickness ratios of $t_e/t_i \geq 1.0$, the different k-factors can be conservatively approximated with a straight line and hence they can be described with a linear function (Figure 8.17).

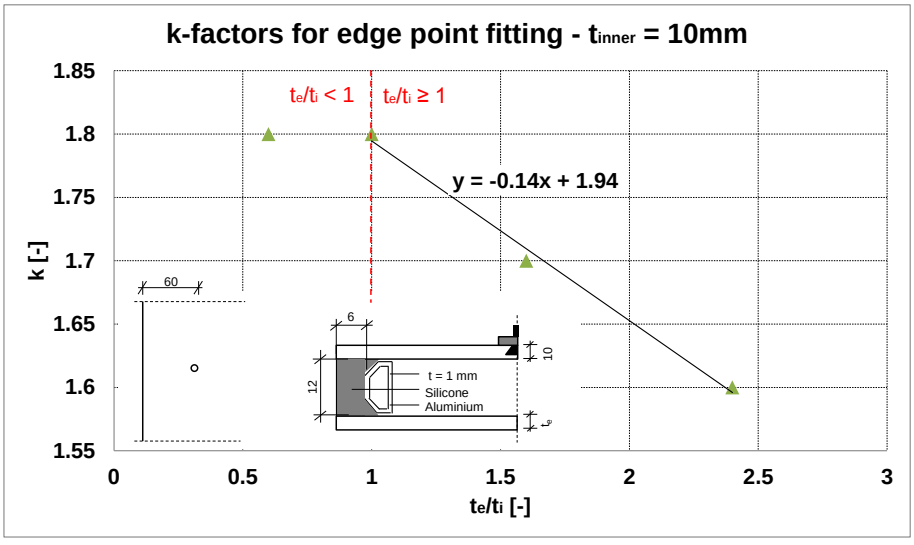

Figure 8.17 Determination of the k-factors for t_e/t_i > 1.0, t_i = 10 mm, e =60 mm

For the thickness ratios t_e/t_i < 1.0, the k-factor is indicated with k = 1.80. This procedure for the deviation of the k-factors can be applied to each edge distance of the Fischer undercut anchor and each inner glass pane thickness (annexe C). In this way, it is possible to conservatively indicate a k-factor in dependency of the thickness ratio of the inner and outer glass pane and the edge distances (Table 8.5 and Table 8.6). The k-

factors for $t_e/t_i \geq 1$ are conservatively approximated by one single equation for each inner glass pane thickness t_e = 10 mm and t_e = 12 mm (see also annexe C).

Table 8.5 k-factors for the inner glass pane thickness t_i = 10 mm, edge point fitting

ti	e	$t_e/t_i < 1.0$	$t_e/t_i \geq 1.0$
[mm]	[mm]	[-]	[-]
	60	1.8	
	90	1.8	
10	150	1.8	$-0.14 \cdot t_e/t_i + 1.94$
	200	1.8	
	300	1.7	

Table 8.6 k-factors for the inner glass pane thickness t_i = 12 mm, edge point fitting

ti	e	$t_e/t_i < 1.0$	$t_e/t_i \geq 1.0$
[mm]	[mm]	[-]	[-]
	60	1.9	
	90	1.9	
12	150	1.8	$-0.13 \cdot t_e/t_i + 1.95$
	200	1.8	
	300	1.8	

Corner point fittings:

It can be numerically shown that for a small edge distance ($e_x \leq L_x/10$ and $e_y \leq L_y/10$) of the corner point fittings, the moments in the glass pane are in equilibrium with the moments in the Fischer undercut anchor and that no continuity of the moments in the glass pane arises. In consequence the k-factor is k = 1.0, independently from the pane thicknesses and the edge bond stiffness values. For higher edge distances of the corner point fittings ($e_x > L_x/10$ or $e_y > L_y/10$), a continuity of the moments in the glass pane occurs and two different cases are distinguished:

i. Asymmetric overhang

For an asymmetric overhang of the corner fitting ($e_x \neq e_y$), the continuity of the moment in the glass pane appears in the direction of the higher edge distance. This is the same case than for an edge point fitting. For a corner point fitting with an asymmetric overhang, it is therefore proposed to conservatively apply the same k-factor as for the edge point fitting.

ii. Symmetric overhang

For a symmetric overhang of the corner point fitting ($e_x = e_y$), the continuity of the moments in the glass pane arises in two directions (Figure 8.18). If the point fitting does not contribute to the transfer of the self-weight, the moments M_x and M_y in the point fitting are zero (Beyer, 2007). Hence, the k-factor is numerically determined with a die plate under biaxial bending (Figure 8.19).

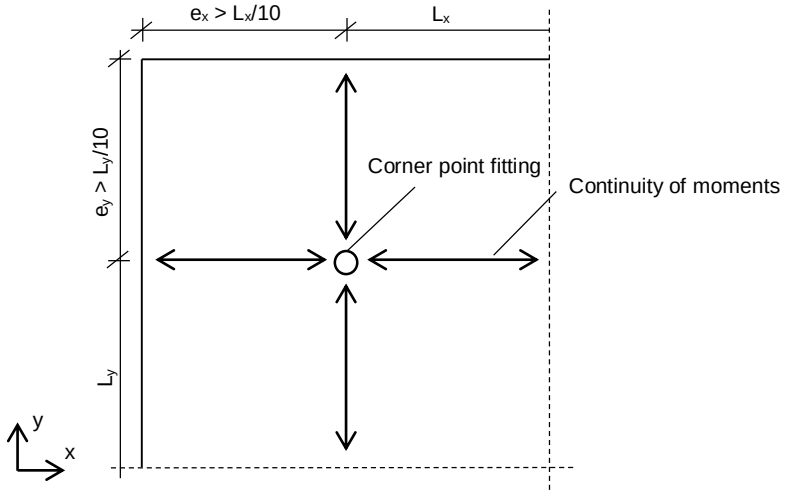

Figure 8.18 Symmetric overhang of a corner point fitting and continuity of the moments in the glass pane

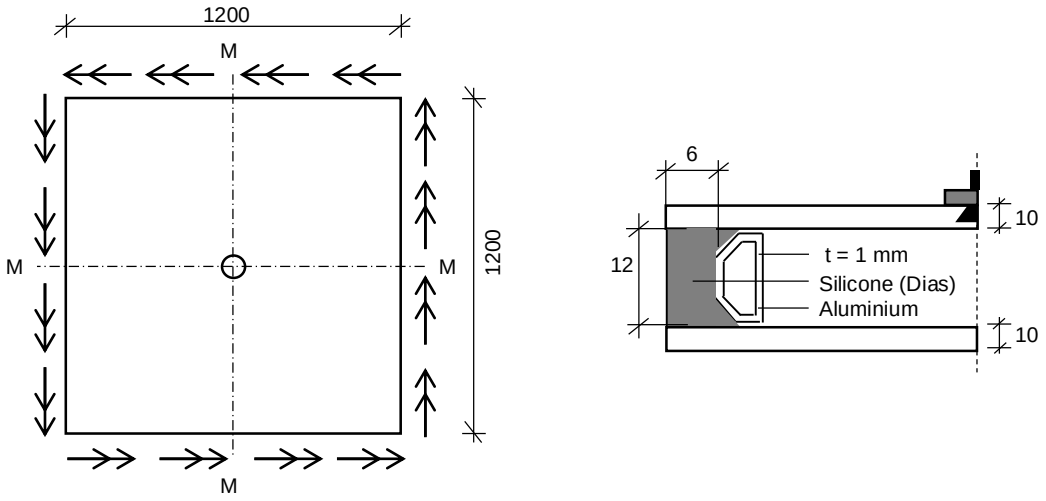

Figure 8.19 Geometry of the FE-model of the glass pane under biaxial bending

It can be shown, that the k-factor for a corner point fitting with a symmetric overhang is independent from the thickness ratio of the inner and outer glass pane and the edge bond stiffness. In consequence, the stress concentration factor only depends on the thickness of the inner glass pane (Table 8.7).

Table 8.7 k-factors, corner point fitting with symmetrical overhang

t_i	k
[mm]	[-]
10	1.4
12	1.4

8.6 Derivation of the verification inequalities for the inner glass pane

According to the extended SLG-method, the verification of the inner glass pane with the Fischer undercut anchor is carried out in two areas of the glass pane:

- The field ranges (mid-span and edge of the glass plate)
- The borehole area (connection “Fischer undercut anchor – glass”)

8.6.1 The field ranges

The field ranges are sufficiently distant from the borehole and they are not affected by the stress concentrations at the borehole in consequence.

The verification of the field ranges consist in the limitation of the maximal tensile stresses and deformations:

$$\sigma_{\mathrm{Field,act}} \leq \sigma_{\mathrm{Field,rec}} \quad \textbf{(8-1)}$$

$$f_{\mathrm{Field,act}} \leq f_{\mathrm{Field,rec}} \quad \textbf{(8-2)}$$

With:

$\sigma_{\mathrm{Field,rec}}$ = Permissible stress (i.e. $\sigma_{\mathrm{Field,rec}}$ = 50 N/mm^2 (Z-70.2-122))

$f_{\mathrm{Field,rec}}$ = Permissible deformation (i.e. $f_{\mathrm{Field,rec}}$ < l/100 (Z-70.2-122))

The acting maximal tensile stresses $\sigma_{\mathrm{Field,act}}$ and deformations $f_{\mathrm{Field,act}}$ are numerically determined with the 2D FE-model described in chapter 5.

8.6.2 The borehole area

The verification of the connection of the Fischer undercut anchor in the glass pane consists in limiting the maximal tensile stress peaks at the borehole. The maximal allowable stresses can be numerically derived by means of the ultimate loads and moments which are experimentally determined in the component tests in chapter 6. The component tests and the corresponding numerical simulation reveal two different locations for the break inducing stress peaks at the borehole:

- The ultimate normal force N_d in the Fischer anchor creates maximal tensile stresses $\sigma_{N,max}$ which are maximal along the rim of the borehole (black circle in Figure 8.20). They correspond to tangential stresses in the peripheral direction of the borehole.
- The stress plot of the borehole for the Fischer undercut anchor under the ultimate shear load V_d and the stress plot for the anchor under the ultimate moment load M_d show that the maximal stresses $\sigma_{V,max}$ and $\sigma_{M,max}$ are located at the fillet of the borehole (Figure 8.21 and Figure 8.22). Both stress components are equivalent and act in the same direction. Their position at the fillet however depends on the direction of the shear load and the moment.

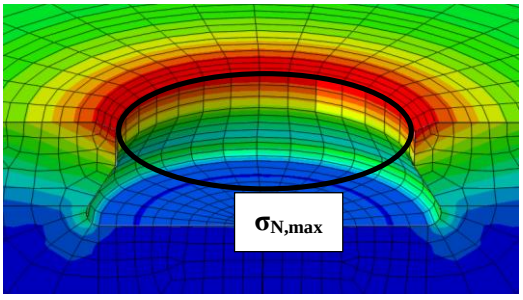

Figure 8.20 Maximal tensile stress – Tension load

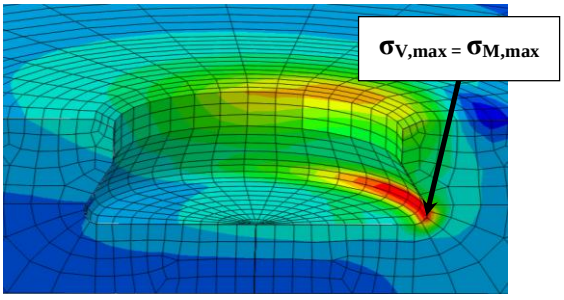

Figure 8.21 Maximal tensile stress –Shear load

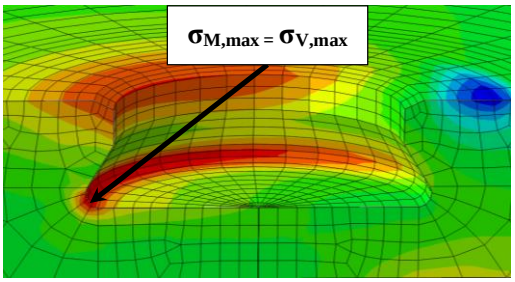

Figure 8.22 Maximal tensile stress – Moment load

In consequence, the stress peak has to be limited at these two positions (Figure 8.23).

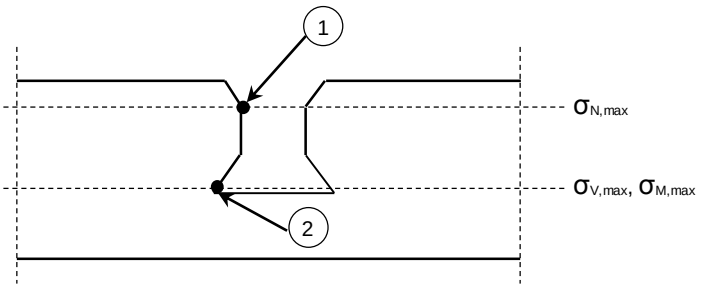

Figure 8.23 The two positions for the verification of the connection "Fischer undercut anchor – glass"

This leads to the two following verification inequalities:

Position 1:

$$\frac{\sigma_{N,max}+\alpha_V\cdot\sigma_{V,max}+\alpha_M\cdot\sigma_{M,max}+k\cdot\sigma_{glob,60}}{\sigma_{d,1}} \leq 1.0 \qquad \textbf{(8-3)}$$

Position 2:

$$\frac{\alpha_N\cdot\sigma_{N,max}+\sigma_{V,max}+\sigma_{M,max}+\alpha_k\cdot k\cdot\sigma_{glob,60}}{\sigma_{d,2}} \leq 1.0 \qquad \textbf{(8-4)}$$

With:

$\sigma_{N,max}$ = Stress peak at position 1 due to a tension load in the undercut anchor

$\sigma_{V,max}$ = Stress peak at position 2 due to a shear load in the undercut anchor

$\sigma_{M,max}$ = Stress peak at position 2 due to a moment load in the undercut anchor

$\sigma_{glob,60}$ = Maximal global stress component at the rim of the local area (r = 60 mm)

$\sigma_{rec,1}$ = Permissible stress in position 1

$\sigma_{rec,2}$ = Permissible stress in position 2

k = Stress concentration factor (section 8.5.3)

In the inequalities (8-3) and (8-4), the different stress components are linearly superimposed. In fact, numerical investigations of the stress plots reveal that the stress components act in the same direction in position 1 and position 2. This justifies their conservative superposition.

The stress components $\sigma_{N,max}$, $\sigma_{V,max}$ and $\sigma_{M,max}$ are determined with the transfer functions (section 8.5.2). The tension force, the resulting shear force and the resulting moment load in the Fischer undercut anchors are numerically determined with the 2D FE-model of chapter 5 and subsequently converted to the corresponding stress components with

help of the transfer functions (section 8.5.2). The resulting shear loads and moments are determined direction true by superposition of the components (Figure 8.24).

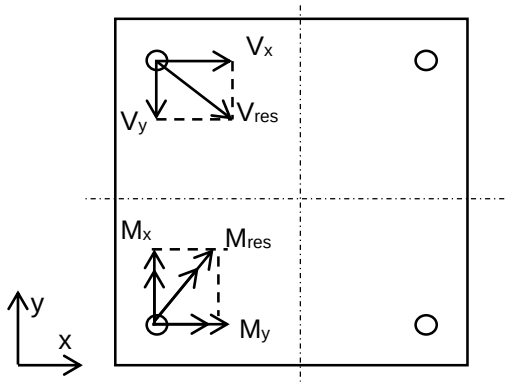

Figure 8.24 Definition of the resulting shear loads and moments

$$M_{res} = \sqrt{M_x^2 + M_y^2} \quad \textbf{(8-5)}$$

$$V_{res} = \sqrt{V_x^2 + V_y^2} \quad \textbf{(8-6)}$$

The maximal global stress component $\sigma_{glob,60}$ is numerically determined with the 2D FE-model at the rim of the local area (section 8.5.1).

The stress factor α_N relates the maximal stress component $\sigma_{N,max}$ at position 1 for a given tension load to the corresponding maximal stress component at position 2. The stress factors α_V and α_M link the maximal stress components at position 2 for a given pure shear load respectively for a given moment load to the corresponding maximal stress components at position 1. The factor α_k interrelates the maximal stress component $k \cdot \sigma_{glob,60}$ occurring at the rim of the borehole at position 1 due to the pure bending of the glass pane (Figure 8.25) to the corresponding maximal stress component at position 2.

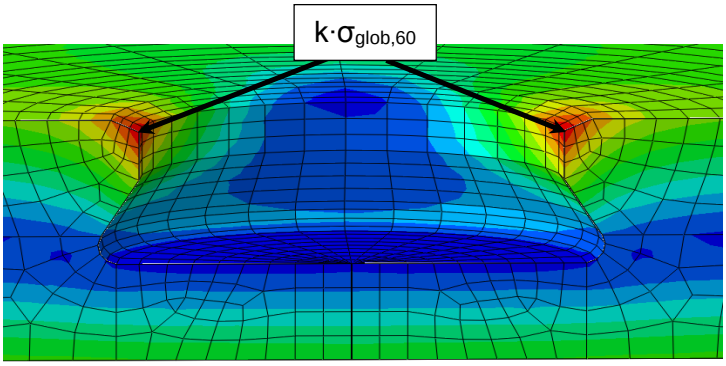

Figure 8.25 The maximal stress component at the borehole due the pure bending of the glass pane

The stress factors depend on the plate thickness of the inner pane and they are determined with the calibrated FE-models, which are used for the deviation of the transfer functions (Table 8.8).

Table 8.8 Stress factors in dependency of the inner pane thickness

t_i	α_N	α_V	α_M	α_k
[mm]	[-]	[-]	[-]	[-]
10	0.40	0.75	0.86	0.50
12	0.54	0.83	0.67	0.50

The permissible stress values $\sigma_{rec,1}$ and $\sigma_{rec,2}$ (Table 8.9) are determined with the calibrated FE-model of the Fischer undercut anchor in monolithic glass (chapter 6). In fact, the allowable internal forces N_d, V_d and M_d in the Fischer undercut anchor in monolithic glass are determined in the components tests (chapter 6 and (Z-70.2-122)) and converted with the transfer functions for monolithic glass (e.g. Figure 6.14 to Figure 6.16) into the corresponding allowable stress values. N_d delivers the permissible stress $\sigma_{rec,1}$ at position 1. V_d and M_d deliver the permissible stress $\sigma_{rec,2}$ at position 2. Thereby it is insignificant whether the allowable stress values at the borehole are derived by using monolithic glass or IGU, because the allowable stress values only depends on the material glass and the borehole geometry, which are the same in both cases.

Table 8.9 Permissible stresses at the borehole

Position	$\sigma_{5\%\text{-fractile}}$	γ	σ_{rec}
[-]	[N/mm²]	[-]	[N/mm²]
1	114	2.4	47
2	57	2.4	23

8.6.3 Consideration of eccentricities

In (Beyer, 2007), a procedure for the consideration of eccentric moments in point fitted single glazing with the Fischer undercut anchor is described. This procedure is exactly the same for point fitted IGU with the Fischer undercut anchor. Therefore it is shortly described in this section.

The Fischer undercut anchor FZP-G-Z is elastically clamped into the glass pane. Thus, the connection to the substructure creates an additional moment M_G due to the self-weight of the pane (Beyer, 2007). This moment has to be considered in the design of the point fitted IGU.

In Figure 8.26, the static system for the determination of the moment M_G is shown.

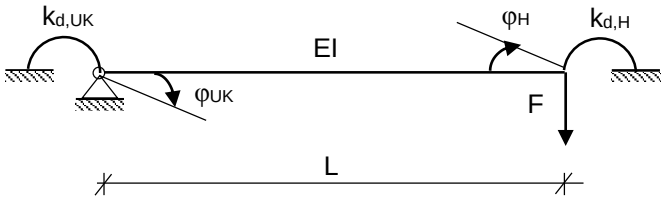

Figure 8.26 Static system for the determination of the eccentric moment M_G, from (Beyer, 2007)

It follows from (Beyer, 2007):

$$M_G = FL \frac{\frac{L}{2EI} + \frac{1}{k_{rot,Sub}}}{\frac{L}{EI} + \frac{1}{k_{rot,Sub}} + \frac{1}{k_{rot,FZP-G-Z}}} \quad \textbf{(8-7)}$$

With:

$k_{rot,Sub}$ = Rotational stiffness of the substructure

$k_{rot,FZP-G-Z}$ = Rotational stiffness of the Fischer undercut anchor

L = Length of the lever arm

E = Young's modulus of the lever arm

I = Moment of inertia of the lever arm

The force F corresponds to the self-weight of the point fitted IGU divided by the number of the Fischer undercut anchors which transfer the self-weight.

8.7 General application procedure of the extended SLG-method

The general application procedure of the extended SLG-method is given in Figure 8.27:

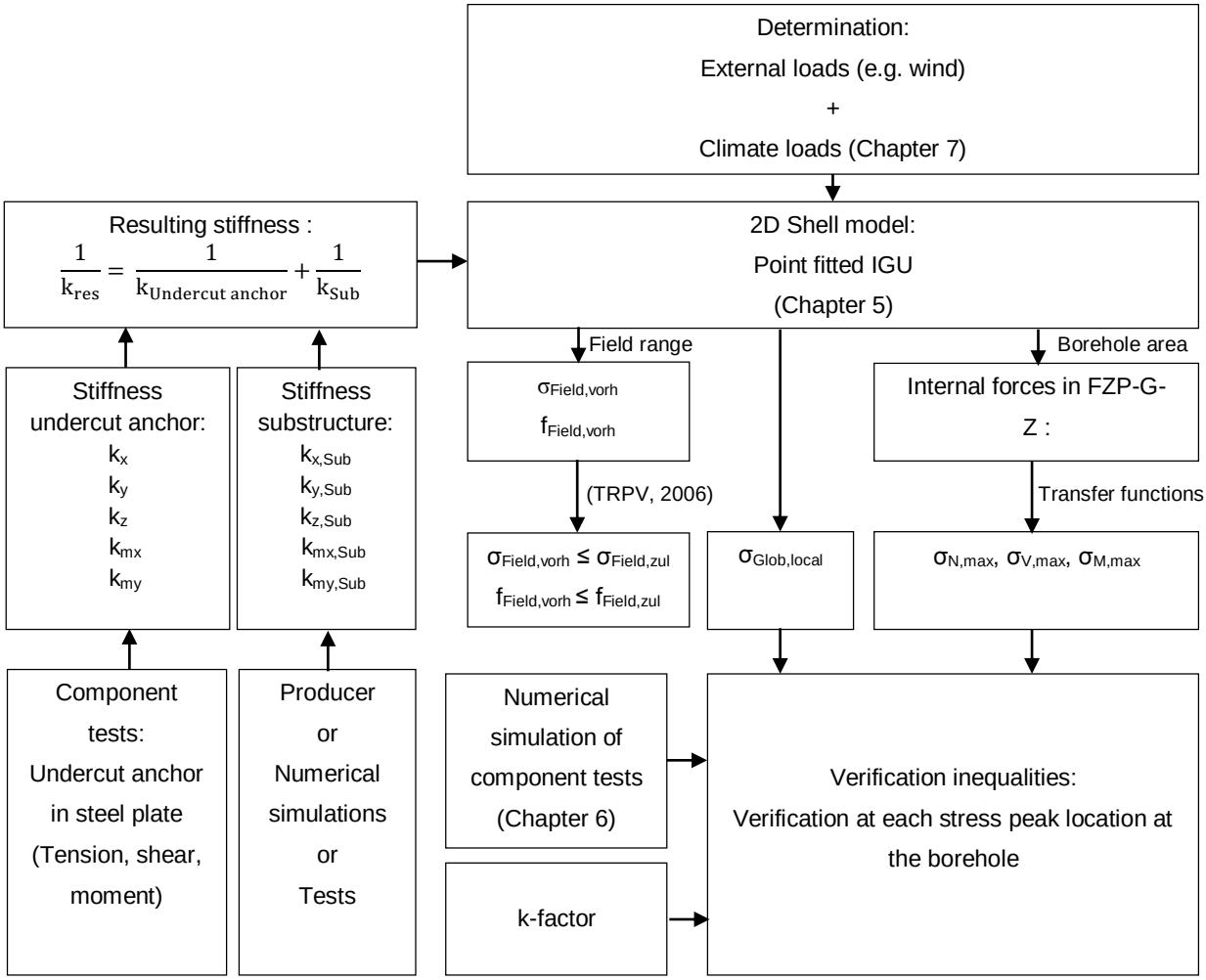

Figure 8.27 General application procedure of the extended SLG-method

8.8 Parameter study on the stress peak at the borehole

For the designing engineer, the knowledge of the parameters which influence the stress peak at the borehole of the proposed point fitted IGU with the Fischer undercut anchor and the dual-sealed edge bond system is of high interest. The objectives of the parameter study are the identification of the influencing parameters and the investigation of their influence on the stress peak by trend. In this way, it is tried to identify a tendency for each parameters leading to a reduction of the stress concentration.

8.8.1 Definition of the parameters for the parameter study

As it is the case for single glazing, the stress peak at the borehole of a point fitted insulation glass units primary depends on the following parameters:

- The dimensions of the point fitted IGU (l_x x l_y)

- The edge distance of the point fittings in the inner glass pane (e_x x e_y)
- The thickness of the inner glass pane (t_i)
- The external loads acting on the inner and/or the outer glass pane (p_i, p_e)

Additionally the following parameters could have an influence on the stress peak at the borehole:

- The thickness of the outer glass pane (t_e)
- The thickness of the cavity respectively the height of the silicone bite (d)
- The width of the silicone bite (b)
- The stiffness of the silicone sealant
- The stiffness of the spacer materials
- The stiffness of the PIB
- The stiffness of the substructure

The above mentioned parameters characterize the static system of the point fitted IGU. It is however important to notice that in insulation glass, the climate loads depend on the static system and thus on the parameters. Hence, a change of one parameter implies a variation of the static system and of the climate loads in parallel. In consequence, the dependency of the stress peak on the static system and on the corresponding climate loads cannot be decoupled.

8.8.2 Procedure

In section 8.8.1, the dependency of the stress peak on the static system of the point fitted IGU and the related climate loads is highlighted. Both depend on the mentioned parameters. The parameters however influence the static system and the climate loads in different forms. For instance, a reduction of the inner and/or outer pane thicknesses (t_i, t_e) leads to a decrease of the climate loads which act on each pane. If at the same time however the edge distances (e_x x e_y) of the point fittings are increased, the climate loads increase again. This means that the parameters interact and hence it is impossible to formulate a global dependency of the stress peak for each parameter separately.

In order to reduce the effort of the parameter study, the influence of only a selected number of parameters on the stress peak is tendentiously determined in this research work.

In point fitted insulation glass units with undercut anchors, the edge bond system is involved in the load transfer mechanism and transmits a part of the external loads from

the outer to the inner glass pane (section 4.5.2). The load is subsequently transferred from the inner glass pane to the anchors. Consequently, the stiffness of the edge bond system in combination with its edge distance could have an influence on the load path and thus on the stress peak at the borehole. Additionally, the producers propose linear elastic material laws for numerical simulation of the silicone sealant (section 8.4). Silicone however is hyper-elastic in nature. Therefore the focus is mainly put on the parameters concerning the edge bond system and the edge distance of the Fischer anchors:

- The stiffness of the spacer materials
- The stiffness of the silicone sealant
- The thickness of the cavity respectively the height of the silicone bite (d)
- The width of the silicone bite (b)
- The stiffness of the PIB
- The edge distance of the point fittings in the inner glass pane (e_x x e_y)
- The stiffness of the substructure

In addition, the influence of the substructure stiffness on the stress peak is analysed.

The influence on the stress peak at the borehole of the above mentioned parameters are systematically investigated by means of the verified and calibrated 3D FE-model, which is presented in chapter 8. The size of the IGU and the thicknesses of the inner and outer glass pane are fixed. Therefore the investigation concerns a tendential determination of the influence of the different parameters.

8.8.3 Geometry and FE-model of the point fitted IGU

The geometry of the point fitted IGU with the Fischer undercut anchor is shown in **Figure 8.28.**

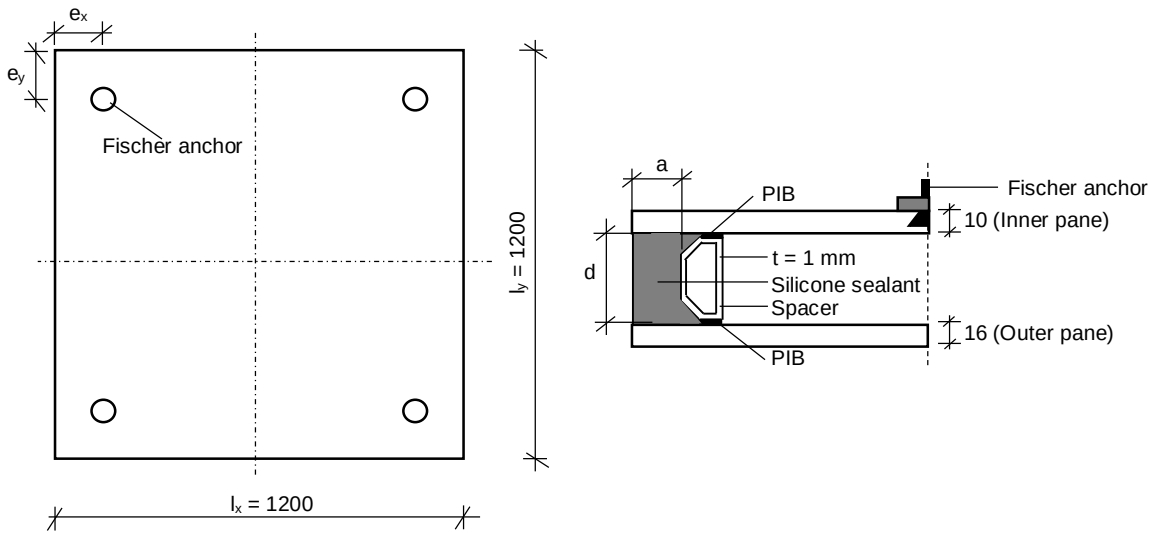

Figure 8.28 Geometry of the point fitted IGU

The different configurations of the edge bond geometries, the edge distances of the Fischer undercut anchors and the materials laws are summarized in the Table 8.10 to Table 8.12.

Table 8.10 Configurations of the edge bond geometries

Configuration	a [mm]	d [mm]
1	6	12
2	16	12
3	6	16
4	16	16

Table 8.11 Edge distances of the Fischer undercut anchors

e_x x e_y [mm]
60 x 60
90 x 90
150 x 150
200 x 200

Table 8.12 Material laws for the different edge bond components

Component	Material	Type	Material law	
			E [N/mm²]	ϑ [-]
Silicone sealant	Structural silicone DC 993	Linear elastic	1 2.4 4.8	0.48
		Hyper-elastic [Dias]	-	-
Spacer	Stainless steel	Linear elastic	190 000	0.3
	Aluminium		70 000	
	Polypropylene (PP)		1000	
	Polycarbonate (PC)		2000	

The material properties Young's modulus E and Poisson's ratio v are fixed for the glass panes to E = 70 000 N/mm² and ϑ = 0.23. The maximal allowable distance of e_x x e_y = 300x300 mm for the Fischer undercut anchor according to (Z-70.2-122) leads to meaningless positions of the Fischer anchors in the IGU and hence the distance is not considered in the parameter study.

In the 3D FE-model (Figure 8.29), the borehole, the edge seal system and the point fittings are modelled with their exact geometries and material properties. Contact definitions consider the load transfer between the point fitting and the glass pane in case of contact and the separation of both elements. A detailed description of the mesh generation and the element types for the different components are given in section 9.5.1. The connection between the point fitting and the substructure is statically modelled as a clamped support. To save calculation time, only a quarter of the 3D FE-model is modelled.

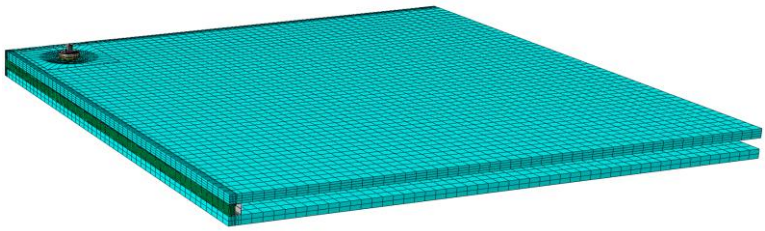

Figure 8.29 3D FE-model of the point fitted IGU with the Fischer undercut anchor

8.8.4 Loading of the point fitted IGU

The highest stress peaks at the borehole occur for the Fischer undercut anchors under traction. In this context, the decisive load case consists in the extreme climate load case “winter” according to (DIN 18008-2) (Table 7.2) in combination with a wind suction load acting on the outer glass pane.

A wind suction load of $p_{e,w}$ = -2.5 kN/m^2, which commonly occurs in façade applications, is applied on the outer glass pane. For each configuration of the IGU, the wind and the climate loads are converted by means of the extended climate load model (chapter 7) into resulting surface loads acting on each glass pane.

8.8.5 The stress peak at the borehole

For the given IGU geometry (section 8.8.3) and load case (section 8.8.4), the stress peak is located at the rim of the borehole, which is oriented towards the free edge of the IGU. The location is shown in Figure 8.30.

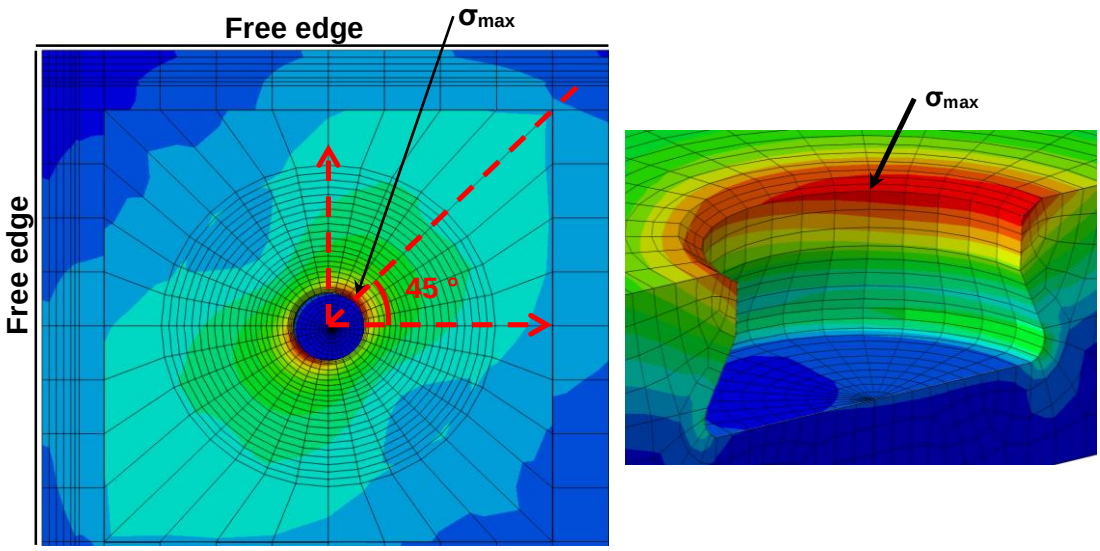

Figure 8.30 Location of the stress peak for the given IGU geometry and the given load case

8.8.6 Influence of the spacer material on the stress peak at the borehole

The influence on the stress peak of the different spacer materials (Table 8.12) is investigated in dependency of the edge distance of the Fischer anchors for edge bond configuration 1 (Table 8.10) and the hyper-elastic material law (Dias, 2013) for the silicone sealant.

The stress peaks obtained for the different materials of the spacer are shown in Figure 8.31.

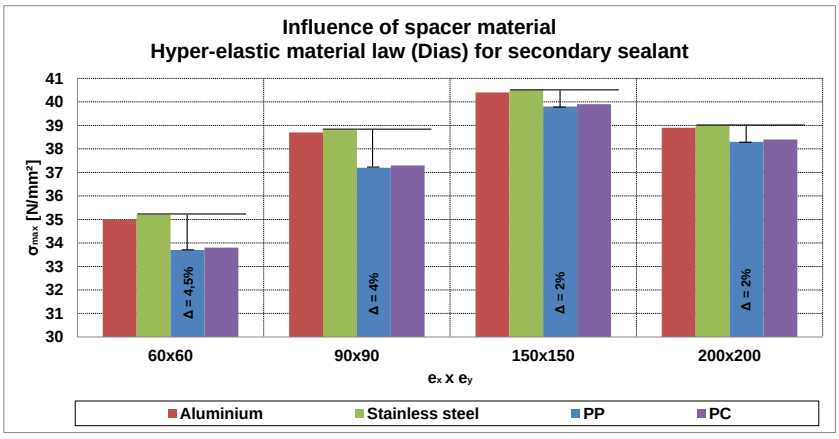

Figure 8.31 Influence of the spacer material on the stress peak at the borehole, edge seal configuration 1

As higher the spacer stiffness is, as higher the stress peak at the borehole is. In fact, the highest stress peaks are observed for the metal spacers (stainless steel and aluminium) and the lowest peaks are obtained for the plastic spacers (polypropylene and polycarbonate). In all cases, the maximal difference for the stress peak is noticed

between the stainless steel spacer and the spacer made of polypropylene. This difference however decreases with increasing edge distances of the anchors from Δ = 4.5% for the edge distance of 60x60 mm to Δ = 2% for the edge distance of 200x200 mm. The influence of the spacer material on the stress peak is marginally.

A comparison of the stress distributions along the radial path does not reveal a dependency of the stresses near the borehole on the stiffness of the spacer material (Figure 8.32).

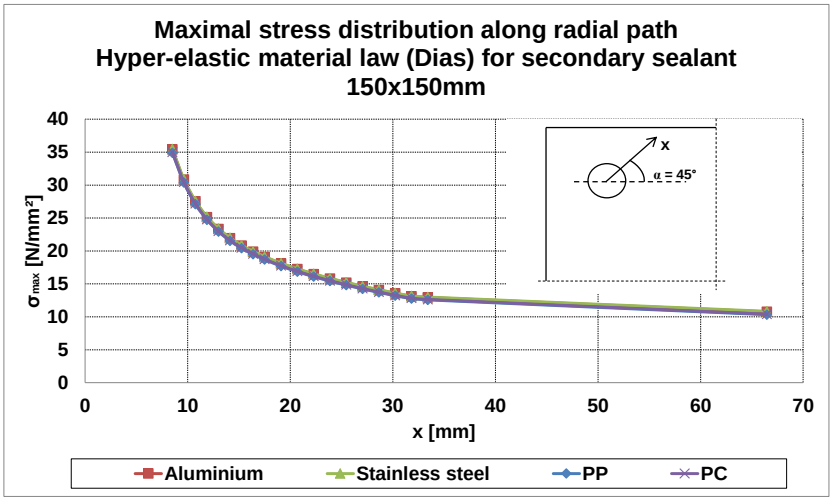

Figure 8.32 Stress distribution along the radial path, edge seal configuration 1, 150x150 mm

8.8.7 Influence of the PIB stiffness on the stress peak at the borehole

To analyse the influence of the primary sealant on the stress peak at the borehole, the stress peaks were calculated with two different FE-models of the edge bond. On one hand a FE-model accounting for the soft material law of the PIB (Figure 8.33) and on the other hand a numerical model without the primary sealant (Figure 8.34).

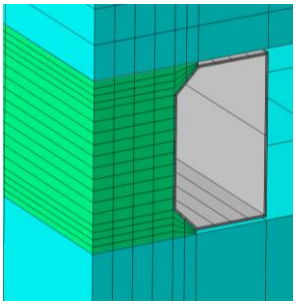

Figure 8.33 Edge bond without PIB

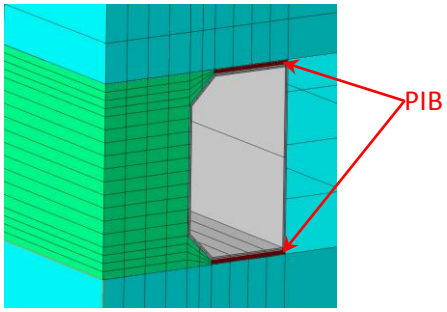

Figure 8.34 Edge bond with PIB

According to (Schäfer, 2002), a linear elastic material law with a Young's modulus E = 0.7 10^{-6} N/m^2 and a Poisson's ration ϑ = 0.48 is applied for the PIB.

The influence of the stiffness of the primary sealant PIB on the stress peak for the different edge distances of the Fischer undercut anchors is investigated for edge seal configuration 1 and the hyperelastic material law according to (Dias, 2013) for the silicone sealant (Figure 8.35).

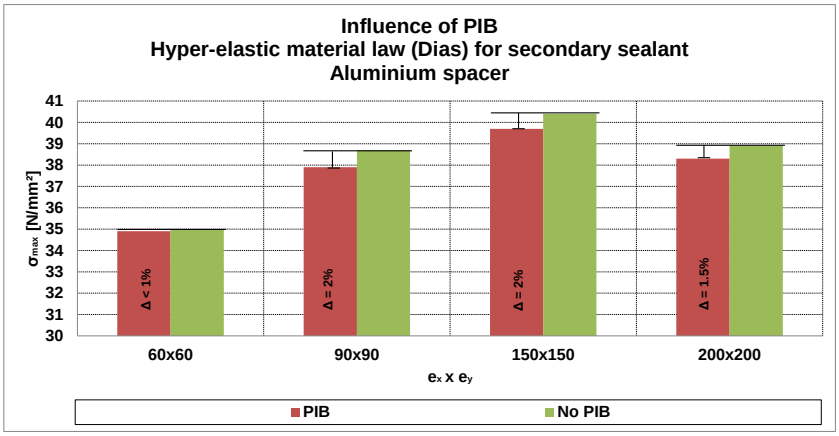

Figure 8.35 Influence of the PIB on the stress peak at the borehole, edge seal configuration 1

The stress peaks which are determined with the numerical model without the PIB are higher than the stress peaks calculated with the model with the PIB. For all edge distances of the Fischer undercut anchors, the difference is however smaller than 2%. In addition, the distributions of the maximal stresses along the radial path are almost identic. In Figure 8.36, the distribution for an edge distance of e_x x e_y = 90x90 mm for the Fischer anchors is exemplarily shown.

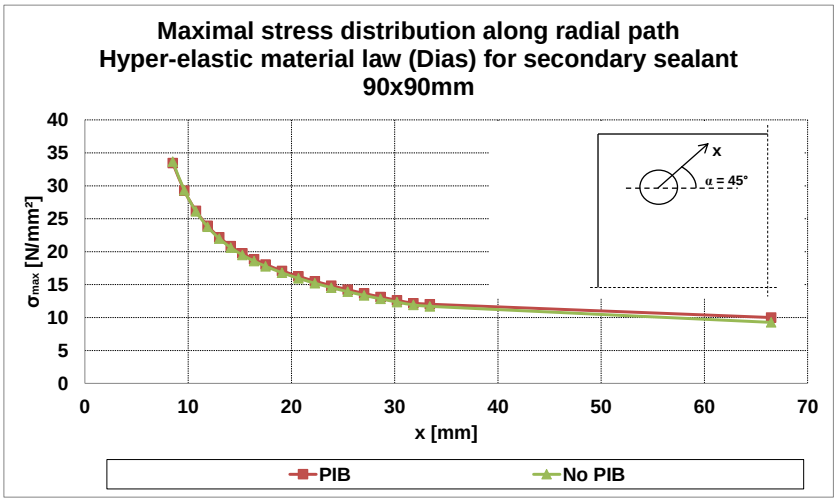

Figure 8.36 Stress distribution, edge seal configuration 1, 90x90 mm

In conclusion, the influence of the primary sealant PIB on the stress peak is insignificant.

8.8.8 Influence of the secondary sealant stiffness on the stress peak at the borehole

The stress peaks are determined for the different edge seal configurations, edge distances of the Fischer undercut anchors and silicone material laws (Figure 8.37 to Figure 8.40). The spacer material is in all cases aluminium.

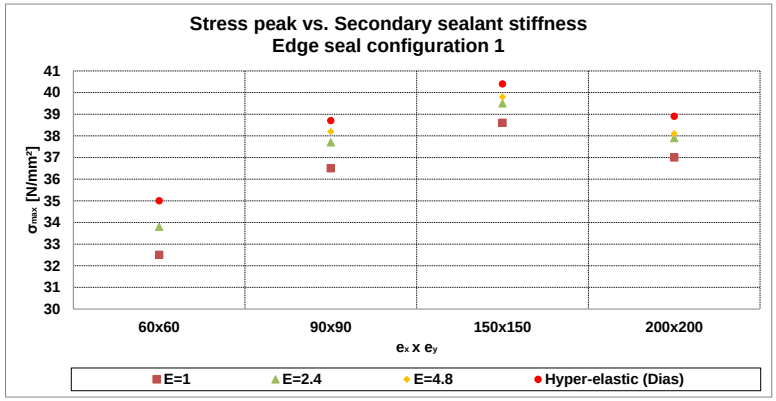

Figure 8.37 Stress peak vs. secondary sealant, edge seal configuration 1, aluminium spacer

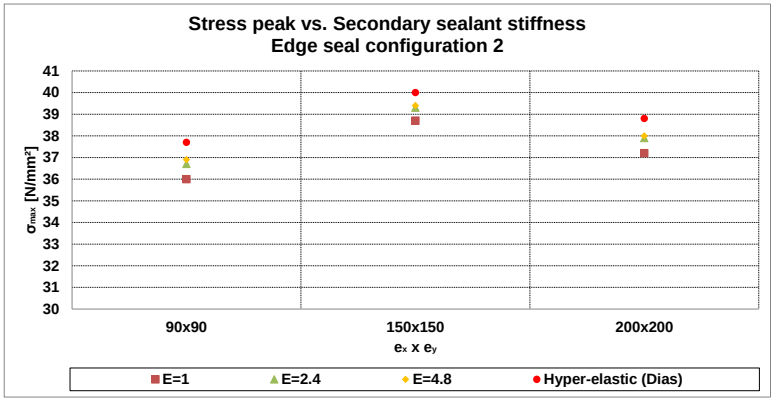

Figure 8.38 Stress peak vs. secondary sealant, edge seal configuration 2, aluminium spacer

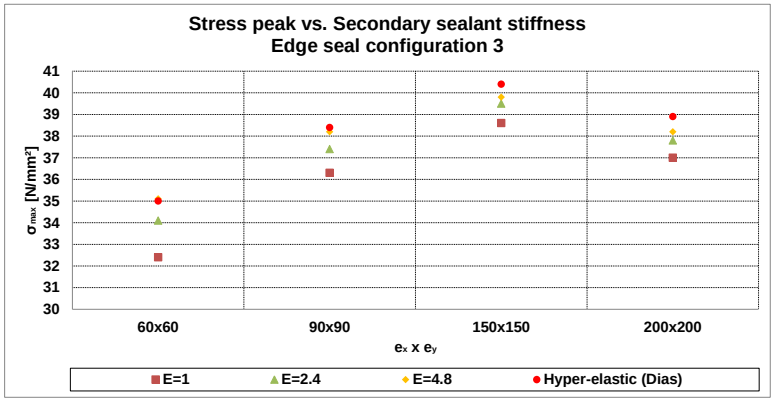

Figure 8.39 Stress peak vs. secondary sealant, edge seal configuration 3, aluminium spacer

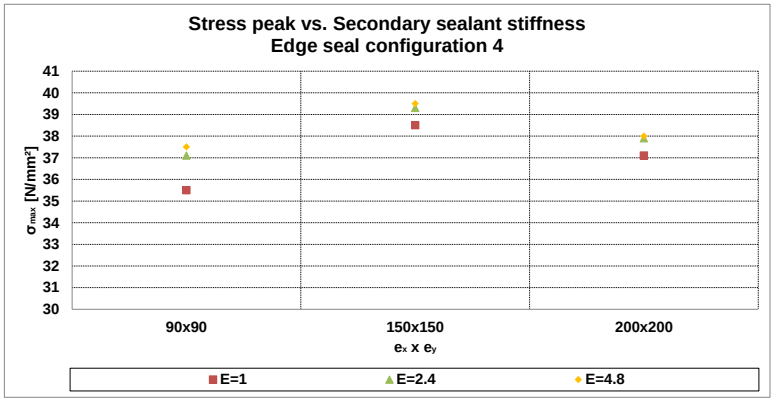

Figure 8.40 Stress peak vs. secondary sealant, edge seal configuration 4, aluminium spacer

Independently of the edge seal configuration, the highest stress peak is observed for the hyper-elastic material law of *Dias* (Dias, 2013) and the lowest stress peak is obtained for the linear elastic material law for the silicone sealant with an Young's modulus of E = 1 N/mm^2. The deviation between both values is low and it varies between 4% and 8% in function of the edge seal configuration and the edge distance of the undercut anchors. In fact, for each edge distance and edge seal configuration, the stress peak increases with increasing sealant stiffness. Additionally the stress peak increases between the edge distances of 60x60 mm and 150x150 mm and decreases from 150x150 mm to 200x200 mm. The highest stress peaks are noticed for an edge distance of 150x150 mm and the lowest for an edge distance of 60x60 mm. The differences in the stress peak values between the edge distances of 150x150 mm and 60x60 mm are about 15 %. This behaviour is observed for each silicone material law and edge bond configuration. The reason for the decrease in the stress peak between the edge distances of 150x150 mm and 200x200 mm consists in a change of the load transfer area between the Fischer undercut anchor and the glass pane. In Figure 8.41 and Figure 8.42, the contact pressures between the anchor and the borehole wall are shown for the edge distances of 150x150 mm respectively 200x200 mm. The areas in red indicate a load transfer between the Fischer anchor and the glass, while no loads are transferred between both elements in the blue areas. It is seen, that in both cases the spacer disk is not in contact with the glass pane (blue ring around the borehole). Consequently the forces are exclusively transmitted between the steel bolt of the Fischer undercut anchor and the wall of the borehole (red area).

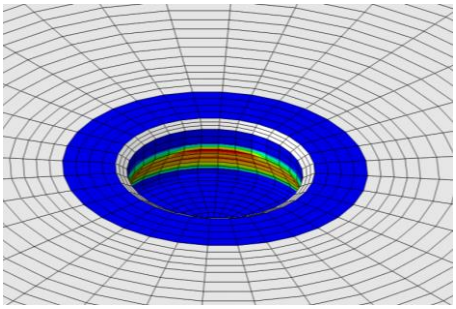

Figure 8.41 Contact area FZP-G-Z/Glass, 150x150 mm

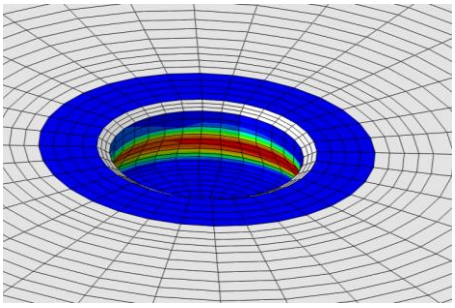

Figure 8.42 Contact area FZP-G-Z/Glass, 200x200 mm

The contact forces for the edge distance of 200x200 mm are transmitted over a bigger contact area (in red) than it is the case for the edge distance of 150x150 mm. This change in the contact area leads to the reduction of the stress peak at the rim of the borehole.

The stress distributions along the radial path on which the stress peak occurs (Figure 8.43 and Figure 8.44) reveal that the influence of the secondary sealant stiffness on the stress peak depends on the edge distance of the point fittings.

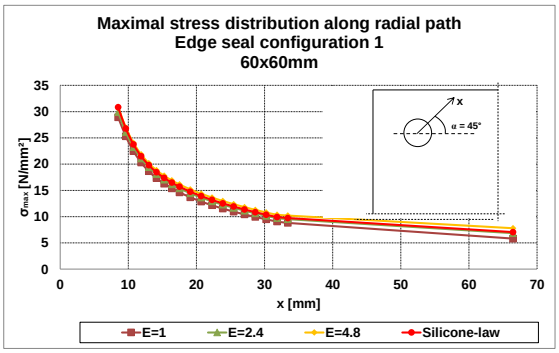

Figure 8.43 Stress distribution, edge seal configuration 1, 60x60 mm

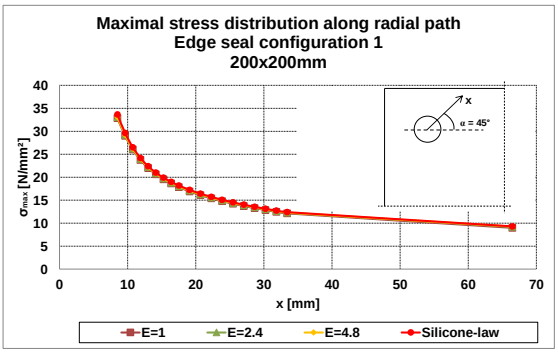

Figure 8.44 Stress distribution, edge seal configuration 1, 200x200 mm

For the edge distance of 60x60 mm for the Fischer undercut anchors, differences in the stress distributions for the different edge seal material laws are observed. The maximal difference amounts 5 % at a distance of > 35 mm. For an edge desistance of 200x200 mm, no deviations in the stress distributions are noticed anymore. The curves are perfectly superimposed. The reasons for the dependency of the stress distributions on the edge distances consist in the different contact areas between the Fischer anchor and the glass pane in function of the edge distances.

In conclusion, the highest stress peaks are obtained for the hyper-elastic material law according to *Dias* (Dias, 2013) for the secondary sealant and this independently from the edge distance of the point fittings and the configuration of the secondary sealant. In contrast, the linear elastic material laws which are delivered by the producers lead to lower stress peaks. The maximal difference for the stress peak calculated with the hyper-elastic material law and the linear elastic laws is about 8%. In addition, a dependency of the stress distributions on the stiffness of the secondary sealant is observed for small edge distances. Thus, the stiffness of the secondary sealant has an influence on the stress peak at the borehole and on the radial stress distribution in the borehole area. Moreover, an influence of the edge distance on the stress peaks is noticed. It decreases with increasing edge distance of the Fischer undercut anchors. This can be explained by a change the load transfer area between the point fitting and the glass pane.

8.8.9 Influence on the edge seal geometry on the stress peak at the borehole

The stress peaks at the borehole are numerically determined for the four edge seal configurations in Table 8.10, the edge distances in Table 8.11 and the different material

laws in Table 8.12 (Figure 8.45 to Figure 8.48). The spacer is made of aluminium. For the edge distance of 60x60 mm, the two edge seal configurations 2 and 4 (Table 8.10) are not investigated, since the two edge configurations are not used in practice.

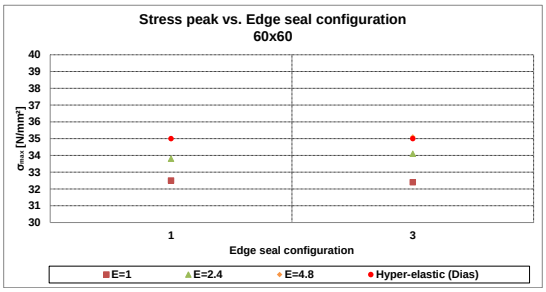

Figure 8.45 Stress peak vs. edge seal configuration, 60x60 mm

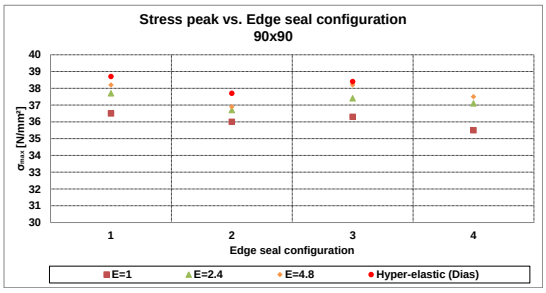

Figure 8.46 Stress peak vs. edge seal configuration, 90x90 mm

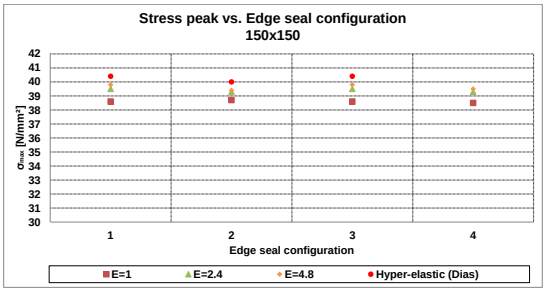

Figure 8.47 Stress peak vs. edge seal configuration, 150x150 mm

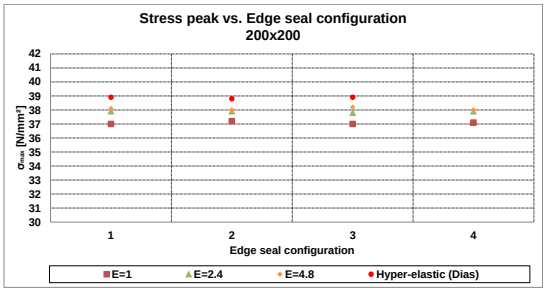

Figure 8.48 Stress peak vs. edge seal configuration, 200x200 mm

For the edge distances 90x90 mm and 150x150 mm of the Fischer undercut anchors, the stress peak slightly decreases between the edge seal configurations 1 and 2 and the edge seal configurations 3 and 4. The maximal decrease amounts 2.5%. For higher edge distances (e.g. 200x200 mm) a decrease of the stress peak cannot be noticed anymore between these edge configurations. This is the case for each material law for the secondary sealant. The difference between the edge seal configuration 1 and 2 respectively the edge seal configuration 3 and 4 consists in each case in the width of the bite of the secondary sealant. Thus, the width of the secondary sealant bite has a marginal influence on the stress peak at the borehole and the influence decreases with increasing edge distances of the Fischer anchors. In consequence, it can be neglected.

Independently of the material law for the silicone sealant, the stress peak does not vary between the edge seal configurations 1 and 3 and the edge seal configuration 2 and 4. The difference is less than 1%. The height of the silicone sealant consequently does not influence the stress peak at the borehole.

8.8.10 Influence of the substructure stiffness on the stress peak at the borehole

The stress peaks at the borehole are numerically calculated in dependency of the stiffness of the substructure (Table 8.13) for edge seal configuration 1 and the different edge distances of the point fittings (Table 8.11). Two limit cases are investigated for the substructure: a soft substructure with low stiffness values and a rigid substructure with infinite stiffness values.

Table 8.13 Stiffness values of the fictive substructure

Spring stiffness	k_x [N/mm]	k_y [N/mm]	k_z [N/mm]	k_{mx} [Nmm/rad]	k_{my} [Nmm/rad]
Soft substructure	100	100	100	100	100
Rigid substructure	∞	∞	∞	∞	∞

The silicone sealant is described with the hyper-elastic material law of *Dias* (Dias, 2013) and the spacer material is aluminium.

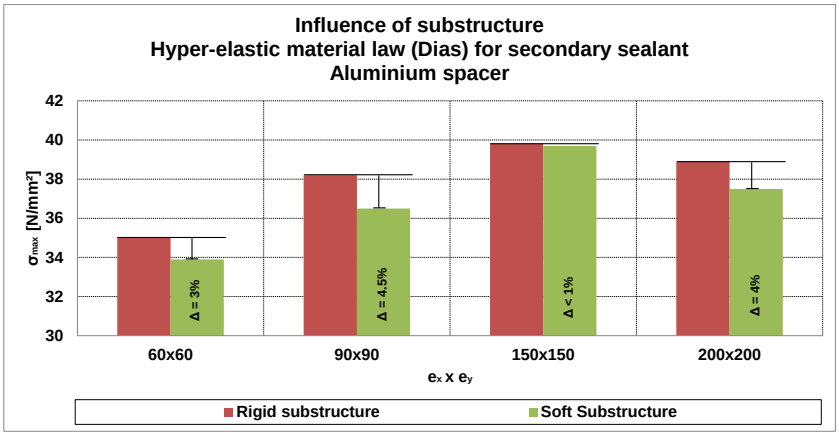

Figure 8.49 Stress peak vs. substructure stiffness, edge seal configuration 1

The maximal difference between the stress peaks is noticed for the edge distance of 90x90 mm of the Fischer anchors and it amounts 4.5 % (Figure 8.49). In consequence, the stiffness of the substructure does not influence the stress peak at the borehole. The same observation is done for the stress distribution along the radial path where the stress peak occurs (Figure 8.50).

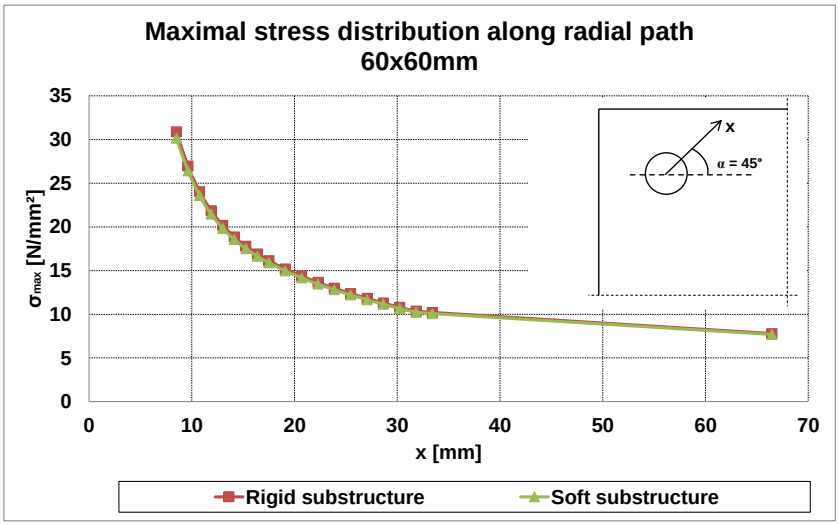

Figure 8.50 Stress distribution, edge seal configuration 1, 60x60 mm

8.9 Summary and conclusion

The SLG-method developed in (Beyer, 2007) is only valid for the design of point fitted single and laminated glazing.

The method is therefore extended for the design of point fitted insulation glass with undercut anchors. The extension is shown on the basis of a specific point fitting system, as to know the Fischer undercut anchor FZP-G-Z. The approach for the extension presented is nevertheless valid for all type of undercut point fittings in insulation glass. The only difference consists in the quantitative change of the key parameters of the SLG-method.

In a first step, the different parameters of the point fitted IGU with the Fischer undercut anchor which influence the key parameters of the SLG-method (the size of the local area, the transfer functions and the stress concentration factors) are identified. This is done by a comparison of the undercut point fitted IGU to point fitted single glazing.

In a second step, the SLG-method is extended by adapting its key parameters to the system of the point fitted insulation glass unit with the Fischer undercut anchor and the duel-sealed edge bond system. It is shown that the location of the stress peak at the borehole of the point fitted IGU with the Fischer undercut anchor depends on the loading level and that, in contrary to point fitted single and laminated glazing, it can occur at the surface wall of the borehole which is oriented towards the free edge of the IGU. In consequence, the size of the local area is to be adapted to r = 60 mm, the minimal allowable edge distance of the Fischer undercut anchor. The transfer functions depend

on the size of the local area and of the thickness of the inner glass pane. They are numerically derived for inner pane thicknesses of t_i = 10 mm and t_i = 12 mm. For the numerical determination of the stress concentration factors (k-factors), the Fischer undercut anchors are classified into two categories: corner point fittings and edge point fittings. It is shown that the k-factors for the edge point fittings depend on the edge distance of the anchors, the stiffness values of the silicone sealant and the ratio of the inner and outer glass panes. No influence of the spacer material and of the geometry of the secondary sealant on the k-factors is observed. With regards to the low influence of the stiffness of the secondary sealant on the k-factors, one single value for the k-factor is conservatively derived for a whole range of stiffness values of the silicone sealant for a given edge distance of the Fischer anchor and a given thickness ratio of the glass panes. Finally the k-factors for the edge point fittings are numerically derived as a function of the edge distances of the Fischer anchors and the ratio of the inner and outer glass panes of the IGU. Concerning the corner point fittings, the factor depends on the edge distance of the undercut anchor. If the edge distance is low ($e_x \leq L_x/10$ and $e_y \leq L_y/10$), the k-factor is k = 1.0. In the case of higher edge distances (e.g. $e_x > L_x/10$ or $e_y > L_y/10$) it is differed between a symmetric and an asymmetric overhang of the undercut anchor. The k-factor is k = 1.4 for a symmetric overhang of the point fitting. For an asymmetric overhang, it is proposed to apply the same k-factor than for an edge point fitting with the same edge distance and thickness ratios of the glass panes.

In a third step, the inequalities for the verification of the inner glass pane of the point fitted IGU with the Fischer undercut anchors according to the extended SLG-method are indicated. The different factors which are essential for the practical application of the inequalities are derived.

In a fourth step, the general application procedure of the extended SLG-method is resumed in form of a flow chart.

In a last step, a parameter study concerning the tendentious influence of the edge bond stiffness and geometry on the stress peak at the rim of the borehole is presented. The study reveals the stiffness of the silicone sealant to have a slight influence on the stress peak. It is observed that an increase of the sealant stiffness causes an increase of the stress peak The highest values are achieved with the hyper-elastic material law of *Dias* (Dias, 2013) and the lowest values are found for a linear elastic material law with an Young's modulus of E = 1.0 N/mm^2. The difference between the lowest and highest stress peaks for the different material laws for the silicone sealant is about 8%. In conclusion the influence is only marginally and justifies the conservative approach to define one single value for the stress concentration factor for a whole range of sealant

stiffness values. Furthermore, a dependency of the stress peak at the borehole on the edge distance of the Fischer undercut anchors is observed. Between the edge distances of 60x60 mm and 150x150 mm, the stress peak increases with increasing edge distance. For the edge distance of 150x150 mm, the stress peak is maximal. A further increase of the edge distance leads to a decrease of the stress peak. This is for instance the case for the edge distance of 200x200 mm. The decrease is caused by a change in the contact area between the point fitting and the wall of the borehole for higher edge distances of the anchors. The influence of the edge bond geometry (height and width of the silicone sealant), the spacer material and the PIB on the stress peak is found to be marginally. It is important to notice, that the size of the point fitted insulation glass unit and that the thicknesses of the inner and outer glass panes are fixed for the parameter study. Therefore the results of the study only tendentiously reflect the influence of the different parameters on the stress peak. For other IGU sizes it is probable that the values quantitatively change.

In the flow-chart in Figure 8.51, the general application procedure of the extended SLG-method (Figure 8.27) is applied to the specific case of for the point fitted IGU with the Fischer undercut anchor and the dual-sealed edge bond system as proposed in section 4.4

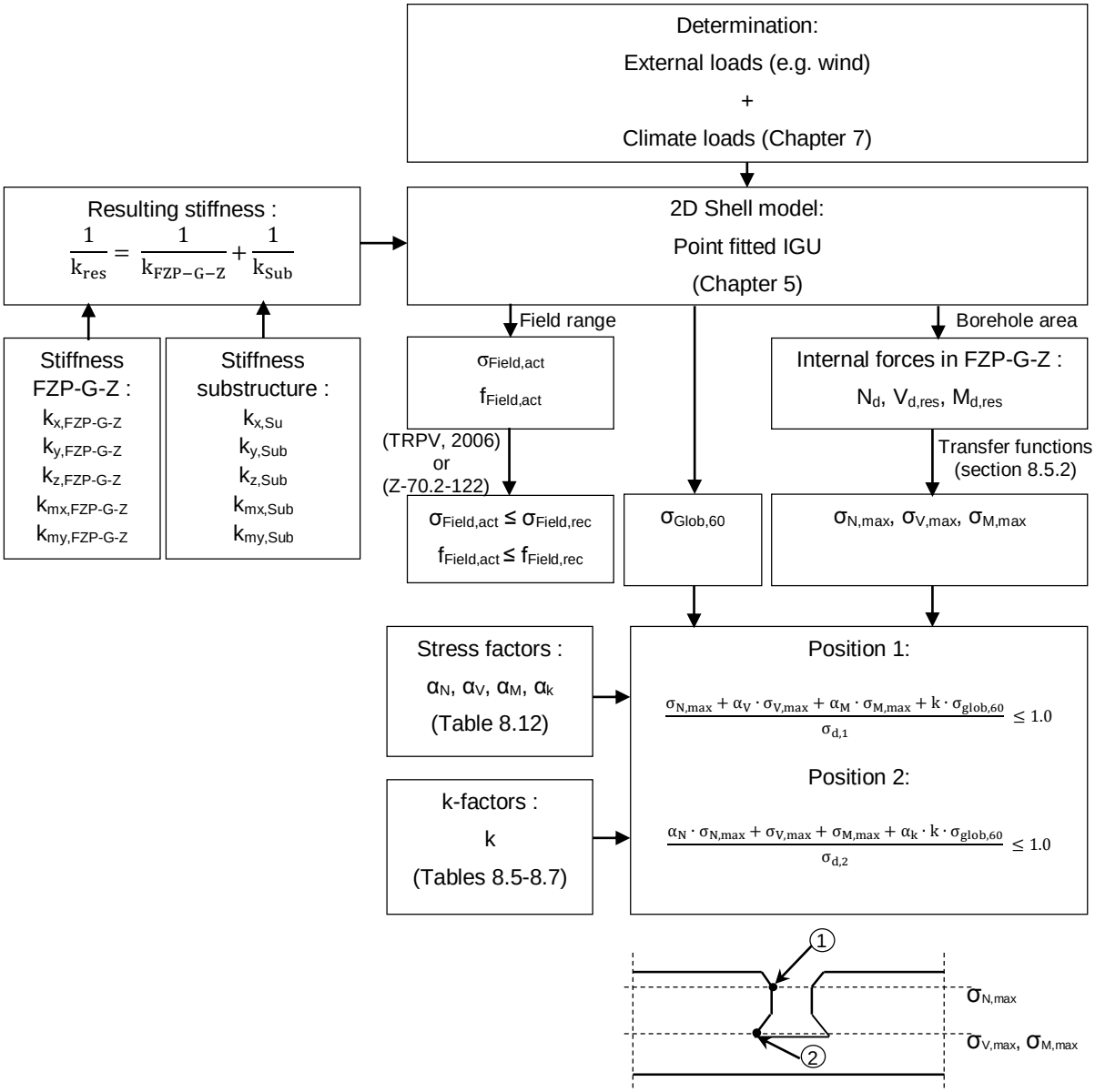

Figure 8.51 Application of the extended SLG-method to the point fitted IGU with the Fischer undercut anchor

9 Large scale tests

9.1 Objectives

Large scale tests are conducted on the new point fitted insulation glass unit with the Fischer undercut anchor proposed.

Three different objectives are pursued:

First of all, the numerical model of the point fitted IGU with the Fischer undercut anchor is verified by the test results. Therefore, the deformations and the strains of the glass panes are determined with the numerical model for selected load cases and compared to the test results.

Secondly, the extended climate load model is experimentally verified. The expected pressure in the glazing cavity is calculated by means of the extended climate load model and compared to the pressure measured during the tests. Additionally, the deformations and strains of the glass panes are numerically determined with the resulting surface loads delivered by the extended climate load model and checked against the test values.

Finally, the ultimate load bearing resistance of the insulation glass unit is determined and the failure prediction of the extended SLG-method is proofed. In the tests, the loading is increased until a failure occurs in the edge bond respectively in the point fitting. The corresponding failure stresses are calculated with the numerical model and checked against the values delivered by the extended SLG-method.

9.2 Test set-up

The point fitted insulation glass units are mounted in a horizontal position with the standardized substructure system “SystemOne” from the *Fischer-company* on two vertical steel U-profiles. The vertical U-profiles are fixed to two horizontal U-profiles, which are connected to two concrete foots (Figure 9.2).

The substructure “SystemOne” consists of four aluminium brackets and two aluminium bars (Figure 9.3 and Figure 9.4). The brackets are clipped on the two aluminium bars, which are connected to the two vertical U-profiles (Figure 9.5). The Fischer anchors are fixed to the brackets. The brackets are free to slide on the aluminium bars and assure an isostatic support of the IGU.

The advantage of the “SystemOne” substructure system consists in the easy and quick mounting procedure of the test samples and the known stiffness values of the system (Table 9.1).

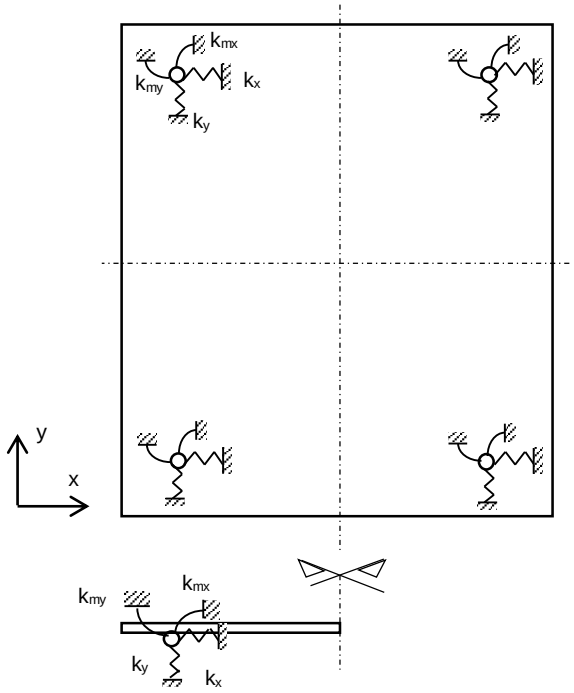

Figure 9.1 Spring stiffness definition

Table 9.1 Spring stiffness of the substructure system "SystemOne »

Spring stiffness	k_x [N/mm]	k_y [N/mm]	k_z [N/mm]	k_{mx} [Nmm/rad]	k_{my} [Nmm/rad]
SystemOne	1111	1111	1.00E+10	9.50E+05	7.96E+05

The known stiffness values of the substructure system are considered in the numerical simulations of te large scale tests.

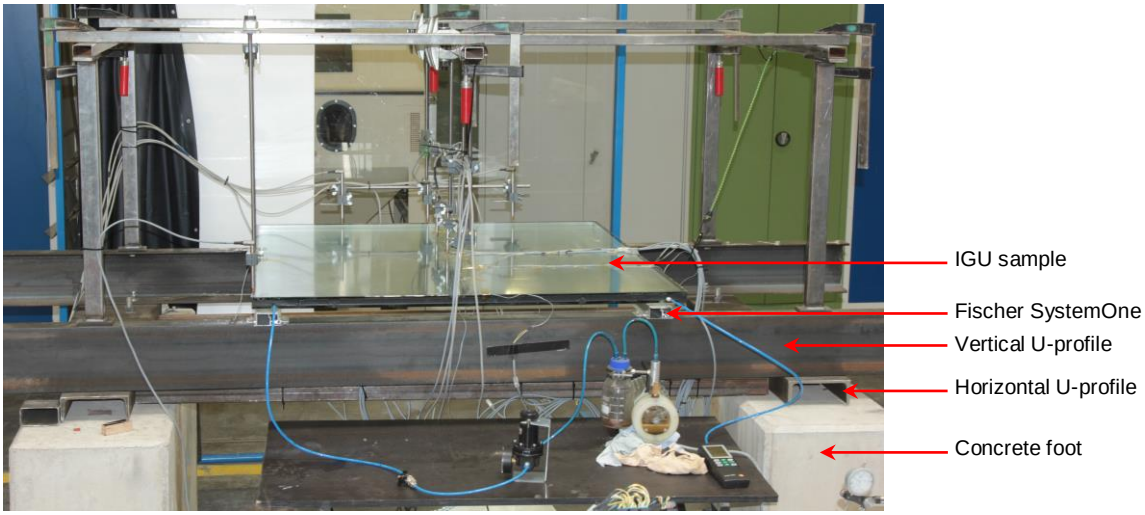

Figure 9.2 Test set-up

Figure 9.3 Sliding bracket with the Fischer undercut anchor

Figure 9.4 The sliding bracket clipped on the aluminium bar

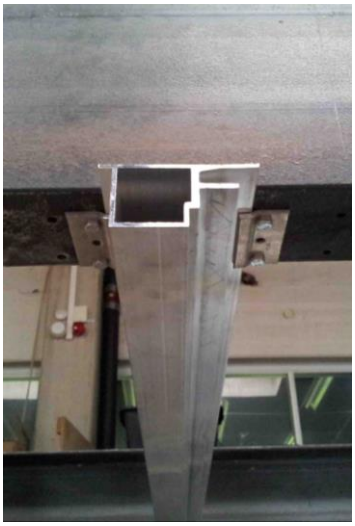

Figure 9.5 Connection of the aluminium bars to the U-profiles

The point fitted insulation glass samples can be mounted in two different positions:

- Configuration 1: The IGU is installed on the top side of the standing U-profiles and the Fischer undercut anchors are subjected to compression (Figure 9.6).
- Configuration 2: The IGU is installed on the bottom side of the standing U-profiles and the Fischer undercut anchors are subjected to tension (Figure 9.7).

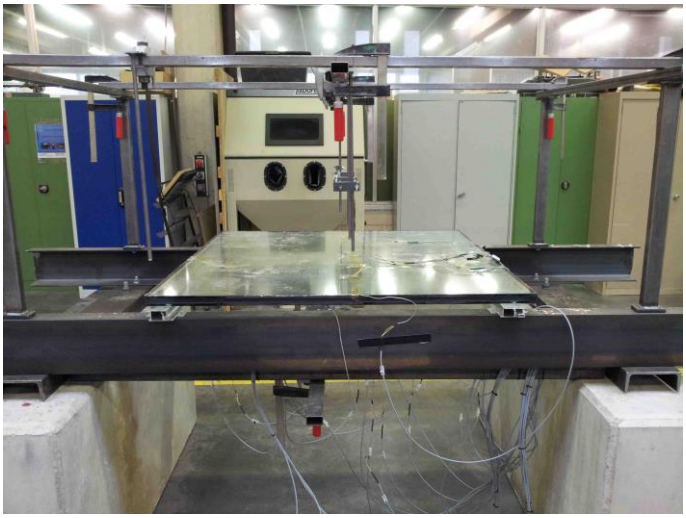

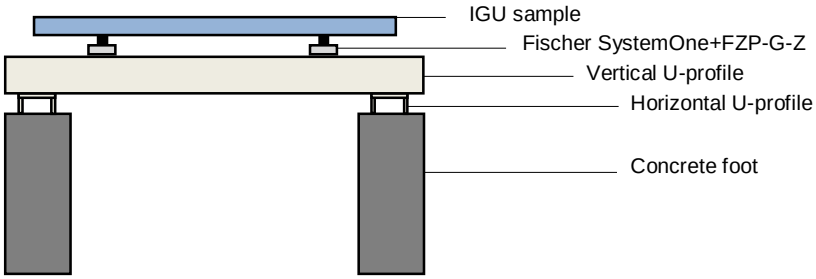

Figure 9.6 Configuration 1: The IGU sample installed on top of the U-profiles (Point fittings under compression)

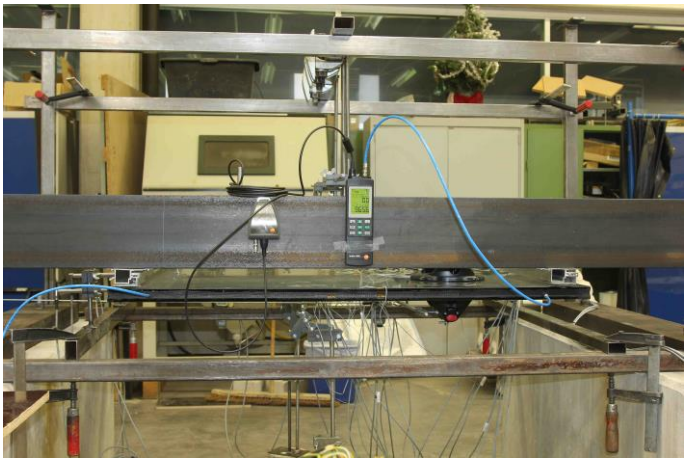

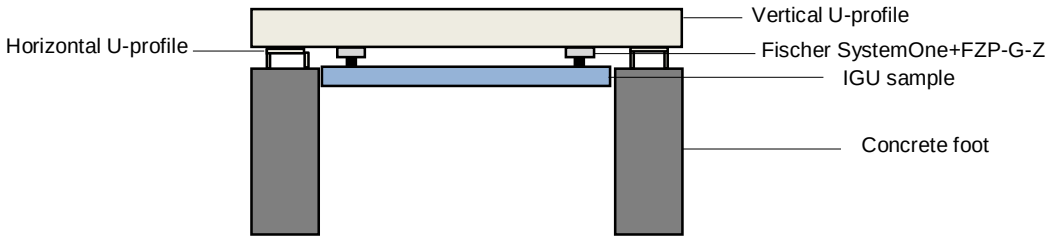

Figure 9.7 Configuration 2: The IGU sample installed on the bottom side of the U-profiles (Point fittings under traction)

During the tests, wind loads, climate loads and the self-weight are applied on the IGU samples.

The wind pressure loads are simulated by putting sandbags directly on the glass panes. In this way, wind pressure loads acting on the outer and inner glass pane can be simulated for configuration 1 (Figure 9.8) respectively for configuration 2 (Figure 9.9).

Figure 9.8 Sandbags on outer glass pane (Configuration 1)

Figure 9.9 Sandbags on inner glass pane (Configuration 2)

For configuration 2, the wind suction loads on the outer pane are induced with sandbags, which are put on a wooden plate fixed on a steel frame. The frame is glued with silicone (Ködiglaze S from Kömmerling) on four positions to the outer glass pane (Figure 9.10 and Figure 9.11).

Figure 9.10 Connection of the steel frame to the outer pane

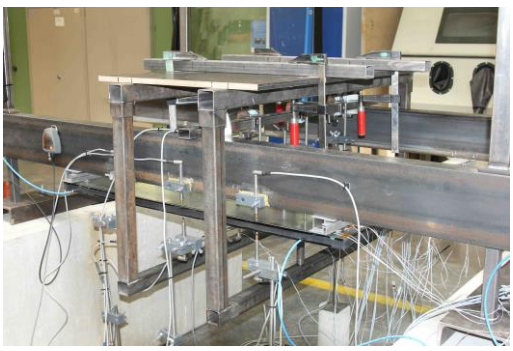

Figure 9.11 Steel frame with wooden plate for the loading of the outer pane

The climate loads are considered with the installation of an over- or underpressure in the glazing cavity. To regulate the pressure, a needle is drilled through the edge seal into the glazing cavity and connected to a compressor or a vacuum pump (Figure 9.13). The pressure is measured with a manometer, which is related via a second needle to the cavity (Figure 9.14).

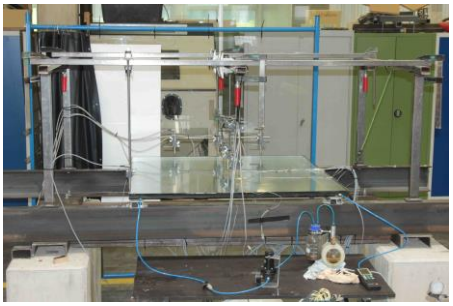

Figure 9.12 Pressure regulation set-up

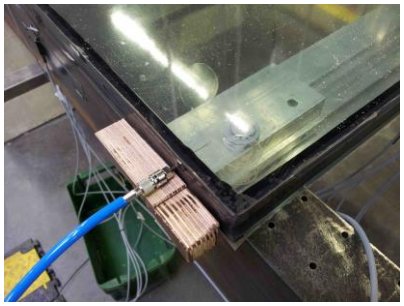

Figure 9.13 Needle in the cavity

Figure 9.14 Manometer

The self-weight of the glass panes of the IGU is simulated with steel weights, which are attached via steel wires on suction cups mounted on the inner and outer glass panes (Figure 9.15).

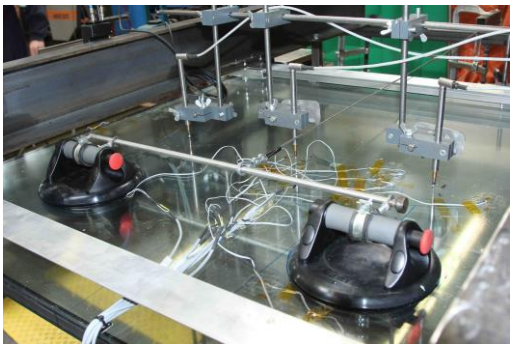

Figure 9.15 Assembling for the application of the self-weight

9.3 Test specimens

For each test, the test specimen is a quadratic point fitted insulation glass units with four Fischer undercut anchors. The edge bond is a structural dual-sealed system with a standard geometry. The primary and secondary sealants are made of polyisobutylene

respectively Dow Corning DC 993 structural silicone. Aluminium is chosen for the metal spacer and the gas in the cavity is air.

The dimensions and the materials of the test specimens are presented in Figure 9.16:

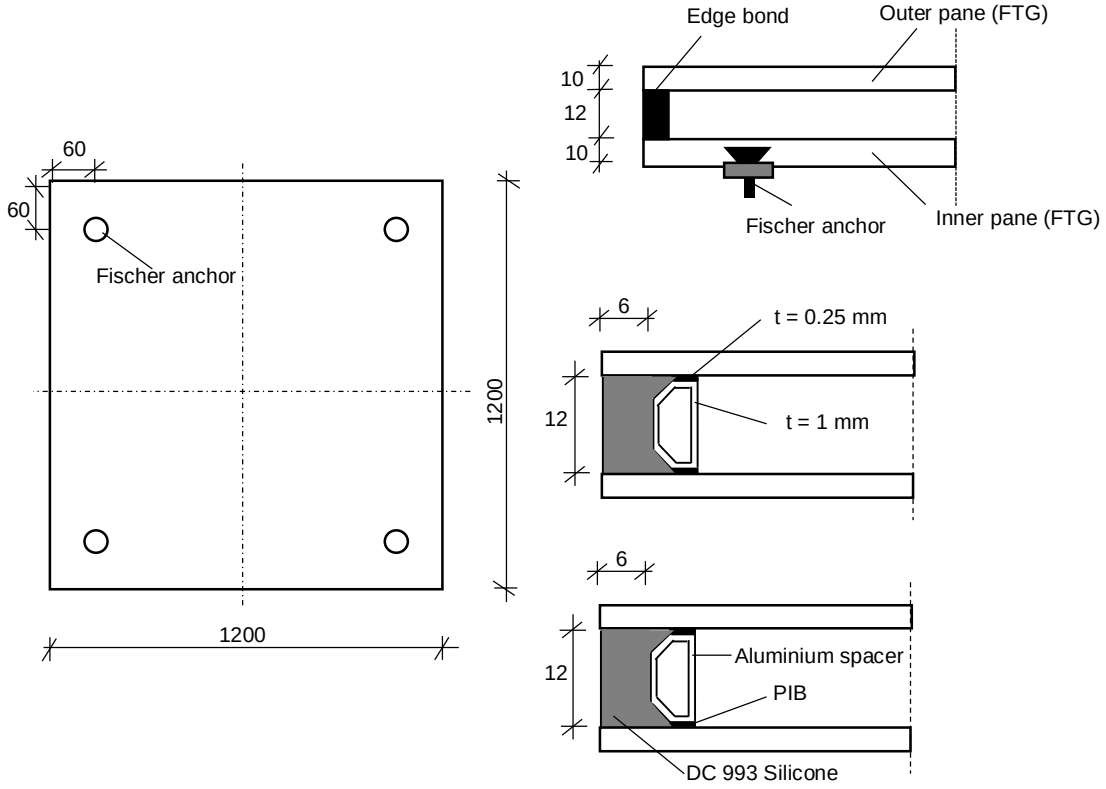

Figure 9.16 Dimensions of the test specimens and materials for the edge bond system

The prestress of the inner and outer glass pane of each test specimens are measured with the *SCALP-04* (Figure 9.17). The measurement points are shown in Figure 9.18.

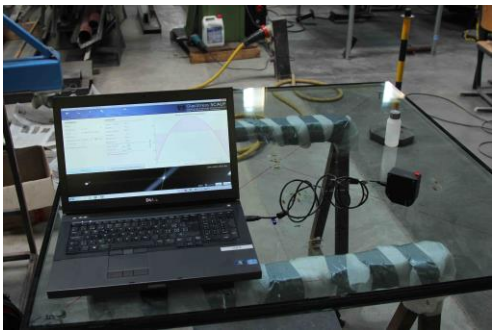

Figure 9.17 Prestress measurement with the SCALP-04 polariscope

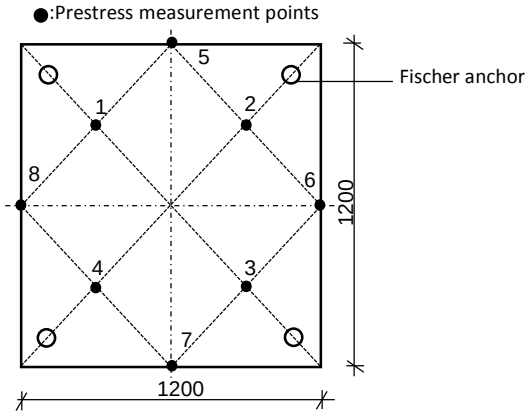

Figure 9.18 Prestress measurement points

The thermal prestress in the measurement points of the inner and outer glass pane is averaged and is about σ_V = 100 N/mm² for both panes. As for the component tests in chapter 5, the prestress value corresponds to the lowest commonly acceptable limit of tolerance for the prestress of fully tempered glass. In fact, fully tempered glass with a low prestress level has explicitly been commanded for the IGU specimens in the framework of the large scale tests. A similar procedure is applied in (Beyer, 2007) for single glazing. In this way, the ultimate load bearing resistance of the Fischer undercut anchor in IGU is determined on the conservative side. In addition, it can be proofed that the extended SLG-method is able to conservatively predict the failure of the connection for the worst case concerning the prestress level.

A plastic foil is glued on both glass panes to retain the glass fragments in case of glass fracture.

9.4 Test description and test program

Four different tests are conducted on the point fitted insulation glass units with the Fischer undercut anchor as described in Figure 9.16. In this section, the description and the program for each test is presented.

i. 1. Test:

In the first test, the specimen is mounted on the test set-up according to configuration 1 (Figure 9.6). Four different load cases are investigated in order to achieve three different aims:

For the two first load cases, the winter respectively the summer climate loads are simulated by installing a corresponding pressure difference in the glazing cavity (Figure 9.19 and Figure 9.20).

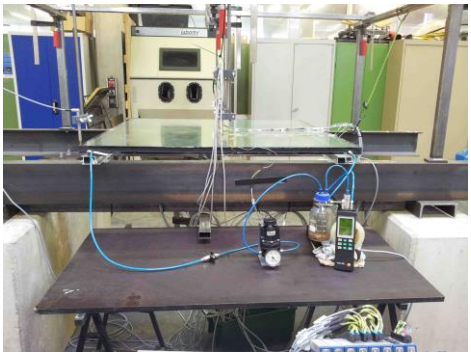

Figure 9.19 Set-up for the winter loads

Figure 9.20 Set-up for the summer loads

No external loads are applied for the two load cases. The resulting surface loads acting on each the inner and outer glass pane directly result from the pressure difference in the cavity and they are applied on the FE-model of the IGU. A comparison between the numerical results for the deformations and strains of the glass panes and the test values along defined paths verifies the numerical model of the IGU with the Fischer undercut anchor.

For the third load case, an underpressure corresponding to the winter load case according to (DIN 18008-2) is installed in the cavity in a first load step. Subsequently, a wind pressure load of 3 kN/m² is applied on the outer glass pane in three steps of each 1 kN/m² (Figure 9.21).

Figure 9.21 The wind pressure load applied with sandbags

The deformations and strains of the glass panes are measured for each load step. Additionally, the pressure change in the cavity due to the wind pressure load is measured with a manometer. The test values are compared to the numerical results which are determined with the resulting surface loads delivered by the extended climate load model. In this way, the climate load model is experimentally verified.

In the fourth load case, an overpressure is installed in the glazing cavity and increased until a failure occurs in the edge bond (Figure 9.22). Finally it is analysed if the numerical model is able to predict the failure in the edge sealant.

Figure 9.22 Overpressure in the glazing cavity

At the end of each load case, the test sample is totally discharged and a total recovering of the glass panes and the edge bond is observed.

A detailed test program for the 1. test and a measurement plan for the strains in the inner and outer glass pane are given in annexe D.

ii. 2. Test:

For the second test, the IGU is mounted on the test set-up according to configuration 2 (Figure 9.7) and wind pressure loads are applied on the inner pane. The test is conducted with the aim to induce a failure of the connection Fischer anchor - glass and to verify if

the extended SLG-method predicts the failure on the conservative side. For configuration 2, the point fittings are subjected to tension and the premature failure of the connection is consequently assured.

In preparation of the test, a hole is drilled through the edge bond to allow a pressure balance between the glazing cavity and the environment. After the balancing, the cavity is hermetically sealed and no initial pressure difference is installed in the cavity consequently.

A wind pressure load is applied on the inner glass pane (Figure 9.23) and increased in nine load steps until failure of the connection.

Figure 9.23 Sandbags on the inner pane

For each load step, the deformations and strains of the inner and outer glass pane as well as the pressure difference in the glazing cavity are measured along defined paths for comparison to the numerical results.

A detailed test program for the 2. test and a measurement plan for the strains in the inner and outer glass pane are given in annexe D.

iii. 3. Test:

In the third test, the IGU is installed on the test set-up according to configuration 2. Wind pressure loads are applied on the inner pane and an underpressure corresponding to the winter climate loads is installed in the cavity. In addition, the self-weight of the unit is considered (Figure 9.24). The aim of the third test consists in inducing a failure in the connection Fischer anchor – glass. The experimental failure stress is checked against the value delivered by the extended SLG-method in order to verify if the method conservatively predicts the failure.

In a first load step, the self-weight is applied by means of steel weights as shown in Figure 9.15. The total weight of the inner and outer glass pane is all in all 72 kg. The weight of the edge seal system and the Fischer undercut anchors is neglected.

In a second load step, the underpressure for the simulation of the winter climate loads is installed in the cavity.

In further load steps, a wind pressure load is applied on the inner glass pane and increased until failure of the Fischer anchor.

Figure 9.24 Application of the self-weight, the wind loads and the winter climate loads

As for the second test, the deformations and strains are measured during the test along defined paths and compared to the results delivered by the verified numerical model of the point fitted IGU.

A detailed test program for the 3. test and a measurement plan for the strains in the inner and outer glass pane are given in annexe D.

iv. 4. Test:

The specimen is mounted on the test set-up according to configuration 2 (Figure 9.7). Wind suction loads are applied on the outer pane and an underpressure corresponding to the winter climate loads is installed in the cavity. The objective of the fourth test consists in increasing the wind suction load on the outer pane until failure of the connection Fischer anchor – glass. In comparison to the second and third test, the wind loads in the fourth test act on the outer pane and are transferred via the edge bond to the inner pane and subsequently to the point fitting. This load path changes the stress level at the borehole and thus the failure load of the connection. The fourth test allows the experimental investigation of the dependency of the connection resistance on the load path. As for the second and third test, the failure stress at the borehole is determined with the extended SLG-method in order to verify its accuracy for the given load case.

In the first load step, the underpressure corresponding to the winter climate loads is installed in the glazing cavity.

In a second step, the steel frame for the application of the wind loads is mounted.

In a last step, the outer pane is gradually charged with a sandbag (Figure 9.25) to simulate the wind suction loads until failure of the connection Fischer anchor-glass.

Figure 9.25 Loading of the outer glass pane with a sandbag

During the test, the deformations and strains of the glass panes are measured along defined paths and compared to the numerical values delivered by the verified FE-model of the point fitted IGU with the Fischer undercut anchors.

A detailed test program for the 4. test and a measurement plan for the strains in the inner and outer glass pane are given in annexe D.

9.5 Numerical models of the test specimen

The large scale tests are simulated with two FE-models of the point fitted IGU with the Fischer undercut anchors: a complex 3D model with solid elements and a simple 2D model with shell elements for the glass panes are developed with the FE-software ABAQUS®.

The 3D model is calibrated with the test data and delivers the equivalent stress peak at the borehole corresponding to the experimental failure load. Additionally, the model is used in the procedure for the experimental verification of the extended climate load model.

The 2D model is verified with the test data and is used for the verification process of the extended SLG-method.

9.5.1 3D Solid FE–model

The 3D FE-model of the test sample accounts for the exact geometry of the borehole, the point fitting and the edge bond. In fact the calibrated and verified numerical model of the Fischer anchor FZP-G-Z in single glazing (Chapter 6) is implemented in the insulation glass unit. Contact definitions between the point fitting and the glass pane consider the separation of the point fitting from the glass and the load transfer in case of contact. To save calculation time, double-symmetry is capitalised and only a quarter of the IGU is modelled. In the case where the self-weight is considered, half of the IGU is modelled.

For the simulation of the large scale tests, the wind and climate loads are transferred to resulting surface loads by means of the extended climate load model. In the numerical model, the resulting surface loads are applied on the inner and outer glass pane (Figure 9.26).

The connection of the point fittings to the substructure is simulated by springs with the stiffness values of the substructure system “SystemOne” (Figure 9.27).

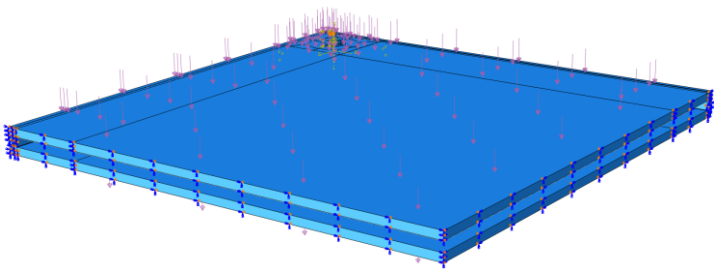

Figure 9.26 Load application on the 3D FE-model and boundaries

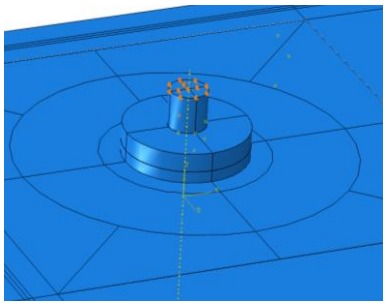

Figure 9.27 Spring supports for the FZP-G-Z

The glass panes are modelled with the solid element type C3D8I, an 8-node linear brick with incompatible nodes to overcome the shear locking problems, which occur in bending problems. The mesh configuration for the inner pane and in the borehole area is described in section 6.3.2. A regular mesh configuration with two elements over the thickness is generated for the outer glass pane. The mesh generation for the glass panes is shown in Figure 9.28.

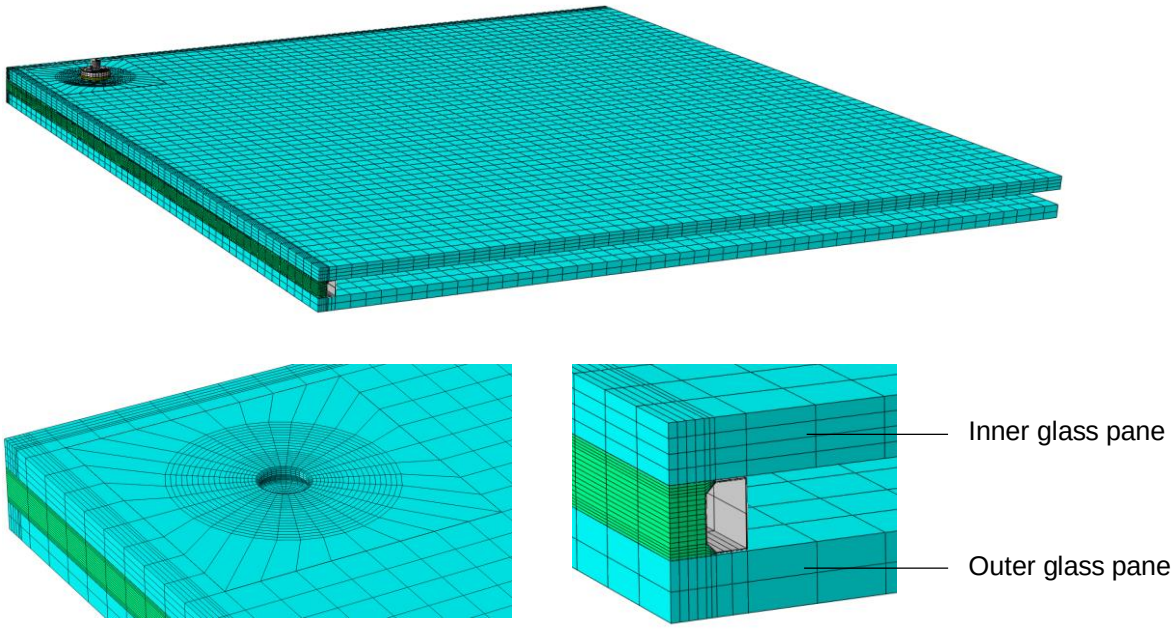

Figure 9.28 Mesh generation for the glass panes

Concerning the edge bond system, the silicone sealant is modelled with 8-node linear brick, hybrid and constant pressure solid elements C3D8H. Hybrid elements are indispensable for the modelling of the sealant, because silicone is a nearly uncompressible material and the pressure stress in the element cannot be computed from the displacement of the nodes. The hybrid element adds an additional degree of freedom to overcome this problem. The primary sealant PIB is not modelled, as it is assumed that it does not have a structural function. For the metal spacer, the same element type C3D3I as for the glass panes is used. The mesh generation for the glass panes is shown in Figure 9.29.

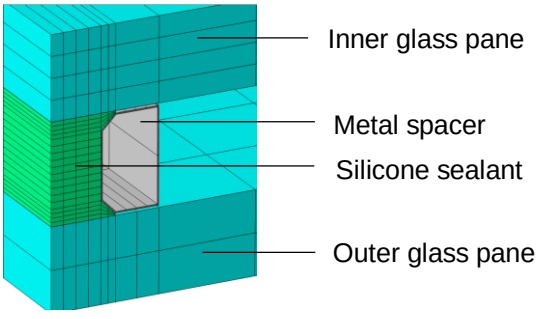

Figure 9.29 Mesh generation for the edge bond components

The metal components of the Fischer undercut point fitting, as to know the round nut and the anchor are modelled with 8-node linear and reduced integration brick elements

C3D8R. Reduced integration elements are adequate for the two components, because they are not subjected to high bending moments and the risk of shear locking problems is reduced. The spacer disk and the plastic plug are implemented with the C3D8H elements, the same element type that is used for the silicone sealant.

The material properties of the different components of the point fitted IGU are shown in Table 9.2.

Table 9.2 Material properties implemented in ABAQUS®

Component	Material	Material law		
		Type	E [N/mm²]	ϑ [-]
Glass pane	Glass	Linear elastic	70 000	0.23
Secondary sealant	Structural silicone DC 993	Hyperelastic (Dias, 2013)	-	-
Metal spacer	Aluminium	Linear elastic	70 000	0.3
Bolt	Stainless steel	Linear elastic	190 000	0.3
Spacer disk	Polyamide	Linear elastic	1000	0.4
Round nut	Stainless steel	Linear elastic	190 000	0.3
Plastic plug	Polyurethane	Linear elastic	80	0.4

9.5.2 Simple 2D FE-model

A detailed description of the simple 2D FE-model is given in chapter 5. Hence, only a short recapitulation of the description is presented in the following:

In the 2D FE-model, the Fischer anchors and the substructure are simulated by springs arranged in series with corresponding stiffness values. The resulting stiffness values of the springs are given in Table 9.3. The complex undercut borehole geometry and the point fittings with the contact definitions are not modelled.

The inner and outer glass panes are modelled with 4-node general-purpose shell elements S4 (Figure 9.30).

The edge bond is modelled with its exact geometry and with its different components (e.g. silicone sealant and metal spacer) by using the same solid element type as in the 3D FE-model.

The same material properties are used than for the 3D model (Table 9.2).

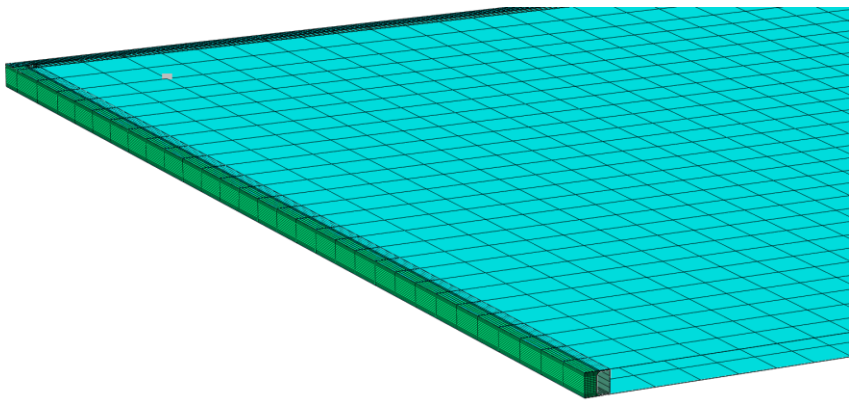

Figure 9.30 Simple 2D FE-model of the point fitted IGU with the Fischer undercut anchor

Table 9.3 Resulting spring stiffness of the Fischer anchors FZP-G-Z and the substructure "SystemOne"

Spring stiffness	k_x [N/mm]	k_y [N/mm]	k_z [N/mm]	k_{mx} [Nmm/rad]	k_{my} [Nmm/rad]
FZP-G-Z	895	895	1.00E+07	4.72E+05	4.97E+05

9.6 Test results

In the following section, the results of each test are presented and compared to the numerical results. In those cases, where the deformations of the glass panes in the tests exceed 20% of the pane thickness (Raecke), a non-linear numerical calculation is done to take into account the membrane effects.

9.6.1 1. Test – Verification of the numerical models

The 3D Solid and simple 2D FE-models are verified by comparing the numerical results for the deformations and the strains of the inner and outer glass pane to the experimental values. This is done for the two loads cases "Winter" and "Summer".

For the load case "Winter" (Table 9.4), the experimental values are compared to the numerical results for each load step.

Table 9.4 The load case "Winter"

Load case	Objective	Load step	Δp [mbar]	p_{ex} [kN/m²]	g [kg]
Winter (Δp = -15 mbar)	Verfication of FE-model	1	-3	0	0
		2	-6	0	0
		3	-9	0	0
		4	-12	0	0
		5	-15	0	0

In Figure 9.31, the experimental values of the deformations at the mid-span of the inner and outer glass pane are compared to the corresponding numerical values of the 3D FE-model.

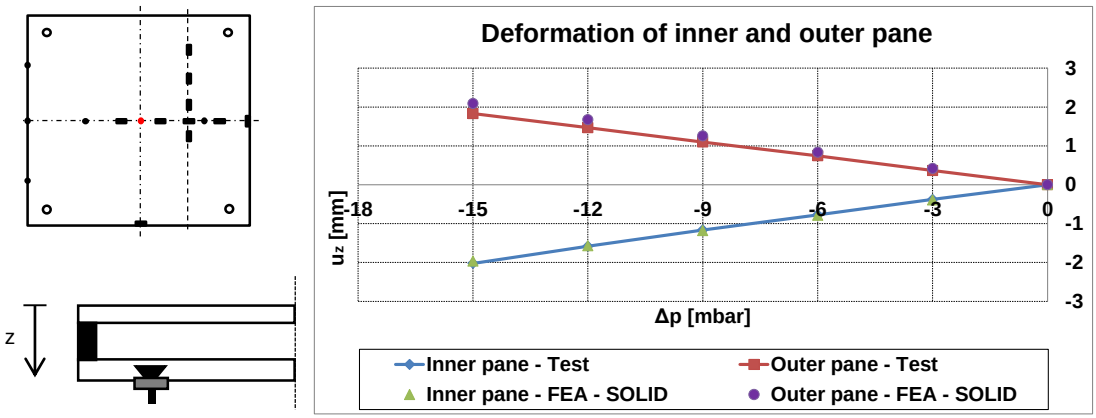

Figure 9.31 Deformations of the inner and outer glass pane and comparison to the 3D Solid FE-model, 1. Test, Load case "Winter"

Both glass panes deform towards the cavity due to the underpressure. The deformations increase linearly because of the linear elastic material behaviour of glass. A good correspondence between the experimental and numerical results is noticed. The maximal deviation is less than 4 %.

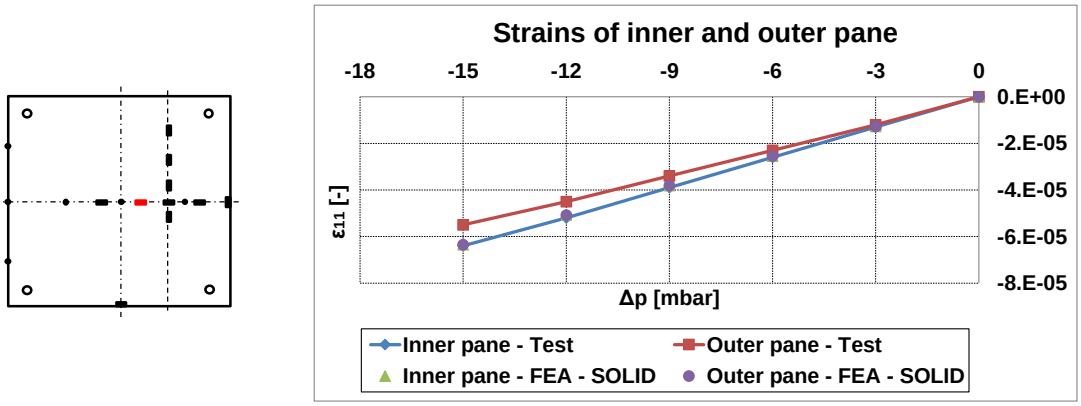

Figure 9.32 Strains of the inner and outer glass pane and comparison to the 3D Solid FE-model, 1. Test, Load case "Winter

The strains of the inner and outer glass pane at a distance of 20 mm from the centre are shown in Figure 9.32. The surface of each glass pane is under compression and a good accordance to the numerical results is observed with a maximal deviation of 5 %.

The deformation of the silicone sealant is measured by recording the deformations of the inner and outer glass pane at the edge of the IGU (Figure 9.33).

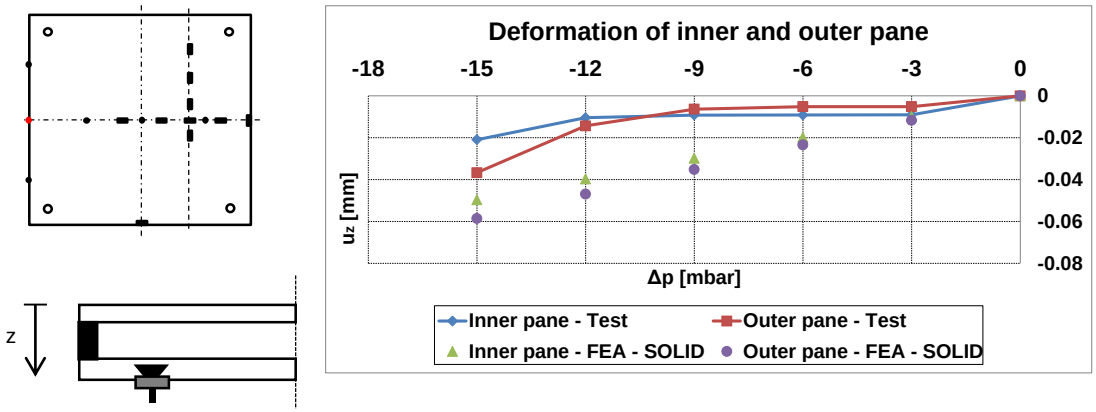

Figure 9.33 Deformation of the inner and outer glass pane at the edge and comparison to the 3D Solid FE-model, 1. Test, Load case "Winter"

The measured deformations of each glass pane increase irregularly and cannot be reproduced by a numerical simulation ($\Delta > 50\%$). The deformations are too small (< 0.05 mm) to be recorded with high accuracy.

The experimental values are additionally compared to the numerical results delivered by the simple 2D FE-model.

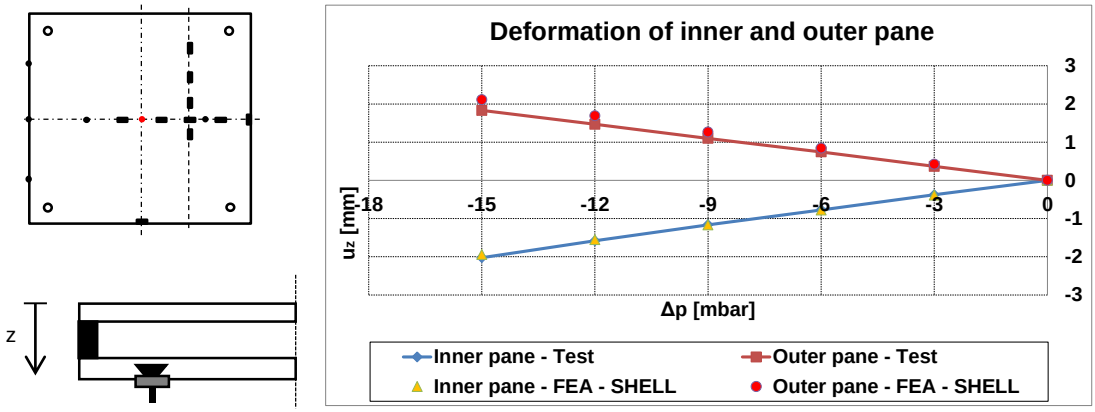

Figure 9.34 Deformations of the inner and outer glass pane and comparison to the simple 2D FE-model, 1. Test, Load case "Winter"

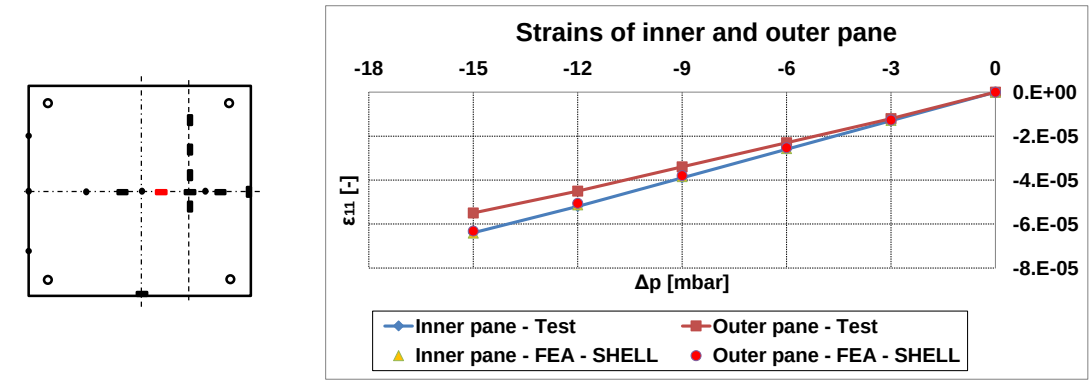

Figure 9.35 Strains of the inner and outer glass pane and comparison to the 2D Shell FE-model, 1. Test, Load case "Winter

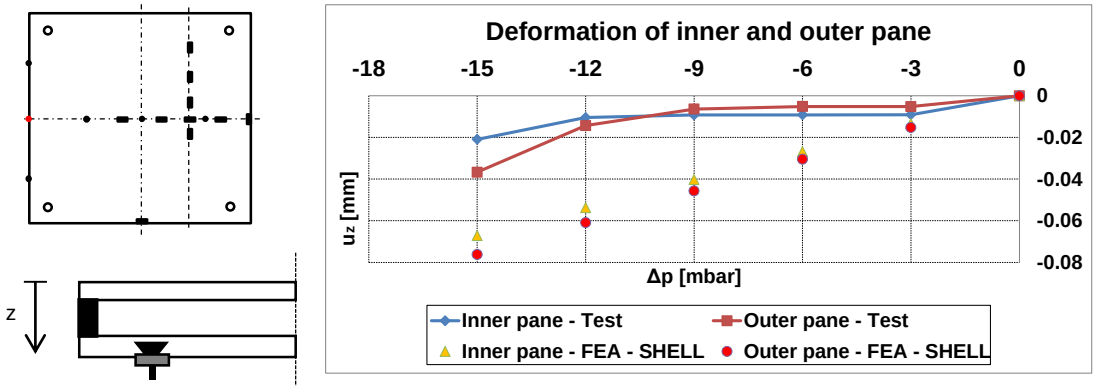

Figure 9.36 Deformation of the inner and outer glass pane at the edge and comparison to the simple 2D FE-model, 1. Test, Load case "Winter"

As for the 3D Solid FE-model, a good correspondence between the experimental and numerical results is noticed for the deformations in the mid-span of the glass panes and the strains (Figure 9.34 and Figure 9.35). For the deformations of the edge bond, no

compliance of the results is observed due to the small deformations of the glass panes at their edges (Figure 9.36).

A comparison between the deformations and strains delivered by the 3D Solid and the simple 2D FE-model along path 0 is shown in Figure 9.37 and Figure 9.38. An excellent conformity of the results is noticed.

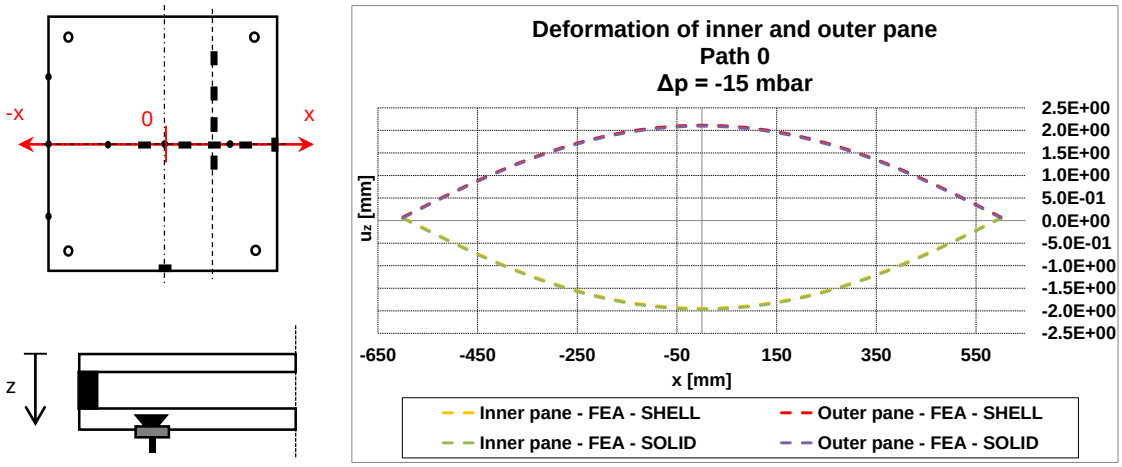

Figure 9.37 Comparison of the deformations along path 0 between the 3D Solid and the simple 2D FE-model, Load case "Winter"

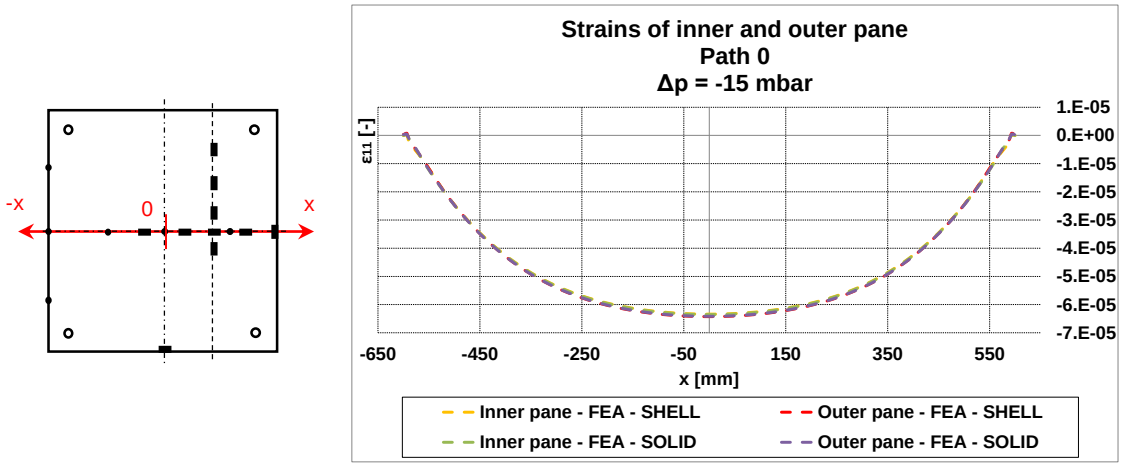

Figure 9.38 Comparison of the strains along path 0 between the 3D Solid and the simple 2D FE-model, Load case "Winter"

Further test results and their comparison to the numerical values are presented in annexe D. A good accordance of the results is observed.

For the load case "Summer" (Table 9.5), the same comparisons than for the load case "Winter" are done.

Table 9.5 The load case "Summer"

Load case	Objective	Load step	Δp [mbar]	p_{ex} [kN/m²]	g [kg]
Summer (Δp = +15 mbar)	Verfication of FE-model	1	3	0	0
		2	6	0	0
		3	9	0	0
		4	12	0	0
		5	15	0	0

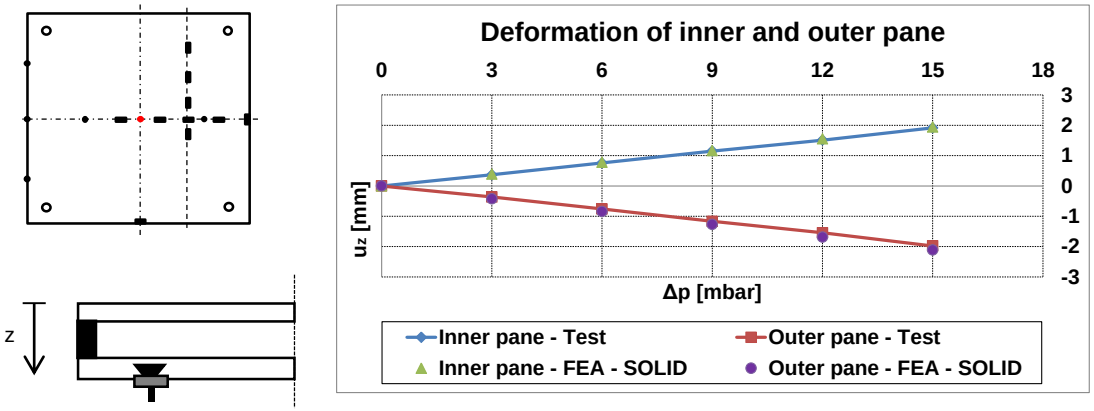

Figure 9.39 Deformations of the inner and outer glass pane and comparison to the 3D Solid FE-model, 1. Test, Load case "Summer"

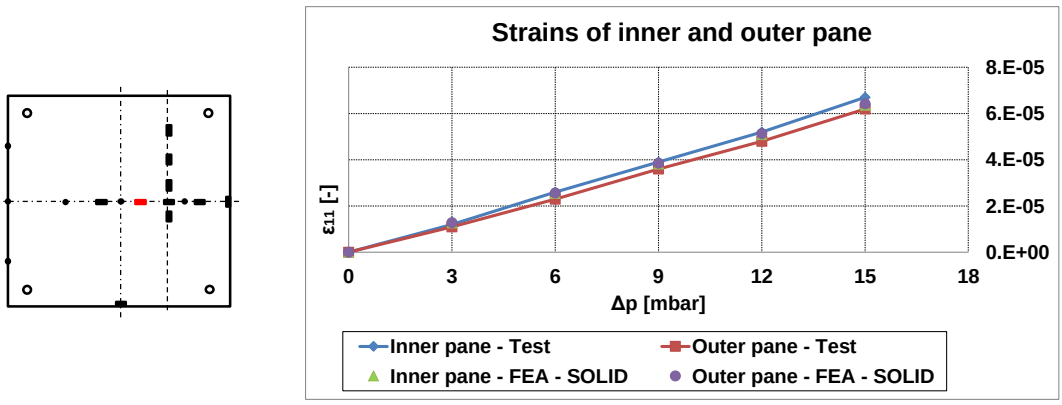

Figure 9.40 Strains of the inner and outer glass pane and comparison to the 3D Solid FE-model, 1. Test, Load case "Summer"

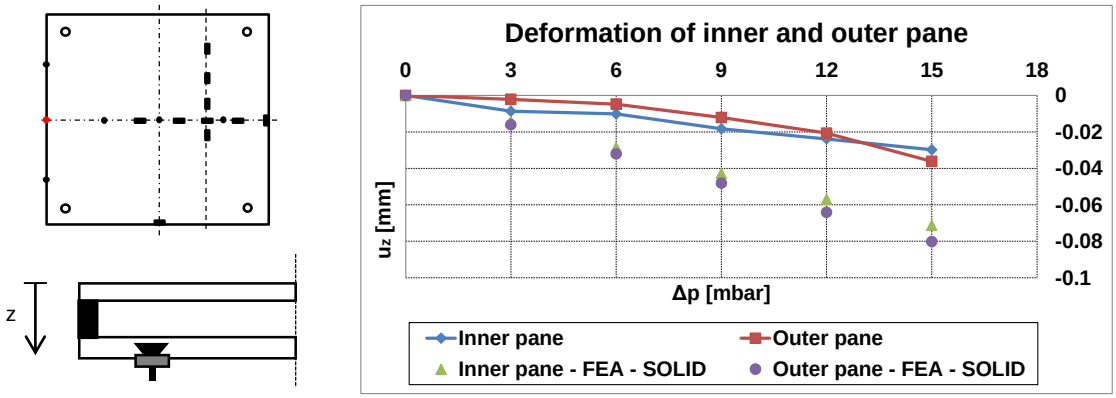

Figure 9.41 Deformation of the inner and outer glass pane at the edge and comparison to the 3D Solid FE-model, 1. Test, Load case "Summer"

Due to the overpressure in the cavity, the inner and outer glass panes bend towards the exterior (Figure 9.39) and the outer surface of each pane is under traction (Figure 9.40). The experimental and numerical values perfectly coincide (Δ < 5%), except for the deformations at the edge of the glass pane (Figure 9.41) for the known reasons.

The comparison of the test results to the values delivered by the simple 2D FE-model as well as the comparison along path 0 and path 1 is presented in annexe D. In both cases, a good conformity is noticed as well.

In conclusion, the 3D solid and the simple 2D FE-model models are experimentally verified and they are able to correctly simulate the deformations and strains of each glass pane of the point fitted IGU with the Fischer undercut anchors. The missing PIB in the numerical models does not affect the results. From this follows, that the PIB does not influence the global behaviour of the point fitted IGU and consequently it can be neglected. Additionally, a comparison between the results of the two models reveals their analogy. Thus, the 3D solid model can be used for the experimental verification of the extended climate load model and the simple 2D FE-model can be applied for the verification of the extended SLG-method.

9.6.2 1. Test – Experimental verification of the extended climate load model

The experimental verification of the extended climate load model is done for the load case presented in Table 9.6.

Table 9.6 The load case "Winter + Wind pressure load on outer glass pane"

Load case	Objective	Load step	Δp [mbar]	p_{ex} [kN/m²]	g [kg]
Winter + 3 kN/m²	Experimental verification of extended climate load model	1	-15	0	0
		2	-10.7	1	0
		3	-7	2	0
		4	-3.3	3	0

For each load step, the resulting surface loads and the pressure difference between the cavity and the environment are determined by means of the extended climate load model. The resulting surface loads are applied on the inner and outer glass pane in the 3D Solid FE-model and the corresponding deformations and strains are calculated. A comparison between the numerical determined deformations and strains and the experimental values verifies the extended climate load model.

The verification procedure is resumed in Figure 9.42.

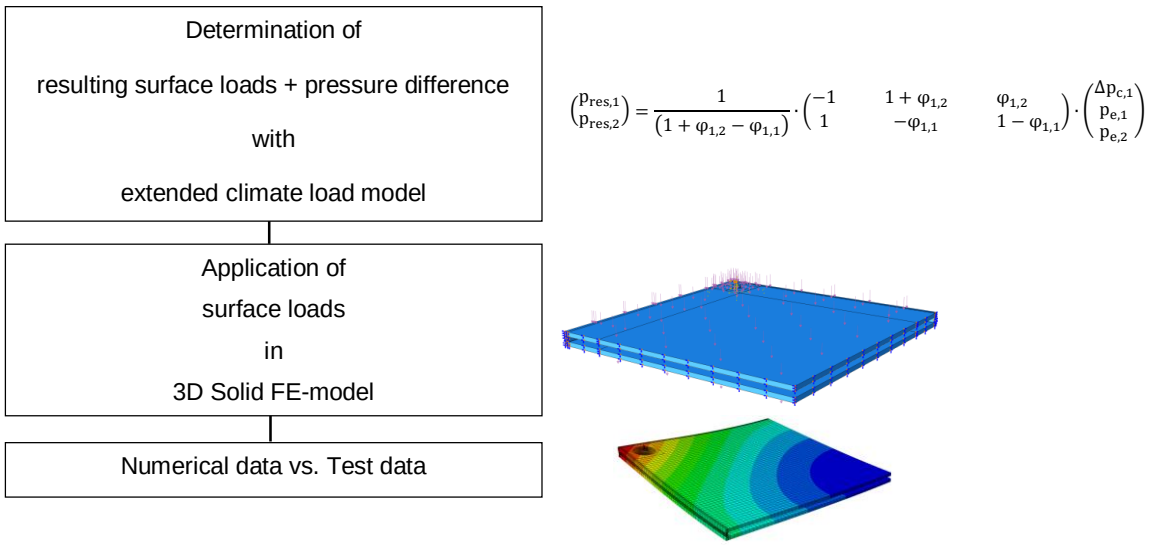

Figure 9.42 Verification procedure for the extended climate load model

In Figure 9.43, the mid-span deformations of the inner and outer glass pane are plotted against the different load steps. The experimental and numerical values coincide with high accuracy (Δ < 4%). For the first load step, the break in the deformation curve of the inner glass pane corresponds to the change in direction of its bending curve. In fact, due to the underpressure in the cavity in the first load step, the inner pane deforms towards the cavity. The loading of the outer glass pane in the second load step then induces a deformation of the inner plan toward the exterior. For the load step 4, the experimental

value for the inner glass pane was not measured, because the displacement sensor has been removed for security reason.

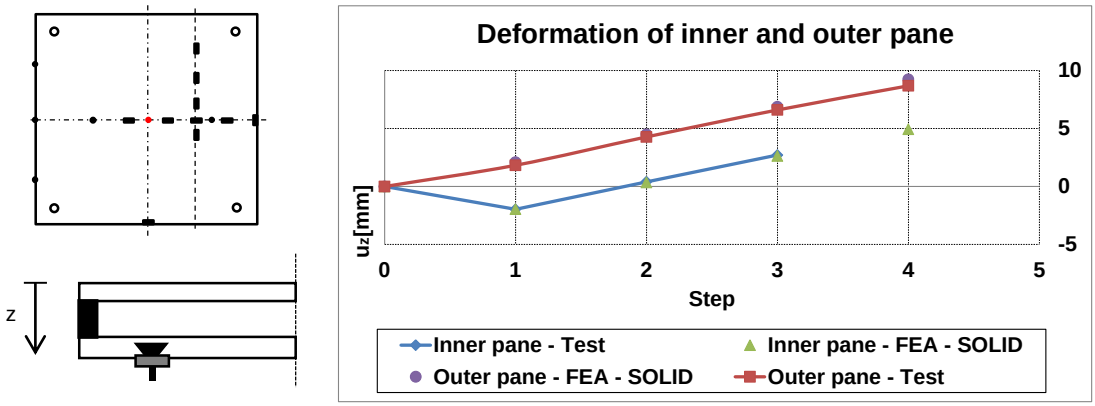

Figure 9.43 Deformations of the inner and outer glass pane and comparison to the 3D Solid FE-model, 1. Test, Load case "Winter + Wind pressure load on outer glass pane"

A good accordance between the test and the numerical results is noticed for the strains at a distance of 20 mm from the centre of the glass panes (Figure 9.44). The deviations for the outer glass pane ($\Delta > 15\%$) are higher than for the inner glass pane ($\Delta < 5\%$).

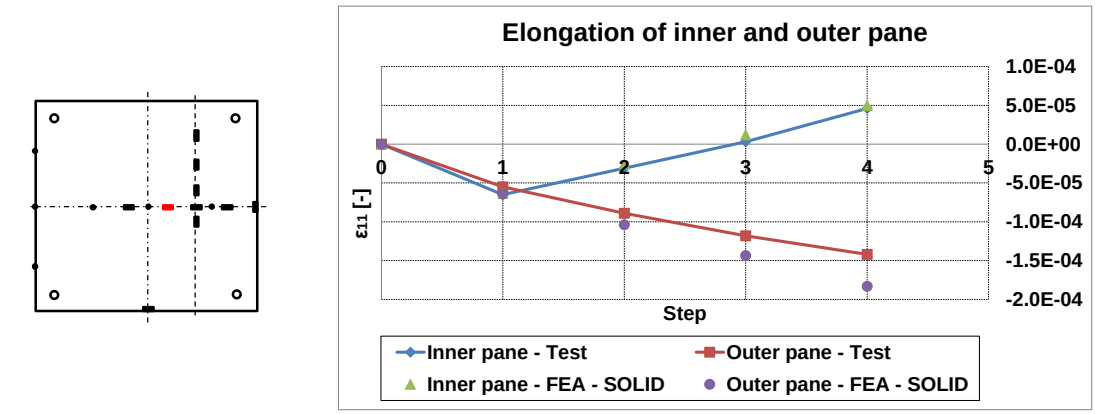

Figure 9.44 Strains of the inner and outer glass pane and comparison to the 3D Solid FE-model, 1. Test, Load case "Winter + Wind pressure load on inner glass pane"

The reason for the higher deviation is the inhomogeneous loading of the outer glass pane with sandbags in order to leave a gap for the measurement equipment (Figure 9.45).

Figure 9.45 Gap in the centre of the IGU for the installation of the displacement sensors along path 0

In contrary to the first load cases “Winter” and “Summer”, the displacement at the edges of the glass pane can be measured with a satisfying precision (Figure 9.46).

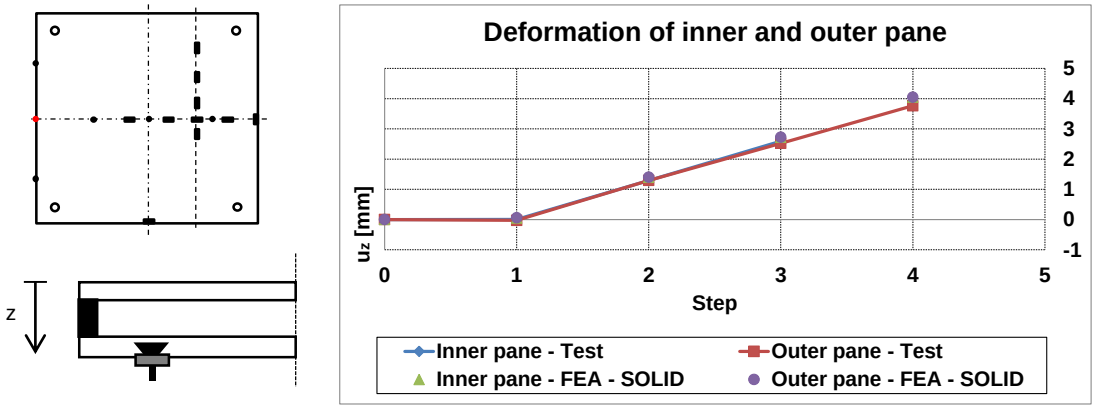

Figure 9.46 Deformation of the inner and outer glass pane at the edge and comparison to the 3D Solid FE-model, 1. Test, Load case “Winter + Wind pressure load on inner pane”

A good concordance between the test and the FE-data is noticed. As for the strain measurement, the deviations between the experimental and numerical values for the deformations of the outer glass pane ($\Delta \approx 8$ %) are higher than for the inner glass pane ($\Delta \approx 4$ %). In addition, the similar values for the inner and outer glass pane reveal the rigid behaviour of the edge seal system under loading.

Further results concerning the comparison of the experimental and numerical deformations and strains along path 0 and path 1 are presented in annexe D.

For each load step, the pressure difference between the cavity and the environment is determined with the extended climate load model and compared to the pressure difference measured during the test. The results are shown in Figure 9.47.

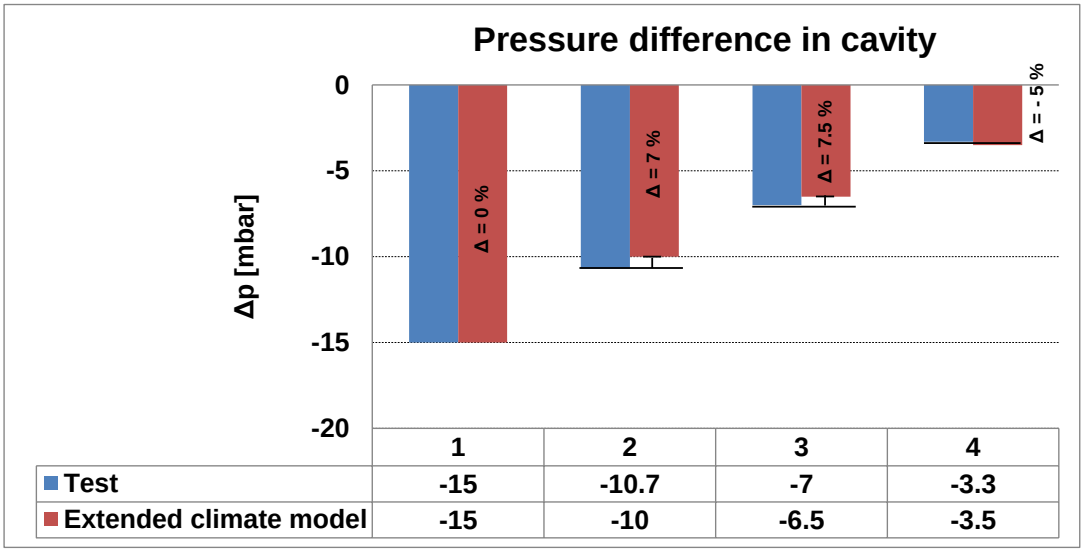

Figure 9.47 Pressure difference in the cavity

The maximal deviation is about 7.5 % and the extended climate load model hence allows a precise prediction of the pressure difference in the cavity for the different load steps.

In conclusion, the resulting surface loads which are calculated with the extended climate load model can be applied in the numerical model for the precise determination of the deformations and stresses in the glass panes. Moreover, the extended climate load model precisely predicts the pressure change in the cavity due to an external loading. In consequence, the extended climate load model can be applied for the design of point fitted insulation glass units with the Fischer undercut anchor.

9.6.3 1. Test – Failure prediction of the edge bond

In the fourth load case, an overpressure is installed in the glazing cavity and increased until a failure occurs in the edge bond (Table 9.7).

Table 9.7 The load case "Overpressure"

Load case	Objective	Load step	Δp [mbar]	p_{ex} [kN/m²]	g [kg]
Overpressure	Failure in edge bond	1	160	0	0

The failure in the edge bond occurs at an overpressure of 160 mbar and consists in the rupture (cohesive failure) of the silicone sealant over a length of ca. 1080 mm between the point fittings. The rupture is located close to the inner glass pane (Figure 9.48).

Figure 9.48 Location and rupture of the silicone sealant close to the inner glass pane

The resulting surface loads that correspond to the overpressure of 160 mbar are applied in the 3D Solid model and the opening as well as the tensile stresses in the secondary sealant is numerically determined. The values are compared to the experimental data.

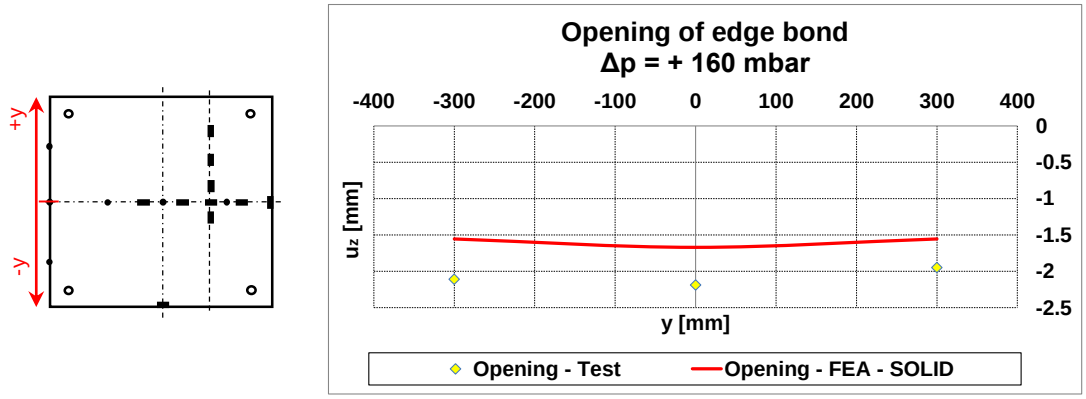

Figure 9.49 Experimental and numerical opening of the edge bond

The FE delivers an opening of the edge bond of nearly 1.5 mm, while an opening of about 2 mm are measured during the test (Figure 9.49). This corresponds to a deviation of 33 %. In fact, the opening of the edge bond in the test is determined by the difference of the measured deformations of the inner and outer glass pane. These deformations are very small (< 0.5 mm) and therefore they are difficult to be measured with high accuracy.

The tensile stress σ_{zz} in the silicone is numerically determined (Figure 9.50). The stress values are readout along the path where the rupture origin is located in the test. The numerical tensile stress area has a length of about 1056 mm and nearly corresponds to the rupture length of ca. 1080 mm, which is measured in the test. The maximal tensile

stress value delivered by FE is about σ_{zz} = 0.65 N/mm^2 and the resistance value found in the tensions tests conducted on dog-bone samples is ca. σ_{zz} = 0.95 N/mm^2 (Dias, 2013). This corresponds to a deviation of 45 %. Hence, the FE-model is not able to predict the failure in the silicone sealant.

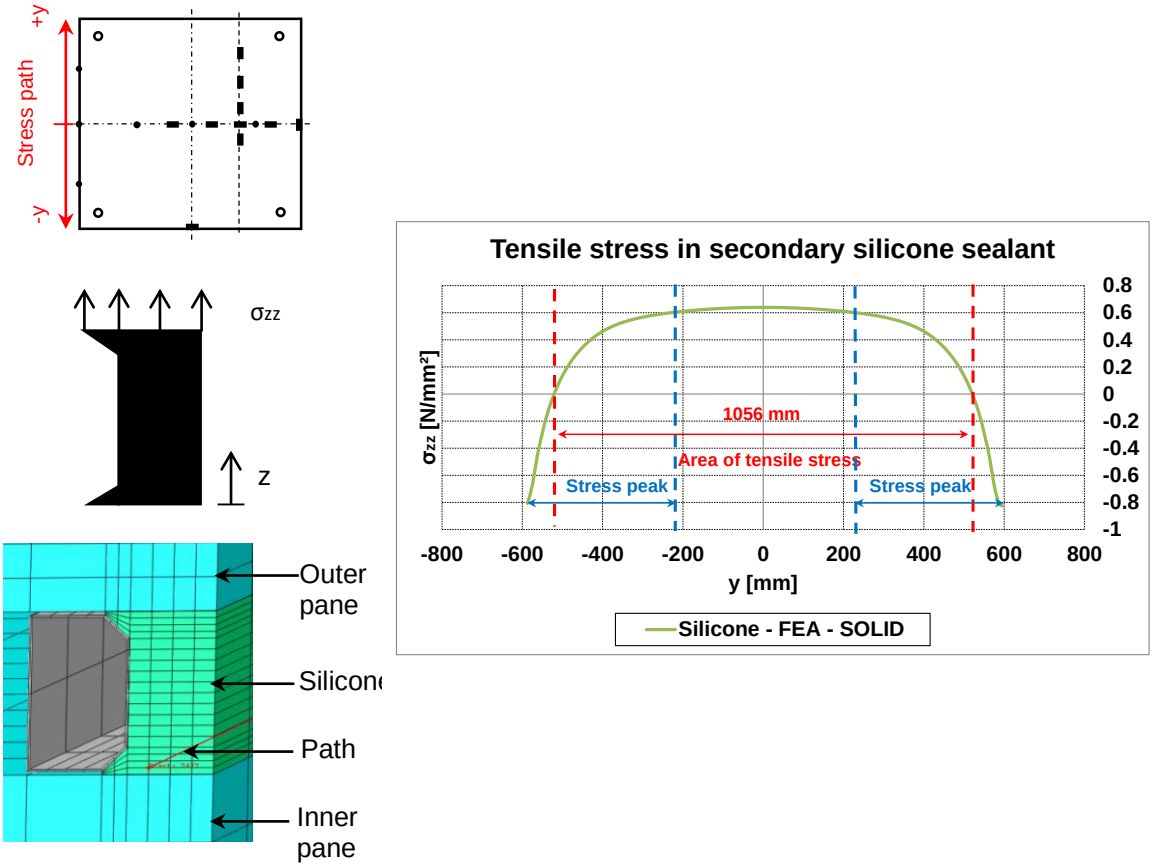

Figure 9.50 Stress path and tensile stress in the silicone sealant

Two reasons can be named for the deviation:

First of all, stress peaks occur in the numerical results for the tensile stresses (blue area in Figure 9.50). These peaks strongly depend on the mesh density and no convergence for the peak values can be attempt (Dias, 2013). Hence, the real value of the peaks remains unknown. Additionally, it is actually unclear whether the stress peaks really exist or if it is a matter of numerical singularities. As the origin of the rupture in the silicone indeed is located in a stress peak area, the failure stress can be hardly predicted with the calibrated FE-model.

Finally, the experimentally determined failure stress of the dog-bone sample in (Dias, 2013) is solely based on pure tension tests. In the large scale tests however a complex

3D stress state with simultaneously operating tensile and shear stresses acts in the silicone. Thus, the resistance values determined in the tension tests in (Dias, 2013) are inadequate for a direct comparison to the failure stress in the large scale tests.

In conclusion, an adequate failure criterion for the hyperelastic material silicone is currently missing and the failure stress in the edge seal cannot be determined accurately by FE. As a result, the novel design concept as proposed in section 4.5.3 foresees the design of the edge bond according the existing method in [ETAG-002]. An alternative solution is proposed in section 11.2.

9.6.4 2. Test – Verification of the extended SLG-method

For the verification of the extended SLG-method, the wind pressure load on the inner glass pane is increased until a failure occurs in the connection Fischer anchor - glass pane (Table 9.8).

Table 9.8 The load case "Wind pressure on inner glass pane"

Load case	Objective	Load step	Δp [mbar]	p_{ex} [kN/m²]	g [kg]
Wind pressure	Failure of FZP-G-Z + Verification of extended SLG-method	0	0	0	0
		1	4.1	1	0
		2	8.2	2	0
		3	12.4	3	0
		4	15.1	3.7	0
		5	16.5	4	0
		6	19.1	4.7	0
		7	20.8	5	0
		8	22.9	5.5	0
		9	0	8.3	0

The failure load corresponds to a wind pressure load of 8.3 kN/m^2 acting on the inner glass pane (Figure 9.51). In load step 9, the needle in the cavity for the pressure measurement was accidentally pulled out of the borehole in the edge seal and pressure equalization between the cavity and the environment took place. Therefore the pressure difference for load step 9 is zero.

The failure consists in a collapse of the connection Fischer anchor – glass pane. The crack origin is located at the borehole and leads to the fracture of the whole inner glass pane, while the outer glass pane remains undamaged (Figure 9.52).

Figure 9.51 Failure load applied with sandbags

Figure 9.52 Failure of the connection

Beside the verification of the extended SLG-method, the strains along two different paths in the borehole area are measured during the second test in order to proof the ability of the 3D FE-model to accurately simulate the stress state near the borehole.

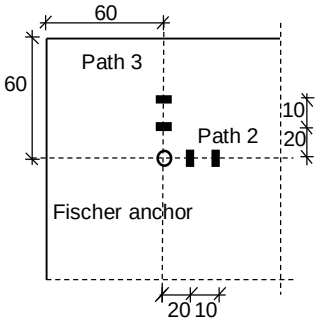

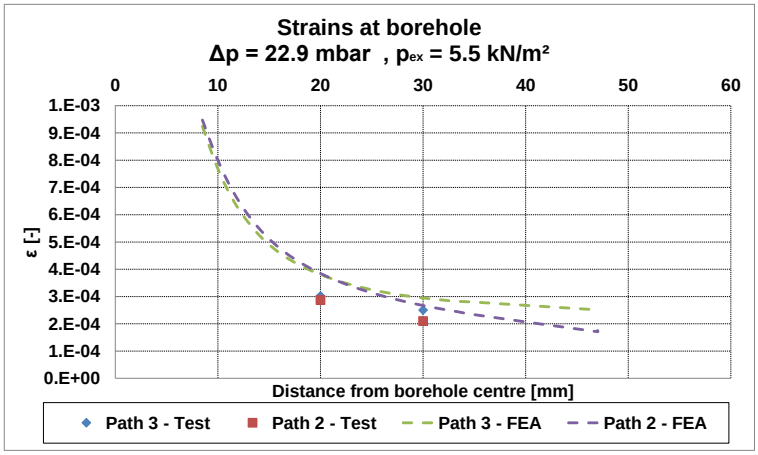

Figure 9.53 Strains along path 2 and path 3 in the borehole area and comparison to the 3D Solid FE-model, 2. Test, Load step 8

In Figure 9.53, a comparison between the strains calculated with the 3D FE-model and the measured strains is shown for load step 8.

The maximal deviation between the test and numerical values is about 18 %. With regards to the inhomogeneous loading of the inner glass pane with sandbags, the deviation is considered as reasonable. Consequently, the 3D Solid FE-model is able to correctly simulate the strain and stress state in the borehole area.

Further test results and the comparison to the numerical values are given in annexe D.

The verification process of the extended SLG-method is resumed in Figure 9.54 (see also chapter 8).

First of all, the failure load is applied (p_{ex} = 8.3 kN/m^2) in the 3D Solid FE-model and the maximal tensile stresses are determined at the two possible failure positions: the rim of the borehole (1) and the fillet of the borehole (2) (Figure 9.55). Secondly, the tensile stress values are calculated according to the extended SLG-method. Therefore, the failure load is applied in the 2D Shell FE-model and the forces and moments in the springs are determined. The spring forces and moments are transferred with the transfer functions into local stress components and superimposed with the global stress components. Finally, a comparison to the stress values found with the 3D FE-model verifies the method.

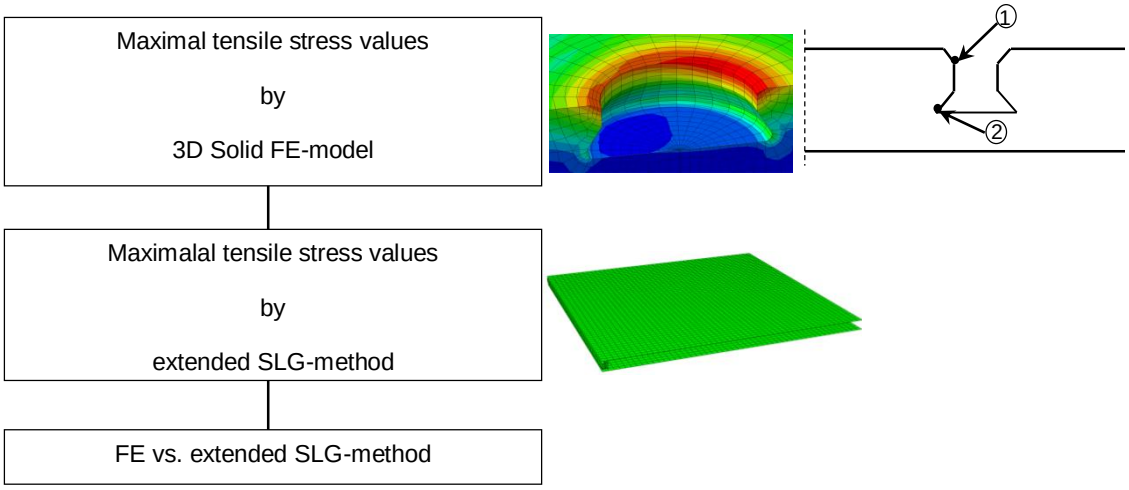

Figure 9.54 Verification procedure of the extended SLG-method

The 3D Solid FE-model delivers a maximal tensile stress of $\sigma_{max,1}$ = 115.6 N/mm^2 at position 1 and a tensile stress of $\sigma_{max,2}$ = 58.7 N/mm^2 at position 2.

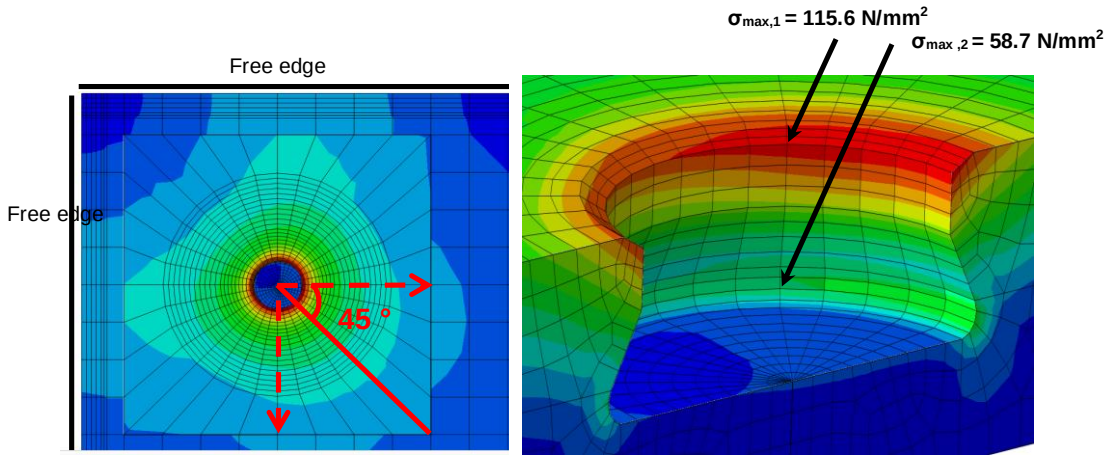

Figure 9.55 Location of the maximal tensile stresses at the borehole in position 1 and position 2, 2. Test

The comparison between the stress values found with the 3D FE-model and the values calculated with the extended SLG-method is resumed in Table 9.9 and Table 9.10.

Table 9.9 Comparison between the 3D Solid FE-model and the extended SLG-method, Position 1, 2. Test

	2D-Shell			Transfer function			Superposition	3D-Solid
N	V_{res}	M_{res}	σ_{glob}	σ_N	σ_V	σ_M	$\sigma_N + 0.75\cdot\sigma_V + 0.86\cdot\sigma_M + k\cdot\sigma_{glob}$	$\sigma_{max,1}$
[N]	[N]	[Nmm]	[N/mm²]	[N/mm²]			[N/mm²]	[N/mm²]
3168	1113	42 668	21	84.3	14.2	66.1	172.8	115.6

Table 9.10 Comparison between the 3D Solid FE-model and the extended SLG-method, Position 2, 2. Test

	2D-Shell			Transfer function			Superposition	3D-Solid
N	V_{res}	M_{res}	σ_{glob}	σ_N	σ_V	σ_M	$0.40\cdot\sigma_N + \sigma_V + \sigma_M + 0.5\cdot k\cdot\sigma_{glob}$	$\sigma_{max,2}$
[N]	[N]	[Nmm]	[N/mm²]	[N/mm²]			[N/mm²]	[N/mm²]
3168	1113	42 668	21	84.3	14.2	66.1	124.5	58.7

For both positions, the extended SLG-method overestimates the maximal tensile stress values found with the calibrated 3D FE-model.

Additionally, the state of failure of the IGU is predicted conservatively if the inequalities (9-1) and (9-2) are fulfilled:

$$\frac{\sigma_N + 0.75\cdot\sigma_V + 0.86\cdot\sigma_M + k\cdot\sigma_{glob}}{\sigma_{\mu,1}} \geq 1 \qquad \textbf{(9-1)}$$

$$\frac{0.40\cdot\sigma_N + \sigma_V + \sigma_M + 0.5\cdot k\cdot\sigma_{glob}}{\sigma_{\mu,2}} \geq 1 \qquad \textbf{(9-2)}$$

In contrast to the verification inequalities, the mean values σ_μ of the breaking stresses are applied in the inequalities (9-1) and (9-2) in order to recalculate the most probable fracture (Table 9.11 and Table 9.12). Hence, no safety factors are considered.

Table 9.11 Verification at position 1, 2. Test

Transfer function			Mean value of breaking stress	Verification
σ_N	σ_V	σ_M	$\sigma_{\mu,1}$	$(\sigma_N + 0.75\cdot\sigma_V + 0.86\cdot\sigma_M + k\cdot\sigma_{glob})/ \sigma_{\mu,1}$
[N/mm²]			[N/mm²]	[-]
84.3	14.2	66.1	128	1.35

Table 9.12 Verification at position 2, 2. Test

Transfer function			Mean value of breaking tension	Verification
σ_N	σ_V	σ_M	$\sigma_{\mu,2}$	$(0.40\cdot\sigma_N + \sigma_V + \cdot\sigma_M + 0.5\cdot k\cdot\sigma_{glob})/ \sigma_{\mu,2}$
[N/mm²]			[N/mm²]	[-]
84.3	14.2	66.1	72	1.73

For position 1 and 2, the inequalities (9-1) respectively (9-2) are fulfilled. The failure stress is overestimated with 73 %.

In conclusion, the extended SLG-method allows a safe design of point fitted IGU with the Fischer undercut anchor for the investigated load case.

9.6.5 3. Test – Verification of extended SLG-method for additional shear

In the third test, it is verified if the SLG-method is able to predict the failure of the connection under consideration of additional shear forces. Therefore the self-weight of the two glass panes of the IGU is applied with steel plates as described in section 8.4 and the wind pressure load on the inner glass pane is increased until failure of the connection Fischer anchor - glass.

The different load steps are resumed in Table 9.13.

Table 9.13 The load case "Self-weight + Winter + Self-weight"

Load case	Objective	Load step	Δp [mbar]	p_{ex} [kN/m²]	g [kg]
Self-weight + Winter (Δp = -15 mbar) + Wind pressure	Failure of FZP-G-Z + Verification of extended SLG-method under consideration of the self-weight	0	0	0	0
		1	0	0	72
		2	-15	0	72
		3	-9.8	1	72
		4	-5.6	2	72
		5	-2.0	3	72
		6	2.8	4	72
		7	11.7	5	72
		8	(16.3)*	7.5	72

*: Determined with the extended climate load model

The failure of the connection is induced by a wind pressure load of 7.5 kN/m^2 applied on the inner glass pane and an overpressure of Δp = 16.3 mbar in the cavity (Figure 9.56). As for the second test, only the inner glass pane breaks and the outer glass pane remains unharmed (Figure 9.57). The pressure difference in the cavity for load step 8 could not be measured. For unknown reasons, the nanometre did not display any values for the last load step. The value in Table 9.13 is therefore calculated with the verified extended climate load model and corresponds to an overpressure of 16.3 mbar.

Figure 9.56 Application of failure load

Figure 9.57 Fracture of inner glass pane

Similar to the second test, the strains along two paths in the borehole area are measured during the test and compared to the values of the 3D FE-model (Figure 9.58).

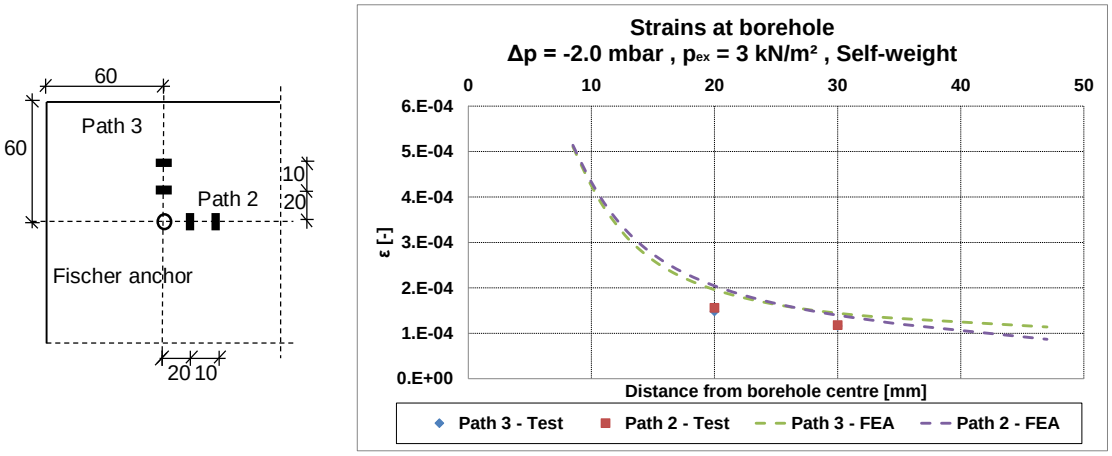

Figure 9.58 Strains along path 2 and path 3 in the borehole area and comparison to the 3D Solid FE-model, 3. Test, Load step 5

The maximal deviation between the numerical and experimental results is about 20 %. The difference results from to the inhomogeneous loading of the inner glass pane with sandbags that cannot be perfectly simulated with the FE-model. Consequently, the

numerical model adequately simulates the strains and stresses in the borehole area under consideration of the self-weight of the insulation glass unit.

More test results and their comparison to the numerical output are shown in annexe D.

For the failure load, the 3D Solid FE-model delivers a maximal tensile stress of $\sigma_{max,1}$ = 113.8 N/mm² at position 1 and a tensile stress of $\sigma_{max,2}$ = 51.9 N/mm² at position 2. The tensile stresses are located at the same positions than in the second test without consideration of the self-weight. Compared to the second test, the maximal tensile stresses are slightly lower (Figure 9.59).

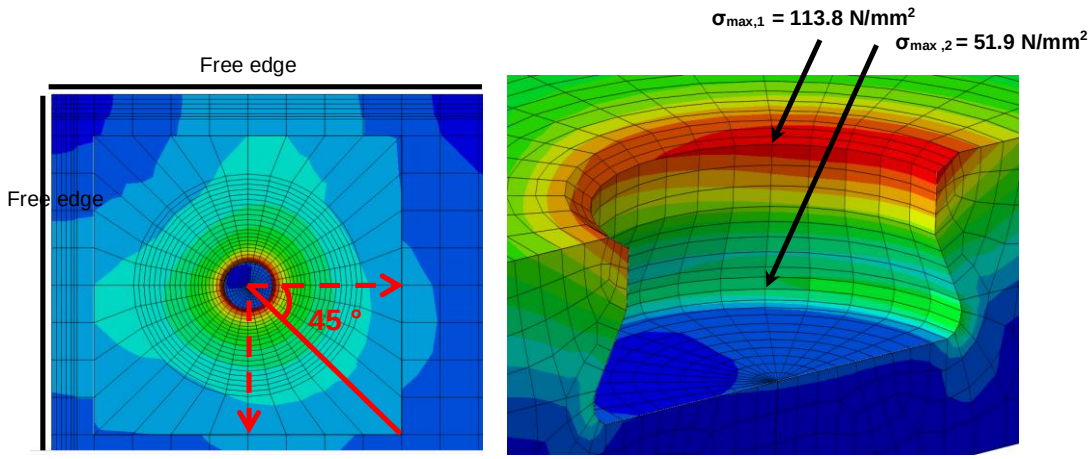

Figure 9.59 Location of the maximal tensile stresses at the borehole in position 1 and position 2, 3. Test

As for the second test, the extended SLG-method is verified according to the procedure described in Figure 9.54.

The maximal tensile stresses are calculated according to the extended SLG-method and compared to the stresses of the 3D FE-model (Table 9.14 and Table 9.15).

Table 9.14 Comparison between the 3D Solid FE-model and the extended SLG-method, Position 1, 3. Test

	2D-Shell			Transfer function			Superposition	3D-Solid
N	V_{res}	M_{res}	σ_{glob}	σ_N	σ_V	σ_M	$\sigma_N + 0.75\cdot\sigma_V + 0.86\cdot\sigma_M + k\cdot\sigma_{glob}$	$\sigma_{max,1}$
[N]	[N]	[Nmm]	[N/mm²]	[N/mm²]			[N/mm²]	[N/mm²]
2882	860	37559.1	22.5	76.7	11	58.2	157.5	113.8

Table 9.15 Comparison between the 3D Solid FE-model and the extended SLG-method, Position 2, 3. Test

	2D-Shell			Transfer function			Superposition	3D-Solid
N	V_{res}	M_{res}	σ_{glob}	σ_N	σ_V	σ_M	$\sigma_N + 0.75\cdot\sigma_V + 0.86\cdot\sigma_M + k\cdot\sigma_{glob}$	$\sigma_{max,2}$
[N]	[N]	[Nmm]	[N/mm²]	[N/mm²]			[N/mm²]	[N/mm²]
2882	860	37559.1	22.5	76.7	11	58.2	111.1	51.9

Moreover, it is verified if the extended SLG-method conservatively predicts the state of failure of the IGU (Table 9.16 and Table 9.17). According to the inequalities (9-1) and (9-2):

Table 9.16 Verification at position 1, 3. Test

Transfer function			Mean value of breaking tension	Verification
σ_N	σ_V	σ_M	$\sigma_{\mu,1}$	$(\sigma_N + 0.75\cdot\sigma_V + 0.86\cdot\sigma_M + k\cdot\sigma_{glob})/ \sigma_{\mu,1}$
[N/mm²]			[N/mm²]	[-]
76.7	11	58.2	128	1.23

Table 9.17 Verification at position 2, 3. Test

Transfer function			Mean value of breaking tension	Verification
σ_N	σ_V	σ_M	$\sigma_{\mu,2}$	$(0.40\cdot\sigma_N + \sigma_V + \cdot\sigma_M + 0.5\cdot k\cdot\sigma_{glob})/ \sigma_{\mu,2}$
[N/mm²]			[N/mm²]	[-]
76.7	11	58.2	72	1.54

The extended SLG-method overestimates the failure stress with 54%. In conclusion, the extended SLG-method conservatively predicts the failure stresses at the borehole and it allows a safe design of the point fitted IGU with the Fischer undercut anchors under consideration of additional shear forces due to the self-weight of the unit.

9.6.6 4. Test – Verification of extended SLG-method for load on outer pane

In the fourth test, a wind suction load is applied on the outer glass pane (Figure 9.25) and it is increased until the connection Fischer anchor – glass fails. In this way, it is checked whether the extended SLG-method safely predicts the failure if the load is transferred via the edge seal system from the outer to the inner glass pane. In parallel, the ability of the FE-models (3D and 2D) to correctly simulate the deformation and stress state of the inner and outer glass pane for this load case is verified. The different load steps are presented in Table 9.18.

Table 9.18 The load case "Winter + Wind suction load on outer glass pane"

Load case	Objective	Load step	Δp [mbar]	p_{ex} [kN/m²]	g [kg]
Winter (Δp = -15 mbar) + Wind suction	Failure of FZP-G-Z + Verification of extended SLG-method	0	0	0.0	0
		1	-15	0.0	0
		2	-18	0.3	0
		3	-27.2	1.3	0
		4	-37.6	2.3	0
		5	-46.9	3.3	0
		6	-56	4.3	0
		7	-66.5	5.7	0

The failure of the connection occurs at a wind suction load of p_{ex} = 5.7 kN/m^2 and an underpressure of Δp = -66.5 mbar in the cavity (Figure 9.60). Only the inner glass pane breaks due to the failure of the connection point fitting - glass and the outer pane remains undamaged (Figure 9.61).

Figure 9.60 Application of wind suction load

Figure 9.61 Glass fracture of inner pane

It is important to notice the four local load introduction of the wind suction load (Figure 9.10). Since the extended climate load model is only valid for surface loads, it cannot be applied to determine the resulting surface loads in this specific case. In the 3D Solid FE-model, the wind suction loads and the pressure difference in the cavity are locally applied (Figure 9.62) respectively applied as surface loads on the inner and outer glass pane (Figure 9.63) in consequence.

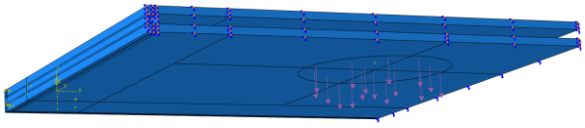

Figure 9.62 Local introduction of wind loads

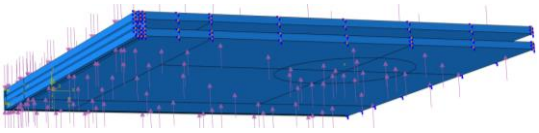

Figure 9.63 Pressure difference in the cavity

In Figure 9.64, the measured deformations in the mid-span of the glass panes are compared to the numerical values delivered by the 3D Solid FE-model.

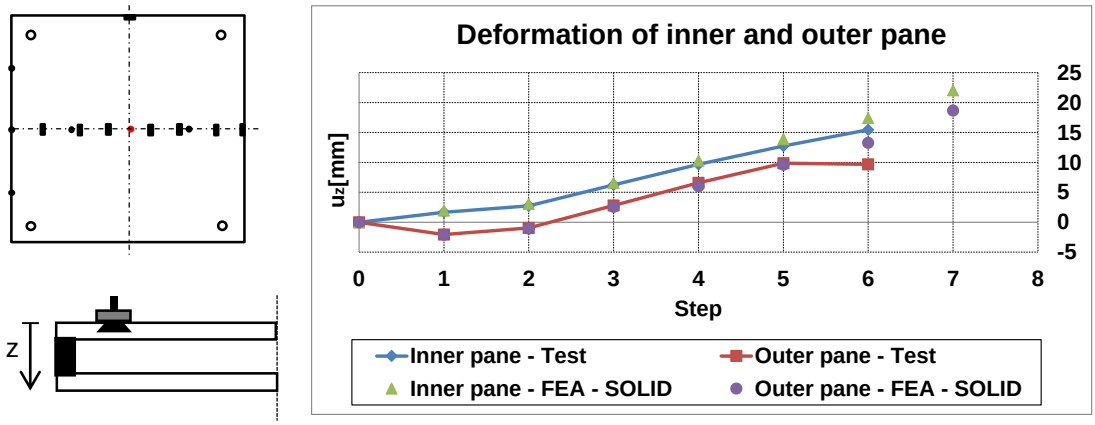

Figure 9.64 Deformations of the inner and outer glass pane and comparison to the 3D Solid FE-model, 4. Test,

An excellent accordance between the results is observed. The deviation is less than 5%. From up load step 6, a comparison between the measured deformations in the test and the numerical deformations is no longer possible, because the displacement sensors have been removed for security reasons.

Concerning the strains at a distance of 20 mm from the centre of the glass panes, a good correspondence between the test and the FE data is observed for the outer glass pane (Figure 9.65). The maximal deviation is 13%. For the inner glass pane, the deviations are getting higher with higher loading and reach a maximum of about 70 %. It is assumed that the corresponding strain gauge did not work properly during the test.

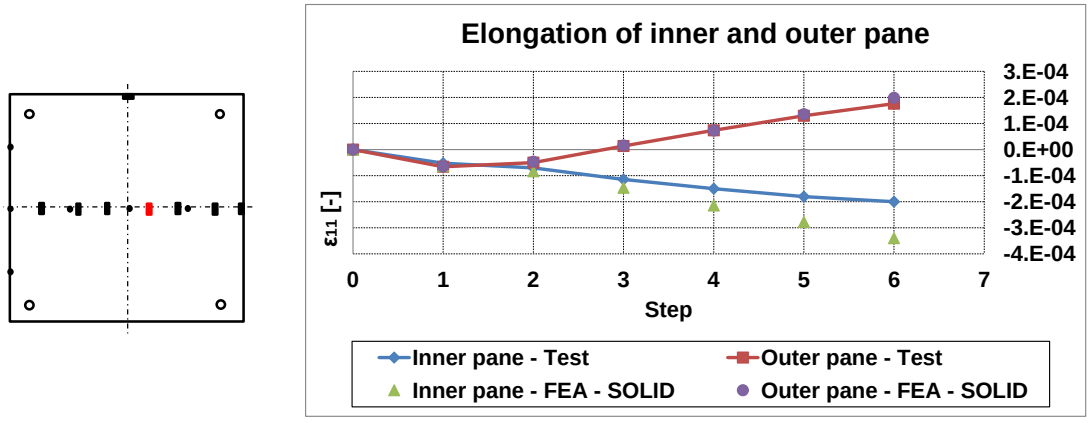

Figure 9.65 Strains of the inner and outer glass pane and comparison to the 3D Solid FE-model, 4. Test

The measured and calculated strains along the different paths defined in the borehole area are presented in Figure 9.66.

A good correspondence is observed. The maximal deviation is about 18%.

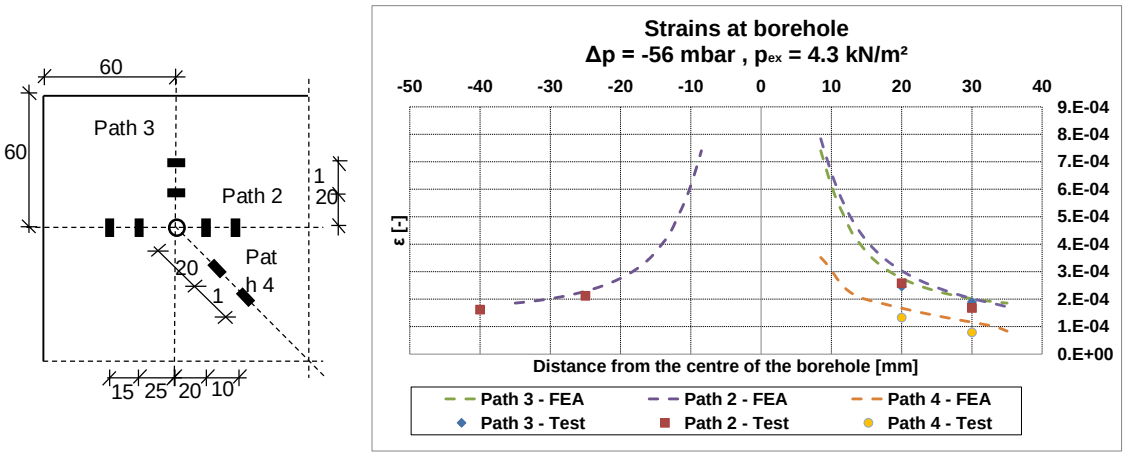

Figure 9.66 Strains along path 2, path 3 and path 4 in the borehole area and comparison to the 3D Solid FE-model, 4. Test, Load step 6

Further comparisons between the test and the FE - results are indicated in annexe D. The comparisons proof the ability of the numerical models to accurately simulate the deformation and stress state in the inner and outer glass pane when the load is introduced on the outer glass pane.

For the failure load, the maximal tensile stresses of $\sigma_{max,1}$ = 107.4 N/mm² and $\sigma_{max,2}$ = 52.8 N/mm² are found by the 3D Solid FE-model for the position 1 respectively the position 2 (Figure 9.67).

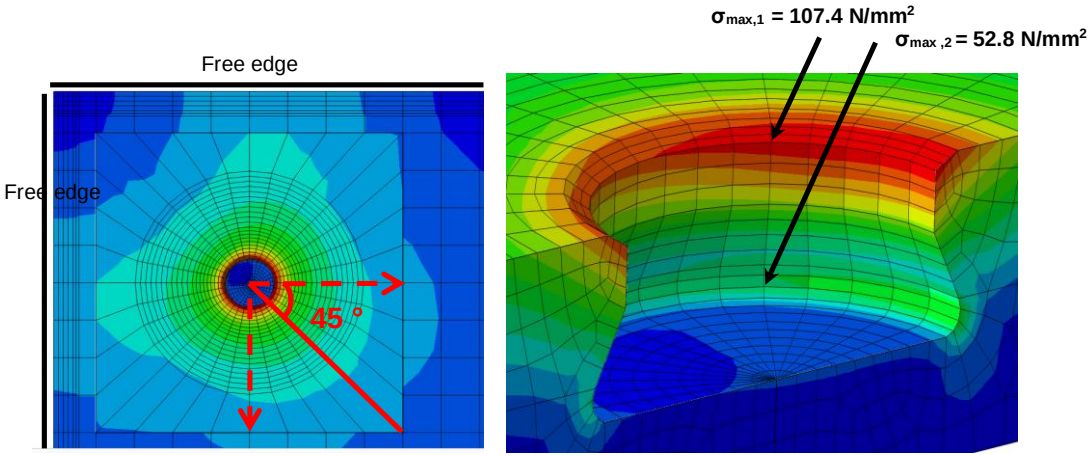

Figure 9.67 Location of the maximal tensile stresses at the borehole in position 1 and position 2, 4. Test

As for the second and third test, the failure stresses are determined in the two positions 1 and 2 and compared to the stress values found with the 3D Solid FE-model (Table 9.19 and Table 9.20).

Table 9.19 Comparison between the 3D Solid FE-model and the extended SLG-method, Position 1, 4. Test

	2D-Shell			Transfer function			Superposition	3D-Solid
N	V_{res}	M_{res}	σ_{glob}	σ_N	σ_V	σ_M	$\sigma_N + 0.75\cdot\sigma_V + 0.86\cdot\sigma_M + k\cdot\sigma_{glob}$	$\sigma_{max,1}$
[N]	[N]	[Nmm]	[N/mm²]	[N/mm²]			[N/mm²]	[N/mm²]
2516	1073	41217	19.3	66.9	13.7	63.8	151.3	107.4

Table 9.20 Comparison between the 3D Solid FE-model and the extended SLG-method, Position 2, 4. Test

	2D-Shell			Transfer function			Superposition	3D-Solid
N	V_{res}	M_{res}	σ_{glob}	σ_N	σ_V	σ_M	$0.40\cdot\sigma_N + \sigma_V + \sigma_M + 0.5\cdot k\cdot\sigma_{glob}$	$\sigma_{max,2}$
[N]	[N]	[Nmm]	[N/mm²]	[N/mm²]			[N/mm²]	[N/mm²]
2516	1073	41217	19.3	66.9	13.7	63.8	113.9	52.8

In both cases, the extended SLG-method overestimates the failure stresses which are determined with the numerical model.

Additionally, the state of failure is predicted by the extended SLG-method with help of the inequalities (9-1) and (9-2) (Table 9.21 and Table 9.22).

Table 9.21 Verification at position 1, 4. Test

Transfer function			Mean value of breaking tension	Superposition
σ_N	σ_V	σ_M	$\sigma_{\mu,1}$	$(\sigma_N + 0.75\cdot\sigma_V + 0.86\cdot\sigma_M + k\cdot\sigma_{glob})/\ \sigma_{\mu,1}$
[N/mm²]			[N/mm²]	[-]
66.9	13.7	63.8	128	1.18

Table 9.22 Verification at position 2, 4. Test

Transfer function			Mean value of breaking tension	Superposition
σ_N	σ_V	σ_M	$\sigma_{\mu,2}$	$(0.40\cdot\sigma_N + \sigma_V + \cdot\sigma_M + 0.5\cdot k\cdot\sigma_{glob})/\ \sigma_{\mu,2}$
[N/mm²]			[N/mm²]	[-]
66.9	13.7	63.8	72	1.58

The extended SLG-method conservatively predicts the failure of the connection Fischer anchor - glass. The failure stress is overestimated by 58%.

In conclusion, the extended SLG-method permits a safe design of point fitted IGU with the Fischer undercut anchor under consideration of wind suction loads acting on the outer glass pane.

9.7 Summary and conclusion

Large scale tests are conducted on four samples of the proposed insulation glass unit with the Fischer undercut anchors.

In the first test, three different objectives are pursued:

First of all, the simple 2D FE-model and the 3D Solid FE-model of the point fitted IGU are verified by the numerical simulation of the test for the load cases “Winter” and “Summer”. A good accordance between the numerically results and the corresponding test data for the different load steps and along the defined paths for given load step proofs the accuracy of both numerical models. Consequently, the two FE-models are experimentally verified.

Secondly, the extended climate load model developed in chapter 6 is experimentally verified. For an underpressure in the glazing cavity corresponding to the climate load “Winter” in (DIN 18008-2) and a wind pressure load of 3 kN/m^2 acting on the outer glass pane, the deformations and strains of the glass panes as well as the pressure difference in the cavity are measured during the test. The corresponding resulting surface loads are determined with the extended climate load model and applied on the inner and outer glass pane in the verified 3D and 2D FE-models of the IGU. The deformations and strains are calculated with the numerical model and compared to the experimental values. Additionally, the pressure difference in the cavity is determined with the extended climate load model and compared to measured difference in the test. The values for the pressure difference perfectly matches with a deviation of less than 8% and a good correspondence between the numerical and experimental deformations and strains is observed. In consequence, the extended climate load model delivers the accurate resulting surface loads and pressure difference that correspond to given climate conditions. In consequence, the extended climate load model is experimentally verified.

Finally, the ability of the numerical model to predict the failure in the edge bond is checked. An overpressure is installed in the glazing cavity and increased until a failure in the edge bond system occurs. A cohesive failure (rupture) of the secondary silicone sealant is induced for an overpressure of 160 mbar at the edge of the IGU. The rupture extends over a length corresponding to the distance between two adjacent point fittings. The numerical model underestimates the failure stress in the silicone that is found in (Dias, 2013). Two different reasons can be given: on one hand, the stress peaks occurring in the numerical model do not allow to accurately determine the real failure stress. On the other hand, the failure stress found in the tension test in (Dias, 2013) is based on pure tension, while a complex 3D stress state acts in the silicone of the large scale tests. A direct comparison is hence not accurate. In conclusion, a failure criterion for silicone is currently missing and the calibrated numerical model does not allow the failure prediction in the edge seal system.

In the other three tests, the extended SLG-method developed in chapter 8 is experimentally verified for different load cases occurring in practice. These load cases include a wind pressure load on the inner glass pane, a wind suction load on the outer glass pane with an underpressure in the cavity as well as the self-weight of the IGU. It is shown, that the method conservatively predicts the failure in the connection Fischer anchor – glass for each load case. For the studied load cases, the extended SLG-method overestimates the failure stress in a range of 54% - 73%. Consequently, the extended SLG-method allows a safe design of the point fitted IGU with the Fischer undercut anchor.

In conclusion, the complex 3D Solid FE-model of the point fitted IGU, which is used for the extension of the SLG-method, is verified. It precisely simulates the stress state in the borehole area as well as the deformations and stresses of the outer and inner glass pane. The simple 2D FE-model is also verified with the test data. It delivers the same results than the 3D model and consequently it can be used for the design of the point fitted IGU with the Fischer undercut anchors. Furthermore the good correspondence between the numerical simulations and the tests proof that the primary sealant PIB does not influence the global behaviour of the IGU. In addition, the extended climate load model is experimentally verified and it is shown that the extended SLG-method safely predicts the failure in the connection Fischer anchor – glass for common loads in practice. Finally, the extended climate load model and the extended SLG-method are adequate for the design of point fitted IGU with the Fischer undercut anchors.

10 The general design concept of point fitted IGU with undercut anchor

A novel design concept for point fitted IGU with undercut anchors is proposed in section 4.5. In this chapter, the application procedure of the concept for the point fitted IGU is presented in form of a flow-chart. The verification steps for the different components of the point fitted IGU are highlighted with the corresponding inequalities and/or standards.

This research work was synthesised during a transition period between the technical rules ((TRV-2006), (TRAV, 2003), (TRPV, 2006)) and the standard (DIN 18008), which has taken place in Germany. This change implies the conversion of the deterministic global to the partial safety concept. However, the transition phase has not been completely accomplished yet. For instance, the actions on a point fitted IGU and the glass resistance values in the undisturbed areas of the glass panes can be currently determined with the semi-probabilistic approach according to (DIN 1055) respectively (DIN 18008). The general technical approvals of the different point fitting types though are still based on the global safety concept and so do the approval of the Fischer undercut anchor (Z-70.2-122) (SLG-method). In addition, (DIN 18008-3) does not regulate undercut point fitting systems and the designing engineer has to base on the general technical approvals for the design of the undercut anchors. This situation raises the question which concept to use for the design of the point fitted IGU with undercut anchors. To assure a design which is continuously based on the same safety concept, it is proposed to apply the novel design concept according to the global safety concept. The concept is summarized in Figure 10.1.

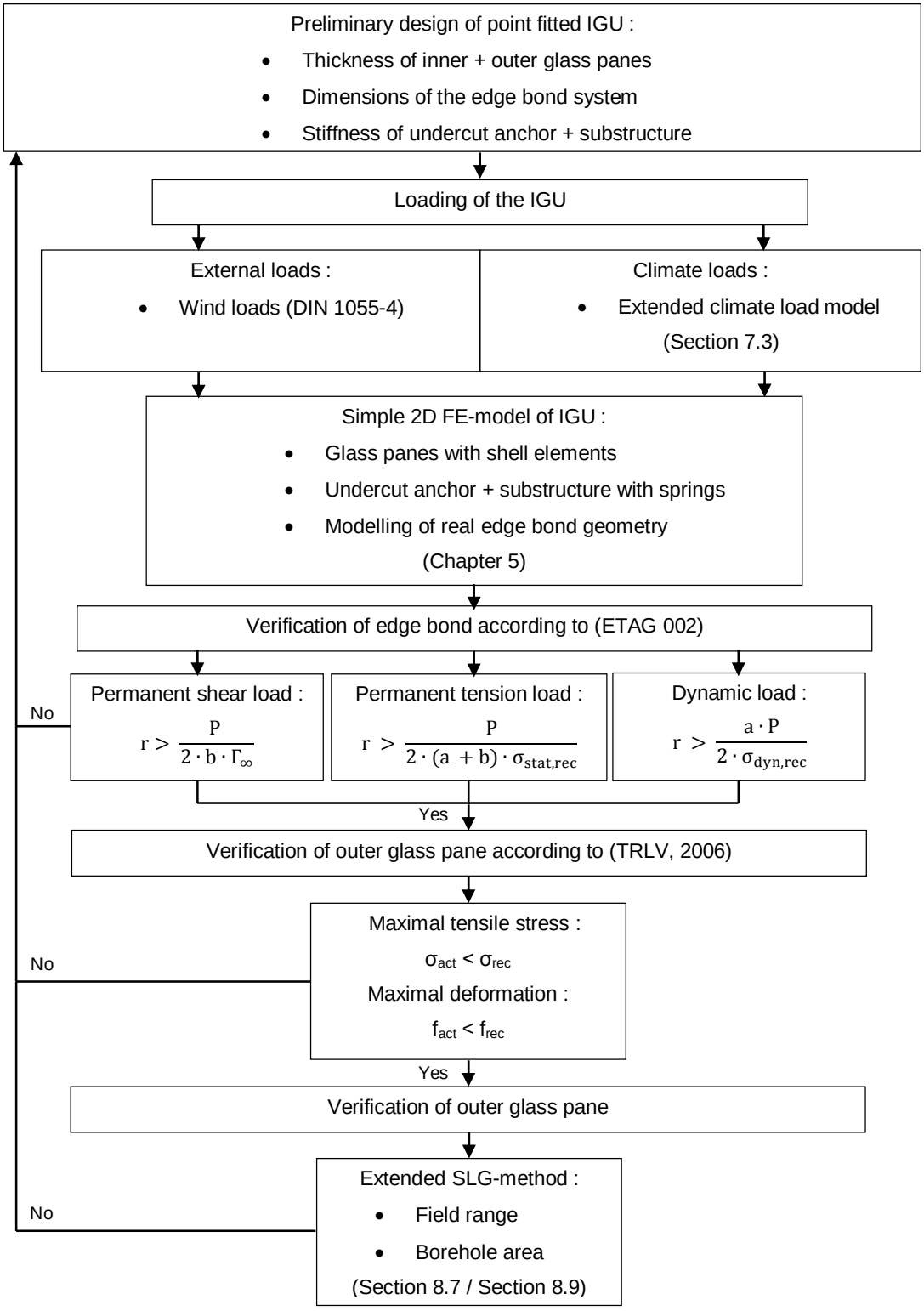

Figure 10.1 The application procedure of the novel design concept proposed in this research work

An example with this design concept is carried out in annexe E.

11 Summary, conclusion and recommendations

11.1 Summary

A summary with the main outputs are shown in Figure 11.1:

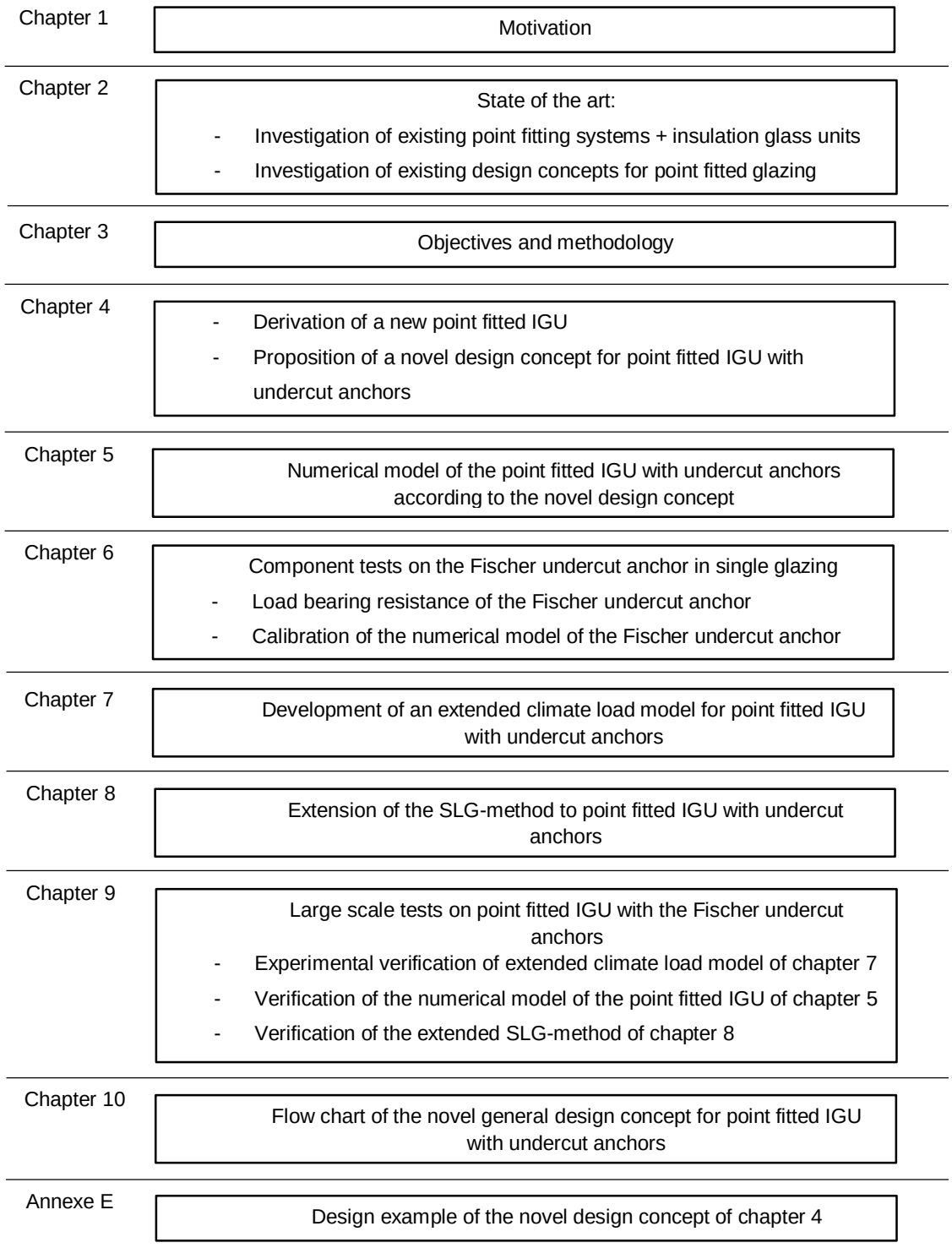

Figure 11.1 The summary and the main outputs

11.2 Recommendations

In future research, the following optimisations of the unit and the design concept are recommended:

1. Laminated glazing for the inner and/or outer glass pane

In laminated glazing, the fitting is anchored in the second ply and its ultimate load bearing resistance is higher than in monolithic glass (Z-70.2-122). In addition, the glass fragments are retained by the interlayer in case of glass failure and do not fall off the façade with the risk to cause serious injuries. The application of the Fischer anchor in laminated glazing requires the investigation of the time dependent behaviour of the interlayers in order to define an additional factor, which considers the degree of the shear coupling between both plies for the different loadings and the corresponding loading rates. The derived factor will enter in the adaption procedure of the key parameters of the SLG-method. The investigation implicates further tests on different interlayer materials and an appropriate interlayer material will have to be chosen.

2. Determination of spring stiffness values for the dual-sealed edge system

In future, component test will be conducted on common edge bond geometries in order to define their translational and rotational stiffness values. The tests include tension, compression, shear and moment tests. The test will be conducted with different loading rates to investigate the change in the stiffness of the edge bond system. Additionally, the tests will be repeated with artificial aged test samples with the goal to consider the stiffness changes of the edge bond system under climate conditions. In this way, it will be possible to replace the edge bond systems in the simple 2D FE-model as described in chapter 5 with springs. In addition, the component tests will allow the formulation of a SLS criterion, i.e. permissible values for the maximal deformations and rotations of the edge bond under traction and shear respectively moment loads for a whole range of common edge bond geometries. For the verification in the SLS, the maximal deformations and rotations of the edge bond will be numerically determined in form of the deformations and rotations in the springs and compared to the permissible values.

3. Formulation of a failure criterion for silicone – Design of edge bond

It will be necessary to investigate the origins of the stress peaks in the silicone sealant with the aim to find an answer to the question if the peaks are real or if they are a numerical singularity. In addition, a general failure criterion for silicone materials will have to be formulated. An ongoing research work at the University of Luxembourg deals with this problematic (Staudt, 2014). Finally, the formulation of a failure criterion will allow the

definition of an ULS criterion for the edge bond, i.e. permissible values for the maximal tensile, shear and/or moment loads in the sealant system. For the verification in the ULS, the maximal forces and moments of the edge bond will be numerically determined in form of the loads in the springs and compared to the permissible values. As a result, the SLS and ULS criterions will allow a more optimized design of the edge seal system than the verification according to [ETAG-002].

4. Verification of the tightness of the edge seal system

The large scale tests in chapter 9 will have to be repeated under long-term loading in order to investigate the tightness of the chosen edge bond system. The large scale tests should be done in combination with the tests described in (DIN EN 1279) on order to proof the tightness of the edge bond system during its service life.

5. Fatigue of the Fischer undercut anchor and the edge bond system

The wind and climate loads subject the IGU to cyclic loading and the fatigue needs to be considered. Thus, the quasi-static component tests conducted on the Fischer undercut anchor in single glazing will have to be repeated under cycling loading in order to define the *Wöhler* – curves for Fischer anchor in glass. Additionally, the fatigue behaviour of the stainless steel thread of the anchor has to be analysed. The continuous and discontinuous damage (*Mullin's* effect) of the silicone sealant is already included in the material law of *Dias* (Dias, 2013). The fatigue behaviour of the overall edge bond system is however unknown. Cyclic component tests (tension, shear and moments) will have to be conducted on common edge bond systems in order to determine their *Wöhler* – curves.

6. Investigation of the load bearing behaviour of the IGU under temperature

The large scale tests described in chapter 9 will have to be repeated with the application of different temperatures on the inner and outer glass pane. It is proposed to conduct the test in a climate chamber with the possibility to uniformly regulate the heating and cooling.

7. Development of a mechanical retaining system for the IGU

A failure of the inner glass pane or in the edge bond leads to the falling off the façade of the overall IGU respectively of the outer glass pane. In both cases, the risk of serious injuries is given and in consequence, the IGU has to be mechanically retained in case of failure. Therefore a corresponding mechanically device will have to be developed.

12 References

Albrecht, N. (2004). *Lastabtragungsmechanismus im Lochbereich punktgestützter Glastafeln* (Doctoral dissertation). Universität Fridericiana zu Karlsruhe, Germany.

Besserud, K., Mazurek, A., Carbary, L.D., Rubis, K., Black, A.J., Misson, D., & Bergers, M. (2012). Durability of Cold-Bent Insulating Glass Units. In F. Bos, C. Louter & F. Veer (Eds.), *Challenging Glass 3-Conference on Architectural and Structural Applications of Glass* (pp. 785-817). Delft, The Netherlands: IOS Press.

Beyer, J. (2007). *Ein Beitrag zum Bemessungskonzept für punktgestützte Glastafeln* (Doctoral dissertation). Technische Universität Darmstadt, Germany.

Beyer, J. (2009). Glass design using the SLG-method. Retrieved from http://www.glassfiles.com/articles/glass-design-using-slg-method

Bostik. (2008). *V-70 : High strength structural glazing silicone adhesive sealant* (Technical data sheet). Retrieved from http://www.hoganswholesale.com.au/files/Bostik-V70-TDS.pdf

Brendler, S., & Schneider, S. (2004). Bemessung von punktgelagerten Verglasungen mit verifizierten Finite-Elemente-Modellen, *DIBt-Mitteilungen*, *35(6)*, 196-203.

Bucak, Ö. (1999). Glas im konstruktiven Ingenieurbau, *Stahlbaukalender 1999*, 515.

Bundesministerium für Umwelt, Naturschutz und Reaktorsicherheit (BMU). (2009). *EnEV 2009 : Verordnung über energiesparenden Wärmeschutz und energiesparende Anlagentechnik bei Gebäuden*. Retrieved from http://www.enev-online.org/enev_2009_volltext/index.htm

Cruz, P.J.S., Carvalho P.L., Silva, E., & Rocha, P. (2014). Embedded point fittings in laminated and double insulating units. In C. Louter, F. Bos, J. Belis & J.-P. Lebet (Eds.), *Challenging Glass 4 & COST Action TU0905 Final Conference* (pp. 331-338). Lausanne, Switzerland: Taylor & Francis Group.

Dias, V. (2013). *Development of adhesives constitutive material laws for the assessment of bonded steel to glass partial composite beams* (Doctoral dissertation). University of Luxembourg, Luxembourg.

Deutsches Institut für Bautechnik. (2003). *TRAV : Technische Regeln für die Verwendung von absturzsichernden Verglasungen* (TRAV). Berlin, Germany: DiBt.

Deutsches Institut für Bautechnik. (2006). *TRLV : Technische Regeln für die Verwendung von linienförmig gelagerten Verglasungen* (TRLV). Berlin, Germany: DiBt.

Deutsches Institut für Bautechnik. (2006). *TRPV : Technische Regeln für die Bemessung und Ausführung punktförmig gelagerter Verglasungen* (TRPV). Berlin, Germany: DiBt.

Deutsches Institut für Bautechnik. (2004). *Z-70.2-99 : Punktgehaltene Verglasungen mit Glasslinie-Tellerhaltern : Allgemeine bauaufsichtliche Zulassung (Z-70.2-99)*. Berlin, Germany: DiBt.

Deutsches Institut für Bautechnik. (2007). *Z-70.2-122 : Punktgehaltene Verglasung mit fischer Zykon Punkthaltern : Allgemeine bauaufsichtliche Zulassung (FZP-G-Z)* (Z-70.2-122). Berlin, Germany: DiBt.

Deutsches Institut für Normung. (2005). *DIN EN 1055 : Einwirkungen auf Tragwerke* (DIN EN 1055). Berlin, Germany: Beuth Verlag.

Deutsches Institut für Normung. (2005). *DIN EN 1055-4 : Einwirkungen auf Tragwerke - Teil 4 : Windlasten* (DIN EN 1055-4). Berlin, Germany: Beuth Verlag.

Deutsches Institut für Normung. (2001). *DIN EN 1055-100 : Einwirkungen auf Tragwerke - Teil 100 : Grundlagen der Tragwerksplanung, Sicherheitskonzept und Bemessungsregeln* (DIN EN 1055-100). Berlin, Germany: Beuth Verlag.

Deutsches Institut für Normung. (2010). *DIN 1249-10 : Flachglas im Bauwesen – Teil 10 : Chemische und physikalische Eigenschaften* (DIN 1249-10). Berlin, Germany: Beuth Verlag.

Deutsches Institut für Normung. (2004). *DIN EN 1279 : Glas im Bauwesen – Mehrscheiben-Isolierglas* (DIN EN 1279). Berlin, Germany: Beuth Verlag.

Deutsches Institut für Normung. (2004). *DIN EN 1279-1 : Glas im Bauwesen – Mehrscheiben-Isolierglas - Teil 1 : Allgemeines, Masstoleranzen und Vorschriften für die Systembeschreibung* (DIN EN 1279-1). Berlin, Germany: Beuth Verlag.

Deutsches Institut für Normung. (2004). *DIN EN 1279-2 : Glas im Bauwesen – Mehrscheiben-Isolierglas - Teil 2 : Langzeitprüfverfahren und Anforderungen bezüglich Feuchtigkeitsaufnahme* (DIN EN 1279-2). Berlin, Germany: Beuth Verlag.

Deutsches Institut für Normung. (2004*). DIN EN 1279-3 : Glas im Bauwesen – Mehrscheiben-Isolierglas - Teil 3 : Langzeitprüfverfahren und Anforderungen bezüglich Gasverlustrate und Grenzabweichungen für die Gaskonzentration* (DIN EN 1279-3). Berlin, Germany: Beuth Verlag.

Deutsches Institut für Normung. (2004). *DIN EN 1279-4 : Glas im Bauwesen – Mehrscheiben-Isolierglas - Teil 4 : Verfahren zur Prüfung der physikalischen Eigenschaften des Randverbundes* (DIN EN 1279-4). Berlin, Germany: Beuth Verlag.

Deutsches Institut für Normung. (1994). *DIN 1286-1 : Multiple pane insulating glass - Part 1 : Air filled insulating glass units, Long term performance* (DIN 1286-1). Berlin, Germany, Beuth Verlag.

Deutsches Institut für Normung. (2000). *DIN EN 1288-5 : Glas im Bauwesen - Bestimmung der Biegefestigkeit von Glas - Teil 5 : Doppelring-Biegeversuch an plattenförmigen Proben mit kleinen Prüfflächen* (DIN EN 1288-5). Berlin, Germany: Beuth Verlag.

Deutsches Institut für Normung. (2000). *DIN EN 1288-3 : Glas im Bauwesen - Bestimmung der Biegefestigkeit von Glas - Teil 3 : Prüfung von Proben bei zweiseitiger Auflagerung (Vierschneiden-Versuch)* (DIN EN 1288-3). Berlin, Germany: Beuth Verlag.

Deutsches Institut für Normung. (2011). *DIN EN 1863 : Glas im Bauwesen - Teilvorgespanntes Kalknatronglas* (DIN EN 1863). Berlin, Germany: Beuth Verlag.

Deutsches Institut für Normung. (2002). *DIN EN 1990 : Grundlagen der Tragwerksplanung* (DIN EN 1990). Berlin, Germany: Beuth Verlag.

Deutsches Institut für Normung. (2005). *DIN EN 1991-4 : Einwirkung auf Tragwerke - Teil 4: Allgemeine Einwirkungen, Windlasten* (DIN EN 1991-4). Berlin, Germany: Beuth Verlag.

Deutsches Institut für Normung. (2010). *DIN 18008 : Glas im Bauwesen - Bemessungs- und Konstruktionsregeln* (DIN 18008). Berlin, Germany: Beuth Verlag.

Deutsches Institut für Normung. (2010). *DIN 18008-1 : Glas im Bauwesen - Bemessungs- und Konstruktionsregeln - Teil 1: Begriffe und allgemeine Grundlagen* (DIN 18008-1). Berlin, Germany: Beuth Verlag.

Deutsches Institut für Normung. (2010*). DIN 18008-2 : Glas im Bauwesen - Bemessungs- und Konstruktionsregeln - Teil 2: Linienförmig gelagerte Verglasungen* (DIN 18008-2). Berlin, Germany: Beuth Verlag.

Deutsches Institut für Normung. (2013). *DIN 18008-3 : Glas im Bauwesen - Bemessungs- und Konstruktionsregeln - Teil 3: Punktförmig gelagerte Verglasungen* (DIN 18008-3). Berlin, Germany: Beuth Verlag.

Deutsches Institut für Normung. (2013). *DIN 18008-4 : Glas im Bauwesen - Bemessungs- und Konstruktionsregeln - Teil 4: Zusatzanforderungen an absturzsichernde Verglasungen* (DIN 18008-4). Berlin, Germany: Beuth Verlag.

Dow Corning. (2004). *Qualitätshandbuch für Isolierglas - Leitfaden für die Verwendung von Silicondichtstoffen bei der Isolierglasfertigung*. Wiesbaden, Germany: Dow Corning GmbH.

European Organisation for Technical Approvals (EOTA). (2012). *ETAG 002 : Structural Sealant Glazing Kits (SSGK)* (ETAG 002). Retrieved from http://ec.europa.eu/enterprise/policies/innovation/policy/lead-market-initiative/files/construction_taskforce_report_en.pdf

Feldmeier, F. (2006). Klimabelastung und Lastverteilung bei Mehrscheiben-Isolierglas. *Stahlbau*, *75(6)*, 467-478.

Fischer. (2006). *A|C|T Advanced Curtain wall Technique : FZP-G-Z point fixing for glass* (Handbook). Waldachtal, Germany: Fischerwerke.

Froli, M., & Leonardo, L. (2012). The Influence of Parameter Setting on the Mechanical Properties of PVB in Lamination Processes. In F. Bos, C. Louter & F. Veer (Eds.), *Challenging Glass 3-Conference on Architectural and Structural Applications of Glass* (pp. 669-678). Delft, The Netherlands: IOS Press.

Hechler O., Dias V., Tibolt M., Odenbreit C, & Zillian A. (2012). Design concept for point fitting of insulation glass units. In *Proceedings of VI International Congress on Architectural Envelopes (ICAE)*. San Sebastian, Spain.

Kasper, R. (2006). Berechnungskonzept für die Bemessung von punktförmig gelagerten Glasscheiben. *Stahlbau*, *75(6)*, 454-461.

Kühlmeyer, M. (2001). *Statistische Auswertungsmethoden für Ingenieure*. Berlin, Germany: Springer-Verlag.

O'Hara, G.P. (1983). *Mechanical Properties of Silicone Rubber in a Closed Volume* (Report ARLCB-TR-83045, SBI-AD-E440224). Large Caliber Weapon Systems Laboratory, Army Armament Research and Development Center.

Panait, A., Cossavella, M., Delsahut, G., Galéa, J-L., & Morcant, K. (2007). Insulating glass units : the effects of seal stresses and deformations on durability and service life. In *Proceedings of Glass Performance Days*. Tampere, Finland.

Raecke, I. *Flächentragwerke I/II – Elastische Platten* (Vorlesungsmanuskript). Magdeburg, Deutschland: Otto-von-Guericke-Universität Magdeburg

Schaller, G. (2013). Schnittgrößenermittlung und Bemessung von Isolierverglasungen. *Bautechnik*, *90(10)*, 441-446.

Schäfer, M. (2002). *Darstellung hochmolekularer und verzweigter Polyisobutene durch Einsatz von Makroinitiatoren, cyclischen Dienen und Initiatormonomeren* (Doctoral dissertation). Technische Universität München, Germany.

Schneider, J. (2001). *Festigkeit und Bemessung punktgelagerter Gläser und stoßbeanspruchter Gläser* (Doctoral dissertation). Technische Universität Darmstadt, Germany

Serafinavicius, T., Lebet, J-P., Louter, C., Kuranovas, A., & Lenkimas, T. (2014). The effects of environmental impacts on durability of laminated glass plates with interlayers (SG, EVA, PVB). In C. Louter, F. Bos, J. Belis & J.-P. Lebet (Eds.), *Challenging Glass 4 & COST Action TU0905 Final Conference* (pp. 199-208). Lausanne, Switzerland: Taylor & Francis Group.

Siebert, B. (2004). *Beitrag zur Berechnung punktgestützter Gläser* (Doctoral dissertation). Technische Universität München, Germany.

Siebert, B. (2006). Anforderungen für ein Berechnungskonzept für die Bemessung punktgelagerter Verglasungen. *Stahlbau*, *75(8)*, 652-657.

Sika. *Sikasil® SG-20 : High strength structural silicone sealant* (Product data sheet). Retrieved from **Error! Hyperlink reference not valid.**

Staudt, Y., Schneider, J., & Odenbreit, C. (2014). Investigation of the material behaviour of bonded connections with silicone. In J. Schneider & B. Weller (Eds.), *Engineered transparency, International conference at Glasstec* (pp. 393-402). Düsseldorf, Germany: Technische Universität Darmstadt & Technische Universität Dresden.

Tibolt, M., Hechler, O., & Odenbreit, C. (2014). Analytical extension of a climate load model for undercut point fitted IGU. In C. Louter, F. Bos, J. Belis & J.-P. Lebet (Eds.), *Challenging Glass 4 & COST Action TU0905 Final Conference* (pp. 199-208). Lausanne, Switzerland: Taylor & Francis Group.

Wellershoff, F., & Sedlacek G. (2005). Glued Connections for New Steel Glass Structures. In *Proceedings of Glass Processing Days (Proc. Intern. Syp.)*. Tampere, Finland: Eas Print Oy.

Wolf, A.T. (2005). Silicone Sealed Insulating Glass Units. *In Proceedings of International symposium on the Application of Architectural Glass (ISAAG) 2004*, 2005.

Wurm, J. (2007). *Glass Structures : Design and construction of self-supporting skins*. Basel, Switzerland: Birkhäuser Verlag.

Young, W.C. (1989). *Roark's Formulars for Stress and Strain* (6th ed.). Singapore: McGraw Hill.

Nomenclature

Greek letters

σ_{max}	[N/mm^2]	Maximum tensile stress
σ_{Fz}	[N/mm^2]	Maximum tensile stress associated to F_z
σ_{Fxy}	[N/mm^2]	Maximum tensile stress associated to F_{xy}
σ_{Mxy}	[N/mm^2]	Maximum tensile stress associated to M_{xy}
σ_{glob}	[N/mm^2]	Global component of maximum tensile stress
σ_{vorh}	[N/mm^2]	Acting maximal tensile stress
σ_{zul}	[N/mm^2]	Permissible tensile stress
Γ_{∞}	[N/mm^2]	Permissible shear stress under permanent load
$\sigma_{stat,rec}$	[N/mm^2]	Permissible static tension stress under permanent load
$\sigma_{dyn,rec}$	[N/mm^2]	Permissible dynamic tension stress under dynamic load
ϑ	[m^3/(kN/m^2)]	Volume coefficient
φ	[-]	Insulation glass factor for linearly supported IGU
α	[-]	Relative volume change of the external pane
α^+	[-]	Relative volume change of the internal pane
δ_0^P	[mm]	Mean deflection of glass pane under the load p
α_0	[-]	Correction value
α_1	[-]	Correction value
α_3	[-]	Correction value
$\max\delta^P$	[mm]	Maximal deflection of glass pane under the load p
δ_1	[mm]	Total mean deflection
δ_1^1	[m/(kN/m^2)]	Mean deflection of the outer glass pane under unit load 1
δ_1^2	[m/(kN/m^2)]]	Elongation or contraction of the cavity under unit load 1 kN/m^2
δ_1^3	[m/(kN/m^2)]]	Mean deflection of the inner glass pane under unit load 1
$\max\delta^1$	[mm]	Maximal deflection of the outer glass pane under unit load

$\max\delta^3$	[mm]	Maximal deflection of the inner glass pane under unit load
σ_V	[N/mm^2]	Thermal prestress at the surface of the glass pane
μ	[-]	Mean value of the log-normal distribution
σ	[-]	Standard deviation of the log-normal distribution
γ_R	[-]	Partial safety factor for the connection “FZP-G-Z – Glass”
γ_S	[-]	Partial safety factor for the loading
γ^*	[-]	Global safety factor for the connection “FZP-G-Z – Glass”
α_R	[-]	Sensivity factor
β	[-]	Reliability index
$\nu_{i,k}$	[m^3/(kN/m^2)]	The enclosed volume of pane i due to a pressure “1” on pane k
$\nu_{pe,i,k}$	[m^3/(kN/m^2)]	The enclosed volume of pane i due to an external surface load “1” on pane k
$\varphi_{i,k}$	[-]	Insulation glass factor for point fitted IGU with undercut anchors
ΔV	[mm^3]	Volume difference of the cavity
ΔT	[K]	Temperature difference in the cavity
Δp_{met}	[N/mm^2]	Barometric pressure difference
ΔH	[m]	Height difference
$\Delta p_{c,1}$	[N/mm^2]	Pressure difference in cavity i due to the climatic changes
$Ø_{Borehole}$	[mm]	Diameter of the borehole
ν	[-]	Poisson’s ratio
$\sigma_{Field,zul}$	[N/mm^2]	Permissible tensile stress in the field range of the glass pane
$\sigma_{Field,act}$	[N/mm^2]	Acting tensile stress in the field range of the glass pane
$\sigma_{N,max}$	[N/mm^2]	Maximum tensile stress peak at the borehole due to a tension load in the undercut anchor
$\sigma_{V,max}$	[N/mm^2]	Maximum tensile stress peak at the borehole due to a shear load in the undercut anchor

$\sigma_{M,max}$	[N/mm²]	Maximum tensile stress peak at the borehole due to a moment load in the undercut anchor
$\sigma_{d,1}$	[N/mm²]	Permissible tensile stress at position 1 at the borehole
$\sigma_{d,2}$	[N/mm²]	Permissible tensile stress at position 2 at the borehole
α_N	[-]	Stress factor associated to the tension load in the FZP-G-Z
α_V	[-]	Stress factor associated to the shear load in the FZP-G-Z
α_M	[-]	Stress factor associated to the moment load in the FZP-G-Z
Δp	[N/mm²]	Pressure difference between the cavity and the environment

Latin letters

F_Z	[N]	Tension load in the point fitting
F_{xy}	[N]	Shear load in the point fitting
M_{xy}	[Nmm]	Moment load in the point fitting
k	[-]	Stress concentration factor
b_{Fxy}	[1/mm²]	Stress component factor associated to F_{xy}
b_{Mxy}	[1/mm³]	Stress component factor associated to M_{xy}
f_{vorh}	[mm]	Deformation of the glass pane
f_{zul}	[mm]	Permissible deformation of the glass pane
r	[mm]	Minimum covering thickness of the silicone sealant
P	[N]	Permanent shear load
a	[mm]	Short edge of the IGU
b	[mm]	Long edge of the IGU
V_i	[mm³]	Volume of the cavity i
T_i	[K]	Temperature in the cavity i
p_{pr}	[N/mm²]	Pressure in cavity at production location
V_{pr}	[mm³]	Volume of cavity at production location

T_{pr}	[K]	Temperature in cavity at production location
$p_{res,e}$	[N/mm^2]	Resulting surface loads on the external glass pane
$p_{res,i}$	[N/mm^2]	Resulting surface loads on the internal glass pane
$p_{ex,e}$	[N/mm^2]	External surface load on external pane
$p_{ex,i}$	[N/mm^2]	External surface load on internal pane
p_a	[N/mm^2]	Barometric pressure
p_m	[N/mm^2]	Atmospheric air pressure
H	[m]	Height of the installation location of the IGU
c_H	[kPa/m]	Factor to consider the dependency of the mean vapour pressure difference on the height
c_T	[kPa/K]	Factor to consider the dependency of the mean vapour pressure difference on the temperature
$p_{res,1}$	[N/mm^2]	Resulting surface loads on the external glass pane
$p_{res,2}$	[N/mm^2]	Resulting surface loads on the internal glass pane
k_x	[N/mm]	Translational stiffness of the point fitting in x-direction
k_y	[N/mm]	Translational stiffness of the point fitting in y-direction
k_z	[N/mm]	Translational stiffness of the point fitting in z-direction
k_{mx}	[Nmm/rad]	Rotational stiffness of the point fitting in x-direction
k_{my}	[Nmm/rad]	Rotational stiffness of the point fitting in y-direction
$k_{x,Sub}$	[N/mm]	Translational stiffness of the substructure in x-direction
$k_{y,Sub}$	[N/mm]	Translational stiffness of the substructure in y-direction
$k_{z,Sub}$	[N/mm]	Translational stiffness of the substructure in z-direction
$k_{mx,Sub}$	[Nmm/rad]	Rotational stiffness of the substructure in x-direction
$k_{my,Sub}$	[Nmm/rad]	Rotational stiffness of the substructure in y-direction
e_x	[mm]	Edge distance of the point fitting in x-direction
e_y	[mm]	Edge distance of the point fitting in y-direction
l_x	[mm]	Edge length of the IGU in x-direction
l_y	[mm]	Edge length of the IGU in y-direction

d	[mm]	Height of the silicone sealant = cavity thickness
t_e	[mm]	Thickness of the outer glass pane
t_i	[mm]	Thickness of the inner glass pane
E	[N/mm^2]	Young's Modulus
N	[N]	Normal force in the point fitting
V	[N]	Shear force in the point fitting
M	[Nmm]	Moment in the point fitting
$f_{field,act}$	[mm]	Maximum deformation in the field range of the inner glass pane
$f_{field,rec}$	[mm]	Permissible deformation in the field range of the inner glass pane
M_G	[Nmm]	Additional moment in the point fitting due to the self-weight
L	[mm]	Length of the lever arm
I	[mm^4]	Moment of inertia of the lever arm
g	[kg]	Self-weight of the IGU
k_n	[-]	Factor depending on the sample size n

A Annexe A – Component tests

A.1 Lilliefors hypothesis testing

The *Lilliefors* hypothesis testing is an extension of the *Kolmogorov-Smirnoff* test with the difference, that there is no need to know the average value and the standard deviation from the population beforehand i.e. the parameters of the probability distribution from previous test data. The average and the standard deviation of the population are estimated by the data from the sample. In fact, the test is based on the maximal difference observed between the empirical and the hypothetic distribution function (Kühlmeyer, 2001).

The null-hypothesis H_0 is defined as follows: *"The sample arises from a log-normal distributed population, which parameters μ and σ are unknown"*. The null-hypothesis H_1 is rejected in favour of the rival hypothesis: *"The sample does not arise from a log-normal distribution"* when inequality (A-1) is fulfilled (Kühlmeyer, 2001):

$$D^* = \max\left\{\left|F_n(F_{max}) - \phi\left(\frac{\ln(F_{max})-\mu}{\sigma}\right)\right|\right\} > D_{s;n} \quad \textbf{(A-1)}$$

With

$$D_{s;n} = \frac{Z_S}{\sqrt{n}+0.11+\frac{0.85}{n}} \quad \textbf{(A-2)}$$

For a confidence level of 95%:

$$Z_S = 0.995 \quad \textbf{(A-3)}$$

If this difference D^* exceeds the critical value $D_{s;n}$, the null hypothesis H_0 is rejected. The *Lilliefors* test is carried out in three steps:

- The average and the standard deviation are estimated from the test samples.
- The cumulative standard distribution function is evaluated with the estimated parameters from the previous step.
- The absolute value of the maximal difference between the empirical distribution function and the estimated distribution function in 2) is determined and compared to tabulated critical values. If the difference does not exceed the critical value, the null hypothesis cannot be rejected and the estimated distribution is validated.

The Lilliefors hypothesis testing is applied to the test data of the component tests described in chapter 6 in order to verify the assumed log-normal distribution:

Table A.1 Lilliefors test of goodness of fit, Series N10

N	Measured		Estimated distribution function		Empirical distribution function		Test values	
n_i	F_{max} [N]	$\ln(F_{max})$ [-]	$\frac{\ln(F_{max})-\mu}{\sigma}$	$\phi\left(\frac{\ln(F_{max})-\mu}{\sigma}\right)$	$F_n(i)=\frac{i}{n}$	$F_n(i-1)=\frac{i-1}{n}$	$\left\lvert\frac{i}{n}-\phi_i\right\rvert$	$\left\lvert\frac{i-1}{n}-\phi_i\right\rvert$
1	4383.93	8.39	-0.60	0.27	0.2	0.0	-0.07	-0.27
2	4385.65	8.39	-0.58	0.28	0.4	0.2	0.12	-0.08
3	4406.21	8.39	-0.40	0.35	0.6	0.4	0.25	0.05
4	4430.44	8.40	-0.18	0.43	0.8	0.6	0.37	0.17
5	4651.62	8.44	1.76	0.96	1.0	0.8	0.04	-0.16
	μ 8.40	σ 0.03					$D^* = 0.37$	

$$D_{s;n} = \frac{0.995}{\sqrt{5}+0.11+\frac{0.85}{5}} = 0.395 > D^* = 0.37$$

The null-hypothesis H_0 cannot be rejected with a confidence level of 95%. In consequence, the sample can be described with a log-normal distribution.

Table A.2 Lilliefors test of goodness of fit, Series N12

N	Measured		Estimated distribution function		Empirical distribution function		Test values	
n_i	F_{max} [N]	$\ln(F_{max})$ [-]	$\frac{\ln(F_{max})-\mu}{\sigma}$	$\phi\left(\frac{\ln(F_{max})-\mu}{\sigma}\right)$	$F_n(i)=\frac{i}{n}$	$F_n(i-1)=\frac{i-1}{n}$	$\left\lvert\frac{i}{n}-\phi_i\right\rvert$	$\left\lvert\frac{i-1}{n}-\phi_i\right\rvert$
1	4967.27	8.51	-1.19	0.12	0.17	0.00	0.05	0.12
2	4990.15	8.52	-1.09	0.14	0.33	0.17	0.20	0.03
3	5211.72	8.56	-0.21	0.42	0.50	0.33	0.08	0.08
4	5380.78	8.59	0.44	0.67	0.67	0.50	0.00	0.17
5	5506.77	8.61	0.91	0.82	0.83	0.67	0.02	0.15
6	5575.13	8.63	1.16	0.88	1.00	0.83	0.12	0.04
	μ 8.57	σ 0.049					$D^* = 0.20$	

$$D_{s;n} = \frac{0.995}{\sqrt{6}+0.11+\frac{0.85}{6}} = 0.368 > D^* = 0.20$$

The null-hypothesis H_0 cannot be rejected with a confidence level of 95%. In consequence, the sample can be described with a log-normal distribution.

Table A.3 Lilliefors test of goodness of fit, Series Q10

N	Measured		Estimated distribution function		Empirical distribution function		Test values	
n_i	F_{max} [N]	ln(F_{max}) [-]	$\frac{\ln(F_{max})-\mu}{\sigma}$	$\phi\left(\frac{\ln(F_{max})-\mu}{\sigma}\right)$	$F_n(i)=\frac{i}{n}$	$F_n(i-1)=\frac{i-1}{n}$	$\left\lvert\frac{i}{n}-\phi_i\right\rvert$	$\left\lvert\frac{i-1}{n}-\phi_i\right\rvert$
1	3923.77	8.27	-1.01	0.16	0.17	0.00	0.01	0.16
2	3997.27	8.29	-0.83	0.20	0.33	0.17	0.13	0.04
3	4039.66	8.30	-0.73	0.23	0.50	0.33	0.27	0.10
4	4461.37	8.40	0.25	0.60	0.67	0.50	0.07	0.10
5	4842.24	8.49	1.05	0.85	0.83	0.67	0.02	0.19
6	4947.75	8.51	1.26	0.90	1.00	0.83	0.10	0.06
	μ 8.38	σ 0.102					$D^* = 0.27$	

$$D_{s;n} = \frac{0.995}{\sqrt{6}+0.11+\frac{0.85}{6}} = 0.368 > D^* = 0.27$$

The null-hypothesis H_0 cannot be rejected with a confidence level of 95%. In consequence, the sample can be described with a log-normal distribution.

Table A.4 Lilliefors test of goodness of fit, Series Q12

N	Measured		Estimated distribution function		Empirical distribution function		Test values	
n_i	F_{max} [N]	ln(F_{max}) [-]	$\frac{\ln(F_{max})-\mu}{\sigma}$	$\phi\left(\frac{\ln(F_{max})-\mu}{\sigma}\right)$	$F_n(i)=\frac{i}{n}$	$F_n(i-1)=\frac{i-1}{n}$	$\left\lvert\frac{i}{n}-\phi_i\right\rvert$	$\left\lvert\frac{i-1}{n}-\phi_i\right\rvert$
1	6320.48	8.75	-1.13	0.13	0.20	0.0	0.07	0.13
2	6441.37	8.77	-0.73	0.23	0.40	0.20	0.17	0.03
3	6613.85	8.80	-0.16	0.44	0.60	0.40	0.16	0.04
4	6902.78	8.84	0.75	0.77	0.80	0.60	0.03	0.17
5	7073.66	8.86	1.27	0.90	1.00	0.80	0.10	0.10
	μ 8.80	σ 0.047					$D^* = 0.17$	

$$D_{s;n} = \frac{0.995}{\sqrt{5}+0.11+\frac{0.85}{5}} = 0.395 > D^* = 0.17$$

The null-hypothesis H_0 cannot be rejected with a confidence level of 95%. In consequence, the sample can be described with a log-normal distribution.

Table A.5 Lilliefors test of goodness of fit, Series NQ10

N	Measured		Estimated distribution function		Empirical distribution function		Test values	
n_i	F_{max} [N]	$\ln(F_{max})$ [-]	$\frac{\ln(F_{max})-\mu}{\sigma}$	$\phi\left(\frac{\ln(F_{max})-\mu}{\sigma}\right)$	$F_n(i)=\frac{i}{n}$	$F_n(i-1)=\frac{i-1}{n}$	$\left\|\frac{i}{n}-\phi_i\right\|$	$\left\|\frac{i-1}{n}-\phi_i\right\|$
1	4477.32	8.41	-0.77	0.22	0.20	0.0	0.02	0.22
2	4498.41	8.41	-0.57	0.29	0.40	0.20	0.11	0.09
3	4516.61	8.42	-0.39	0.35	0.60	0.40	0.25	0.05
4	4557.81	8.42	0.01	0.51	0.80	0.60	0.29	0.09
5	4736.6	8.46	1.71	0.96	1.00	0.80	0.04	0.16
	μ 8.42	σ 0.023					$D^* = 0.29$	

$$D_{s;n} = \frac{0.995}{\sqrt{5}+0.11+\frac{0.85}{5}} = 0.395 > D^* = 0.29$$

The null-hypothesis H_0 cannot be rejected with a confidence level of 95%. In consequence, the sample can be described with a log-normal distribution.

Table A.6 Lilliefors test of goodness of fit, Series NQ12

N	Measured		Estimated distribution function		Empirical distribution function		Test values	
n_i	F_{max} [N]	ln(F_{max}) [-]	$\frac{\ln(F_{max})-\mu}{\sigma}$	$\phi\left(\frac{\ln(F_{max})-\mu}{\sigma}\right)$	$F_n(i)=\frac{i}{n}$	$F_n(i-1)=\frac{i-1}{n}$	$\left\lvert\frac{i}{n}-\phi_i\right\rvert$	$\left\lvert\frac{i-1}{n}-\phi_i\right\rvert$
1	5453.11	8.60	-1.15	0.13	0.20	0.0	0.07	0.13
2	5467.28	8.61	-1.03	0.15	0.40	0.20	0.25	0.05
3	5658.64	8.64	0.58	0.72	0.60	0.40	0.12	0.32
4	5678.53	8.64	0.74	0.77	0.80	0.60	0.03	0.17
5	5692.96	8.65	0.86	0.80	1.00	0.80	0.20	0.00
	μ 8.63	σ 0.021					$D^* = 0.32$	

$$D_{s;n} = \frac{0.995}{\sqrt{5}+0.11+\frac{0.85}{5}} = 0.395 > D^* = 0.32$$

The null-hypothesis H_0 cannot be rejected with a confidence level of 95%. In consequence, the sample can be described with a log-normal distribution.

A.2 Characteristic values of the connection resistance

According to DIN EN 1990, Annexe D7, the characteristic values (5%-fractile) of the connection resistance are determined with equation (A-4):

$$X_k = e^{(m_k - k_n \cdot s_y)} \quad \textbf{(A-4)}$$

With the estimated mean value m_k and standard deviation s_y of the population:

$$m_k = \frac{1}{n} \cdot \sum_{i=1}^{n} \ln(x_i) \quad \textbf{(A-5)}$$

$$s_y = \sqrt{\frac{1}{n-1} \cdot \sum_{i=1}^{n} (\ln(x_i) - m_y)^2} \quad \textbf{(A-6)}$$

k_n is a factor depending on the sample size n. For the component tests, the variation coefficient of the population is unknown from advance information and k_n is consequently determined with Table D.1 in DIN EN 1990.

The characteristic values of the connection resistance are derived for each test series of the component tests described in chapter 6.

Table A.7 Characteristic values of the breaking loads, Series N10

Sample	Number	F_{max}	$\ln(F_{max})$	m_y	$(\ln F_{max} - m_y)^2$	s_y	k_n	$F_{5\%}$
[-]	[-]	[N]	[-]	[-]	[-]	[-]	[-]	[kN]
FTG-10-05	1	4383.93	8.39		0.0002			
FTG-10-04	2	4385.65	8.39		0.0002			
FTG-10-01	3	4406.21	8.39	8.40	0.0001	0.0251	2.33	4.20
FTG-10-08	4	4430.44	8.40		0.0000			
FTG-10-03	5	4651.62	8.44		0.0020			

Table A.8 Characteristic values of the breaking loads, Series N12

Sample	Number	F_{max}	$\ln(F_{max})$	m_y	$(\ln F_{max}-m_y)^2$	s_y	k_n	$F_{5\%}$
[-]	[-]	[N]	[-]	[-]	[-]	[-]	[-]	[kN]
FTG-12-03	1	4967.27	8.51		0.0002			
FTG-12-02	2	4990.15	8.52		0.0002			
FTG-12-01	3	5211.72	8.56	8.57	0.0001	0.0493	2.18	4.73
FTG-12-04	4	5380.78	8.59		0.0000			
FTG-12-05	5	5506.77	8.61		0.0020			
FTG-12-06	6	5575.13	8.63		0.0032			

Table A.9 Characteristic values of the breaking loads, Series Q10

Sample	Number	F_{max}	$\ln(F_{max})$	m_y	$(\ln F_{max}-m_y)^2$	s_y	k_n	$F_{5\%}$
[-]	[-]	[N]	[-]	[-]	[-]	[-]	[-]	[kN]
FTG-10-14	1	3923.77	8.27		0.0106			
FTG-10-15	2	3997.27	8.29		0.0071			
FTG-10-11	3	4039.66	8.30	8.38	0.0055	0.1020	2.18	3.48
FTG-10-10	4	4461.37	8.40		0.0006			
FTG-10-09	5	4842.24	8.49		0.0115			
FTG-10-12	6	4947.75	8.51		0.0166			

Table A.10 Characteristic values of the breaking loads, Series Q12

Sample	Number	F_{max}	$\ln(F_{max})$	m_y	$(\ln F_{max}-m_y)^2$	s_y	k_n	$F_{5\%}$
[-]	[-]	[N]	[-]	[-]	[-]	[-]	[-]	[kN]
FTG-12-12	1	6320.48	8.75		0.0028			
FTG-12-08	2	6441.37	8.77		0.0012			
FTG-12-10	3	6613.85	8.80	8.80	0.0001	0.0469	2.33	5.97
FTG-12-11	4	6902.78	8.84		0.0012			
FTG-12-09	5	7073.66	8.86		0.0035			

Table A.11 Characteristic values of the breaking loads, Series NQ10

Sample	Number	F_{max}	$\ln(F_{max})$	m_y	$(\ln F_{max}-m_y)^2$	s_y	k_n	$F_{5\%}$
[-]	[-]	[N]	[-]	[-]	[-]	[-]	[-]	[kN]
FTG-10-14	1	4477.32	8.41		0.0003			
FTG-10-17	2	4498.41	8.41		0.0002			
FTG-10-18	3	4516.61	8.42	8.42	0.0001	0.0226	2.33	4.32
FTG-10-16	4	4557.81	8.42		0.0000			
FTG-10-15	5	4736.6	8.46		0.0015			

Table A.12 Characteristic values of the breaking loads, Series NQ12

Sample	Number	F_{max}	$\ln(F_{max})$	m_y	$(\ln F_{max}-m_y)^2$	s_y	k_n	$F_{5\%}$
[-]	[-]	[N]	[-]	[-]	[-]	[-]	[-]	[kN]
FTG-12-16	1	5453.11	8.60		0.0006			
FTG-12-14	2	5467.28	8.61		0.0005			
FTG-12-15	3	5658.64	8.64	8.63	0.0002	0.0214	2.33	5.32
FTG-12-13	4	5678.53	8.64		0.0003			
FTG-12-17	5	5692.96	8.65		0.0003			

A.3 Partial safety factors

Table A.13 Partial safety factor, Test series N10

Sample	Number	F_{max}	$\ln(F_{max})$	m_y	s	V_x	k_n	α_R	β	γ_M
[-]	[-]	[N]	[-]	[-]	[-]	[-]	[-]	[-]	[-]	[-]
FTG-10-05	1	4383.93	8.39							
FTG-10-04	2	4385.65	8.39							
FTG-10-01	3	4406.21	8.39	8.40	0.0251	0.025	2.33	0.8	3.8	1.1
FTG-10-08	4	4430.44	8.40							
FTG-10-03	5	4651.62	8.44							

Table A.14 Partial safety factor, Test series N12

Sample	Number	F_{max}	$\ln(F_{max})$	m_y	s	V_x	k_n	α_R	β	γ_R
[-]	[-]	[N]	[-]	[-]	[-]	[-]	[-]	[-]	[-]	[-]
FTG-12-03	1	4967.27	8.51							
FTG-12-02	2	4990.15	8.52							
FTG-12-01	3	5211.72	8.56	8.57	0.0493	0.049	2.18	0.8	3.8	1.1
FTG-12-04	4	5380.78	8.59							
FTG-12-05	5	5506.77	8.61							
FTG-12-06	6	5575.13	8.63							

Table A.15 Partial safety factor, Test series Q10

Sample	Number	F_{max}	$\ln(F_{max})$	m_y	s	V_x	k_n	α_R	β	γ_R
[-]	[-]	[N]	[-]	[-]	[-]	[-]	[-]	[-]	[-]	[-]
FTG-10-14	1	3923.77	8.27							
FTG-10-15	2	3997.27	8.29							
FTG-10-11	3	4039.66	8.30	8.38	0.1020	0.102	2.18	0.8	3.8	1.1
FTG-10-10	4	4461.37	8.40							
FTG-10-09	5	4842.24	8.49							
FTG-10-12	6	4947.75	8.51							

Table A.16 Partial safety factor, Test series Q12

Sample	Number	F_{max}	$\ln(F_{max})$	m_y	s	V_x	k_n	α_R	β	γ_R
[-]	[-]	[N]	[-]	[-]	[-]	[-]	[-]	[-]	[-]	[-]
FTG-12-12	1	6320.48	8.75							
FTG-12-08	2	6441.37	8.77							
FTG-12-10	3	6613.85	8.80	8.80	0.0469	0.047	2.33	0.8	3.8	1.1
FTG-12-11	4	6902.78	8.84							
FTG-12-09	5	7073.66	8.86							

Table A.17 Partial safety factor, Test series NQ10

Sample	Number	F_{max}	$\ln(F_{max})$	m_y	s	V_x	k_n	α_R	β	γ_R
[-]	[-]	[N]	[-]	[-]	[-]	[-]	[-]	[-]	[-]	[-]
FTG-10-14	1	4477.32	8.41							
FTG-10-17	2	4498.41	8.41							
FTG-10-18	3	4516.61	8.42	8.42	0.0226	0.023	2.33	0.8	3.8	1.1
FTG-10-16	4	4557.81	8.42							
FTG-10-15	5	4736.6	8.46							

Table A.18 Partial safety factor, Test series NQ12

Sample	Number	F_{max}	$\ln(F_{max})$	m_y	s	V_x	k_n	α_R	β	γ_R
[-]	[-]	[N]	[-]	[-]	[-]	[-]	[-]	[-]	[-]	[-]
FTG-12-16	1	5453.11	8.60							
FTG-12-14	2	5467.28	8.61							
FTG-12-15	3	5658.64	8.64	8.63	0.0214	0.021	2.33	0.8	3.8	1.1
FTG-12-13	4	5678.53	8.64							
FTG-12-17	5	5692.96	8.65							

A.4 Strain comparison

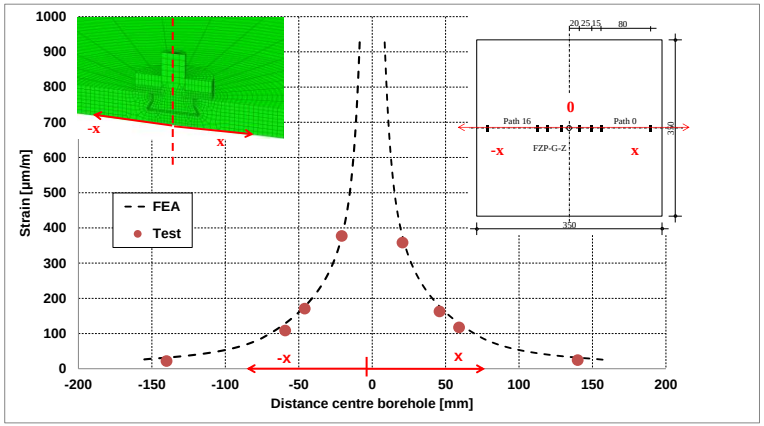

Figure A.1 Measured strains vs. calculated strains, Test series N10, N = 2500 N

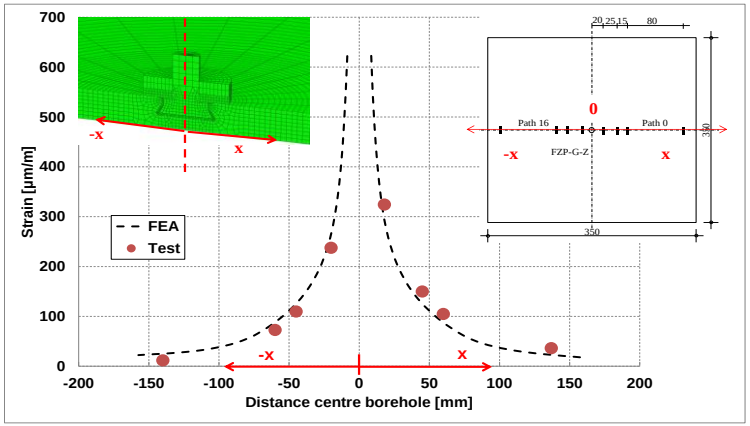

Figure A.2 Measured strains vs. calculated strains, Test series N12, N = 2500 N

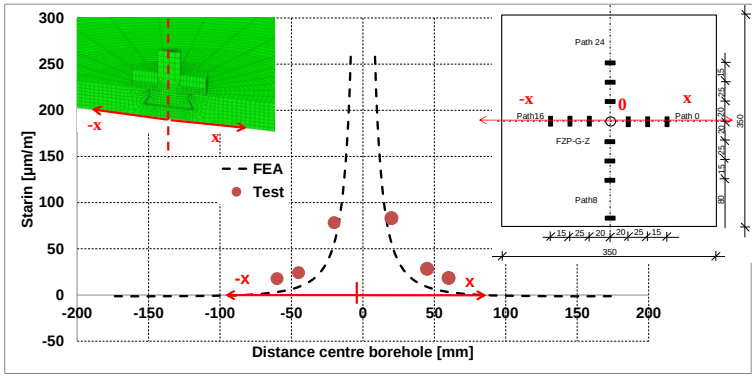

Figure A.3 Measured strains vs. calculated strains, Test series Q10, Q = 2500 N

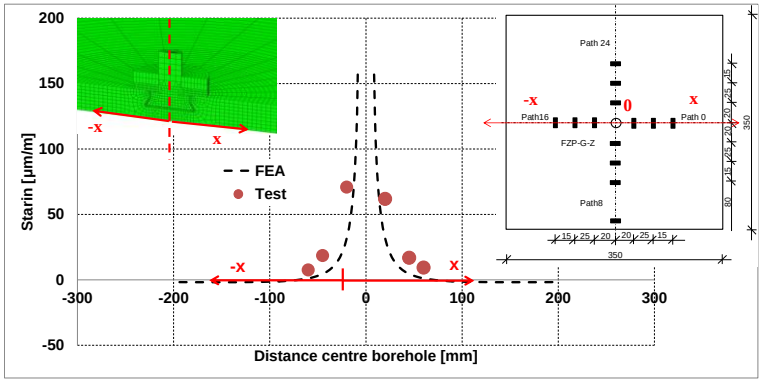

Figure A.4 Measured strains vs. calculated strains, Test series Q12, Q = 2500 N

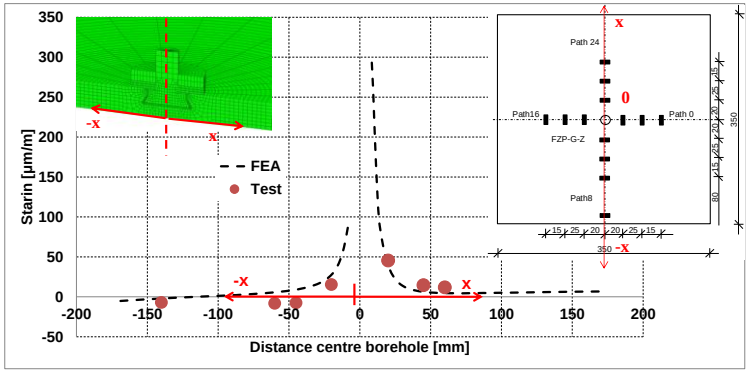

Figure A.5 Measured strains vs. calculated strains, Test series Q10, Q = 2500 N

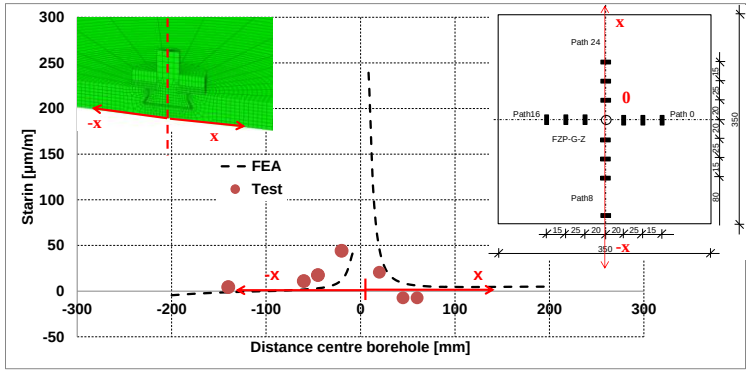

Figure A.6 Measured strains vs. calculated strains, Test series Q12, Q = 2500 N

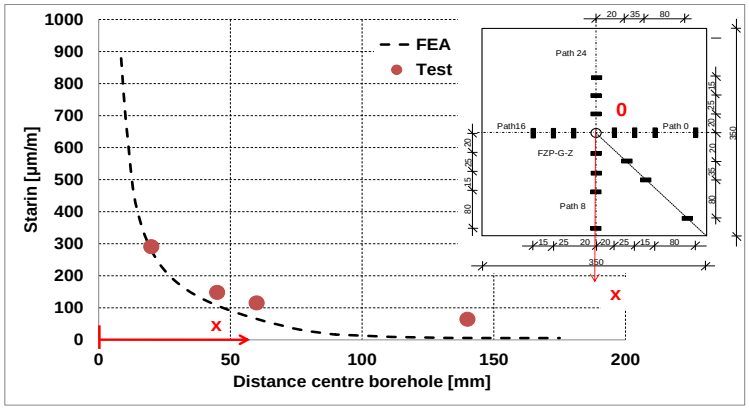

Figure A.7 Measured strains vs. calculated strains, Test series NQ10, N = 2500 N

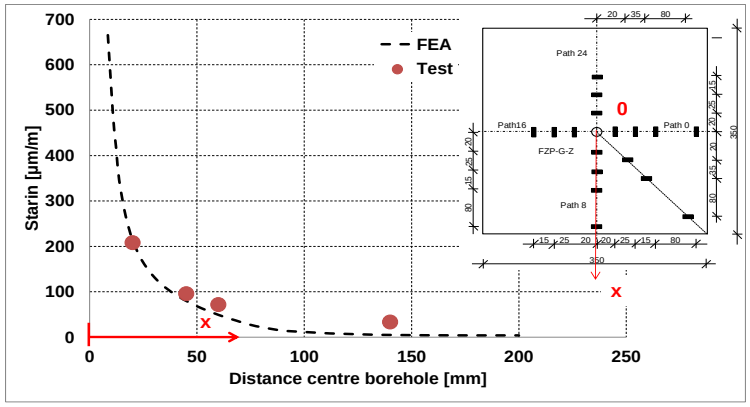

Figure A.8 Measured strains vs. calculated strains, Test series NQ12, N = 2500 N

B Annexe B – Extended climate load model

B.1 General analytical extension of the climate load model to point fitted IGU

As for the model of *Feldmeier*, the deformations of the glass panes are assumed to be small and hence proportional to the loading:

$$\Delta V = \vartheta \cdot p \quad \textbf{(B-1)}$$

ϑ = Volume coefficient for a surface load (pressure) [m^3/kPa]

p = surface load [kN/m^2]

The volume coefficient ϑ is the enclosed volume of the deformed pane due to a surface load or pressure “1” [kN/m^2].

Consequently, the extended climate load model does not account for non-linear effects, e.g. membrane effects.

The volume V_i of cavity i is calculated with equation (B-2):

$$i = 1, \dots, n-1$$

$$V_i = V_{pr,i} - \Delta V_i + \Delta V_{i+1} \quad \textbf{(B-2)}$$

V_i = The volume of cavity i at the installation location of the unit [mm^3]

$V_{pr,i}$ = The volume of cavity i at the production location of the unit [mm^3]

ΔV_i = The volume change of cavity i due to the deformation of pane i [mm^3]

ΔV_{i+1} = The volume change of cavity i due to the deformation of pane $i+1$ [mm^3]

The volume change ΔV_i depends on the deflection of the glass pane i. Due to the coupling of the glass panes via the edge bond however, this deflection also depends on the external loading on each pane and the pressure within each cavity i. The volume change ΔV_i is given by equation (B-3):

$$i = 1, \dots, n-1$$

$$\Delta V_i = \sum_{k=1}^{n} \vartheta_{i,k} \cdot (p_{k-1} - p_k) + \sum_{k=1}^{n} \vartheta_{pe,i,k} \cdot p_{e,k} \quad \textbf{(B-3)}$$

$\vartheta_{i,k}$ = The enclosed volume of pane i due to a pressure “1” on pane k [$m^3/(kN/m^2)$]

$\vartheta_{pe,i,k}$ = The enclosed volume of pane i due to an external surface load “1” on

pane k [$m^3/(kN/m^2)$]

p_k = The pressure acting on pane k [kN/m^2]

p_{k-1} = The pressure acting on pane k-1 [kN/m^2]

$p_{e,k}$ = The external surface load acting on pane k [kN/m^2]

The volume change ΔV_{i+1} is calculated analogue to ΔV_i:

$$i = 1, \dots, n-1$$

$$\Delta V_{i+1} = \sum_{k=1}^{n} \vartheta_{i+1,k} \cdot (p_{k-1} - p_k) + \sum_{k=1}^{n} \vartheta_{pe,i+1,k} \cdot p_{e,k} \quad \textbf{(B-4)}$$

$\vartheta_{i+1,k}$ = The enclosed volume of pane i+1 due to a pressure “1” on pane k [$m^3/(kN/m^2)$]

$\vartheta_{pe,i+1,k}$ = The enclosed volume of pane i+1 due to an external surface load “1” on pane k [$m^3/(kN/m^2)$]

Insertion of the equations (B-3) and (B-4) in equation (B-2) delivers V_i:

$$i = 1, \dots, n-1$$

$$V_i = V_{pr,i} - \sum_{k=1}^{n} \vartheta_{i,k} \cdot (p_{k-1} - p_k) - \sum_{k=1}^{n} \vartheta_{pe,i,k} \cdot p_{e,k} + \sum_{k=1}^{n} \vartheta_{i+1,k} \cdot (p_{k-1} - p_k) + + \sum_{k=1}^{n} \vartheta_{pe,i+1,k} \cdot p_{e,k}$$

$$= V_{pr,i} - \sum_{k=1}^{n} \vartheta_{i,k} \cdot p_{k-1} + \sum_{k=1}^{n} \vartheta_{i,k} \cdot p_k - \sum_{k=1}^{n} \vartheta_{pe,i,k} \cdot p_{e,k} + \sum_{k=1}^{n} \vartheta_{i+1,k} \cdot p_{k-1} - - \sum_{k=1}^{n} \vartheta_{i+1,k} \cdot p_k + \sum_{k=1}^{n} \vartheta_{pe,i+1,k} \cdot p_{e,k}$$

$$= V_{pr,i} + \sum_{k=1}^{n} \{-(\vartheta_{i,k} - \vartheta_{i+1,k}) \cdot p_{k-1} + (\vartheta_{i,k} - \vartheta_{i+1,k}) \cdot p_k\} - \Delta V_{ex,i} \quad \textbf{(B-5)}$$

With:

$$\Delta V_{ex,i} = V_{ex,i} - V_{ex,i+1} \quad \textbf{(B-6)}$$

$$V_{ex,i} = \sum_{k=1}^{n} \vartheta_{pe,i,k} \cdot p_{e,k} \quad \textbf{(B-7)}$$

$$V_{ex,i+1} = \sum_{k=1}^{n} \vartheta_{pe,i+1,k} \cdot p_{e,k} \quad \textbf{(B-8)}$$

As introduced in section 6.2.1, the glass panes are coupled by the encapsulated gas in the cavity. The quantity of each gas in the cavity has been fixed during production (index pr) and rests constant. Consequently, the pressure change of the gas due to the variation of its volume and temperature can be described by the ideal gas law:

$$i = 1, \dots, n-1$$

$$\frac{p_i \cdot V_i}{T_i} = \frac{p_{pr,i} \cdot V_{pr,i}}{T_{pr,i}} \quad \textbf{(B-9)}$$

p_i = The pressure of the gas in cavity i at the installation location [kN/m²]

V_i = The volume of the gas in cavity i at the installation location [mm³]

T_i = The temperature of the gas in cavity i at the installation location [K]

$p_{pr,i}$ = The pressure of the gas in cavity i at the production location [kN/m²]

$V_{pr,i}$ = The volume of the gas in cavity i at the production location [mm³]

$T_{pr,i}$ = The temperature of the gas in cavity i at the production location [K]

The ideal gas law assumes that the pressure, the volume and the temperature are the same in each cavity at production.

Insertion of equation (B-5) in (B-9) delivers equation (B-10):

$$i = 1, \dots, n-1$$

$$p_i \cdot \left[V_{pr,i} + \sum_{k=1}^{n} \left\{-\left(\vartheta_{i,k} - \vartheta_{i+1,k}\right) \cdot p_{k-1} + \left(\vartheta_{i,k} - \vartheta_{i+1,k}\right) \cdot p_k\right\} - \Delta V_{ex,i}\right] = \frac{T_i \cdot p_{pr,i} \cdot V_{pr,i}}{T_{pr,i}}$$

$$p_i \cdot \left[1 + \sum_{k=1}^{n} \left\{-\frac{\left(\vartheta_{i,k} - \vartheta_{i+1,k}\right)}{V_{pr,i}} \cdot p_{k-1} + \frac{\left(\vartheta_{i,k} - \vartheta_{i+1,k}\right)}{V_{pr,i}} \cdot p_k\right\} - \frac{\Delta V_{ex,i}}{V_{pr,i}}\right] = \frac{T_i \cdot p_{pr,i}}{T_{pr,i}} \quad \textbf{(B-10)}$$

With the definition of the under- respectively overpressure in the cavities to the ambient pressure

$$\Delta p_i = p_i - p_a \quad \textbf{(B-11)}$$

p_a = The barometric pressure at the installation location of the IGU.

The system of equation (B-10) is reformulated:

$$(\Delta p_i + p_a) \cdot \left[1 + \sum_{k=1}^{n} \left\{-\frac{\left(\vartheta_{i,k} - \vartheta_{i+1,k}\right)}{V_{pr,i}} \cdot (\Delta p_{k-1} + p_a) + \frac{\left(\vartheta_{i,k} - \vartheta_{i+1,k}\right)}{V_{pr,i}} \cdot (\Delta p_k + p_a)\right\} - \frac{\Delta V_{ex,i}}{V_{pr,i}}\right] = \\ = \frac{T_i \cdot p_{pr,i}}{T_{pr,i}}$$

$$p_a \cdot \left(1 + \frac{\Delta p_i}{p_a}\right) \cdot \left[1 + \sum_{k=1}^{n} \left\{-\frac{\vartheta_{i,k}}{V_{pr,i}} \cdot \Delta p_{k-1} - \frac{\vartheta_{i,k}}{V_{pr,i}} \cdot p_a + \frac{\vartheta_{i+1,k}}{V_{pr,i}} \cdot \Delta p_{k-1} + \frac{\vartheta_{i+1,k}}{V_{pr,i}} \cdot p_a + \frac{\vartheta_{i,k}}{V_{pr,i}} \cdot \right.\right. \\ \left.\left. \cdot \Delta p_k + \frac{\vartheta_{i,k}}{V_{pr,i}} \cdot p_a - \frac{\vartheta_{i+1,k}}{V_{pr,i}} \cdot \Delta p_k - \frac{\vartheta_{i+1,k}}{V_{pr,i}} \cdot p_a\right\} - \frac{\Delta V_{ex,i}}{V_{pr,i}}\right] = \frac{T_i \cdot p_{pr,i}}{T_{pr,i}}$$

$$p_a \cdot \left(1 + \frac{\Delta p_i}{p_a}\right) \cdot \left[1 + \sum_{k=1}^{n} \left\{ -\frac{\vartheta_{i,k}}{V_{pr,i}} \cdot \Delta p_{k-1} + \frac{\vartheta_{i+1,k}}{V_{pr,i}} \cdot \Delta p_{k-1} + \frac{\vartheta_{i,k}}{V_{pr,i}} \cdot \Delta p_k - \frac{\vartheta_{i+1,k}}{V_{pr,i}} \cdot \Delta p_k \right\} - \right.$$

$$\left. - \frac{\Delta V_{ex,i}}{V_{pr,i}} \right] = \frac{T_i \cdot p_{pr,i}}{T_{pr,i}} \qquad \textbf{(B-12)}$$

With the introduction of the dimensionless factors

$$\alpha_{i,k} = \frac{\vartheta_{i,k}}{V_{pr,i}} \cdot p_a \qquad \textbf{(B-13)}$$

$$\alpha^{+}_{i,k} = \frac{\vartheta_{i+1,k}}{V_{pr,i}} \cdot p_a \qquad \textbf{(B-14)}$$

and

$\alpha_{i,k}$ = The relative volume change of pane i due to a loading on pane k

$\alpha^{+}_{i,k}$ = The relative volume change of pane $i+1$ due to a loading on pane k

the equation (B-12) is reformulated to equation (B-15):

$$\left(1 + \frac{\Delta p_i}{p_a}\right) \cdot \left[1 + \sum_{k=1}^{n} \left\{ -\frac{\alpha_{i,k}}{p_a} \cdot \Delta p_{k-1} + \frac{\alpha^{+}_{i,k}}{p_a} \cdot \Delta p_{k-1} + \frac{\alpha_{i,k}}{p_a} \cdot \Delta p_k - \frac{\alpha^{+}_{i,k}}{p_a} \cdot \Delta p_k \right\} - \frac{\Delta V_{ex,i}}{V_{pr,i}} \right] = \frac{T_i \cdot p_{pr,i}}{T_{pr,i} \cdot p_a}$$

$$\left(1 + \frac{\Delta p_i}{p_a}\right) \cdot \left[1 + \sum_{k=1}^{n} \left\{ \left(\alpha^{+}_{i,k} - \alpha_{i,k}\right) \cdot \frac{\Delta p_{k-1}}{p_a} + \left(\alpha_{i,k} - \alpha^{+}_{i,k}\right) \cdot \frac{\Delta p_k}{p_a} \right\} - \frac{\Delta V_{ex,i}}{V_{pr,i}} \right] = \frac{T_i \cdot p_{pr,i}}{T_{pr,i} \cdot p_a}$$

$$1 + \sum_{k=1}^{n} \left\{ \left(\alpha^{+}_{i,k} - \alpha_{i,k}\right) \cdot \frac{\Delta p_{k-1}}{p_a} + \left(\alpha_{i,k} - \alpha^{+}_{i,k}\right) \cdot \frac{\Delta p_k}{p_a} \right\} - \frac{\Delta V_{ex,i}}{V_{pr,i}} + \frac{\Delta p_i}{p_a} + \sum_{k=1}^{n} \left\{ \left(\alpha^{+}_{i,k} - \alpha_{i,k}\right) \cdot \right.$$

$$\left. \frac{\Delta p_{k-1} \cdot \Delta p_i}{p_a^2} + \left(\alpha_{i,k} - \alpha^{+}_{i,k}\right) \cdot \frac{\Delta p_k \cdot \Delta p_i}{p_a^2} \right\} - \frac{\Delta p_i}{p_a} \cdot \frac{\Delta V_{ex,i}}{V_{pr,i}} = \frac{T_i \cdot p_{pr,i}}{T_{pr,i} \cdot p_a} \qquad \textbf{(B-15)}$$

(B-15) is a system of coupled quadratic equations. The system can be solved for the pressure difference Δp_i in each cavity by means of mathematical software. The pressure difference finally delivers the loading of each glass pane. With the aim to deliver an analytical logic, feasible by hand, the system (B-15) is linearised according to (Feldmeier, 2006) with the following assumptions:

- The pressures p_i in the cavities are in the range of the barometric pressure p_a at the installation location.

  $$\left|\frac{\Delta p_i}{p_a}\right| \ll 1$$

- The volume changes $\Delta V_{ex,i}$ due to the external loads are small compared to the volumes $V_{pr,i}$ of the cavities.

$$\left|\frac{\Delta V_{ex,i}}{V_{pr,i}}\right| \ll 1$$

The assumptions allow the linearization of the system (B-15) and leads to the linearised system (B-16):

$$1 + \sum_{k=1}^{n}\left\{\left(\alpha_{i,k}^{+} - \alpha_{i,k}\right)\cdot\frac{\Delta p_{k-1}}{p_a} + \left(\alpha_{i,k} - \alpha_{i,k}^{+}\right)\cdot\frac{\Delta p_k}{p_a}\right\} - \frac{\Delta V_{ex,i}}{V_{pr,i}} + \frac{\Delta p_i}{p_a} + \sum_{k=1}^{n}\left\{\left(\alpha_{i,k}^{+} - \alpha_{i,k}\right)\cdot \frac{\Delta p_{k-1}\cdot\Delta p_i}{p_a^2} + \left(\alpha_{i,k} - \alpha_{i,k}^{+}\right)\cdot\frac{\Delta p_k\cdot\Delta p_i}{p_a^2}\right\} - \frac{\Delta p_i}{p_a}\cdot\frac{\Delta V_{ex,i}}{V_{pr,i}} = \frac{T_i\cdot p_{pr,i}}{T_{pr,i}\cdot p_a}$$

$$\sum_{k=1}^{n}\left\{\left(\alpha_{i,k}^{+} - \alpha_{i,k}\right)\cdot\frac{\Delta p_{k-1}}{p_a} + \left(\alpha_{i,k} - \alpha_{i,k}^{+}\right)\cdot\frac{\Delta p_k}{p_a}\right\} + \frac{\Delta p_i}{p_a} = \frac{\Delta V_{ex,i}}{V_{pr,i}} + \frac{T_i\cdot p_{pr,i}}{T_{pr,i}\cdot p_a} - 1$$

$$\sum_{k=1}^{n}\left\{\left(\alpha_{i,k}^{+} - \alpha_{i,k}\right)\cdot\Delta p_{k-1} + \left(\alpha_{i,k} - \alpha_{i,k}^{+}\right)\cdot\Delta p_k\right\} + \Delta p_i = \frac{\Delta V_{ex,i}}{V_{pr,i}}\cdot p_a +$$

$$+\left(\frac{T_i\cdot p_{pr,i}}{T_{pr,i}\cdot p_a} - 1\right)\cdot p_a \qquad \textbf{(B-16)}$$

The term on the right of equation (B-16) comprehends the external loading and climatic conditions. Similar to (Feldmeier, 2006), pressure differences are introduced respectively:

- The pressure difference in cavity i due to the external loads:

$$\Delta p_{ex,i} = \frac{\Delta V_{ex,i}}{V_{pr,i}}\cdot p_a \qquad \textbf{(B-17)}$$

and

- The pressure difference in cavity i due to the climatic changes:

$$\Delta p_{c,i} = \left(\frac{T_i\cdot p_{pr,i}}{T_{pr,i}\cdot p_a} - 1\right)\cdot p_a \qquad \textbf{(B-18)}$$

The barometric pressure p_a depends on the height of the location and the atmospheric air pressure, which is based on the sea level. It is described by the exponential barometric height formula that can be linearised up to heights of 1000 m:

$$p_a = p_m - c_H\cdot H$$

with

p_m = The atmospheric air pressure [kN/m^2]

H = The height of the location [m]

c_H = Factor to consider the dependency of the mean vapour pressure difference on the height (c_H = 0.012 kPa/m)

For the conditions at the production (index p_r) and installation (index i_n) location, the equation (B-18) is written:

$$\Delta p_{c,i} = \left(\frac{T_i \cdot p_{pr,i}}{T_{pr,i} \cdot p_a} - 1\right) \cdot p_a = \frac{T_{in,i} \cdot p_{pr,i}}{T_{pr,i}} - p_a = \frac{T_{pr,i} + (T_{in,i} - T_{pr,i})}{T_{pr,i}} \cdot \left(p_{m,pr} - c_H \cdot H_{pr}\right) - \\ -\left(p_{m,in} - c_H \cdot H_{in}\right)$$

and can be linearised with an accuracy of 10% (Feldmeier, 2006):

$$\Delta p_{c,i} = c_T \cdot \left(T_{in,i} - T_{pr}\right) - \left(p_{m,in} - p_{m,pr}\right) + c_H\left(H_{in} - H_{pr}\right) \quad \textbf{(B-19)}$$

with

c_T = Factor to consider the dependency of the mean vapour pressure difference on the temperature (c_H = 0.34 kPa/K)

The pressure differences (B-17) and (B-18) are inserted in equation (B-16):

$$\sum_{k=1}^{n}\left\{\left(\alpha_{i,k}^{+} - \alpha_{i,k}\right) \cdot \Delta p_{k-1} + \left(\alpha_{i,k} - \alpha_{i,k}^{+}\right) \cdot \Delta p_k\right\} + \Delta p_i = \Delta p_{ex,i} + \Delta p_{c,i}$$

$$\sum_{k=1}^{n}\left\{\left(\alpha_{i,k}^{+} - \alpha_{i,k}\right) \cdot \Delta p_{k-1} - \left(\alpha_{i,k}^{+} - \alpha_{i,k}\right) \cdot \Delta p_k\right\} + \Delta p_i = \Delta p_{ex,i} + \Delta p_{c,i}$$

Similar to the insulation glass factor in (Feldmeier, 2006), a coupling factor $\varphi_{i,k}$ is defined:

$$\varphi_{i,k} = \alpha_{i,k}^{+} - \alpha_{i,k} \quad \textbf{(B-20)}$$

The factor $\varphi_{i,k}$ considers the coupling of the glass panes via the edge bond system. It indicates the contribution of an external load acting on pane k to the pressure difference in cavity i.

The factor $\varphi_{i,k}$ is inserted in the system of equation (B-16):

$$i = 1, \dots, n-1$$

$$\sum_{k=1}^{n}\left(\varphi_{i,k} \cdot \Delta p_{k-1} - \varphi_{i,k} \cdot \Delta p_k\right) + \Delta p_i = \Delta p_{ex,i} + \Delta p_{c,i}$$

which can be written as a matrix:

$$\begin{pmatrix} 1+\varphi_{1,2}-\varphi_{1,1} & \varphi_{1,3}-\varphi_{1,2} & \cdots & \varphi_{1,n}-\varphi_{1,n-1} \\ \varphi_{2,2}-\varphi_{2,1} & 1+\varphi_{2,3}-\varphi_{2,2} & \cdots & \varphi_{2,n}-\varphi_{2,n-1} \\ \cdots & \cdots & \cdots & \cdots \\ \varphi_{n-1,2}-\varphi_{n-1,1} & \varphi_{n-1,3}-\varphi_{n-1,2} & \cdots & 1+\varphi_{n-1,n}-\varphi_{n-1,n-1} \end{pmatrix} \cdot \begin{pmatrix} \Delta p_1 \\ \Delta p_2 \\ \cdots \\ \Delta p_{n-1} \end{pmatrix} = \begin{pmatrix} \Delta p_{ex,1}+\Delta p_{c,1} \\ \Delta p_{ex,2}+\Delta p_{c,2} \\ \cdots \\ \Delta p_{ex,n-1}+\Delta p_{c,n-1} \end{pmatrix} \quad \textbf{(B-21)}$$

The solution of the matrix delivers the over- respectively the underpressure in each cavity. The pressure is applied as a surface load on each glass pane and can be superimposed with the external surface loads, e.g. wind.

B.2 Application to point fitted double insulation glass with undercut anchors

In this section, the matrix (B-21) is applied to double insulation glass with undercut anchors (Tibolt, 2014).

For double insulation glass, the matrix (B-21) is written in the form of the equation (B-22):

$$\left(\varphi_{1,1} \cdot \cancel{\Delta p_a} - \varphi_{1,1} \cdot \Delta p_1\right) + \left(\varphi_{1,2} \cdot \Delta p_1 - \varphi_{1,2} \cdot \cancel{\Delta p_z}\right) + \Delta p_1 = \Delta p_{ex,1} + \Delta p_{c,1}$$

$$-\varphi_{1,1} \cdot \Delta p_1 + \varphi_{1,2} \cdot \Delta p_1 + \Delta p_1 = \Delta p_{ex,1} + \Delta p_{c,1}$$

$$\left(1+\varphi_{1,2}-\varphi_{1,1}\right) \cdot \Delta p_1 = \Delta p_{ex,1} + \Delta p_{c,1} \quad \textbf{(B-22)}$$

The equation (B-17)

$$\Delta p_{ex,1} = \frac{\Delta V_{ex,1}}{V_{pr,1}} \cdot p_a = \frac{V_{ex,1}-V_{ex,2}}{V_{pr,1}} \cdot p_a = \frac{\vartheta_{pe,1,1} \cdot p_{e,1}+\vartheta_{pe,1,2} \cdot p_{e,2}-\vartheta_{pe,2,1} \cdot p_{e,1}-\vartheta_{pe,2,2} \cdot p_{e,2}}{V_{pr,1}} \cdot p_a$$

$$= \alpha_{1,1} \cdot p_{e,1} + \alpha_{1,2} \cdot p_{e,2} - \alpha_{1,1}^{+} \cdot p_{e,1} - \alpha_{1,2}^{+} \cdot p_{e,2}$$

$$= \left(\alpha_{1,1} - \alpha_{1,1}^{+}\right) \cdot p_{e,1} + \left(\alpha_{1,2} - \alpha_{1,2}^{+}\right) \cdot p_{e,2}$$

is inserted in the equation (B-22) and delivers the equation (B-23):

$$\left(1+\varphi_{1,2}-\varphi_{1,1}\right) \cdot \Delta p_1 = \left(\alpha_{1,1} - \alpha_{1,1}^{+}\right) \cdot p_{e,1} + \left(\alpha_{1,2} - \alpha_{1,2}^{+}\right) \cdot p_{e,2} + \Delta p_{c,1}$$

$$\Delta p_1 = \frac{1}{\left(1+\varphi_{1,2}-\varphi_{1,1}\right)}\left[\left(\alpha_{1,1} - \alpha_{1,1}^{+}\right) \cdot p_{e,1} + \left(\alpha_{1,2} - \alpha_{1,2}^{+}\right) \cdot p_{e,2} + \Delta p_{c,1}\right] \quad \textbf{(B-23)}$$

The resulting surface loads acting on the outer (index 1) respectively the inner pane (index 2) are determined by means of the equations (B-24):

$$\begin{cases} p_{res,1} = p_{e,1} - \Delta p_1 \\ p_{res,2} = p_{e,2} + \Delta p_1 \end{cases} \quad \textbf{(B-24)}$$

The equation (B-23) is inserted in the equation (B-24)

$$\begin{cases} p_{res,1} = p_{e,1} - \Delta p_1 = p_{e,1} - \frac{1}{(1+\varphi_{1,2}-\varphi_{1,1})}\left[\left(\alpha_{1,1} - \alpha_{1,1}^{+}\right) \cdot p_{e,1} + \left(\alpha_{1,2} - \alpha_{1,2}^{+}\right) \cdot p_{e,2} + \Delta p_{c,1}\right] \\ p_{res,2} = p_{e,2} + \Delta p_1 = p_{e,2} - \frac{1}{(1+\varphi_{1,2}-\varphi_{1,1})}\left[\left(\alpha_{1,1} - \alpha_{1,1}^{+}\right) \cdot p_{e,1} + \left(\alpha_{1,2} - \alpha_{1,2}^{+}\right) \cdot p_{e,2} + \Delta p_{c,1}\right] \end{cases}$$

and put in form of a matrix:

$$\begin{pmatrix} p_{res,1} \\ p_{res,2} \end{pmatrix} = \begin{pmatrix} -\frac{1}{(1+\varphi_{1,2}-\varphi_{1,1})} & 1 - \frac{\alpha_{1,1}-\alpha_{1,1}^{+}}{(1+\varphi_{1,2}-\varphi_{1,1})} & -\frac{\alpha_{1,2}-\alpha_{1,2}^{+}}{(1+\varphi_{1,2}-\varphi_{1,1})} \\ \frac{1}{(1+\varphi_{1,2}-\varphi_{1,1})} & \frac{\alpha_{1,1}-\alpha_{1,1}^{+}}{(1+\varphi_{1,2}-\varphi_{1,1})} & 1 + \frac{\alpha_{1,2}-\alpha_{1,2}^{+}}{(1+\varphi_{1,2}-\varphi_{1,1})} \end{pmatrix} \cdot \begin{pmatrix} \Delta p_{c,1} \\ p_{e,1} \\ p_{e,2} \end{pmatrix}$$

$$\begin{pmatrix} p_{res,1} \\ p_{res,2} \end{pmatrix} = \frac{1}{(1+\varphi_{1,2}-\varphi_{1,1})} \cdot \begin{pmatrix} -1 & 1+\varphi_{1,2}-\varphi_{1,1}+\varphi_{1,1} & \varphi_{1,2} \\ 1 & -\varphi_{1,1} & 1+\varphi_{1,2}-\varphi_{1,1}-\varphi_{1,2} \end{pmatrix} \cdot \begin{pmatrix} \Delta p_{c,1} \\ p_{e,1} \\ p_{e,2} \end{pmatrix}$$

$$\begin{pmatrix} p_{res,1} \\ p_{res,2} \end{pmatrix} = \frac{1}{(1+\varphi_{1,2}-\varphi_{1,1})} \cdot \begin{pmatrix} -1 & 1+\varphi_{1,2} & \varphi_{1,2} \\ 1 & -\varphi_{1,1} & 1-\varphi_{1,1} \end{pmatrix} \cdot \begin{pmatrix} \Delta p_{c,1} \\ p_{e,1} \\ p_{e,2} \end{pmatrix} \quad \textbf{(B-25)}$$

The matrix (B-25) allows the determination of the resulting surface load acting on each glass pane under consideration of the climate loads $\Delta p_{c,1}$ and the external surface loads on the outer pane $p_{e,1}$ and the inner pane $p_{e,2}$. The coupling factors $\varphi_{1,1}$ and $\varphi_{1,2}$ depends on the four volume coefficients $\vartheta_{1,1}, \vartheta_{1,2}, \vartheta_{2,1}, \vartheta_{2,2}$ (see equations (B-13), (B-14) and (B-20)). For point fitted insulation glass units with undercut anchors, an analytical solution for the determination of the volume coefficients does not exist. Hence, the user determines the coefficients numerically.

B.3 Application to point fitted triple insulation glass with undercut anchors

The matrix (B-21) can also be applied to triple point fitted insulation glass with undercut anchors and is written in the general form of the system of linear equations (B-26):

$$\begin{cases} \varphi_{1,1} \cdot \Delta p_1 + \left(\varphi_{1,2} \cdot \Delta p_1 - \varphi_{1,2} \cdot \Delta p_2\right) + \varphi_{1,3} \cdot \Delta p_2 + \Delta p_1 \;\; = \Delta p_{ex,1} + \Delta p_{c,1} \\ -\varphi_{2,1} \cdot \Delta p_1 + \left(\varphi_{2,2} \cdot \Delta p_1 - \varphi_{2,2} \cdot \Delta p_2\right) + \varphi_{2,3} \cdot \Delta p_2 + \Delta p_2 = \Delta p_{ex,2} + \Delta p_{c,2} \end{cases} \quad \textbf{(B-26)}$$

For the determination of the resulting surface loads of triple point fitted insulation glass with undercut anchors, the system of linear equations (B-26) has to be solved for the pressure differences Δp_1 and Δp_2 in each cavity. The pressure differences finally allow the calculation of the resulting surface loads.

The solution of the system leads to complex and confusing expressions. For the sake of clarity, the solution is presented for a specific case in this section:

Only the climate loads are considered and no external loads act on the glass panes. The temperatures in the cavities are assumed to be nearly the same.

In this case: $p_{e,2} = p_{e,2} = p_{e,3} = 0$ kN/m² and $\Delta p_{c,1} = \Delta p_{c,2} = \Delta p_c$. The system of equations (B-26) becomes:

$$\begin{cases} \varphi_{1,1} \cdot \Delta p_1 + (\varphi_{1,2} \cdot \Delta p_1 - \varphi_{1,2} \cdot \Delta p_2) + \varphi_{1,3} \cdot \Delta p_2 + \Delta p_1 = \Delta p_c \\ -\varphi_{2,1} \cdot \Delta p_1 + (\varphi_{2,2} \cdot \Delta p_1 - \varphi_{2,2} \cdot \Delta p_2) + \varphi_{2,3} \cdot \Delta p_2 + \Delta p_2 = \Delta p_c \end{cases} \quad \textbf{(B-27)}$$

The system (6-27) is solved for Δp_1 and Δp_2:

$$\Delta p_1 = \frac{(1+\varphi_{1,2}-\varphi_{1,3}+\varphi_{1,2}^2-\varphi_{1,3}\varphi_{2,1}+\varphi_{1,3}\varphi_{2,2}+\varphi_{1,2}\varphi_{2,1}-\varphi_{1,2}\varphi_{2,2}+\varphi_{1,3}\varphi_{1,1}-\varphi_{1,3}\varphi_{1,2}-\varphi_{1,2}\varphi_{1,1})}{(1+\varphi_{1,2}-\varphi_{1,1})\cdot(1+\varphi_{2,3}-\varphi_{2,2})-(\varphi_{2,2}-\varphi_{2,1})\cdot(\varphi_{1,3}-\varphi_{1,2})} \Delta p_c$$

$$\Delta p_2 = \frac{(1+\varphi_{1,2}-\varphi_{1,1}+\varphi_{2,1}-\varphi_{2,2})}{(1+\varphi_{1,2}-\varphi_{1,1})\cdot(1+\varphi_{2,3}-\varphi_{2,2})-(\varphi_{2,2}-\varphi_{2,1})\cdot(\varphi_{1,3}-\varphi_{1,2})} \Delta p_c$$

and herefrom arise the resulting surface loads acting on each glass pane:

$$\begin{cases} p_{res,1} = p_{e,1} - \Delta p_1 \\ p_{res,2} = \Delta p_1 - \Delta p_2 \\ p_{res,3} = \Delta p_2 + p_{e,3} \end{cases}$$

$$\begin{cases} p_{res,1} = -\frac{(1+\varphi_{1,2}-\varphi_{1,3}+\varphi_{1,2}^2-\varphi_{1,3}\varphi_{2,1}+\varphi_{1,3}\varphi_{2,2}+\varphi_{1,2}\varphi_{2,1}-\varphi_{1,2}\varphi_{2,2}+\varphi_{1,3}\varphi_{1,1}-\varphi_{1,3}\varphi_{1,2}-\varphi_{1,2}\varphi_{1,1})}{(1+\varphi_{1,2}-\varphi_{1,1})\cdot(1+\varphi_{2,3}-\varphi_{2,2})-(\varphi_{2,2}-\varphi_{2,1})\cdot(\varphi_{1,3}-\varphi_{1,2})} \Delta p_c \\ p_{res,2} = \frac{(\varphi_{1,1}+\varphi_{2,2}-\varphi_{2,1}-\varphi_{1,3}+\varphi_{1,2}^2-\varphi_{1,3}\varphi_{2,1}+\varphi_{1,3}\varphi_{2,2}+\varphi_{1,2}\varphi_{2,1}-\varphi_{1,2}\varphi_{2,2}+\varphi_{1,3}\varphi_{1,1}-\varphi_{1,3}\varphi_{1,2}-\varphi_{1,2}\varphi_{1,1})}{(1+\varphi_{1,2}-\varphi_{1,1})\cdot(1+\varphi_{2,3}-\varphi_{2,2})-(\varphi_{2,2}-\varphi_{2,1})\cdot(\varphi_{1,3}-\varphi_{1,2})} \Delta p_c \\ p_{res,3} = \frac{(1+\varphi_{1,2}-\varphi_{1,1}+\varphi_{2,1}-\varphi_{2,2})}{(1+\varphi_{1,2}-\varphi_{1,1})\cdot(1+\varphi_{2,3}-\varphi_{2,2})-(\varphi_{2,2}-\varphi_{2,1})\cdot(\varphi_{1,3}-\varphi_{1,2})} \Delta p_c \end{cases}$$

(B-28)

The expressions are still complex, but the distribution of the climate loads on each glass pane can be seen.

From the equations (6-13), (6-14) and (6-20) arise the dependency of the coupling factors on nine volume coefficients $\vartheta_{1,1}$, $\vartheta_{1,2}$, $\vartheta_{2,1}$, $\vartheta_{2,2}$, $\vartheta_{1,3}$, $\vartheta_{3,1}$, $\vartheta_{2,3}$, $\vartheta_{3,2}$, and $\vartheta_{3,3}$. As it is the case for double insulation glass, the coefficients have to be determined numerically. For quick calculation of the climate loads, it is possible to implement the general solution of the system of equations (6-26) into a spreadsheet application tool (e.g. Microsoft Excel).

The volume coefficients are tabulated for 4 standard geometries of point fitted IGU. The size and the thickness of the inner and outer glass panes, the dimensions of the edge bond and

the edge distances of the point fittings correspond to standard values that are commonly used for point fitted insulation glass in glazing façades.

B.4 Volume coefficients for standard geometries of point fitted IGU

The thicknesses t_i = 20 mm and t_e = 16 mm refer to laminated glass of 2 x 10 mm glass panes respectively 2 x 8 mm glass panes.

The volume coefficients are derived for a cavity thickness of 16 mm and are also valid for a cavity thickness of 12 mm.

1200 x 1200 mm

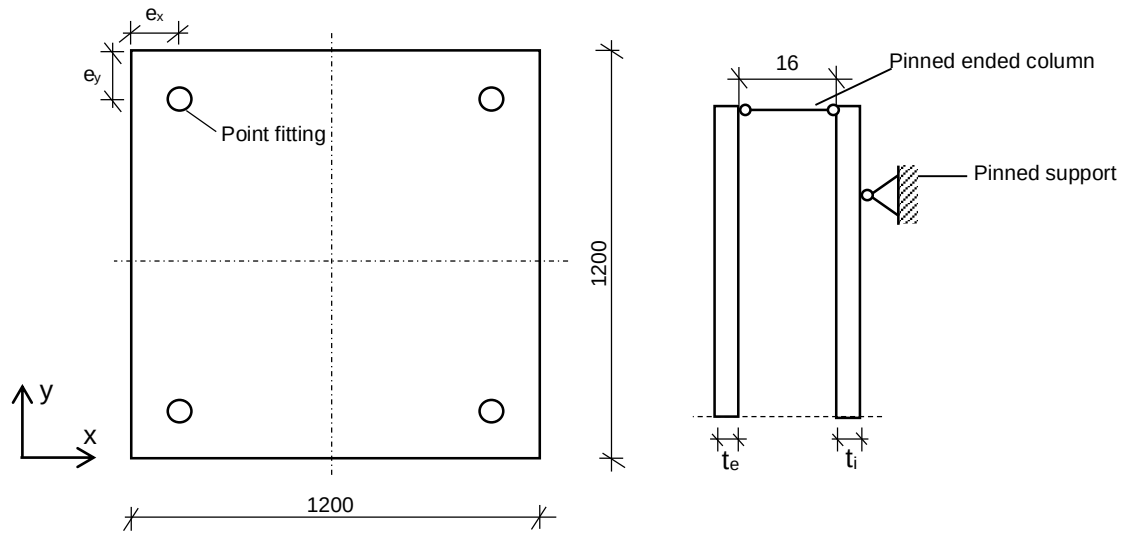

Table B.1 Volume coefficients for edge distance e_x x e_y = 60x60 mm

L_x x L_y	e_x x e_y	t_i	t_e	ϑ_{11}	ϑ_{12}	ϑ_{21}	ϑ_{22}
[mm]	[mm]	[mm]	[mm]	[m^3/(kN/m^2)]	[m^3/(kN/m^2)]	[m^3/(kN/m^2)]	[m^3/(kN/m^2)]
		10	10	0.00285	0.00196	0.00196	0.00273
1200 x 1200	60 x 60	12	10	0.00231	0.00144	0.00144	0.00189
		20	8	0.00209	0.00047	0.00047	0.00056

Table B.2 Volume coefficients for edge distance e_x x e_y = 90x90 mm

L_x x L_y	e_x x e_y	t_i	t_e	ϑ_{11}	ϑ_{12}	ϑ_{21}	ϑ_{22}
[mm]	[mm]	[mm]	[mm]	[m^3/(kN/m^2)]	[m^3/(kN/m^2)]	[m^3/(kN/m^2)]	[m^3/(kN/m^2)]
		10	10	0.00223	0.00128	0.00128	0.00198
1200 x 1200	90 x 90	12	10	0.00185	0.00094	0.00094	0.00135
		20	8	0.00194	0.00031	0.00031	0.00039

2500 x 1200 mm

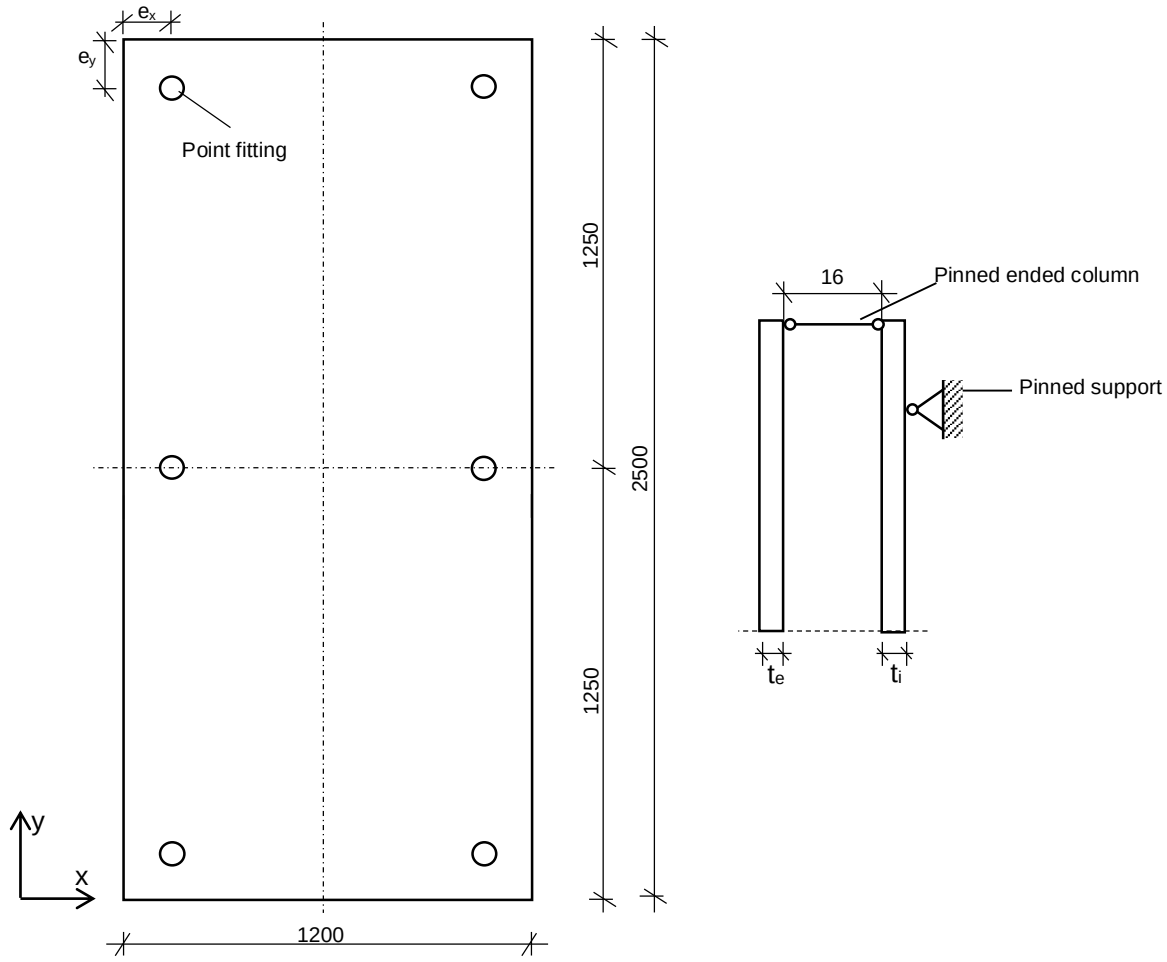

Table B.3 Volume coefficients for edge distance e_x x e_y = 60x60 mm

L_x x L_y	e_x x e_y	t_i	t_e	ϑ_{11}	ϑ_{12}	ϑ_{21}	ϑ_{22}
[mm]	[mm]	[mm]	[mm]	[m³/(kN/m²)]	[m³/(kN/m²)]	[m³/(kN/m²)]	[m³/(kN/m²)]
		10	10	0.00802	0.00239	0.00239	0.00596
2500 x 1200	60 x 60	10	16	0.00277	0.00062	0.00062	0.00419
		12	16	0.00242	0.00070	0.00070	0.00277

Table B.4 Volume coefficients for edge distance e_x x e_y = 150x150 mm

L_x x L_y	e_x x e_y	t_i	t_e	ϑ_{11}	ϑ_{12}	ϑ_{21}	ϑ_{22}
[mm]	[mm]	[mm]	[mm]	[m³/(kN/m²)]	[m³/(kN/m²)]	[m³/(kN/m²)]	[m³/(kN/m²)]
		10	16	0.00358	0.00004	0.00004	0.00193
2500 x 1200	150 x 150	12	16	0.00269	0.00009	0.00009	0.00124
		20	8	0.0095	0.00018	0.00018	0.00043

3000 x 1200 mm

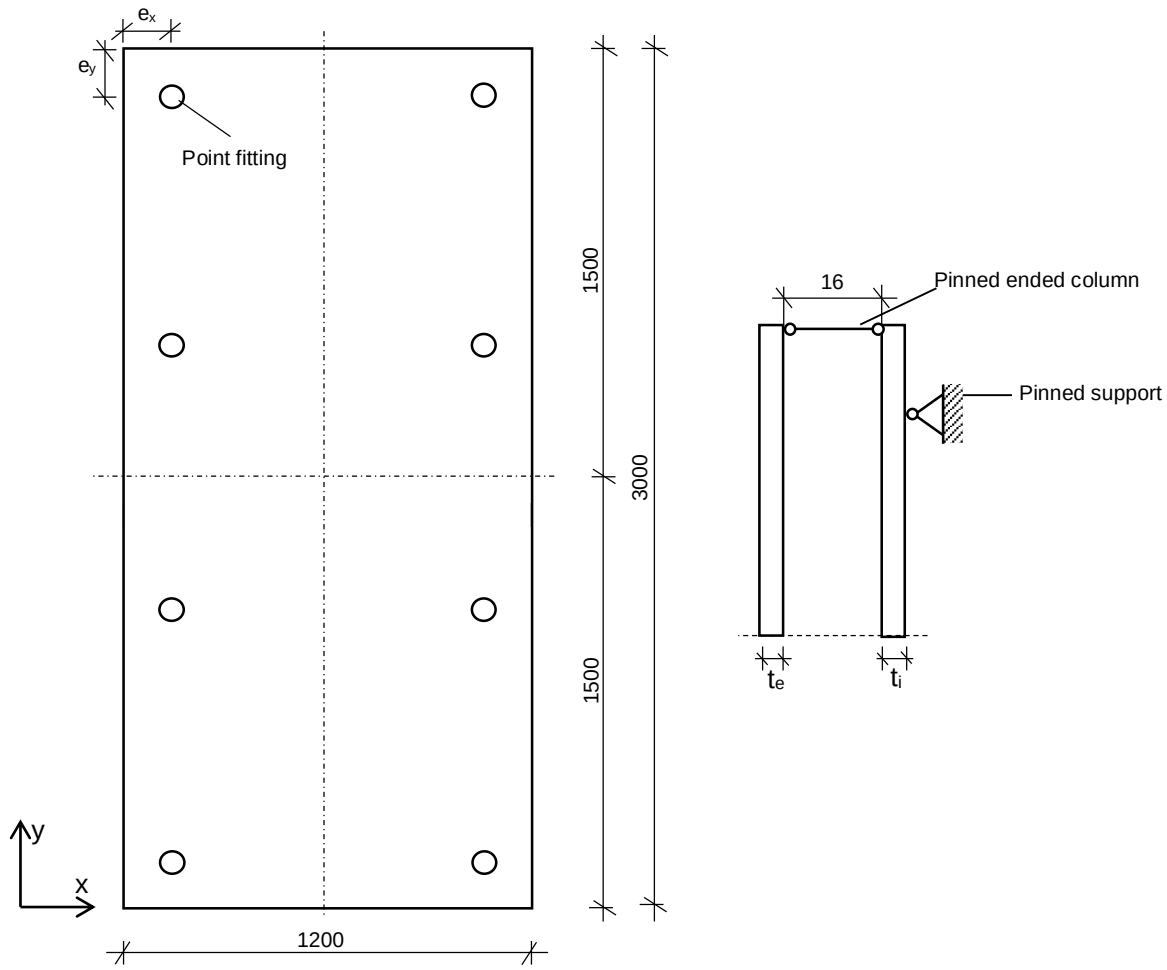

Table B.5 Volume coefficients for edge distance e_x x e_y = 60x60 mm

L_x x L_y [mm]	e_x x e_y [mm]	t_i [mm]	t_e [mm]	ϑ_{11} [$m^3/(kN/m^2)$]	ϑ_{12} [$m^3/(kN/m^2)$]	ϑ_{21} [$m^3/(kN/m^2)$]	ϑ_{22} [$m^3/(kN/m^2)$]
3000 x 1200	60 x 60	10	16	0.00288	0.00012	0.00012	0.00465
		12	10	0.00805	0.00092	0.00092	0.00369
		20	8	0.01278	0.00035	0.00035	0.00095

Table B.6 Volume coefficients for edge distance e_x x e_y = 150x150 mm

L_x x L_y [mm]	e_x x e_y [mm]	t_i [mm]	t_e [mm]	ϑ_{11} [$m^3/(kN/m^2)$]	ϑ_{12} [$m^3/(kN/m^2)$]	ϑ_{21} [$m^3/(kN/m^2)$]	ϑ_{22} [$m^3/(kN/m^2)$]
3000 x 1200	150 x 150	10	16	0.00443	0.0007	0.0007	0.00185
		12	10	0.00827	0.00011	0.00011	0.00137
		20	8	0.01272	0.00002	0.00002	0.00034

2500 x 2000 mm

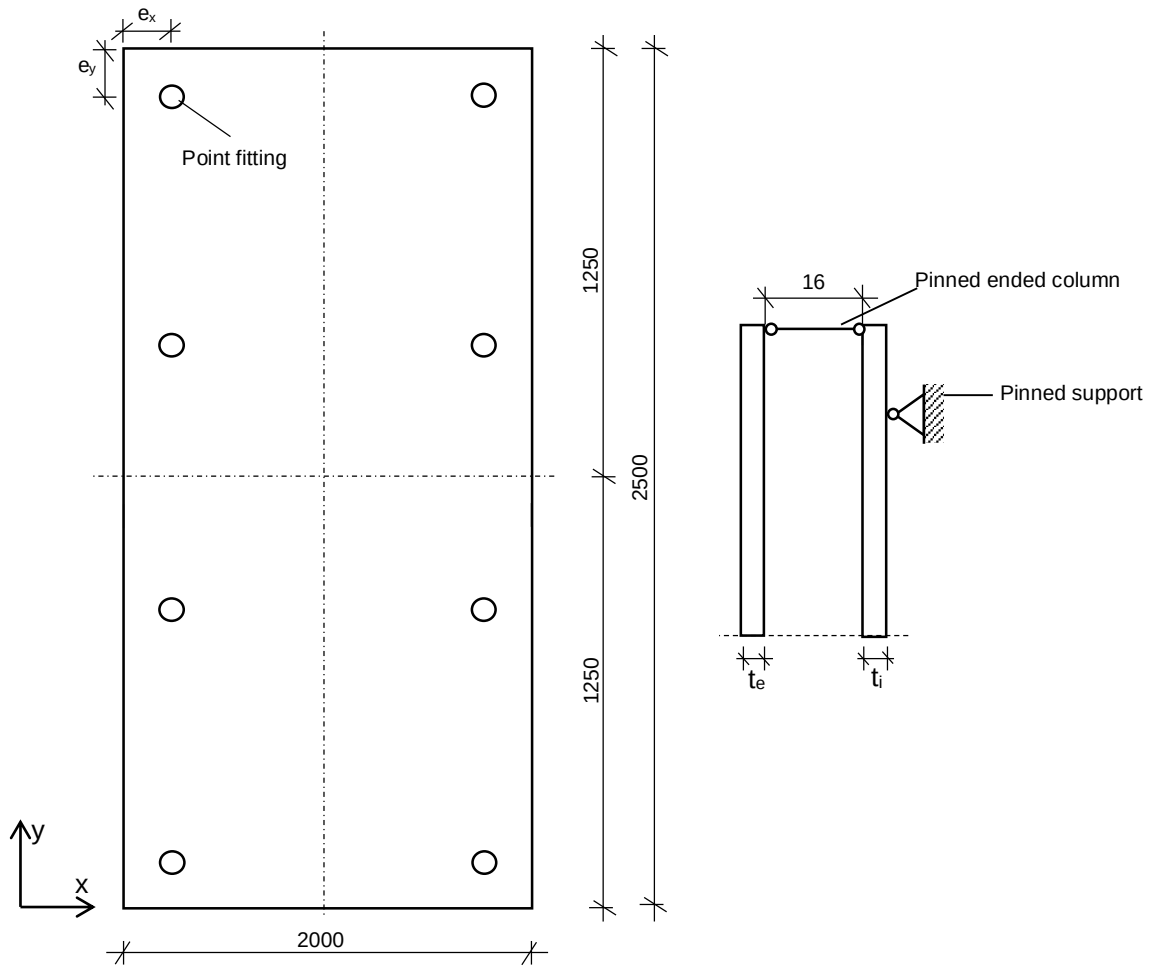

Table B.7 Volume coefficients for edge distance e_x x e_y = 200x200 mm

L_x x L_y [mm]	e_x x e_y [mm]	t_i [mm]	t_e [mm]	ϑ_{11} [m³/(kN/m²)]	ϑ_{12} [m³/(kN/m²)]	ϑ_{21} [m³/(kN/m²)]	ϑ_{22} [m³/(kN/m²)]
2500 x 2000	200 x 200	12	16	0.01638	0.00016	0.00016	0.00976
		20	8	0.06755	0.00161	0.00161	0.00377

C Annexe C – Extension of the SLG-method

C.1 Parameter study for the adaption of the transfer functions

For a given edge bond geometry and outer pane thickness, the transfer functions for the tension force in the point fitting are determined for the different silicone and spacer material laws indicated in Table 8.2. The transfer functions coincide for the different material laws of the silicone sealant (Figure C.1 to Figure C.3). In consequence, the silicone stiffness does not influence the transfer functions.

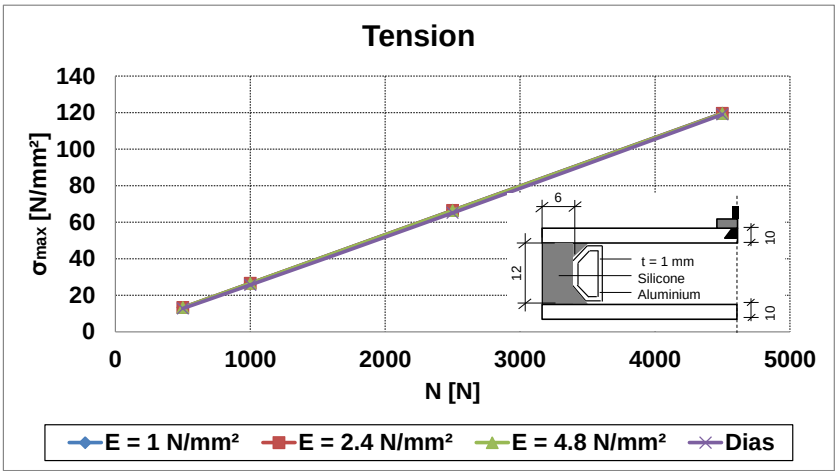

Figure C.1 The transfer functions for the tension loads vs. different silicone material laws

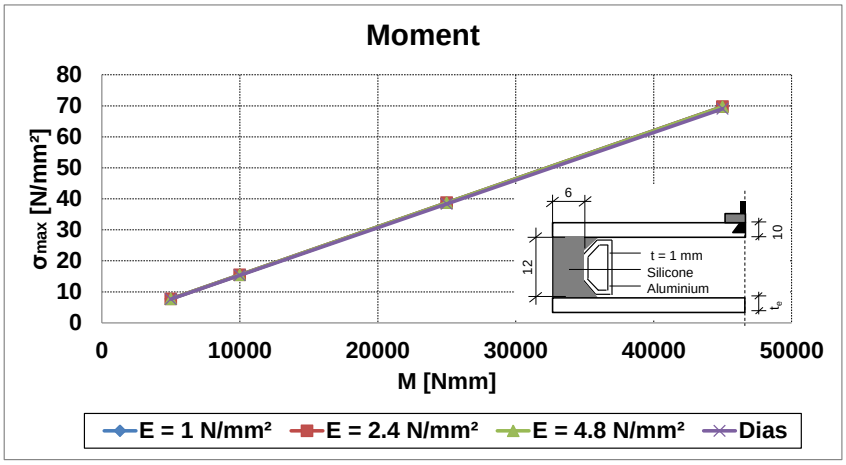

Figure C.2 The transfer functions for the moment loads vs. different silicone material laws

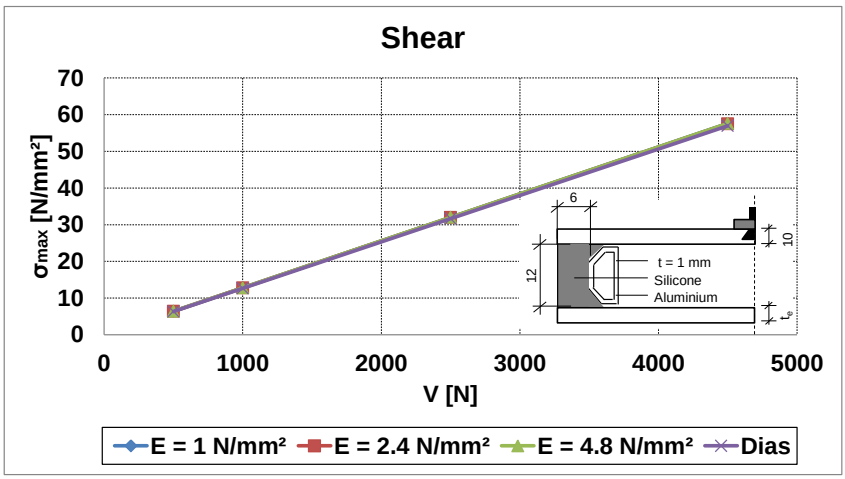

Figure C.3 The transfer functions for the shear loads vs. different silicone material laws

The transfer functions for the different materials of the spacer (Table 8.2) are shown in Figure C.4 to Figure C.6 and no influence of the spacer material on the functions is observed.

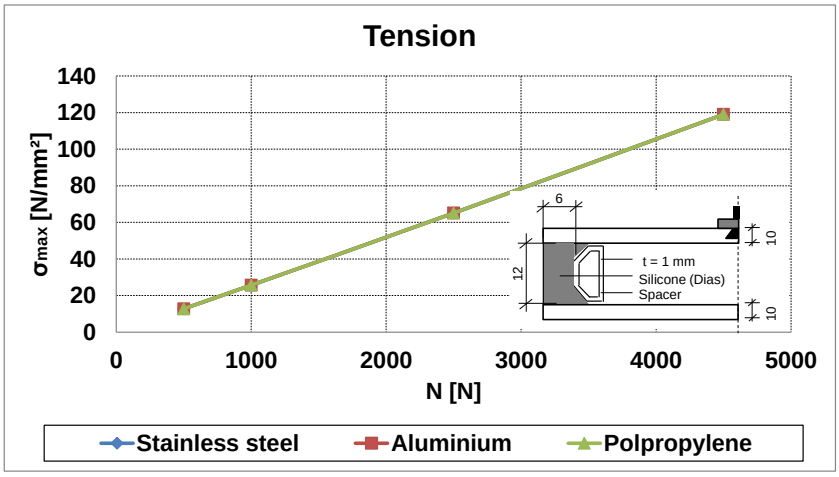

Figure C.4 The transfer functions for the tension loads vs. different silicone material laws

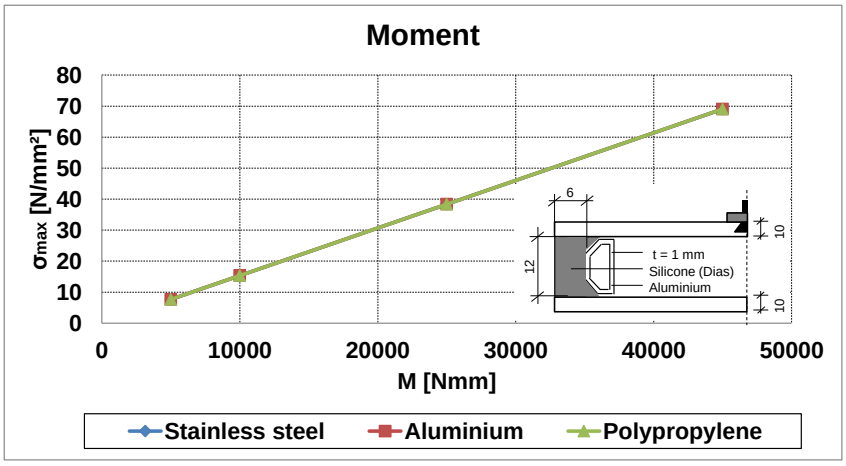

Figure C.5 The transfer functions for the moment loads vs. different spacer materials

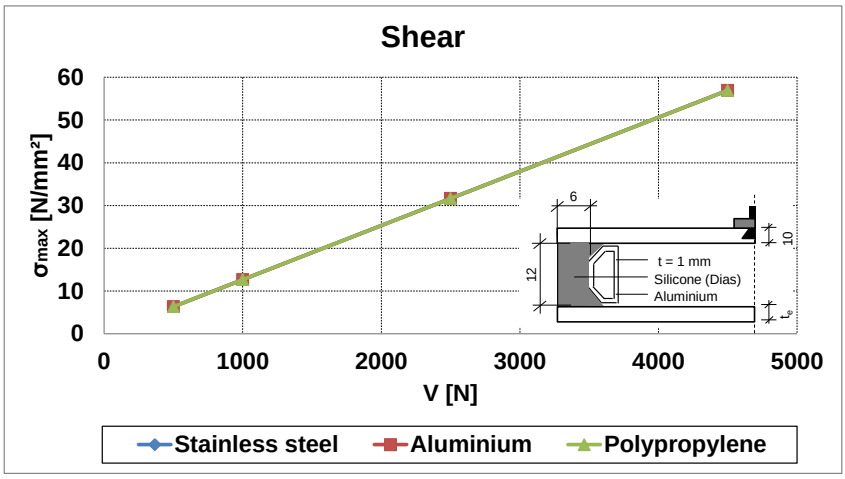

Figure C.6 The transfer functions for the shear loads vs. different spacer materials

For a given silicone sealant law (Hyper-elastic law) and spacer material (Aluminium), the transfer functions are determined for the different edge bond geometries in Table 8.1. The transfer functions perfectly match and the edge bond geometry consequently does not influence the functions (Figure C.7 to Figure C.9).

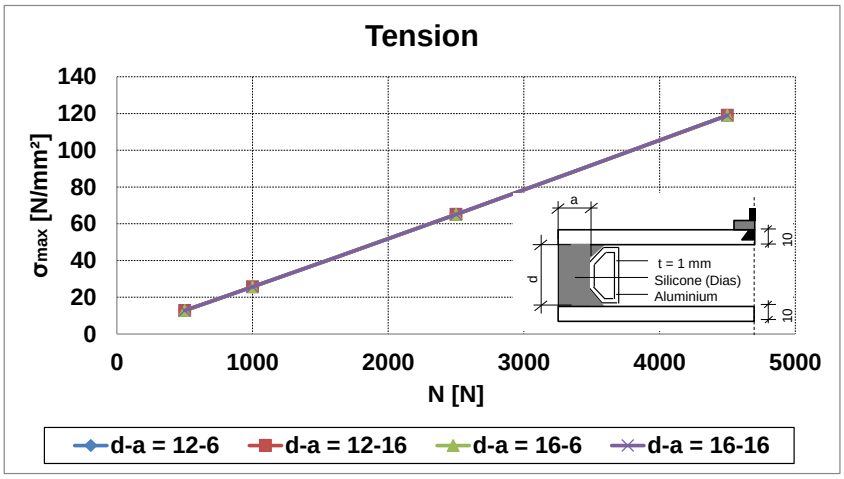

Figure C.7 The transfer functions for the tension loads vs. different edge seal geometries

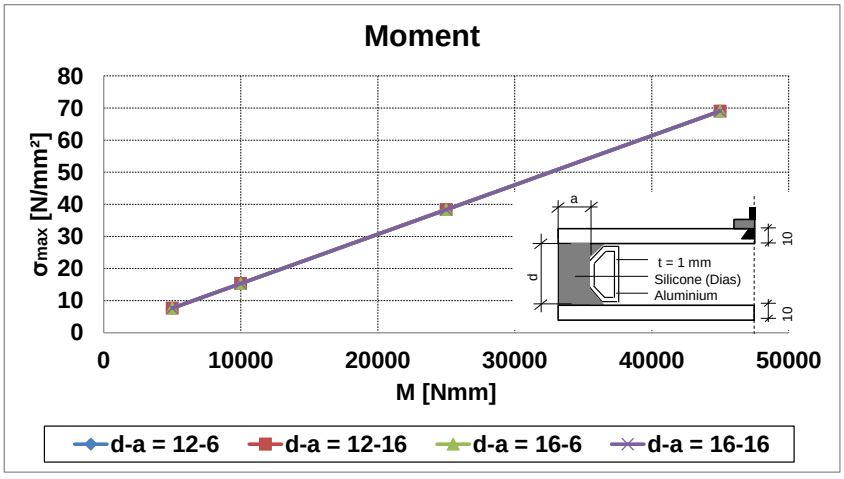

Figure C.8 The transfer functions for the moment loads vs. different edge seal geometries

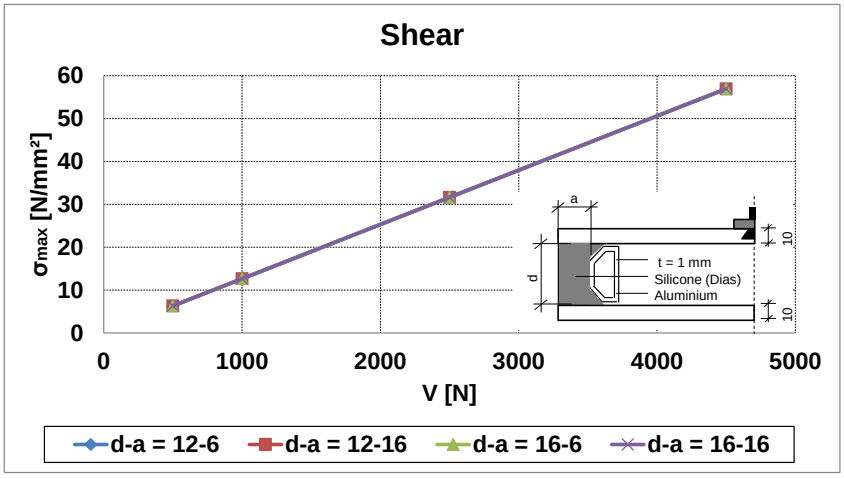

Figure C.9 The transfer functions for the shear loads vs. different edge seal geometries

In Figure C.10 to Figure C.12, the influence of the thickness of the outer pane on the transfer function in investigated and an influence cannot be noticed

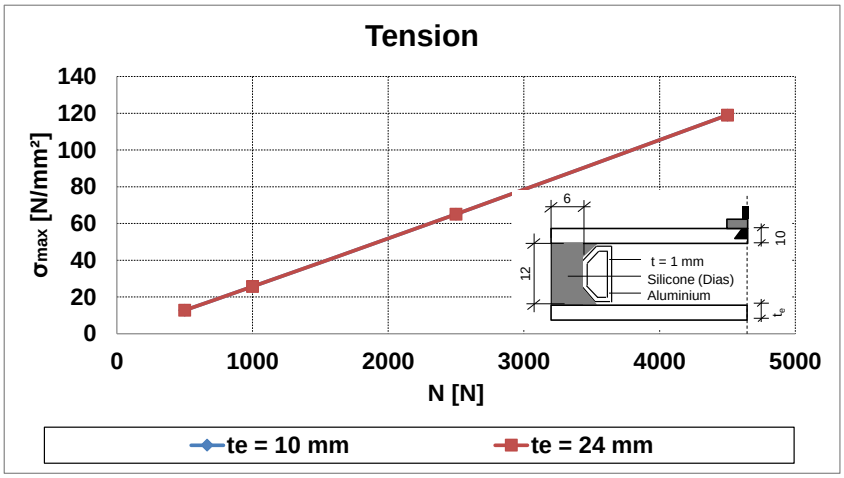

Figure C.10 The transfer functions for the tension loads vs. outer pane thickness

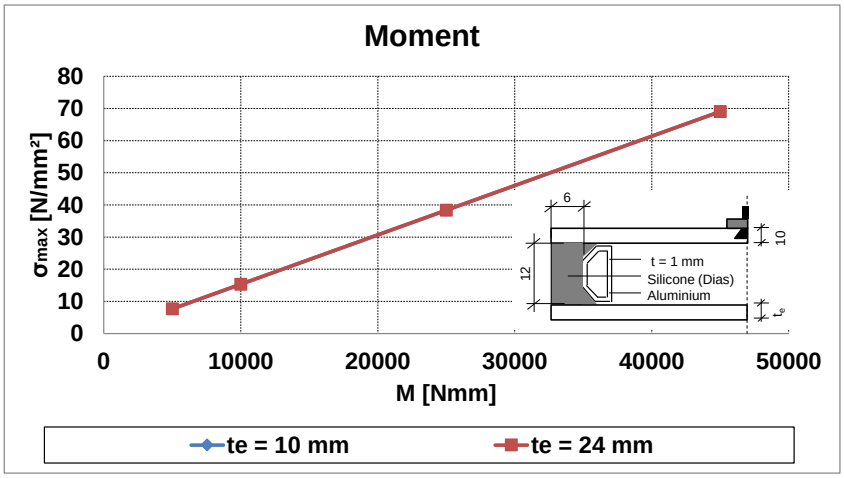

Figure C.11 The transfer functions for the moment loads vs. outer pane thickness

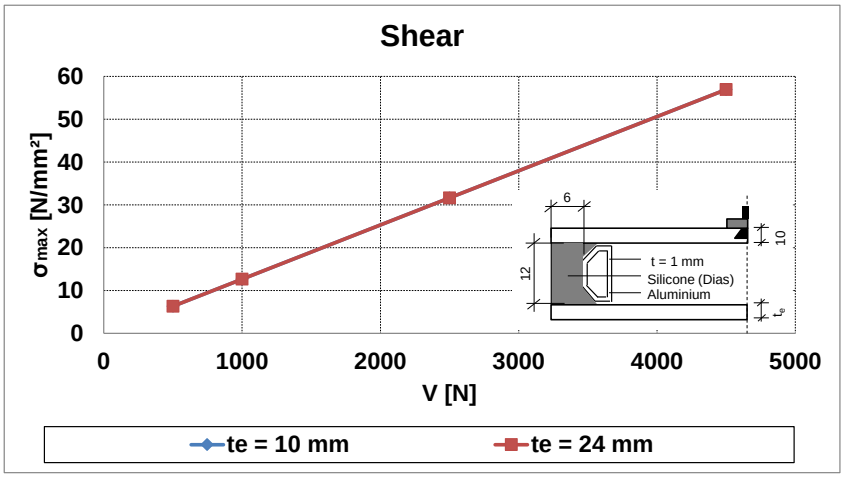

Figure C.12 The transfer functions for the shear loads vs. outer pane thickness

Concerning the thickness of the inner glass pane on the transfer functions, an influence is detected (Figure C.13 to Figure C.15).

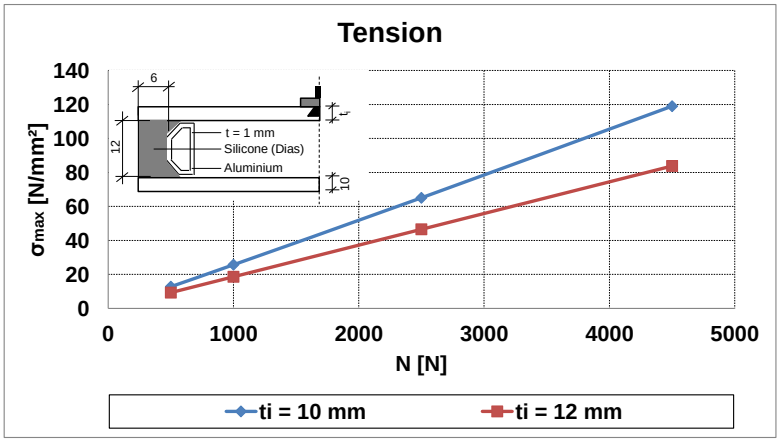

Figure C.13 The transfer functions for the tension loads vs. inner pane thickness

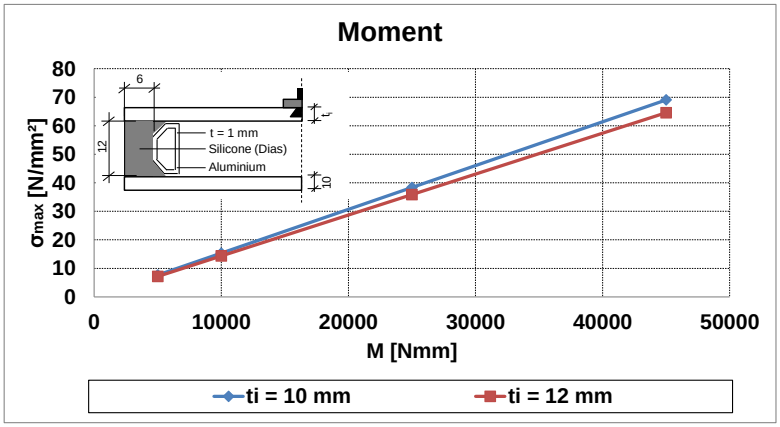

Figure C.14 The transfer functions for the moment loads vs. inner pane thickness

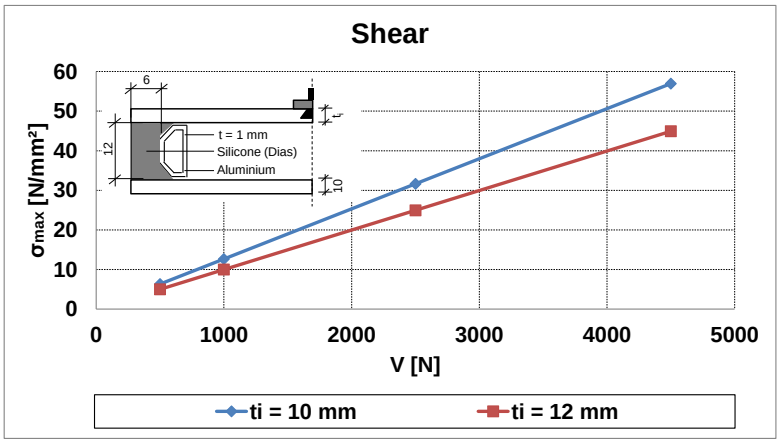

Figure C.15 The transfer functions for the shear loads vs. inner pane thickness

C.2 The transfer functions for t_i = 12mm

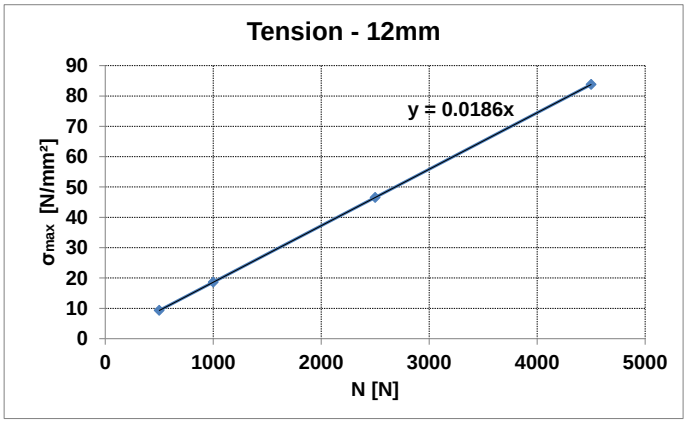

Figure C.16 The transfer function for the tension force in the Fischer undercut anchor, t_i = 12 mm

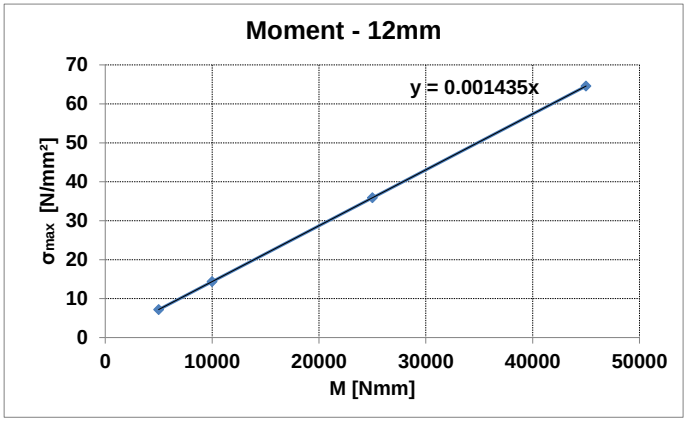

Figure C.17 The transfer function for the moment load in the Fischer undercut anchor, t_i = 12 mm

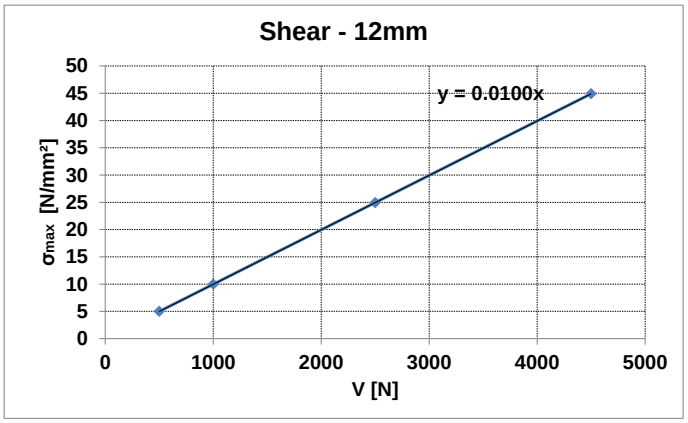

Figure C.18 The transfer function for the shear force in the Fischer undercut anchor, t_i = 12 mm

C.3 Parameter study for the adaption of the k-factors

In the Figure C.19 to Figure C.23, the k-factors are drawn against the thickness ratio of the two glass panes of the IGU for the different silicone material laws in Table 8.2 and the edge bond distances in Table 8.4. The edge sealant geometry and the spacer material are fixed and remain unchanged.

The influence of the stiffness of the silicone sealant on the k-factors increases with increasing thickness ratios and with increasing edge distances of the Fischer anchor. The influence is however slightly pronounced and the maximal deviation is only about 7%. In all cases, the highest values for the k-factors are observed for the hyperelastic material law of *Dias.*

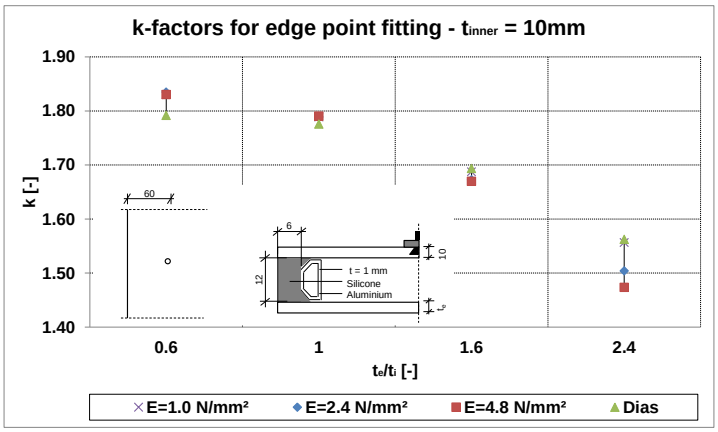

Figure C.19 k-factors for different silicone stiffness values, t_i = 10 mm, e = 60mm

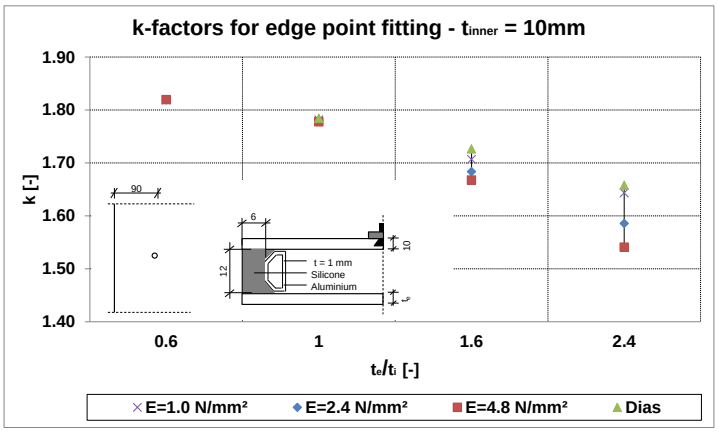

Figure C.20 k-factors for different silicone stiffness values, ti = 10 mm, e = 90mm

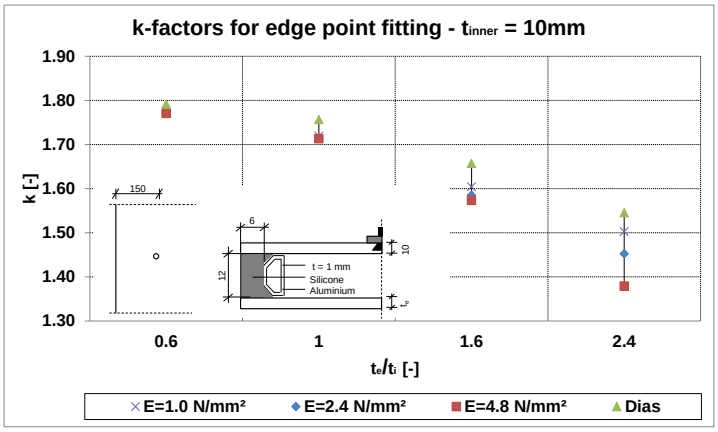

Figure C.21 k-factors for different silicone stiffness values, ti = 10 mm, e = 150mm

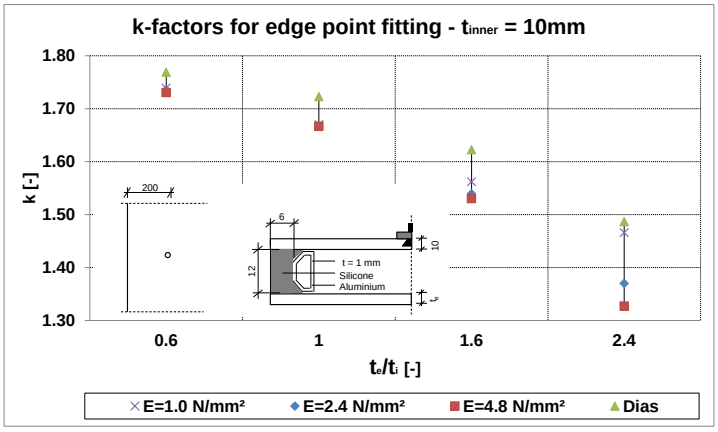

Figure C.22 k-factors for different silicone stiffness values, ti = 10 mm, e = 200mm

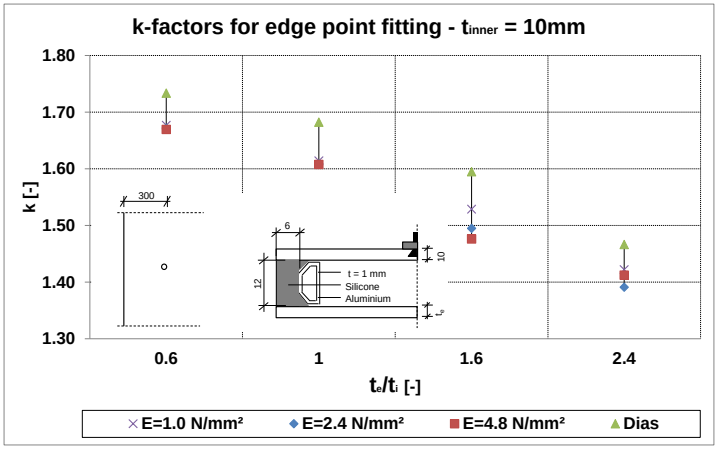

Figure C.23 k-factors for different silicone stiffness values, ti = 10 mm, e = 300mm

Figure C.24 shows the dependency of the k-factors on the spacer materials for a selected edge bond geometry and edge distance of the Fischer undercut anchor. No influence of the spacer material on the k-factor is detected. This is the case for all the different edge bond geometries

(Table 8.1) and edge distances (Table 8.4). Hence, the material of the spacer is not considered in the definition of the stress concentration factors.

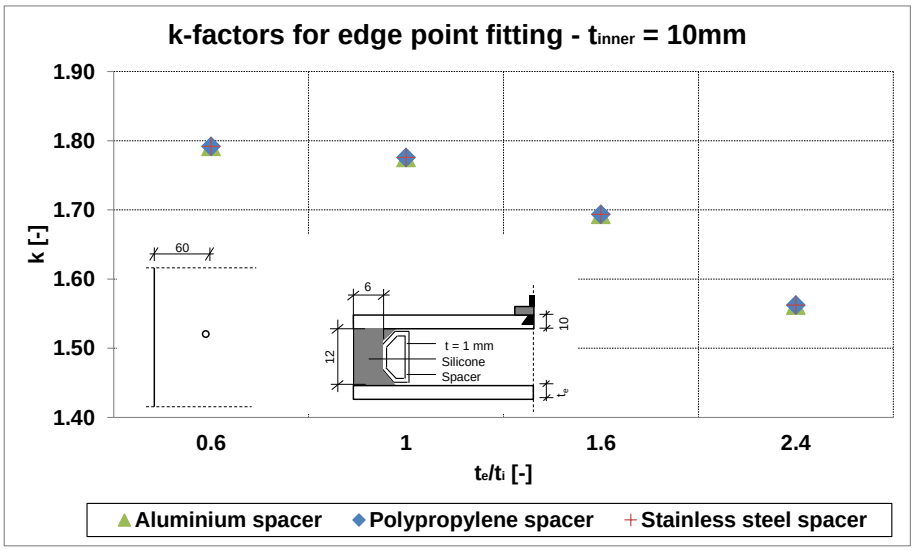

Figure C.24 Influence of the spacer material (stiffness) on the k-factors, t_i = 10 mm, e = 60 mm

The influence of the height of the secondary sealant bite (designated “d” in Figure 8.15) on the stress concentration factor for a given edge distance of the Fischer anchor is presented in Figure C.25. Any influence of the height of the silicone bite on the k-factor is noticed.

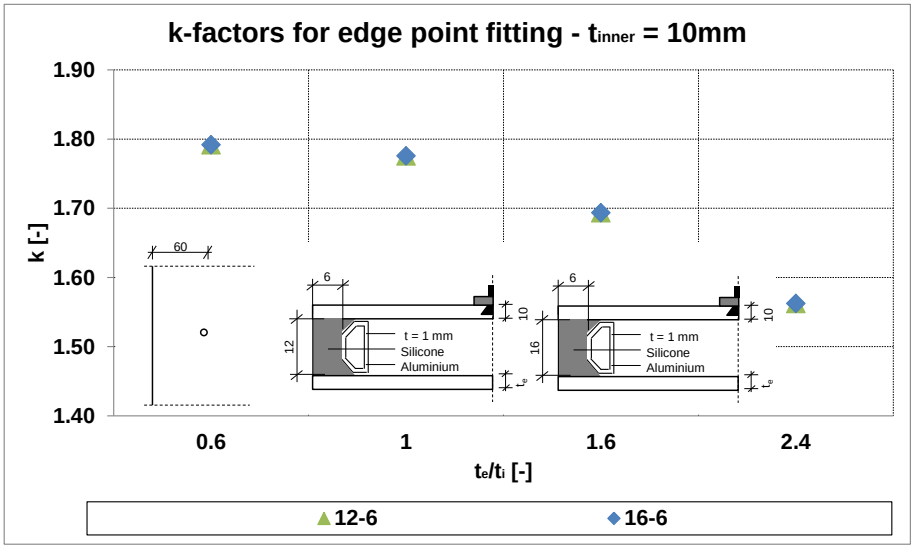

Figure C.25 Influence of the height of the silicone sealant on the k-factors, t_i = 10 mm, e = 60 mm

In Figure C.26, the k-factors are drawn against the various thickness ratios of the glass panes for the different widths of the secondary sealant bite (designated “a” in Figure 8.15). As for the

height of the sealant, no influence of the width of the silicone sealant bite on the k-factor is noticed. This observation can be confirmed for each edge distance.

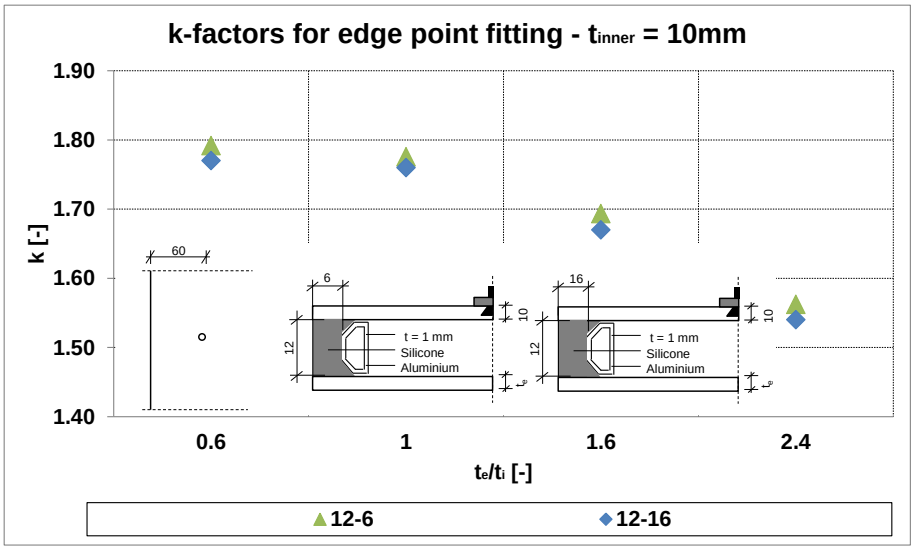

Figure C.26 Influence of the width of the silicone sealant on the k-factors, t_i = 10 mm, e = 60 mm

C.4 The stress concentration factor – Fischer anchor in the edge

In the Figure C.27 to Figure C.31, the stress concentration factors are derived in dependency of the thickness ratio t_e/t_i with an inner pane thickness of t_i = 10 mm.

t_i = 10 mm

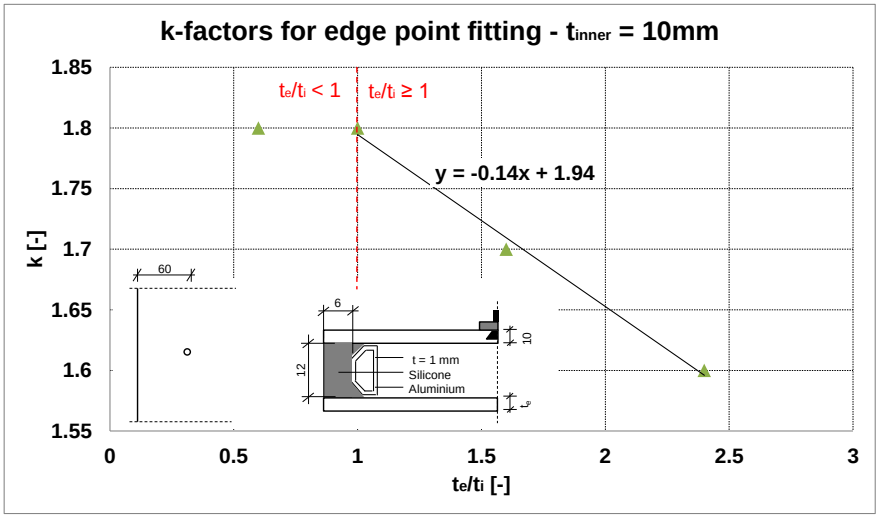

Figure C.27 Determination of the k-factors for t_e/t_i > 1.0, t_i = 10 mm, e = 60mm

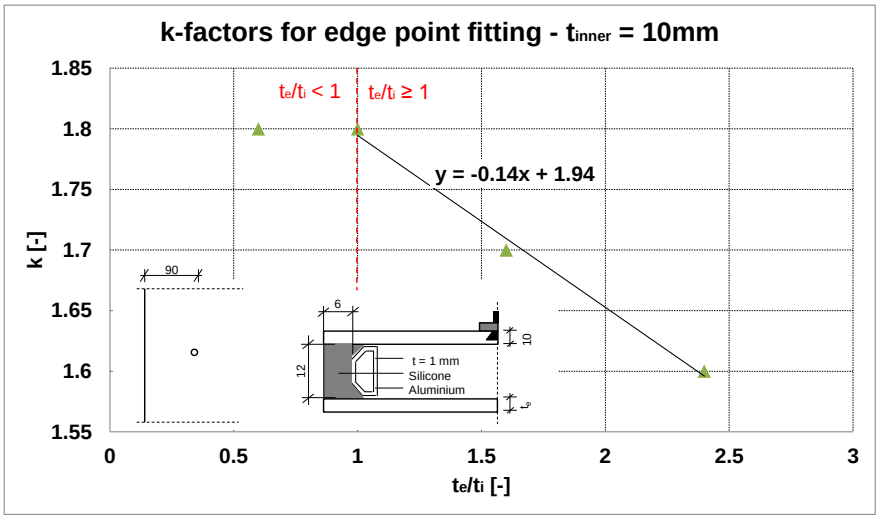

Figure C.28 Determination of the k-factors for $t_e/t_i > 1.0$, $t_i = 10$ mm, e = 90mm

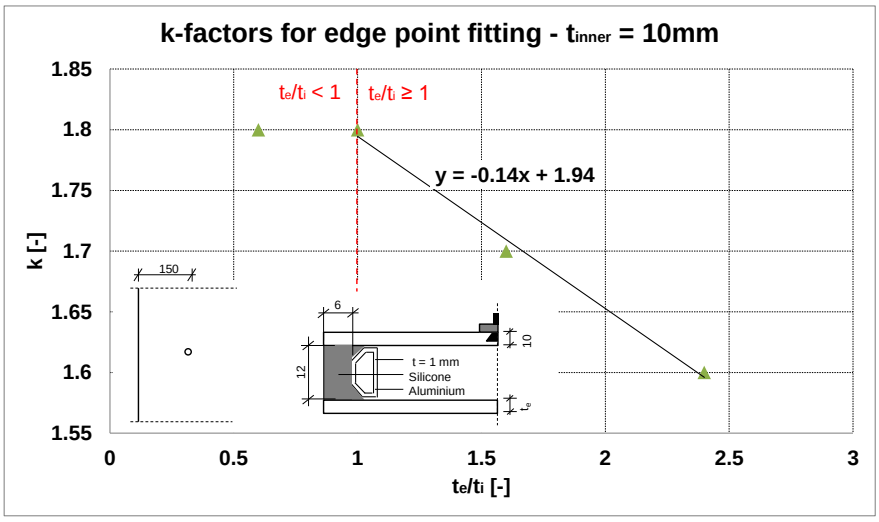

Figure C.29 Determination of the k-factors for $t_e/t_i > 1.0$, $t_i = 10$ mm, e = 150mm

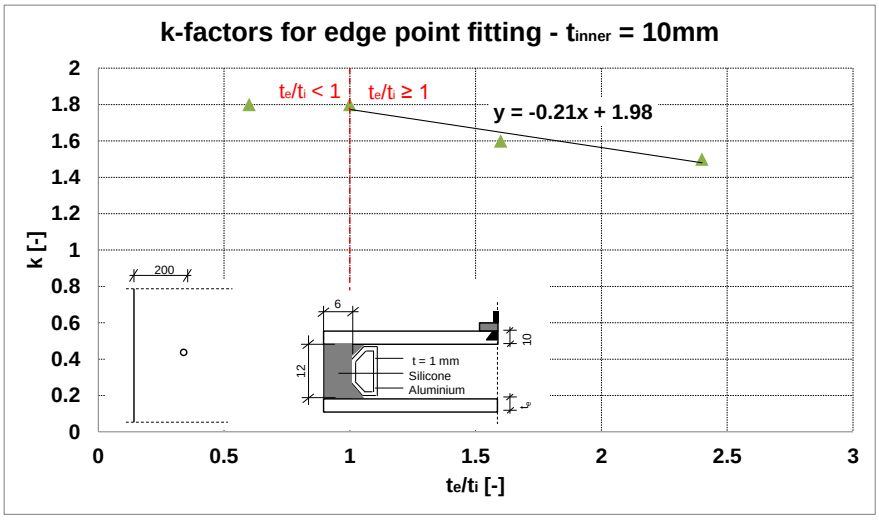

Figure C.30 Determination of the k-factors for $t_e/t_i > 1.0$, $t_i = 10$ mm, e = 200mm

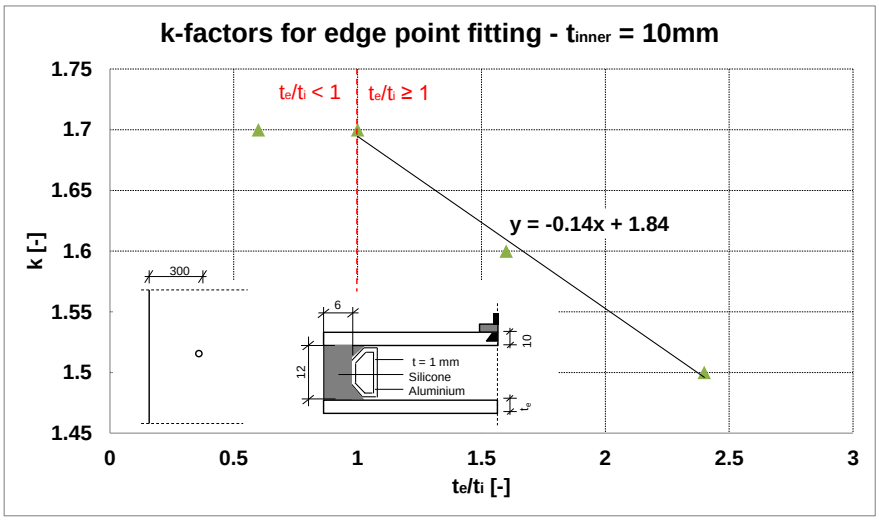

Figure C.31 Determination of the k-factors for $t_e/t_i > 1.0$, $t_i = 10$ mm, e = 300mm

In the Figure C.32 to Figure C.36, the stress concentration factors are derived in dependency of the thickness ratio t_e/t_i with an inner pane thickness of t_i = 12 mm.

t_i = 12 mm

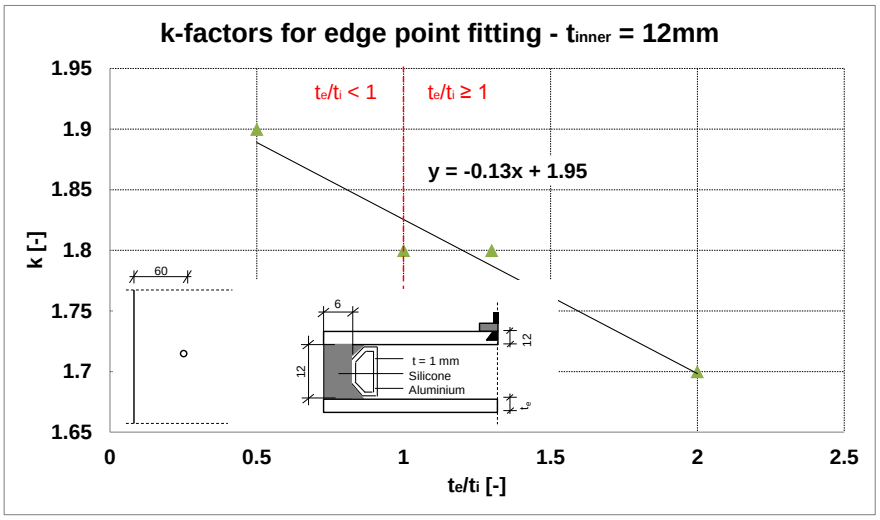

Figure C.32 Determination of the k-factors for t_e/t_i > 1.0, t_i = 12 mm, e = 60mm

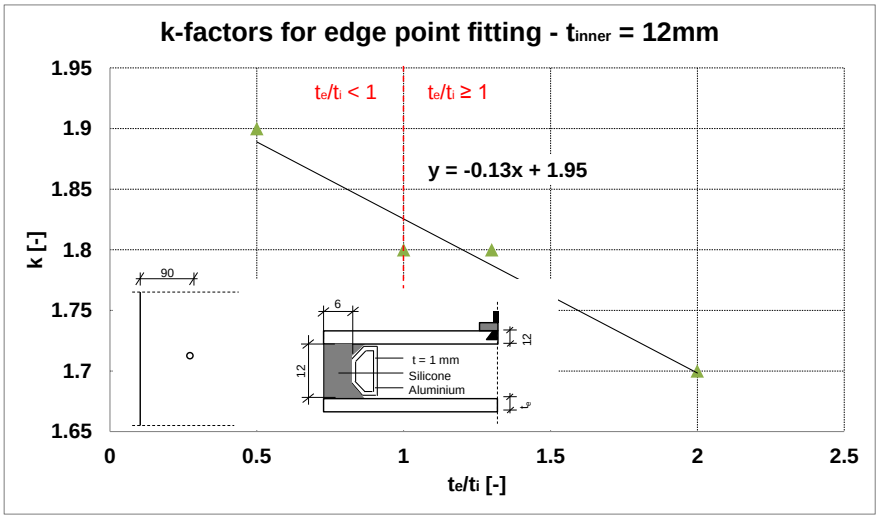

Figure C.33 Determination of the k-factors for t_e/t_i > 1.0, t_i = 12 mm, e = 90mm

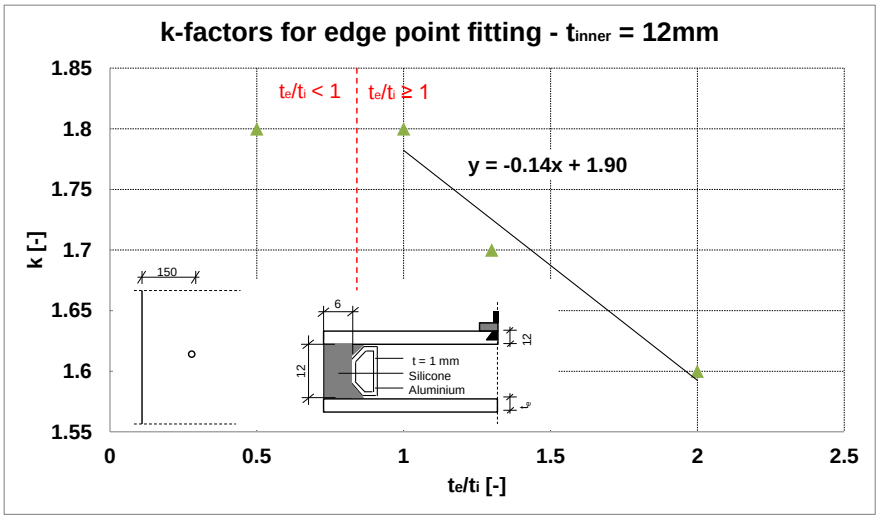

Figure C.34 Determination of the k-factors for $t_e/t_i > 1.0$, $t_i = 12$ mm, e = 150mm

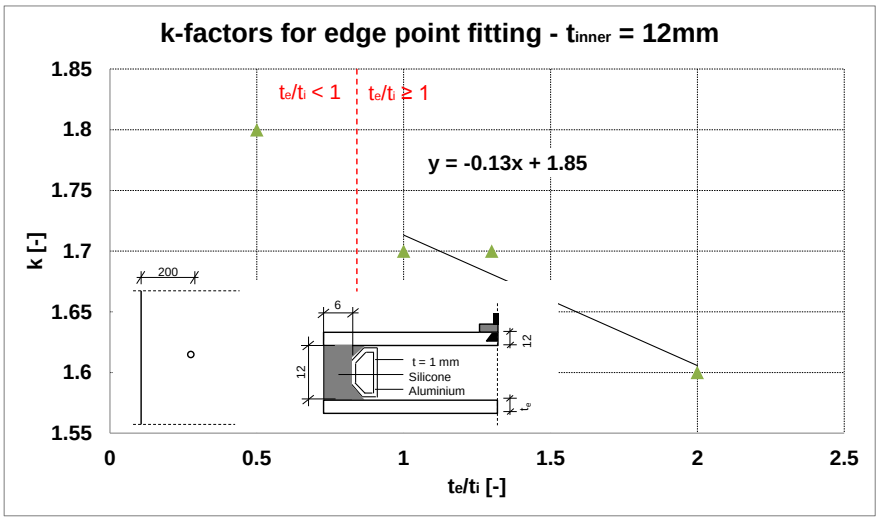

Figure C.35 Determination of the k-factors for $t_e/t_i > 1.0$, $t_i = 12$ mm, e = 200mm

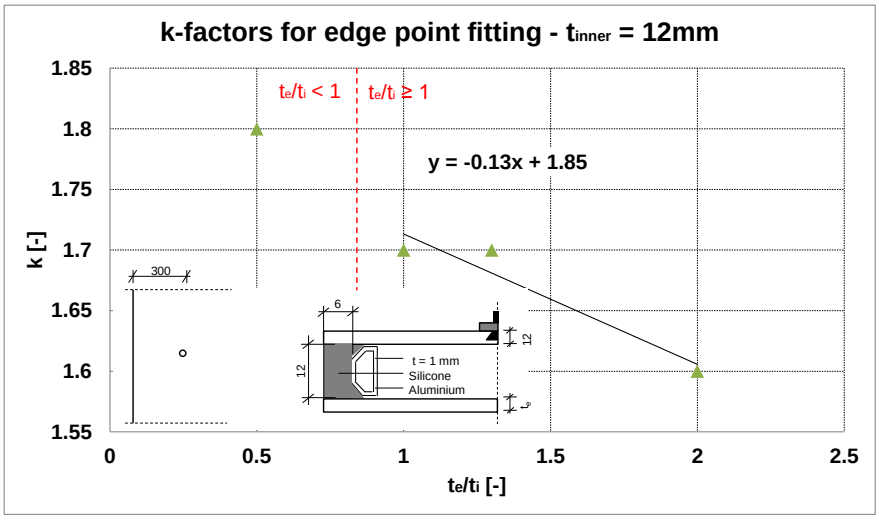

Figure C.36 Determination of the k-factors for t_e/t_i > 1.0, t_i = 12 mm, e = 300mm

D Annexe D – Large scale tests

D.1 1. Test – IGU-O-C1

Table D.1 Test program for 1. test

Specimen	Configuration	Load case	Objective	Load step	Δp [mbar]	p_{ex} [kN/m²]	g [kg]
IGU-O-C1	1	Winter (Δp = -15 mbar)	Verfication of FE-model	1	-3	0	0
				2	-6	0	0
				3	-9	0	0
				4	-12	0	0
				5	-15	0	0
				6	0	0	0
		Summer (Δp = +15 mbar)	Verfication of FE-model	1	3	0	0
				2	6	0	0
				3	9	0	0
				4	12	0	0
				5	15	0	0
				6	0	0	0
		Winter + 3 kN/m²	Experimental verification of extended climate load model	1	-15	0	0
				2	-10.7	1	0
				3	-7	2	0
				4	-3.3	3	0
				5	0	0	0
		Overpressure	Failure in edge bond	1	160	0	0

Δp: Pressure difference in the glazing cavity

p_{ex}: Wind load

g: Self-weight

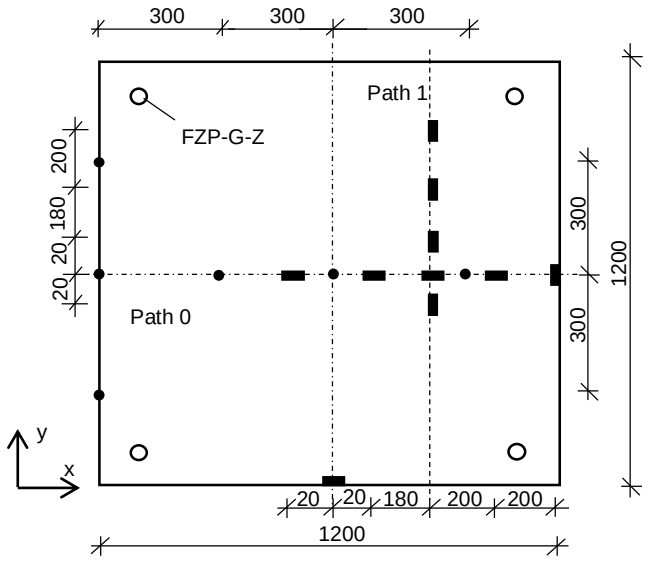

Figure D. 1 Measurement plan for inner glass pane, IGU-O-C1

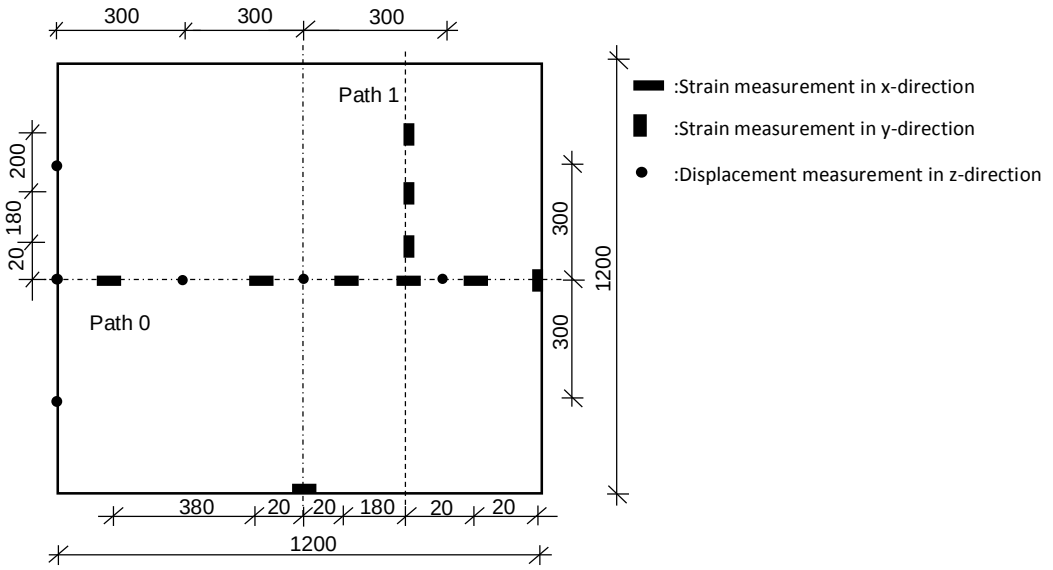

Figure D. 2 Measurement plan for outer glass pane, IGU-O-C1

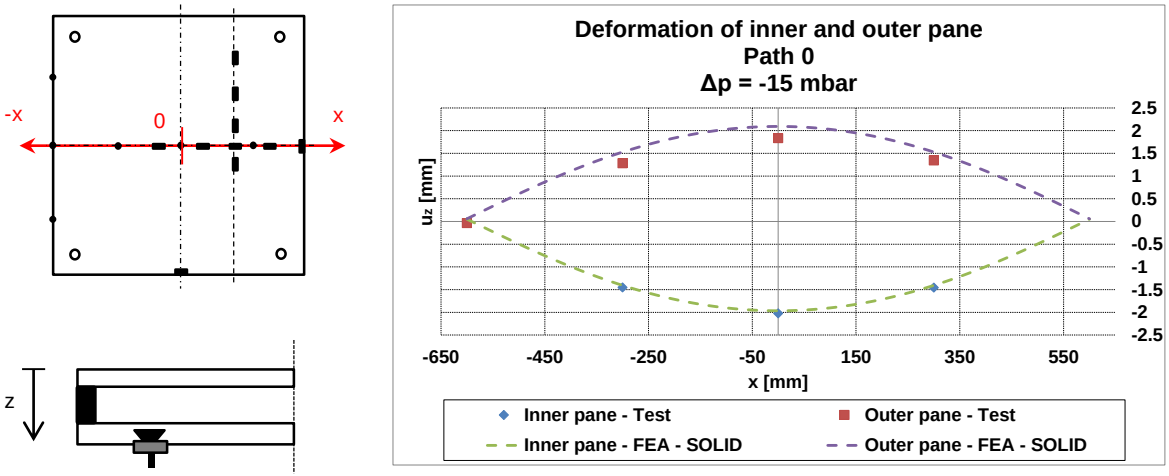

Figure D.3 Deformations of the inner and outer glass pane, Path 0, IGU-O-C1, Load case "Winter"

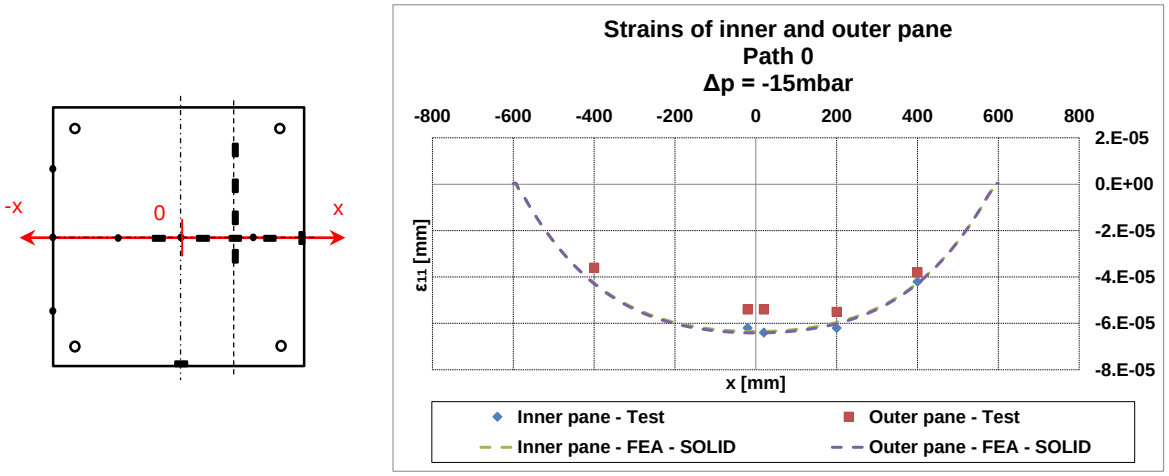

Figure D.4 Strains of the inner and outer glass pane, Path 0, IGU-O-C1, Load case "Winter"

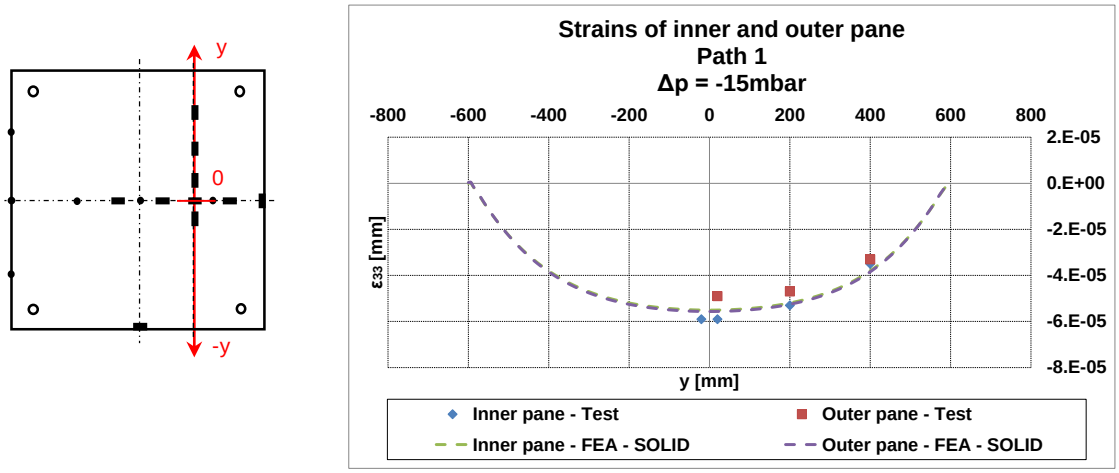

Figure D.5 Strains of the inner and outer glass pane, Path 1, IGU-O-C1, Load case "Winter"

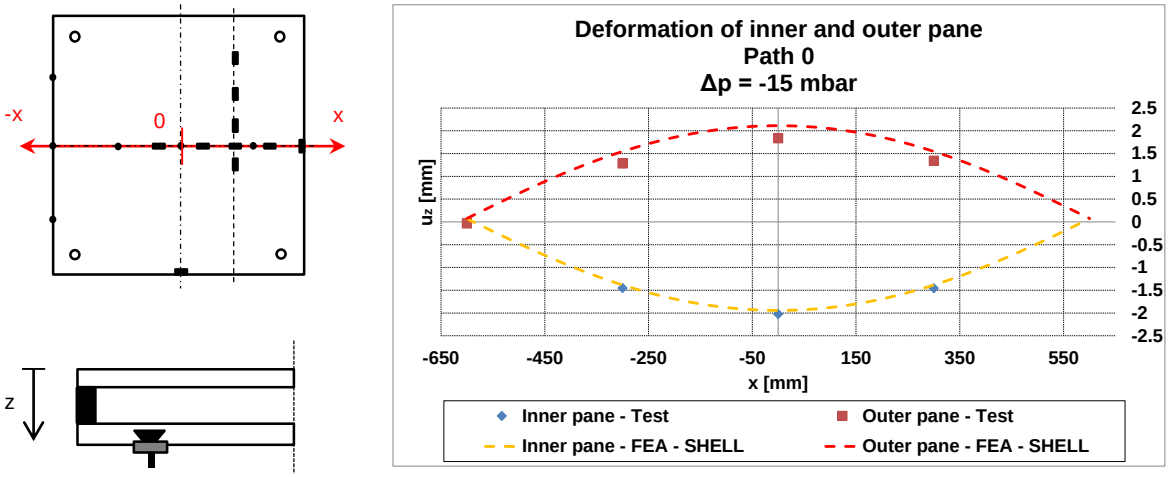

Figure D.6 Deformations of the inner and outer glass pane, Path 0, IGU-O-C1, Load case "Winter"

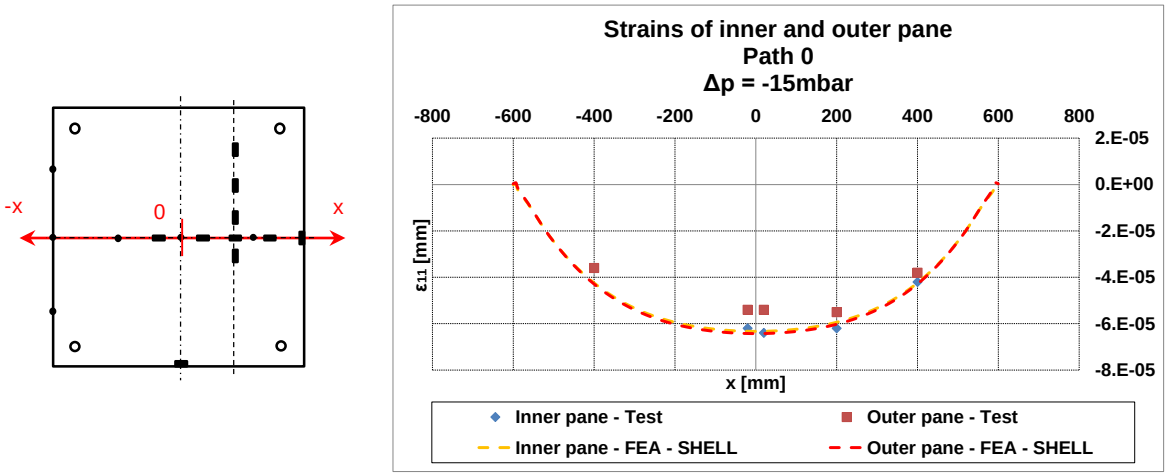

Figure D.7 Strains of the inner and outer glass pane, Path 0, IGU-O-C1, Load case "Winter"

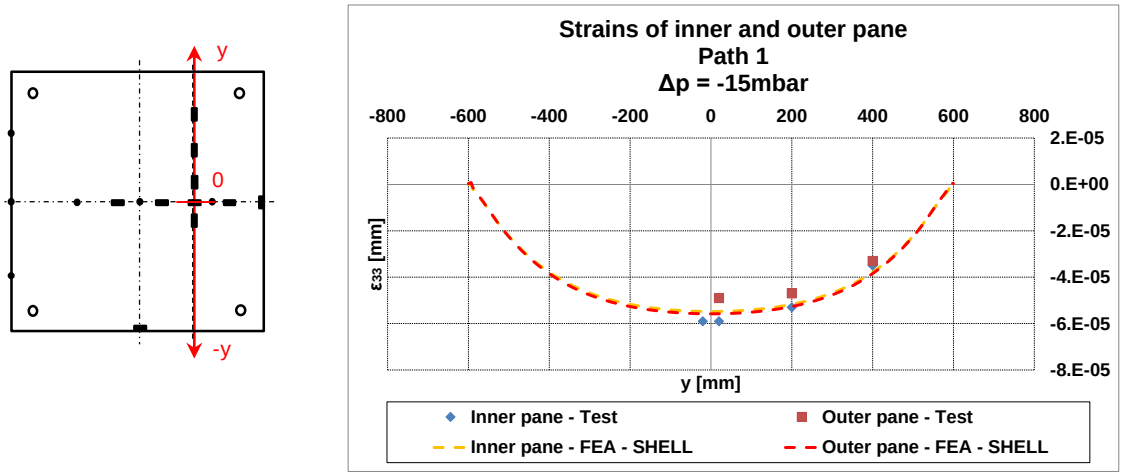

Figure D.8 Strains of the inner and outer glass pane, Path 1, IGU-O-C1, Load case "Winter"

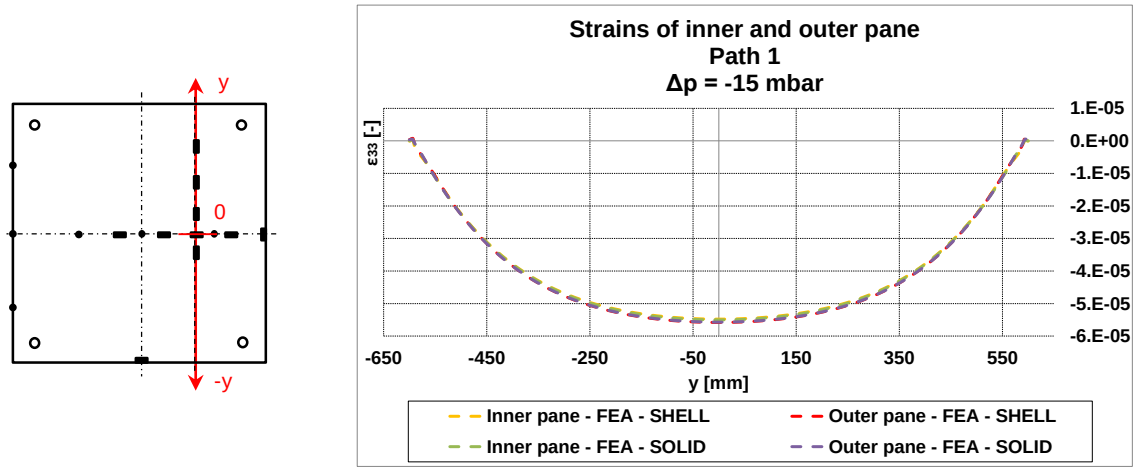

Figure D. 9 Comparison of the strains between the 3D Solid and the simple 2D FE-model, Path 1, IGU-O-C1, Load case "Winter"

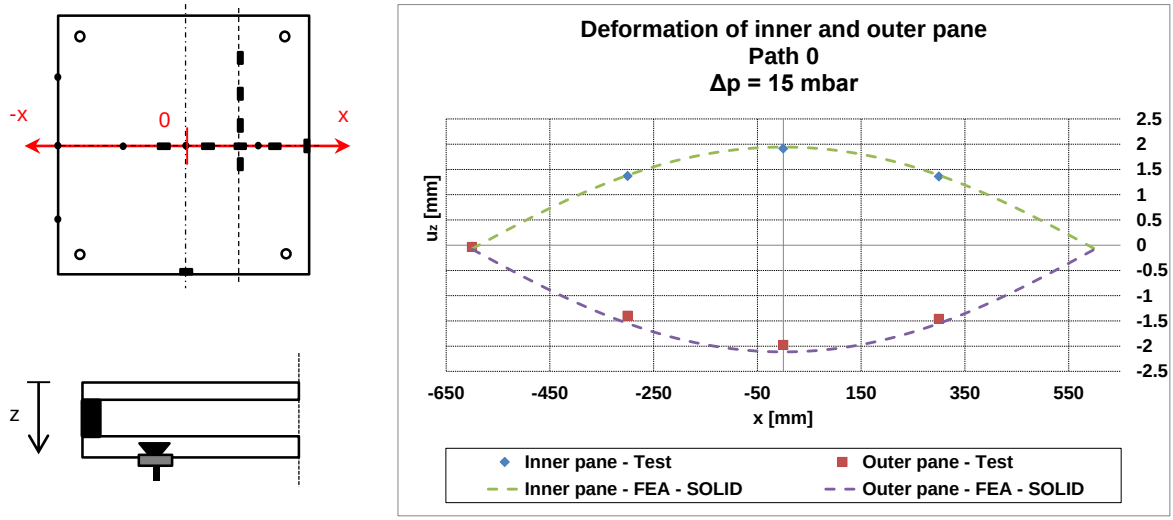

Figure D.10 Deformations of the inner and outer glass pane, Path 0, IGU-O-C1, Load case "Summer"

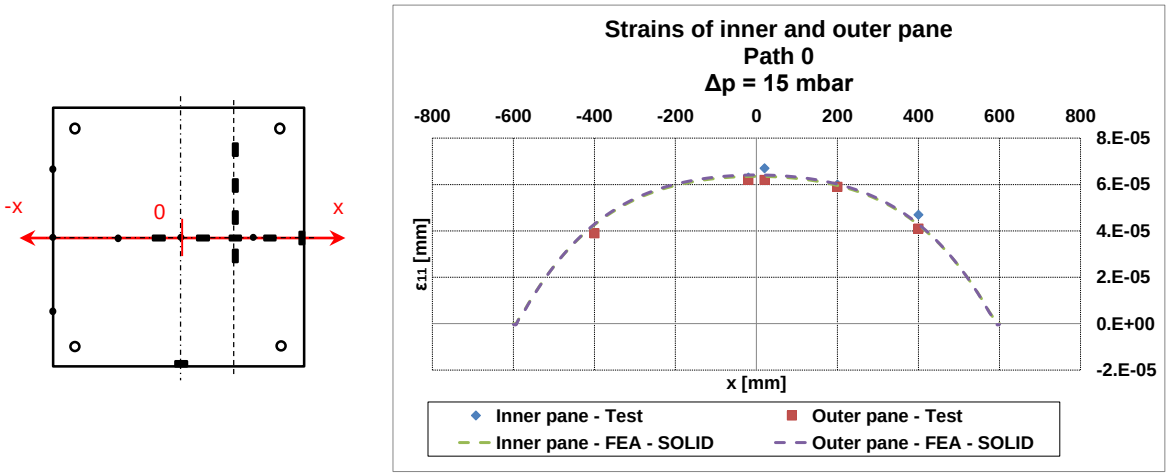

Figure D.11 Strains of the inner and outer glass pane, Path 0, IGU-O-C1, Load case "Summer"

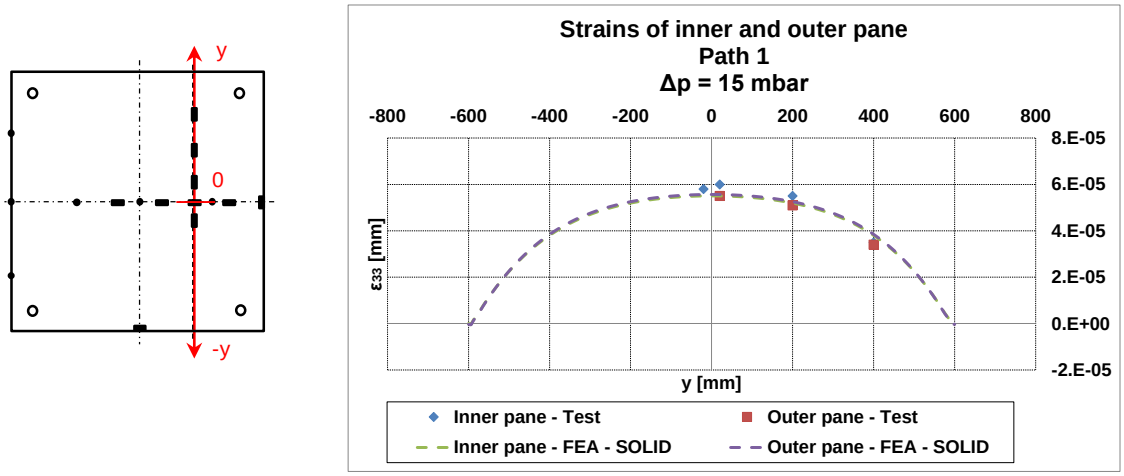

Figure D.12 Strains of the inner and outer glass pane, Path 1, IGU-O-C1, Load case "Summer"

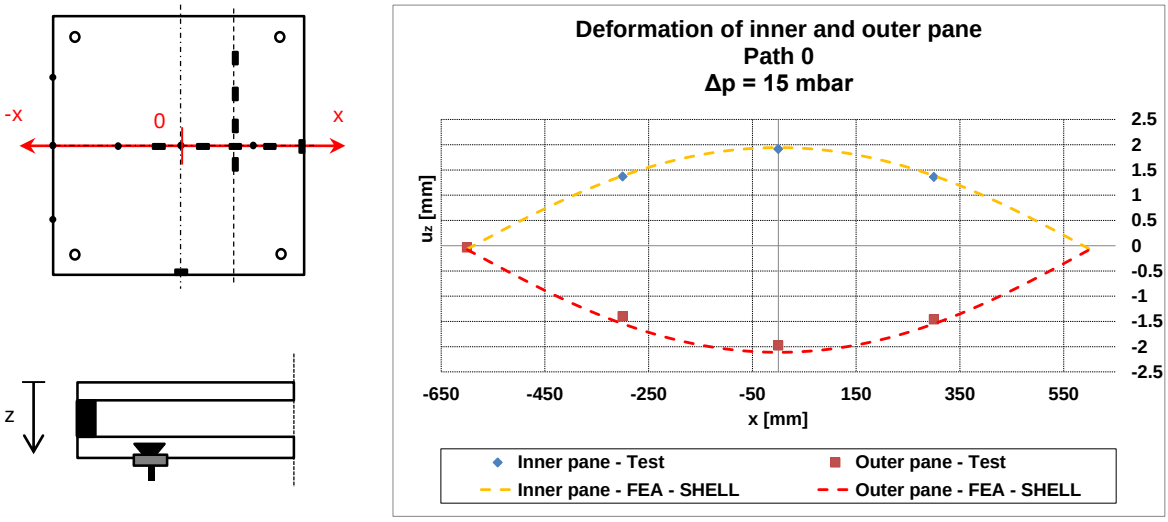

Figure D.13 Deformations of the inner and outer glass pane, Path 0, IGU-O-C1, Load case "Summer"

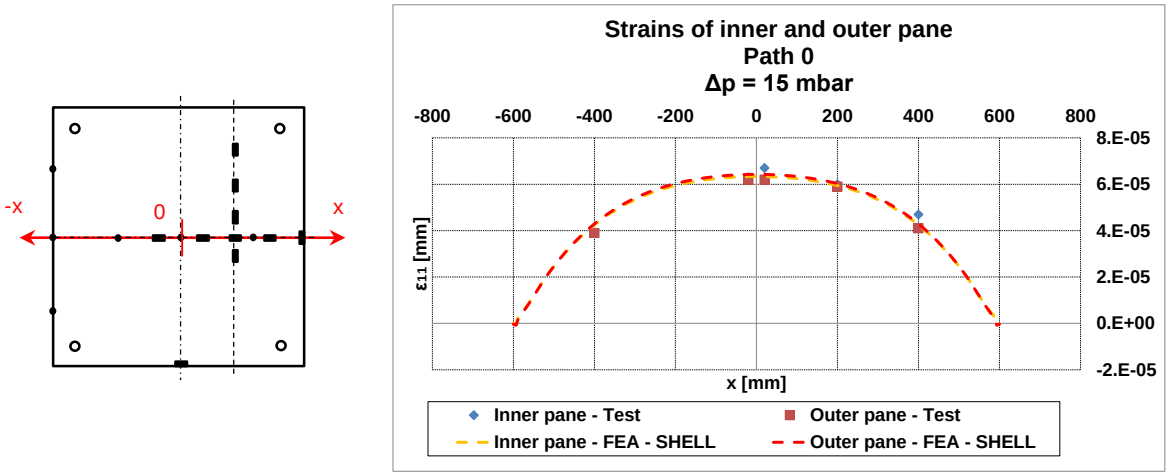

Figure D.14 Strains of the inner and outer glass pane, Path 0, IGU-O-C1, Load case "Summer"

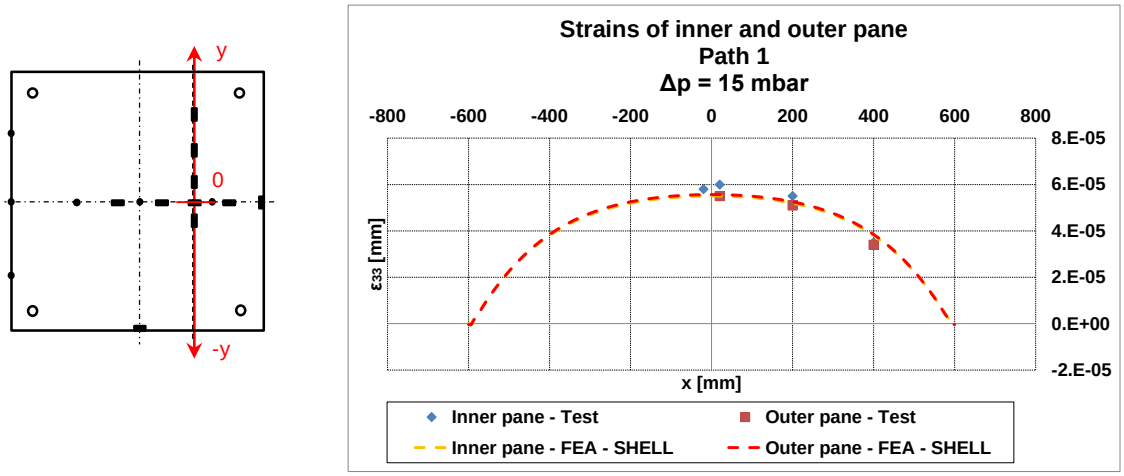

Figure D.15 Strains of the inner and outer glass pane, Path 1, IGU-O-C1, Load case "Summer"

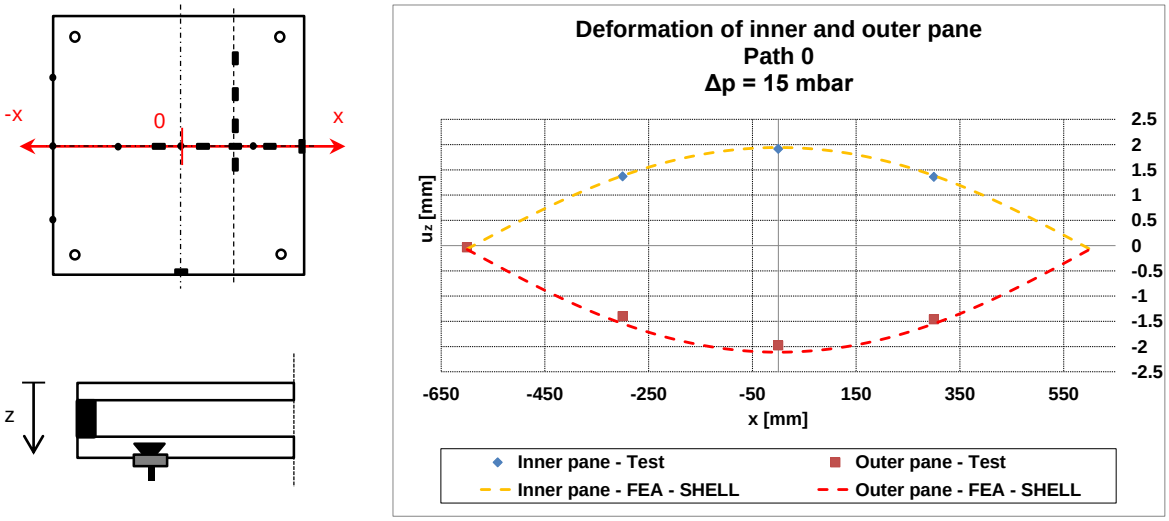

Figure D.16 Deformations of the inner and outer glass pane, Path 0, IGU-O-C1, Load case "Summer"

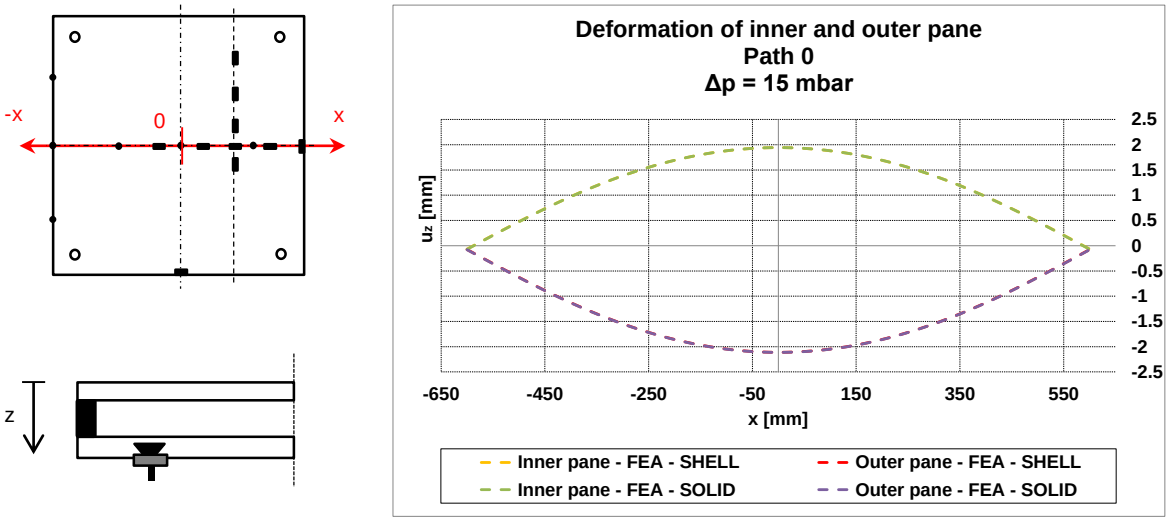

Figure D. 17 Comparison of the deformations between the 3D Solid and the simple 2D FE-model, Path 0, IGU-O-C1, Load case "Summer"

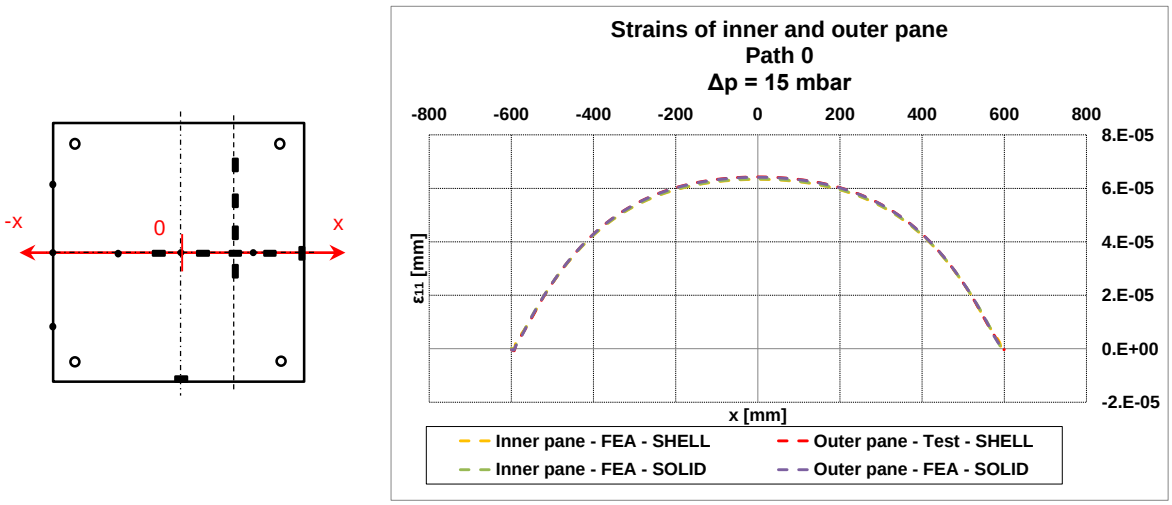

Figure D. 18 Comparison of the strains between the 3D Solid and the simple 2D FE-model, Path 0, IGU-O-C1, Load case "Summer"

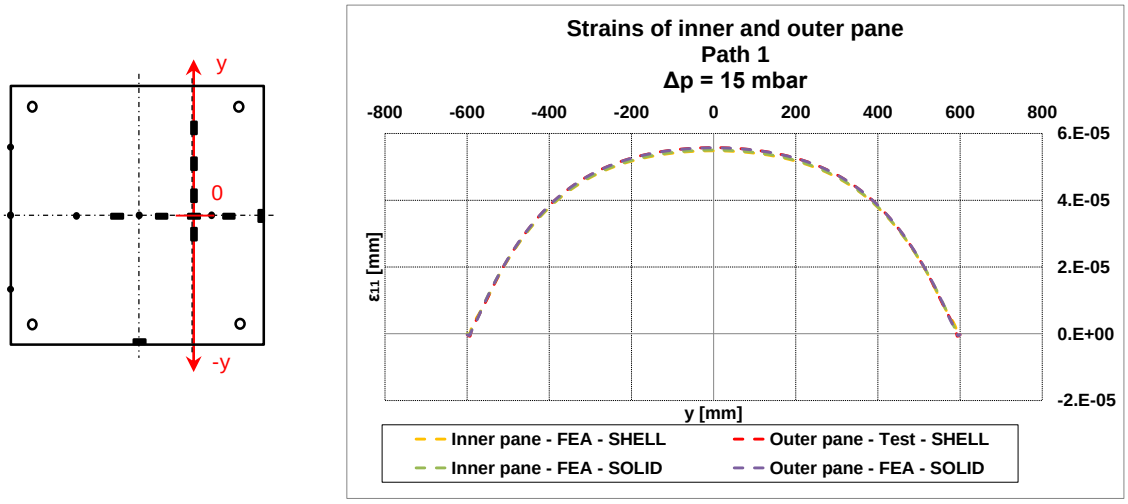

Figure D. 19 Comparison of the strains between the 3D Solid and the simple 2D FE-model, Path 1, IGU-O-C1, Load case "Summer"

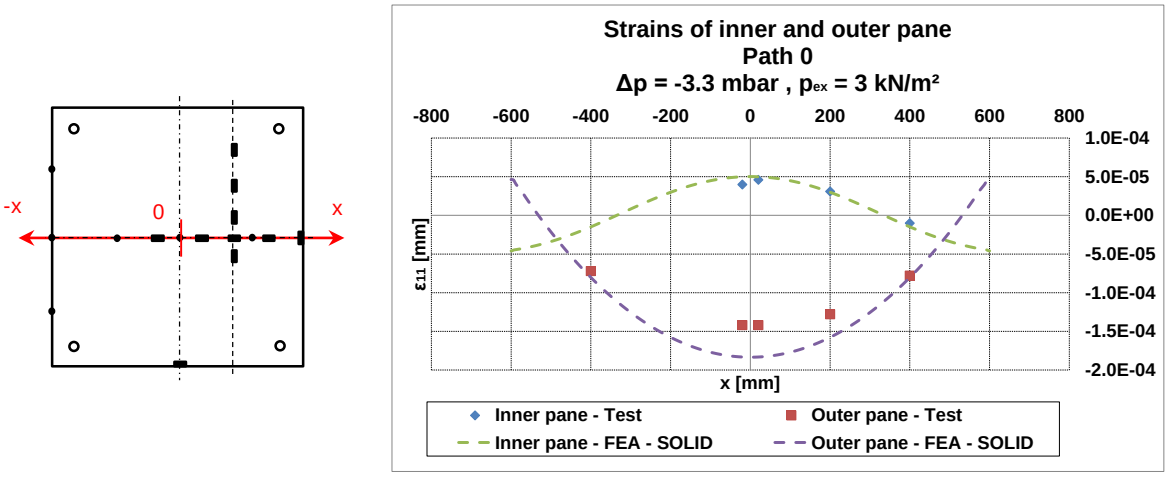

Figure D.20 Strains of the inner and outer glass pane, Path 0, IGU-O-C1, Load case "Wind load + Winter"

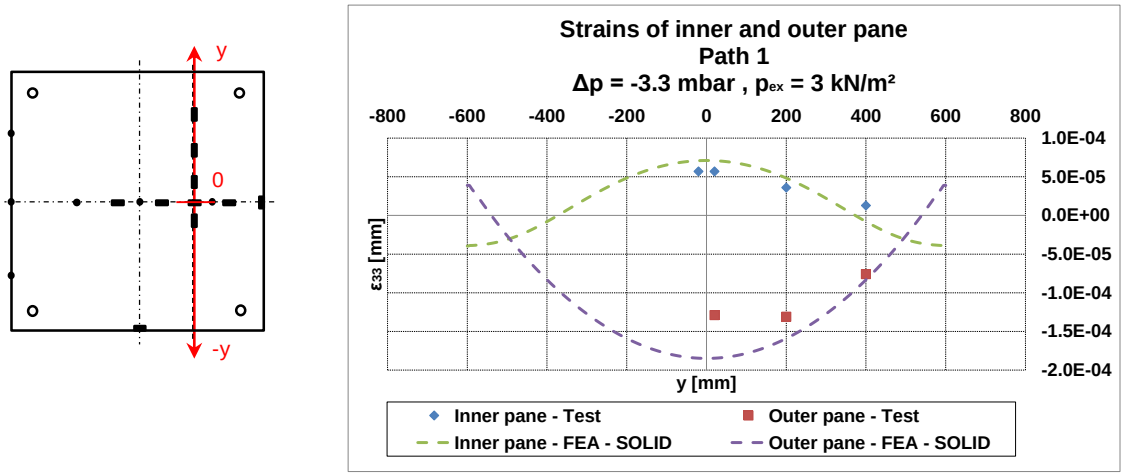

Figure D.21 Strains of the inner and outer glass pane, Path 1, IGU-O-C1, Load case "Wind load + Winter"

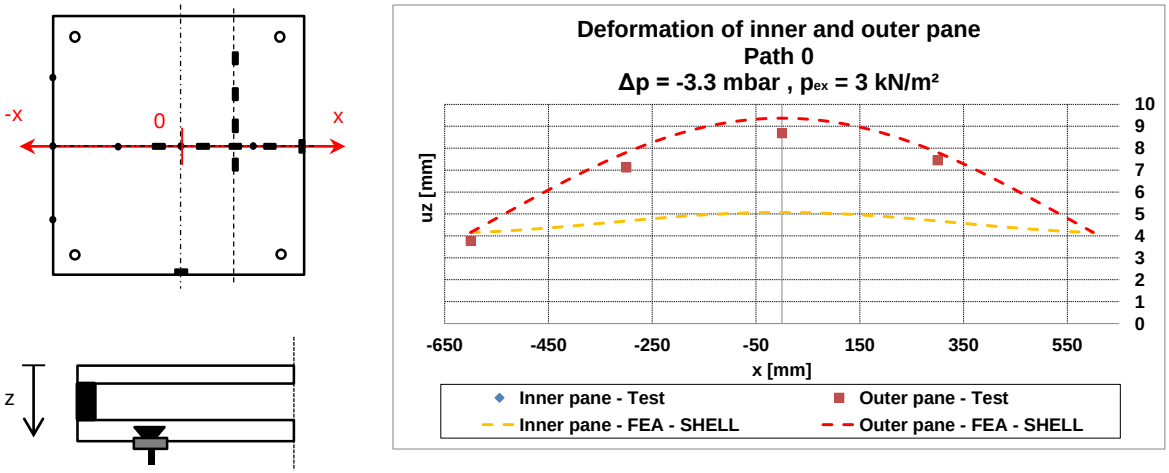

Figure D.22 Deformations of the inner and outer glass pane, Path 0, IGU-O-C1, Load case "Wind load + Winter"

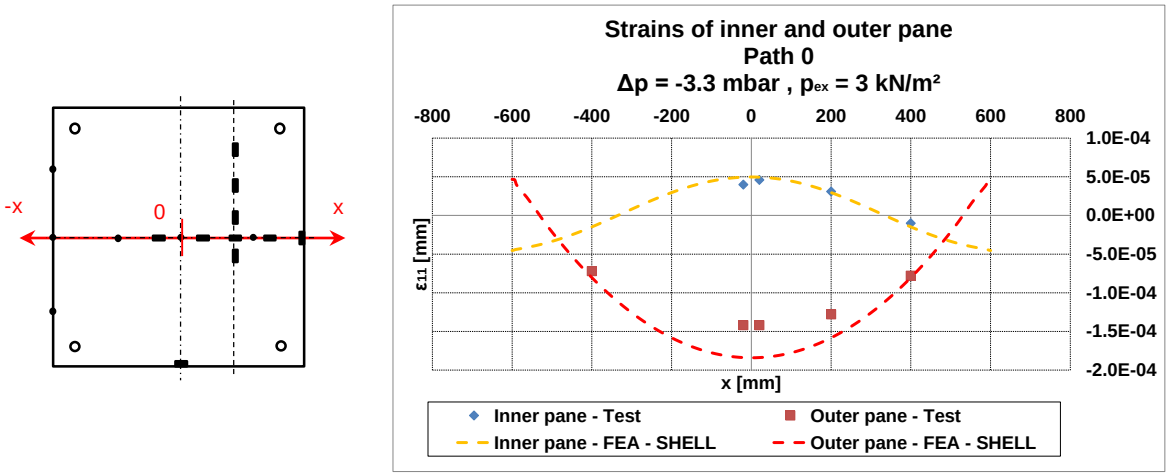

Figure D.23 Strains of the inner and outer glass pane, Path 0, IGU-O-C1, Load case "Wind load + Winter"

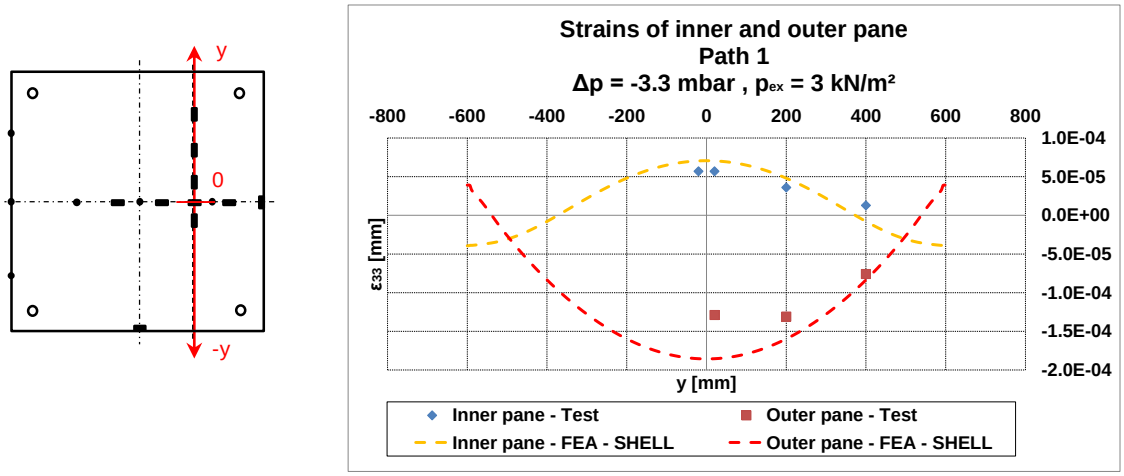

Figure D.24 Strains of the inner and outer glass pane, Path 1, IGU-O-C1, Load case "Wind load + Winter"

D.2 2. Test – IGU-I-C2

Table D.2 Test program for 2. test

Specimen	Configuration	Load case	Objective	Load step	Δp [mbar]	p_{ex} [kN/m²]	g [kg]
IGU-I-C2	2	Wind pressure	Failure of FZP-G-Z + Verification of extended SLG-method	0	0	0	0
				1	4.1	1	0
				2	8.2	2	0
				3	12.4	3	0
				4	15.1	3.7	0
				5	16.5	4	0
				6	19.1	4.7	0
				7	20.8	5	0
				8	22.9	5.5	0
				9	0	8.3	0

Δp: Pressure difference in the glazing cavity

p_{ex}: Wind load

g: Self-weight

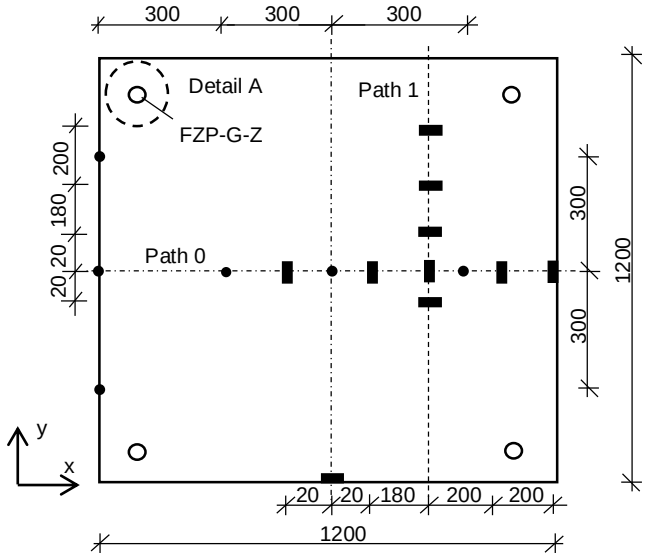

Figure D. 25 Measurement plan for inner glass pane, IGU-I-C2

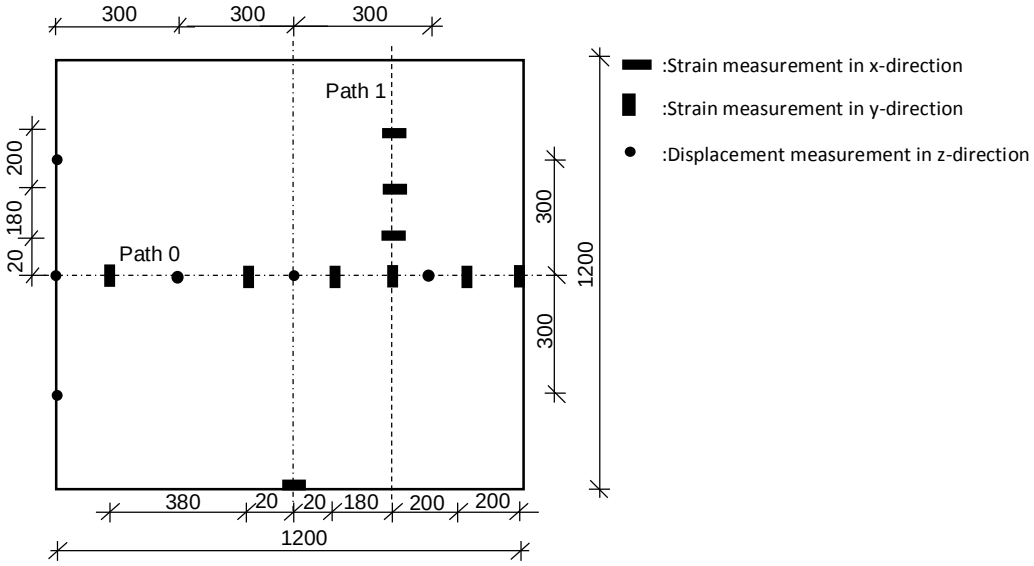

Figure D. 26 Measurement plan for outer glass pane, IGU-I-C2

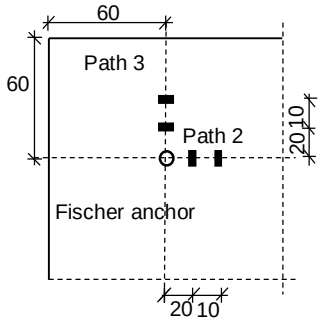

Figure D. 27 Strain measurement at the Fischer anchor, IGU-I-C2

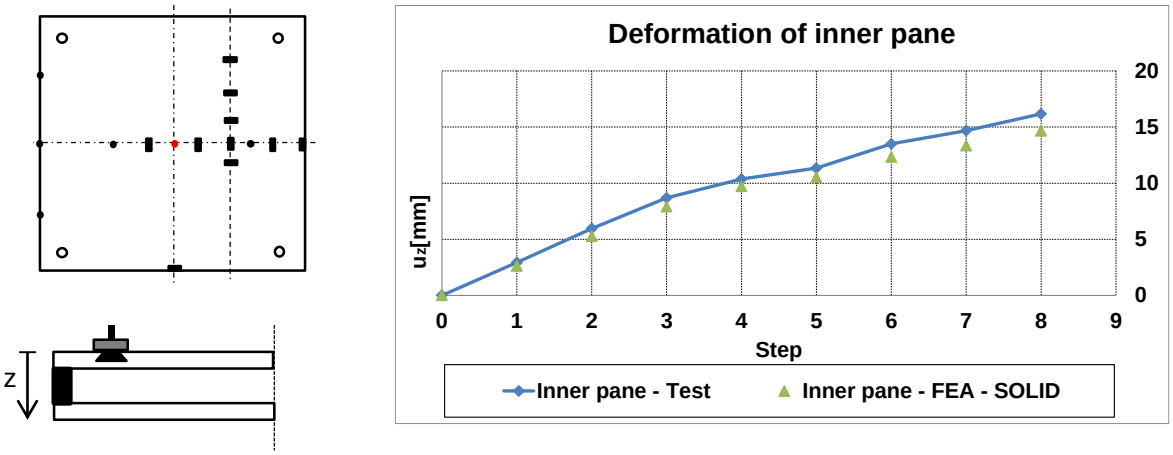

Figure D. 28 Deformation at mid-span of the inner glass pane for the different load steps, IGU-I-C2

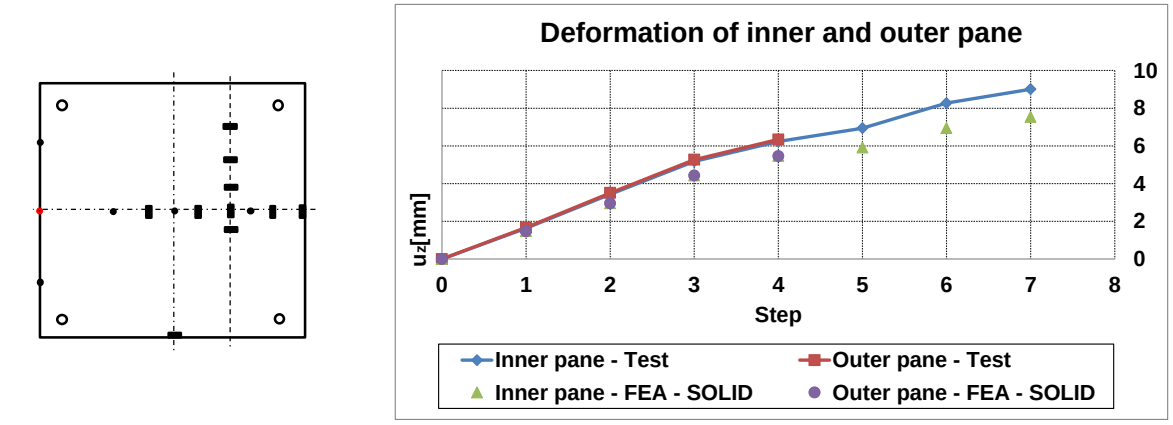

Figure D. 29 Deformation at the edge of the inner and outer glass pane for the different load steps, IGU-I-C2

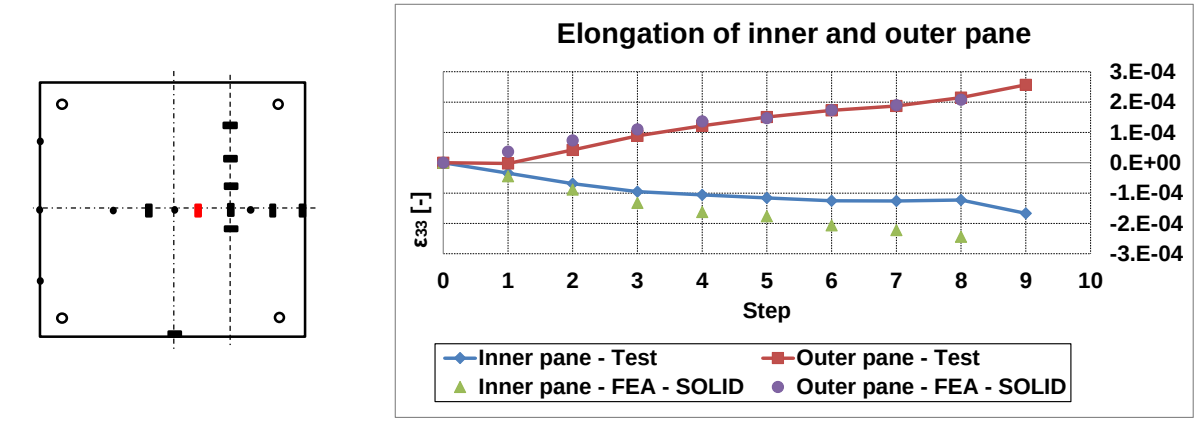

Figure D. 30 Strains of the inner and outer glass pane for the different load steps, IGU-I-C2

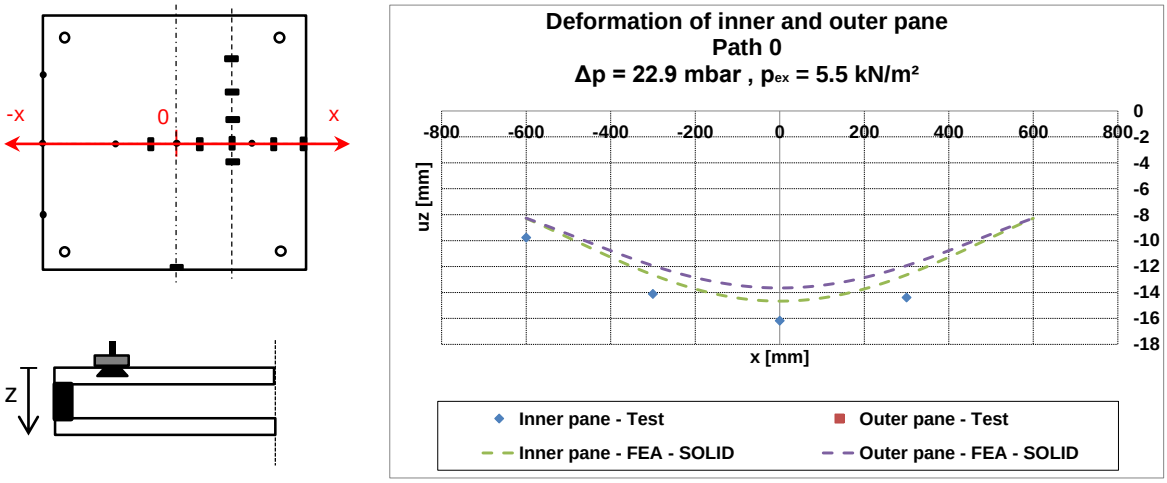

Figure D.31 Deformations of the inner and outer glass pane, Path 0, IGU-I-C2, Load case "Wind load + Ambient"

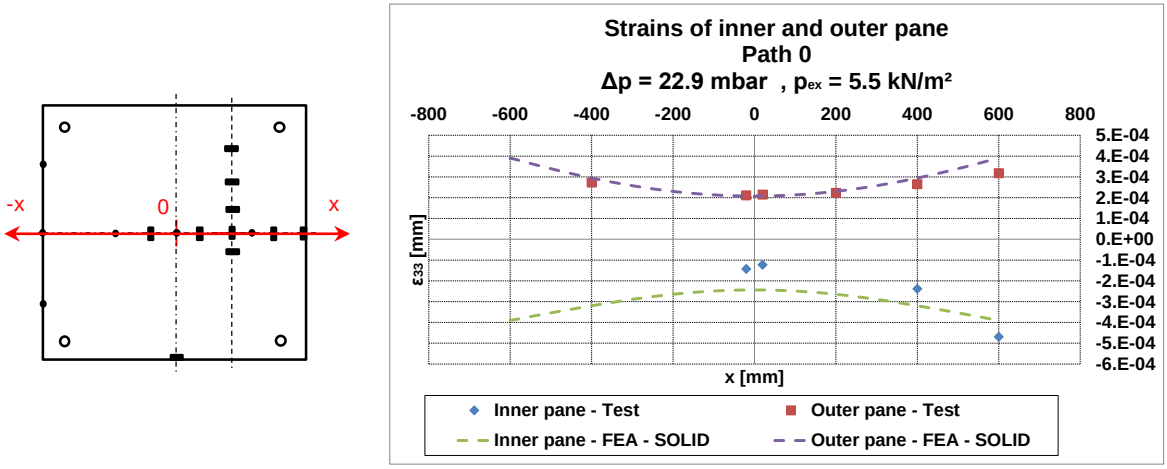

Figure D.32 Strains of the inner and outer glass pane, Path 0, IGU-I-C2, Load case "Wind load + Ambient"

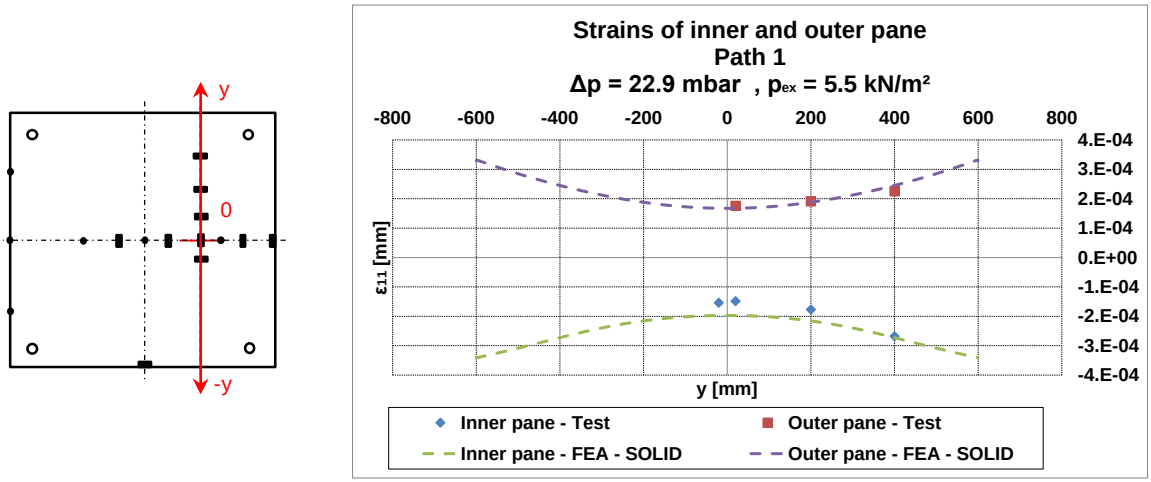

Figure D.33 Strains of the inner and outer glass pane, Path 1, IGU-I-C2, Load case "Wind load + Ambient"

D.3 3. Test – IGU-I-SW-C2

Table D.3 Test program for 3. test

Specimen	Configuration	Load case	Objective	Load step	Δp [mbar]	p_{ex} [kN/m²]	g [kg]
IGU-I-SW-C2	2	Self-weight + Winter (Δp = -15 mbar) + Wind pressure	Failure of FZP-G-Z + Verification of extended SLG-method under consideration of the self-weight	0	0	0	0
				1	0	0	72
				2	-15	0	72
				3	-9.8	1	72
				4	-5.6	2	72
				5	-2.0	3	72
				6	2.8	4	72
				7	11.7	5	72
				8	…	7.5	72

Δp: Pressure difference in the glazing cavity

p_{ex}: Wind load

g: Self-weight

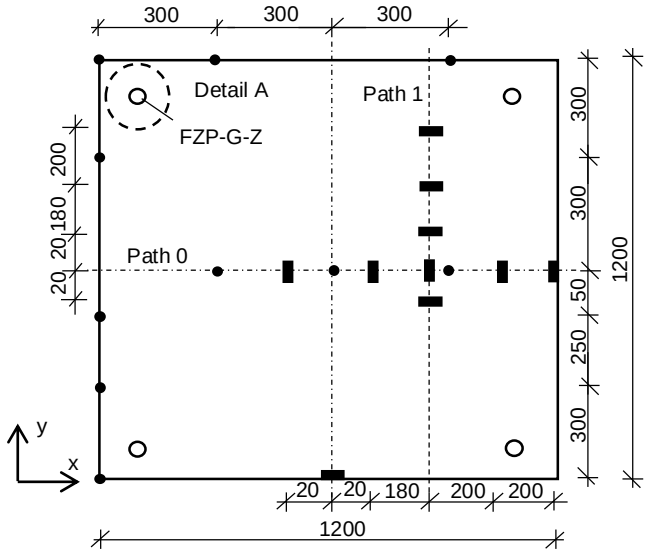

Figure D.34 Measurement plan for inner glass pane, IGU-I-SW-C2

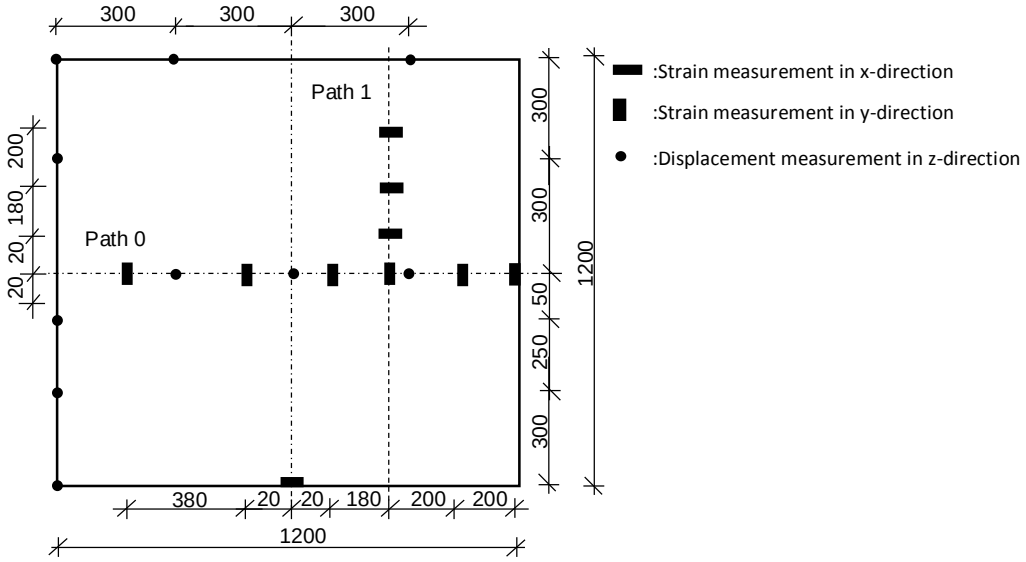

Figure D.35 Measurement plan for outer glass pane, IGU-I-SW-C2

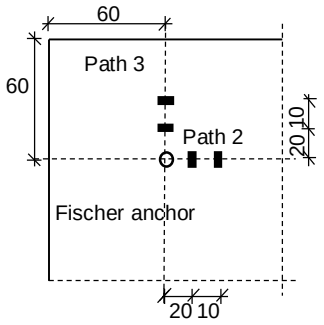

Figure D.36 Strain measurement at the Fischer anchor, IGU-I-SW-C2

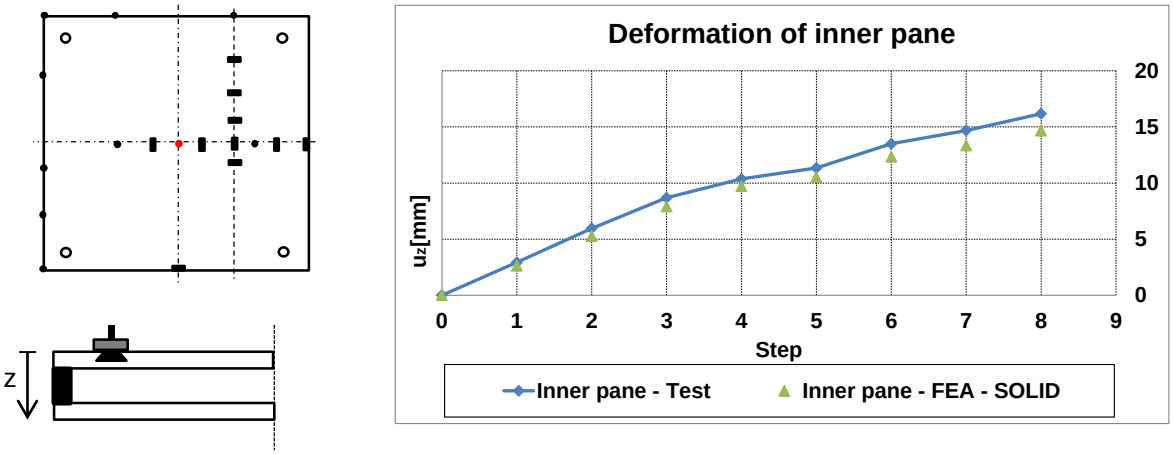

Figure D. 37 Deformation at mid-span of the inner glass pane for the different load steps, IGU-I-SW-C2

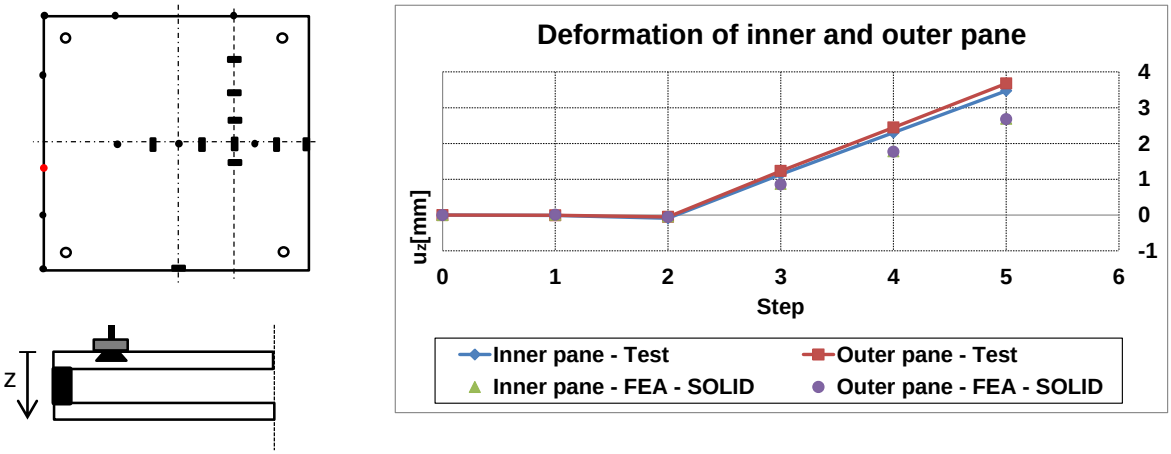

Figure D. 38 Deformation at the edge of the inner and outer glass pane for the different load steps, IGU-I-SW-C2

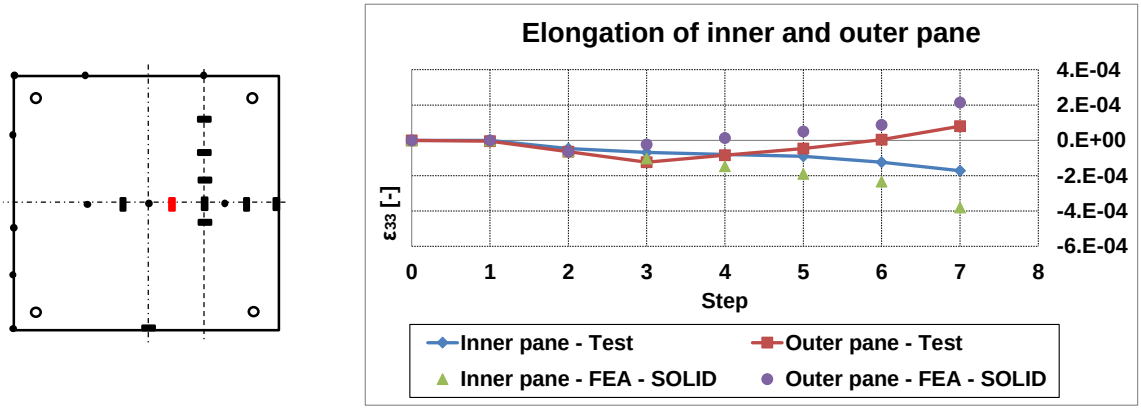

Figure D. 39 Strains of the inner and outer glass pane for the different load steps, IGU-I-SW-C2

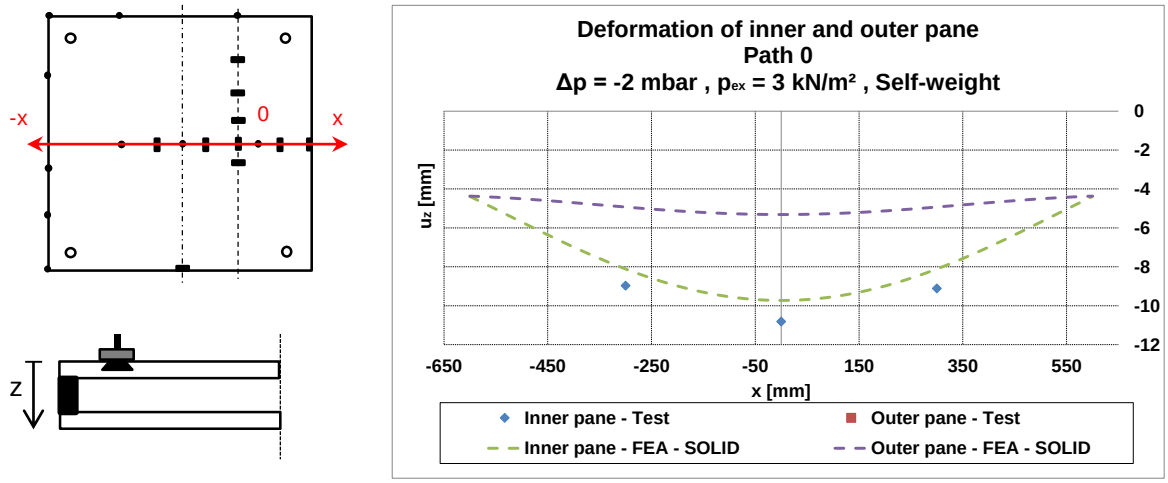

Figure D. 40 Deformations of the inner and outer glass pane, Path 0, IGU-I-SW-C2, Load case "Wind load + Winter + SW"

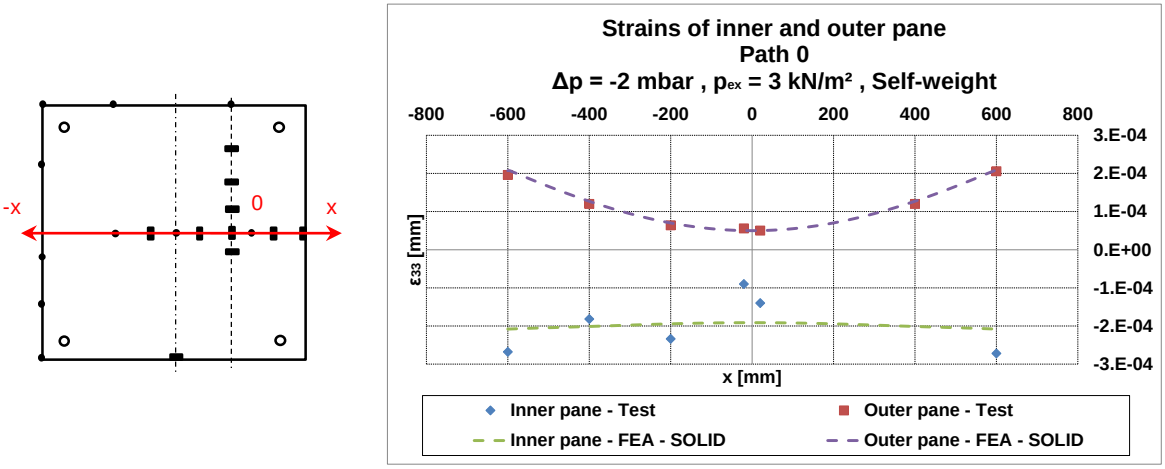

Figure D.41 Strains of the inner and outer glass pane, Path 0, IGU-I-SW-C2, Load case "Wind load + Winter + SW"

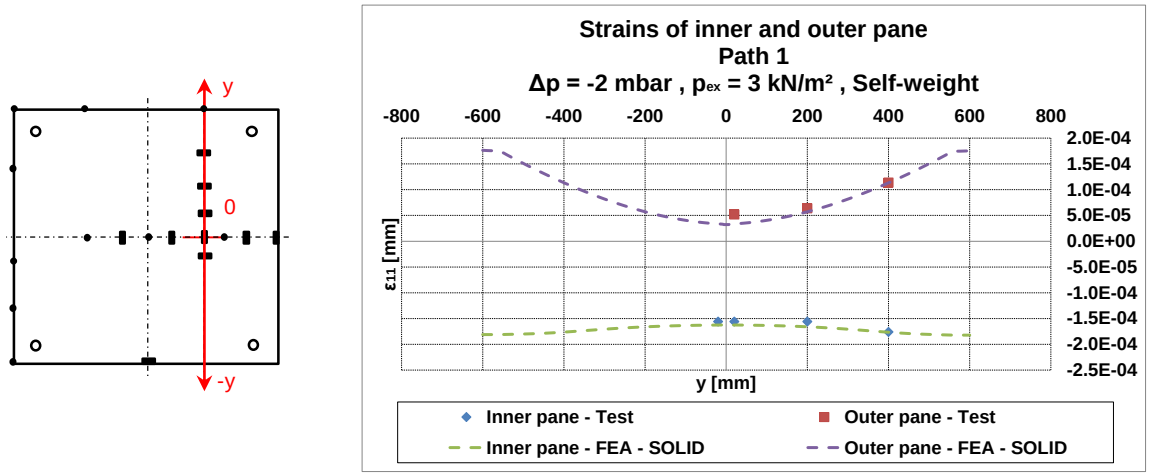

Figure D.42 Strains of the inner and outer glass pane, Path 1, IGU-I-SW-C2, Load case "Wind load + Winter + SW"

D.4 4. Test – IGU-O-C2

Table D. 4 Test program for 4. test

Specimen	Configuration	Load case	Objective	Load step	Δp [mbar]	p_{ex} [kN/m²]	g [kg]
IGU-O-C2	2	Winter (Δp = -15 mbar) + Wind suction	Failure of FZP-G-Z + Verification of extended SLG-method	0	0	0.0	0
				1	-15	0.0	0
				2	-18	0.3	0
				3	-27.2	1.3	0
				4	-37.6	2.3	0
				5	-46.9	3.3	0
				6	-56	4.3	0
				7	-66.5	5.7	0

Δp: Pressure difference in the glazing cavity

p_{ex}: Wind load

g: Self-weight

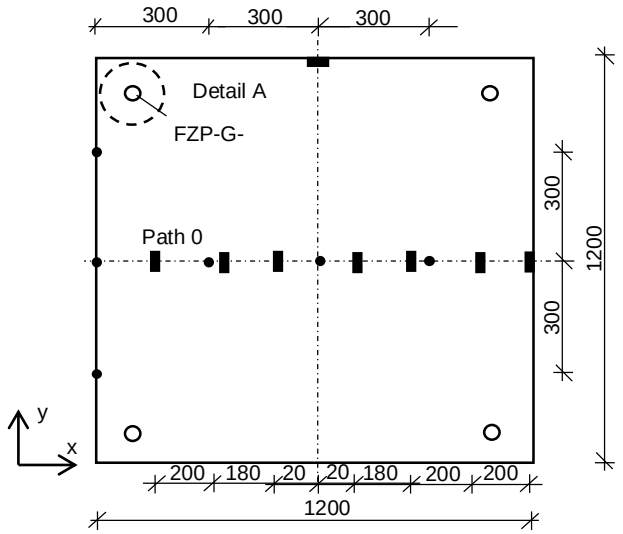

Figure D. 43 Measurement plan for inner glass pane, IGU-O-C2

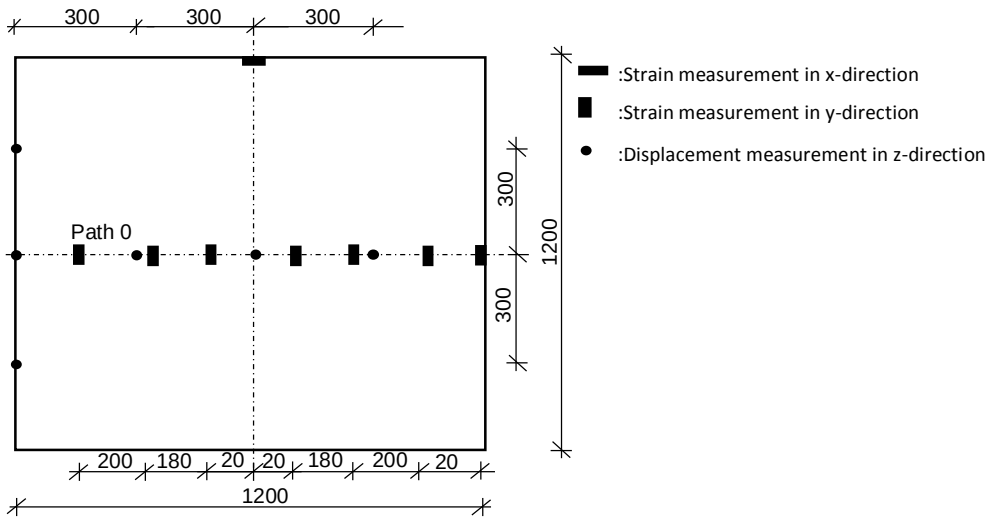

Figure D. 44 Measurement plan for outer glass pane, IGU-O-C2

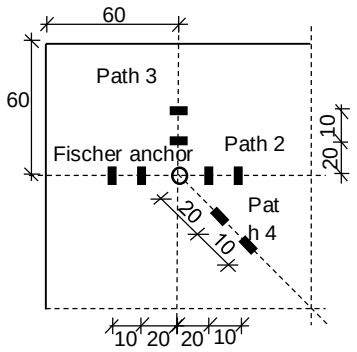

Figure D. 45 Strain measurement at the Fischer anchor, IGU-O-C2

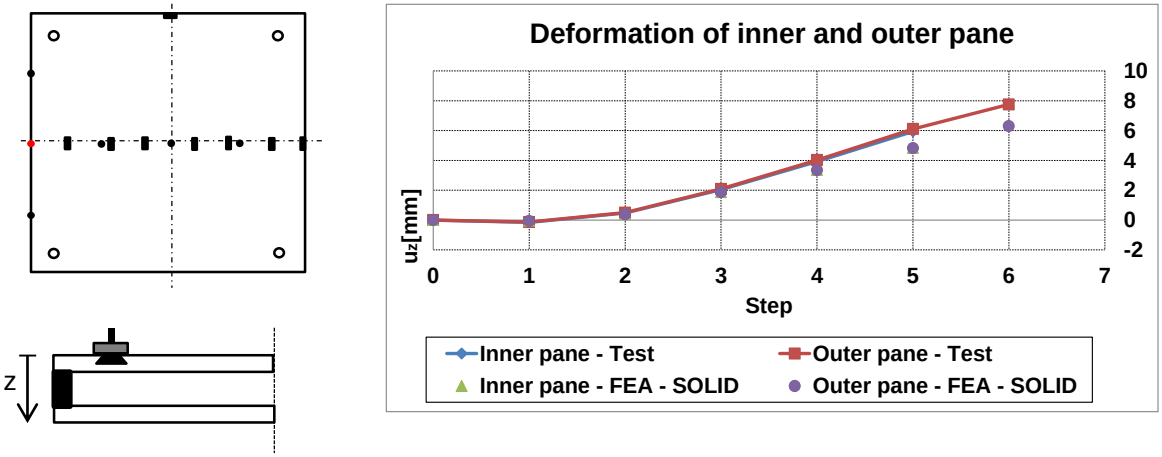

Figure D. 46 Deformation at the edge of the inner and outer glass pane for the different load steps, IGU-O-C2

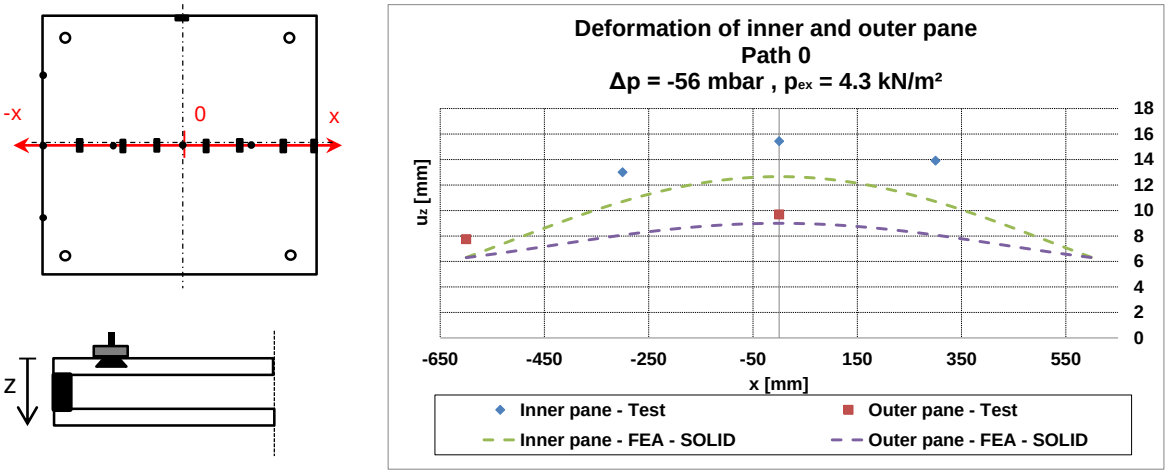

Figure D. 47 Deformations of the inner and outer glass pane, Path 0, IGU-O-C2, Load case "Wind load + Winter"

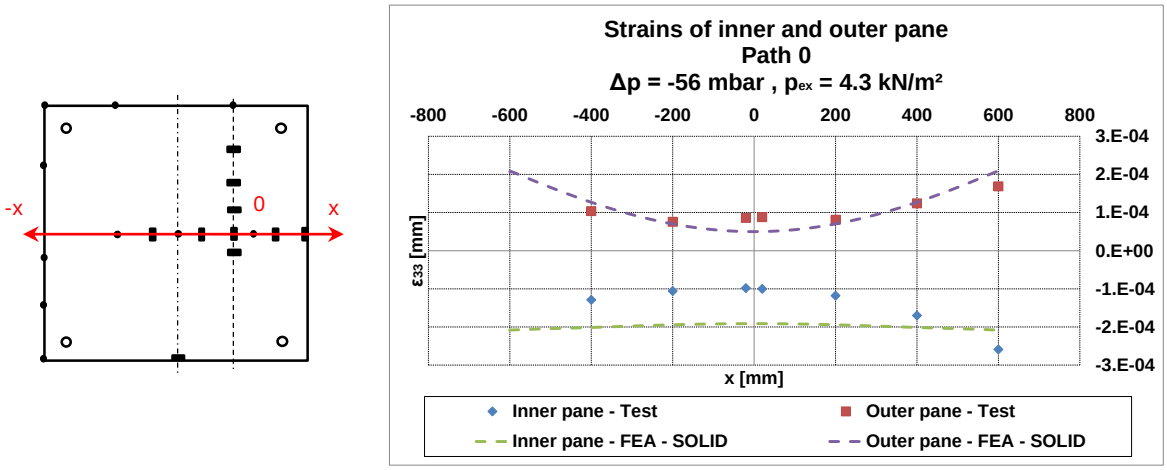

Figure D.48 Strains of the inner and outer glass pane, Path 0, IGU-O-C2, Load case "Wind load + Winter"

E Annexe E – Design example

In order to illustrate the application of the novel general design model, an exemplary geometry of the point fitted IGU with the Fischer undercut anchors is verified. On account of the problems related the adjustment of the standards (chapter 10), the verification is done according to the global safety concept.

E.1 Dimensions of the point fitted IGU

The dimensions and the body of the IGU are shown in Figure E.1

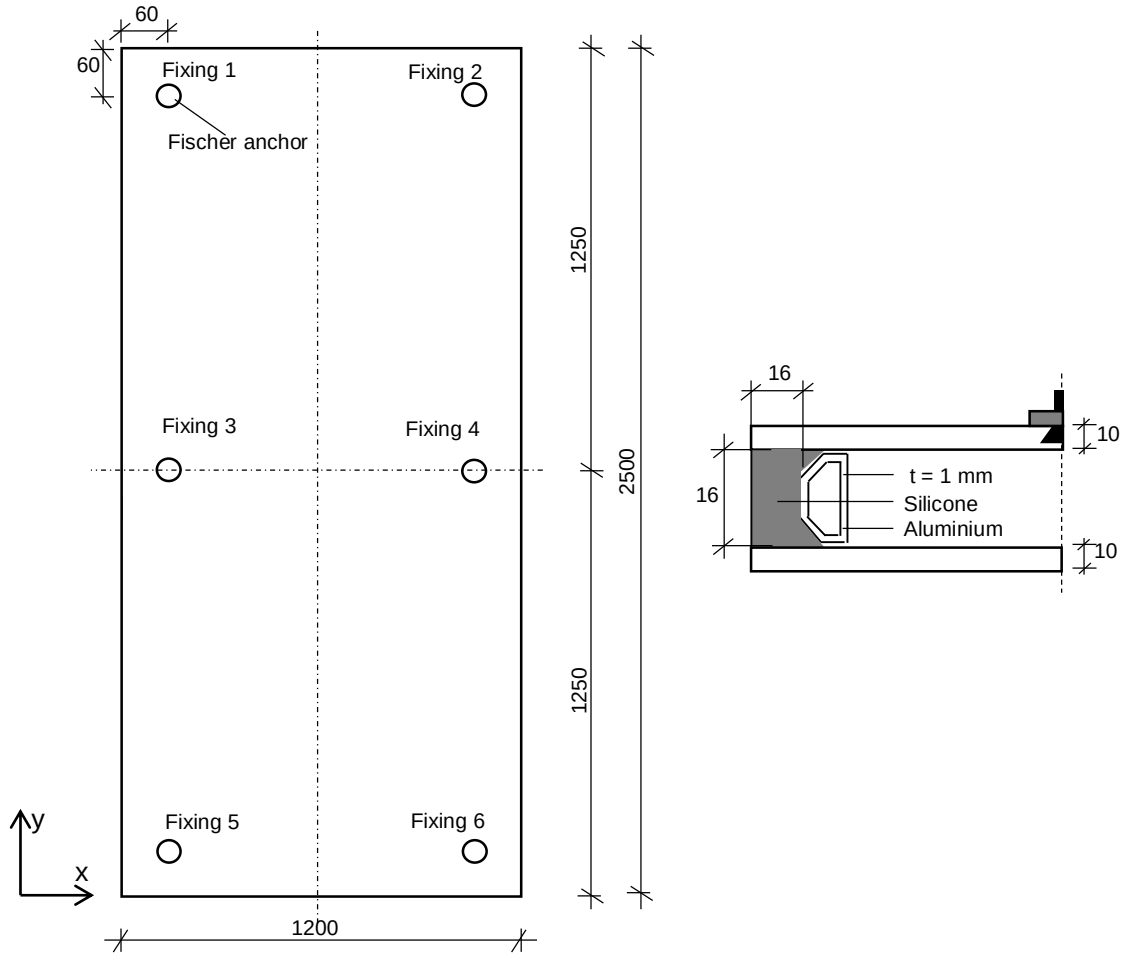

Glass body :

Outer pane :	10 mm FTG (Fully tempered glass – heat soaked)
Edge bond :	- Primary sealant : PIB (t = 0.25 mm)
	- Secondary sealant : Structural silicone DC 993
	- Spacer : Aluminium (t = 0.25 mm)
Inner pane :	10 mm FTG (Fully tempered glass – heat soaked)
FZP-G-Z :	4 x corner fixings
	4 x edge fixings
Inclination :	0° to the vertical

Figure E.1 Dimensions and glass body of the point fitted IGU

The bearing conditions and the substructure are shown in Figure E.2

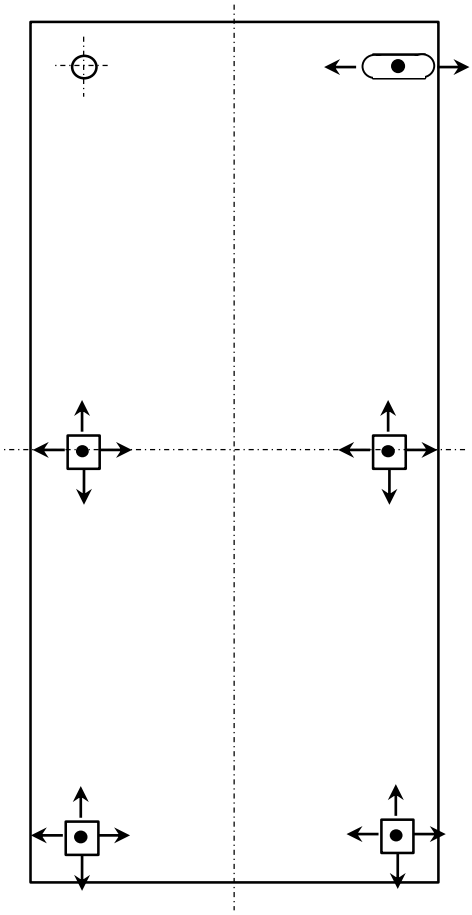

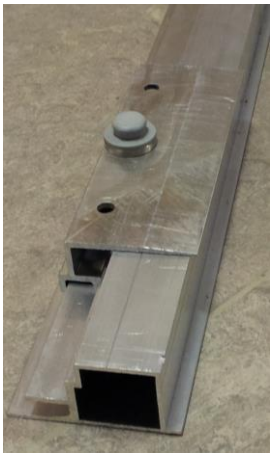

Substructure :

SolutionOne :

Closed hollow profile as transom with L-shaped brackets

Support conditions :

Statically defined in glass pane

Flush assembling : L = 15 mm (Z-70.2-122)

The self-weight is transmitted by the upper two FZP-G-Z

Figure E.2 Bearing of the point fitted IGU

The stiffness of the Fischer anchor FZP-G-Z and the stiffness of the substructure are resumed in resulting spring stiffness values according to equation (E-1):

$$\frac{1}{k_{res}} = \frac{1}{k_{FZP-G-Z}} + \frac{1}{k_{Sub}} \quad \textbf{(E-1)}$$

This is done for the translational and the rotational spring stiffness (Table E.1 and Table E.2). The stiffness values of the Fischer FZP-G-Z and of the substructure “SystemOne” are given in (Fischer, 2007).

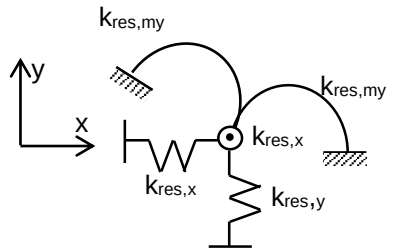

Figure E.3 Definition of the resulting spring stiffness values

Table E.1 translational spring stiffness

	Translational spring stiffness $k_{x,y,z}$ [N/mm]								
	Fixing 1			Fixing 2			Fixing 3-6		
	k_x	k_y	k_z	k_x	k_y	k_z	k_x	k_y	k_z
$k_{FZP-G-Z}$	4600		1.00E+08	4600		1.00E+08	4600		1.00E+08
k_{Sub}	1111		625	0	1111	625	0		625
k_{res}	895	895	625	0	895	625	0	0	625

Table E.2 Rotational spring stiffness

	Rotational spring stiffness k_{rot} [N/mm]					
	Fixing 1		Fixing 2		Fixing 3-6	
	$k_{rot,mx}$	$k_{rot,my}$	$k_{rot,mx}$	$k_{rot,my}$	$k_{rot,mx}$	$k_{rot,my}$
$k_{FZP-G-Z}$	8.59E+05		8.59E+05		8.59E+05	
k_{Sub}	9.50E+05	7.96E+05	9.50E+05	7.96E+05	9.50E+05	7.96E+05
k_{res}	4.51E+05	4.13E+05	4.51E+05	4.13E+05	4.51E+05	4.13E+05

E.2 Loading of the point fitted IGU

The following loads are applied on the insulation glass unit:

- The self-weight of the IGU
- Wind suction load acting on the outer glass pane
- The climate loads

Temperature loads are not considered since the connection of the IGU to the substructure concerns a statically defined system.

The loading cases are named as follows:

- Self-weight of the IGU: Load case 0
- Wind suction loads + climate loads: Load case 1

Self-weight of the IGU

The self-weight of the IGU is composed of the weight of the inner and outer glass pane. The contribution of the edge bond and the point fitting is negligible.

With the density γ_{Glass} = 25 N/mm^2 of the material glass:

Outer pane: 10 mm FTG $g_e = L_x \cdot L_y \cdot t_e \cdot \gamma_{Glass}$
$= 2.5\ m \cdot 1.2\ m \cdot 0.01\ m \cdot 25\ N/mm^2 = 750\ N$

Inner pane: 10 mm FTG $g_i = L_x \cdot L_y \cdot t_i \cdot \gamma_{Glass}$
$= 2.5\ m \cdot 1.2\ m \cdot 0.01\ m \cdot 25\ N/mm^2 = 750\ N$

Only the two upper corner anchors (fixing 1 and fixing 2) transmit the self-weight.

Wind suction load according to (DIN 1055-4)

The design loads for the wind suction load are determined according to (DIN 1055-4). The detailed calculation of the wind loads is not part of the design example. Therefore the value is directly indicated:

Outer pane $p_{e,1} = -1.5\ kN/m^2$ (DIN 1055-4)

Inner pane $p_{e,2} = 0\ kN/m^2$ (DIN 1055-4)

The value for the wind suction load is negative according to the sign convention in chapter 7.

The climate loads

The climate loads are calculated according to the extended climate load model (Chapter 7):

$$\begin{pmatrix} p_{res,1} \\ p_{res,2} \end{pmatrix} = \frac{1}{(1+\varphi_{1,2}-\varphi_{1,1})} \cdot \begin{pmatrix} -1 & 1+\varphi_{1,2} & \varphi_{1,2} \\ 1 & -\varphi_{1,1} & 1-\varphi_{1,1} \end{pmatrix} \cdot \begin{pmatrix} \Delta p_{c,1} \\ p_{e,1} \\ p_{e,2} \end{pmatrix} \quad \textbf{(E-2)}$$

With:

$$\varphi_{1,2} = \alpha_{1,2}^{+} - \alpha_{1,2};\ \varphi_{1,1} = \alpha_{1,1}^{+} - \alpha_{1,1}$$

and

$$\alpha_{1,2} = \frac{\vartheta_{1,2}}{v_{pr,1}} \cdot p_a;\ \alpha_{1,2}^{+} = \frac{\vartheta_{2,2}}{v_{pr,1}} \cdot p_a;\ \alpha_{1,1} = \frac{\vartheta_{1,1}}{v_{pr,1}} \cdot p_a;\ \alpha_{1,1}^{+} = \frac{\vartheta_{2,1}}{v_{pr,1}} \cdot p_a$$

The volume coefficients are tabulated in Table B.3 in annexe B. The determination of the relative volume changes $\alpha_{1,1}$ and $\alpha^{+}_{1,1}$ and the factors $\varphi_{1,1}$ and $\varphi_{1,2}$ leads to the following results:

Table E.3 The coefficients and factors for the determination of the climate loads

$v_{1,1}$	$v_{1,2}$	$v_{2,1}$	$v_{2,2}$	$\alpha_{1,1}$	$\alpha_{1,1}^{+}$	$\alpha_{1,2}$	$\alpha_{1,2}^{+}$	$\varphi_{1,1}$	$\varphi_{1,2}$
[m³/(kN/m²)]	[m³/(kN/m²)]	[m³/(kN/m²)]	[m³/(kN/m²)]	[-]	[-]	[-]	[-]	[-]	[-]
0.00802	0.00239	0.00239	0.00596	16.88	5.03	5.03	12.55	-11.85	7.51

The climate loads are determined with equation (E-2) for the two extreme climate load cases “Winter” and “Summer” according to (DIN 18008-2) or (TRLV, 2006):

Table E.4 The climate loads for the load cases “Winter” and “Summer”

Climate load case	Δp_{met}	ΔT	ΔH	$\Delta p_{c,1}$	$p_{res,1}$	$p_{res,2}$
(DIN 18008-2)	[kN/m²]	[K]	[m]	[kN/m²]	[kN/m²]	[kN/m²]
Winter	+4	-25	-300	-0.16	+0.1	-1.60
Summer	-2	+25	+600	+0.16	-1.4	-0.1

The over- or underpressure Δp_1 inside the glazing cavity of the IGU is an important parameter for the design of the edge sealant. It is determined with equation (B-23):

$$\Delta p_1 = \frac{1}{(1+\varphi_{1,2}-\varphi_{1,1})}\left[\left(\alpha_{1,1} - \alpha_{1,1}^{+}\right) \cdot p_{e,1} + \left(\alpha_{1,2} - \alpha_{1,2}^{+}\right) \cdot p_{e,2} + \Delta p_{c,1}\right]$$

Table E.5 The pressure inside the glazing cavity

Climate load case	Δp_1
	[kN/m²]
Winter	-1.65
Summer	-0.09

E.3 The 2D FE-model of the point fitted IGU

The verification according to the novel design concept in section 4.5 requires a simple 2D FE-model of the point fitted IGU.

In the numerical model:

- The glass panes are modelled with 2D shell elements
- The point fittings are simulated with springs
- The edge bond is modelled with 3D solid elements

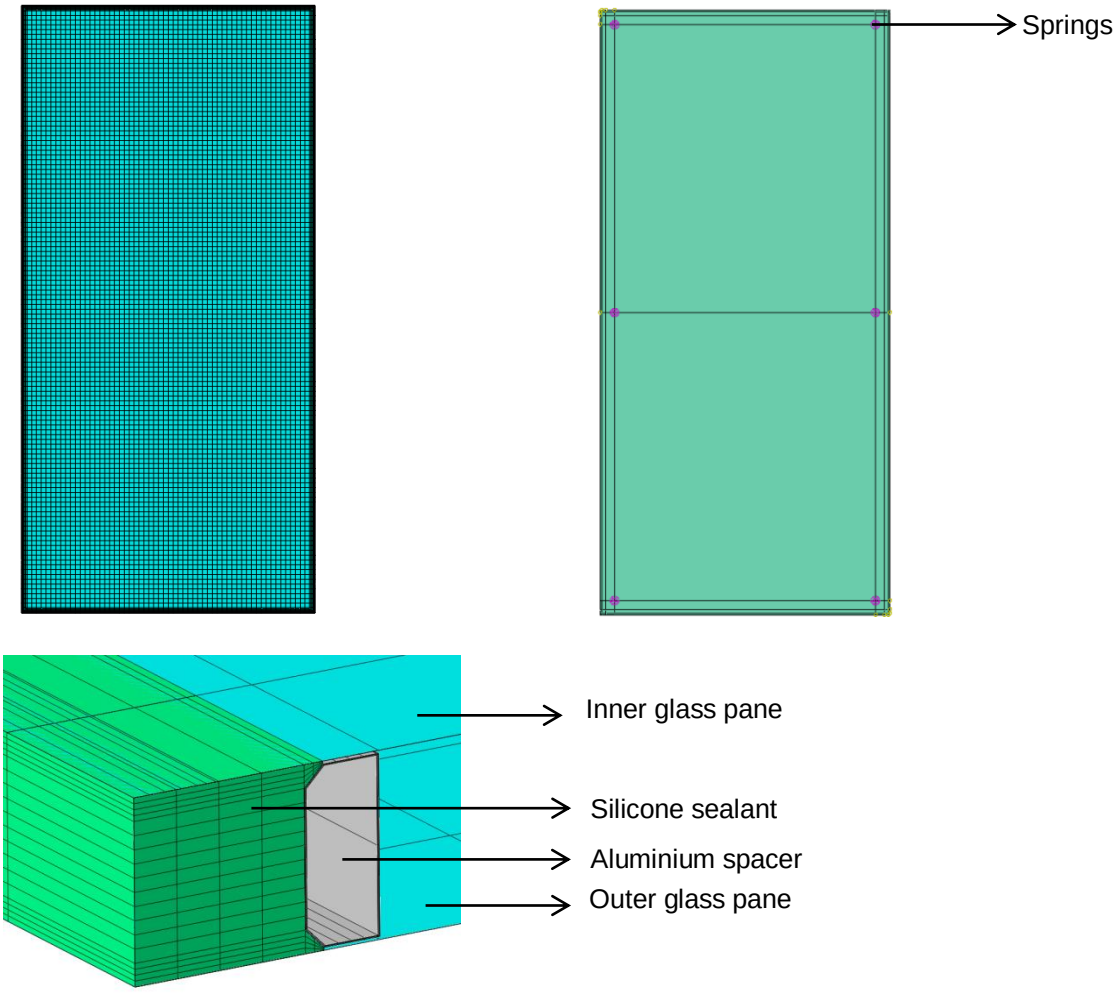

Figure E.4 the simple 2D FE-model for the design of the point fitted IGU with the Fischer undercut anchor

E.4 Verification of the edge bond system according to (ETAG 002)

The novel design concept foresees the verification of the edge seal system according to (ETAG 002).

According to (ETAG 002) the following cases have to be verified (see also section 2.7):

- Transfer of permanent shear loading
- Transfer of permanent tension or compression loading
- Transfer of dynamic loading

In the design example, a permanent tension or compression load does not occur in the edge sealant of the point fitted IGU. Therefore this case is not included in the verification procedure.

Verification of the transfer of permanent shear loads

The following inequality has to be fulfilled by the covering thickness of the secondary sealant to assure the transfer of permanent shear loads:

$$r > \frac{P}{2 \cdot b \cdot \Gamma_\infty} \qquad \text{(ETAG 002)}$$

where:

r = minimum covering thickness [mm]

P = permanent shear load [N/mm^2]

b = long edge of glass pane [mm]

Γ_∞ = shear design stress under permanent load [N/mm^2]

The permanent shear load P corresponds to the self-weight g_e = 750 N of the outer glass pane and according to (Dow Corning, 2004) the shear design stress is Γ_∞ = 0.011 N/mm^2 for the structural silicone DC993.

$$r > \frac{P}{2 \cdot b \cdot \Gamma_\infty} = \frac{750\ \text{N}}{2 \cdot 2500\ \text{mm} \cdot 0.011\ \frac{\text{N}}{\text{mm}^2}} = 13.6\ \text{mm}$$

The present covering thickness r_{vorh} = 16 mm > 13.6 mm and the inequality is fulfilled.

In addition:

r_{vorh} = 16 mm > r_{min} = 6.0 mm (ETAG 002)

Verification of the transfer of dynamic loads

According to (ETAG 002), the secondary sealant is able to transfer dynamic loads if its covering thickness complies with the required minimal covering thickness:

$$r > \frac{a \cdot P}{2 \cdot \sigma_{dyn,des}} \qquad \text{(ETAG 002)}$$

r = minimum covering thickness [mm]

P = overpressure in the glazing cavity [N/mm^2]

a = short edge of glass pane [mm]

$\sigma_{dyn,des}$ = dynamic tension design stress under dynamic load [N/mm^2]

The overpressure in the glazing cavity is indicated in Table E.5 for the summer and winter climate load cases. The decisive load case is the winter loads case with Δp_1 = -1.65 kN/m^2. The dynamic tension design stress is given in (Dow Corning, 2004) and is $\sigma_{dyn,des}$ = 0.14 N/mm^2 for the structural silicone DC993.

$$r > \frac{a \cdot P}{2 \cdot \sigma_{dyn,des}} = \frac{1200\ \text{mm} \cdot 1.65 \cdot 10^5 \frac{\text{N}}{mm^2}}{2 \cdot 0.14 \frac{\text{N}}{\text{mm}^2}} = 7.1\ \text{mm}$$

r_{vorh} = 16 mm > r = 7.1 mm and the minimal covering thickness is respected.

In addition:

r_{vorh} = 16 mm > r_{min} = 6.0 mm (ETAG 002)

In conclusion, the secondary sealant fulfils the requirements according to (ETAG 002).

E.5 Verification of the outer pane

According to the novel design concept, the outer glass pane is verified by checking the maximum deformation and the maximum tensile stresses to the permissible values in (TRLV, 2006) or the design values in (DIN 18008-2). This design example is based on the global safety concept and therefore the permissible values in (TRLV, 2006) are considered.

The permissible deformation is indicated in (TRLV, 2006) with:

$$f_{max,rec} = \frac{L}{100} = \frac{1200\ mm}{100} = 12\ mm$$

Where L is the minimal span of the outer glass pane.

The permissible tensile stress for fully tempered glass is $\sigma_{max,rec}$ = 50 N/mm^2.

The maximum deformations and tensile stresses of the outer glass pane are numerically determined with the 2D FE-model for the climate loading cases “Winter” and “Summer”.

Winter:

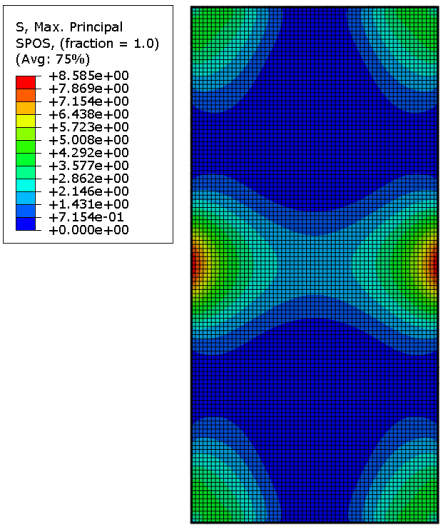

Figure E.5 Maximum tensile stresses – outer pane

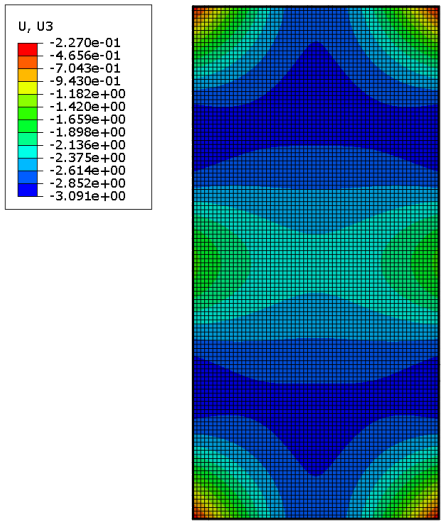

Figure E.6 Maximum deformations – outer pane

Table E.6 Verification of the outer glass pane for the climate loading case “Winter”

Loading case	$\sigma_{max,act}$	$\sigma_{max,rec}$	Check	$f_{max,act}$	$f_{max,rec}$	Check
Winter	[N/mm²]	[N/mm²]	[N/mm²]	[mm]	[mm]	[mm]
0+1	8.6	50	8.6 < 50	3.1	12	3.1 < 12

Summer:

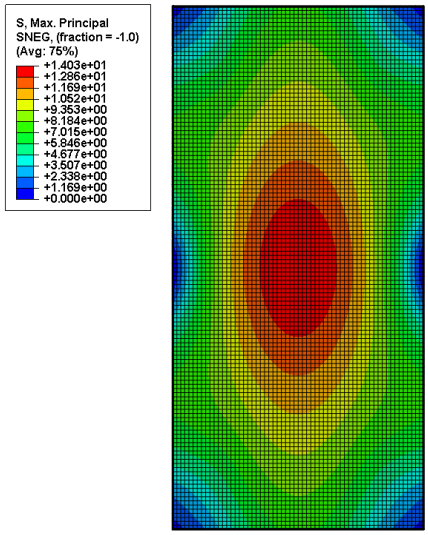

Figure E.7 Maximum tensile stresses – outer pane

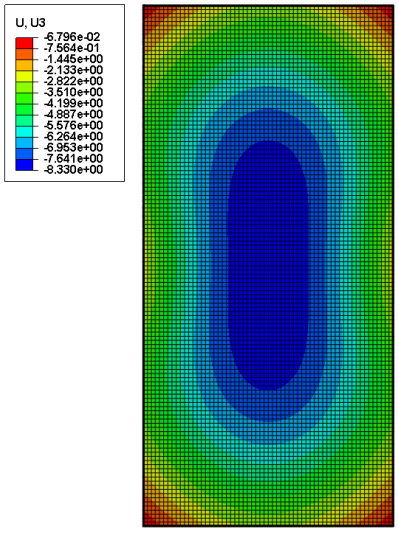

Figure E.8 Maximum deformations – outer pane

Table E.7 Verification of the outer glass pane for the climate loading case "Summer"

Loading case	$\sigma_{max,act}$	$\sigma_{max,rec}$	Check	$f_{max,act}$	$f_{act,rec}$	Check
Summer	[N/mm²]	[N/mm²]	[N/mm²]	[mm]	[mm]	[N/mm²]
0+1	14.0	50	14.0 < 50	8.3	12	8.3 < 50

E.6 Verification of the inner pane

The novel design concept foresees the verification of the inner glass according to the extended SLG-method (Chapter 8).

According to the SLG-method, the verification of the inner pane is divided into two parts:

- The verification of the inner glass pane in the field range
- The verification of the connection “FZP-G-Z – Glass” in the borehole area

Verification of the inner glass pane in the field range

The verification in the field range of the inner glass pane consists in checking the maximum tensile stresses and deformation in the mid-span or at the edge of the glass pane to the permissible values in (TRPV, 2006) or (Z-70.2-122).

According to (Z-70.2-122), the permissible deformation is defined as follows:

$$f_{max,rec} = \frac{L}{100} = \frac{1200 - 2 \cdot 60\ mm}{100} = 10.8\ mm$$

Where L is the minimal span between two Fischer undercut anchors.

The permissible tensile stress amounts $\sigma_{max,rec}$ = 50 N/mm^2 in (Z-70.2-122) for fully tempered glass.

The verification is done for the two climate loading cases “Winter” and “Summer”.

Winter:

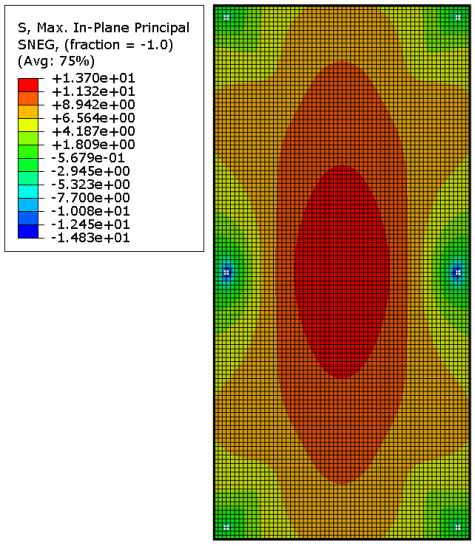

Figure E.9 Maximum tensile stresses – inner pane

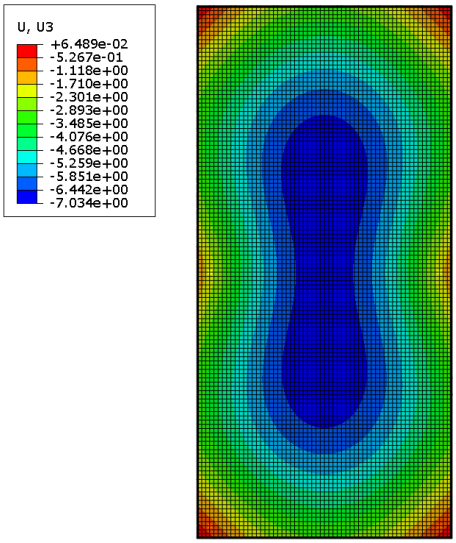

Figure E.10 Maximum deformations – inner pane

Table E.8 Verification of the inner glass pane for the climate loading case "Winter"

Loading case	$\sigma_{max,act}$	$\sigma_{max,rec}$	Check	$f_{max,act}$	$f_{act,rec}$	Check
Winter	[N/mm²]	[N/mm²]	[N/mm²]	[mm]	[mm]	[N/mm²]
0+1	13.7	50	13.7 < 50	7.0	10.8	8.7 < 10.8

Summer:

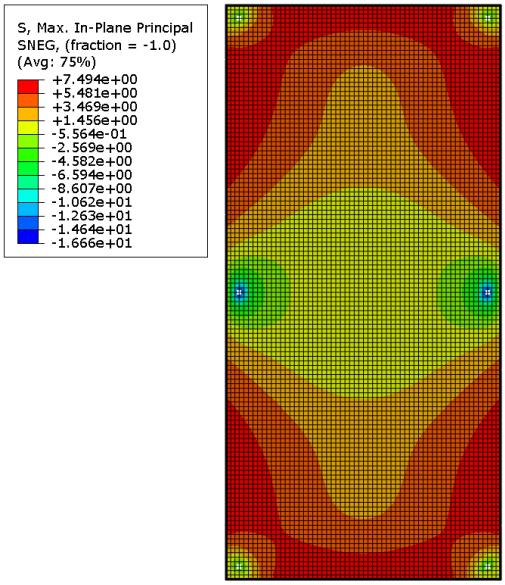

Figure E.11 Maximum tensile stresses – inner pane

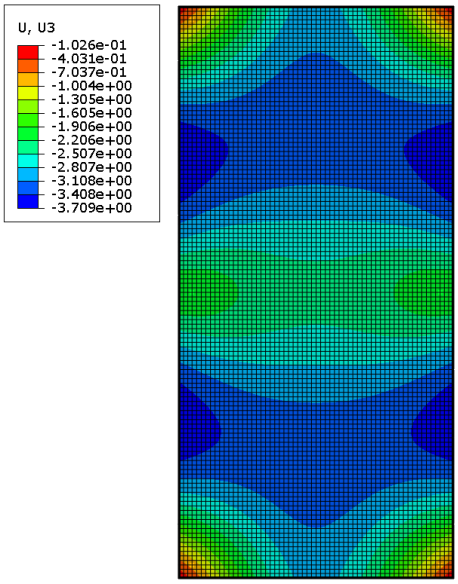

Figure E.12 Maximum deformations – inner pane

Table E.9 Verification of the inner glass pane for the climate loading case "Summer"

Loading case	$\sigma_{max,act}$	$\sigma_{max,rec}$	Check	$f_{max,act}$	$f_{act,rec}$	Check
Winter	[N/mm²]	[N/mm²]	[N/mm²]	[mm]	[mm]	[N/mm²]
0+1	7.5	50	7.5<50	3.7	10.8	3.7<10.8

Verification of the connection "FZP-G-Z – Glass" in the borehole area

For the verification in the borehole area, the maximum tensile stresses are limited in two positions of the borehole (section 8.6.2):

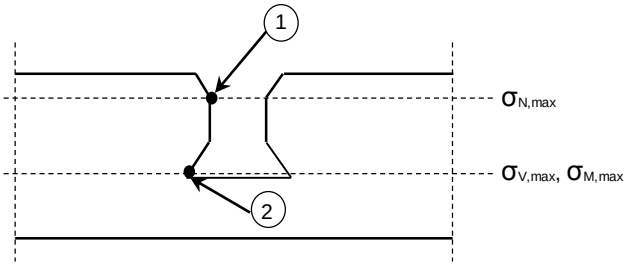

Figure E.13 The two positions at the borehole to be verified

Position 1:

$$\frac{\sigma_{N,max}+\alpha_V\cdot\sigma_{V,max}+\alpha_M\cdot\sigma_{M,max}+k\cdot\sigma_{glob,60}}{\sigma_{d,1}} \leq 1.0$$

Position 2:

$$\frac{\alpha_N\cdot\sigma_{N,max}+\sigma_{V,max}+\sigma_{M,max}+\alpha_k\cdot k\cdot\sigma_{glob,60}}{\sigma_{d,2}} \leq 1.0$$

The verification is done for the climate loading "Winter" and "Summer" for each type of the Fischer anchor: the corner fixings and the edge fixings.

Corner fixing: (Fixing 1 in Figure E.1)

Winter:

The forces and moments in the fixings are numerically determined by means of the 2D FE-model. In fact, they correspond to the forces and moments in the springs.

The eccentric moment M_G due to the self-weight is calculated according to equation (8-7):

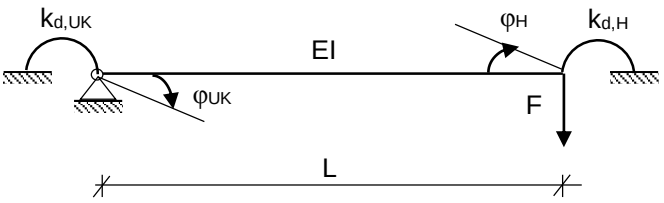

$$M_G = FL\frac{\frac{L}{2EI}+\frac{1}{k_{rot,Sub}}}{\frac{L}{EI}+\frac{1}{k_{rot,Sub}}+\frac{1}{k_{rot,FZP-G-Z}}}$$

Figure E.14 Determination of the eccentric moment M_G due to the self-weight, from (Beyer, 2007)

The parameters for the determination of M_G and the moment M_G are resumed in Table E.10

Table E.10 Parameters for the determination of M_G

L	E	I	$k_{rot,Sub}$	$k_{rot,FZP-G-Z}$	$F=V_y$	M_G
[mm]	[N/mm²]	[mm⁴]	[Nmm/rad]	[Nmm/rad]	[N]	[Nmm]
15	190 000	201	9.50E+05	8.59E+05	750	5385

The maximum tensile stress $\sigma_{glob,60}$ on a circular path with a radius of r = 60 mm around the borehole axis (size of local area) is determined.

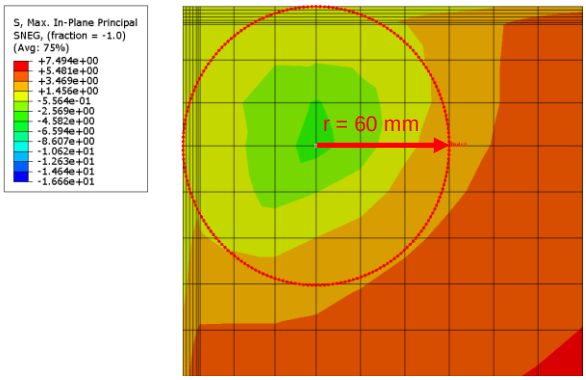

Figure E.15 Determination of the maximal tensile stress $\sigma_{glob,60}$

The k-factor depends on the type of fixing (corner or edge) and its values are resumed in the Table Table 8.5 to Table 8.7. For fixing 1:

$$e_x = e_y = 60\ \text{mm} \leq \frac{L_x = L_y}{10} = \frac{1080\ \text{mm}}{10} = 108\ \text{mm}$$

and the k-factor is k = 1.0.

This leads to the following results:

Table E.11 Forces and moments in the Fischer undercut anchor, fixing 1, Winter, $\sigma_{glob,60}$

Loading case	N_d	M_x		M_x		$M_{d,res}$	V_x	V_y	$V_{d,res}$	k	$\sigma_{glob,60}$
		FE	M_G	FE	M_G						
[-]	[N]	[Nmm]	[Nmm]	[Nmm]	[Nmm]	[Nmm]	[N]	[N]	[N]	[-]	[N/mm²]
0	0	185	0	0	5385		0	750		1	0
1	503	3013	0	3242	0		0	0		1	2.66
Σ	503	3198		8627		9201	0	750	750	-	2.66

The resulting forces and moments are converted to the equivalent tensile stress components with help of the transfer functions (section 8.5.2). For an inner pane with t_i = 10 mm:

$$\sigma_{N,max} = 0.0266 \cdot N_d$$

$$\sigma_{M,max} = 0.0128 \cdot M_d$$

$$\sigma_{V,max} = 0.001550 \cdot V_d$$

The tensile stress components are resumed in Table E.12.

Table E.12 The tensile stress components at the borehole, fixing 1, Winter

FZP-G-Z	N_d	$M_{d,res}$	$V_{d,res}$	$\sigma_{N,max}$	$\sigma_{M,max}$	$\sigma_{V,max}$
[-]	[N]	[Nmm]	[N]	[N/mm²]	[N/mm²]	[N/mm²]
Corner	503	9201	750	13.4	14.26	9.6

The verification in the two positions of the borehole is presented in Table E.13.

Table E.13 Verification of the connection "FZP-G-Z – Glass", fixing 1, Winter

FZP-G-Z	Position	$\sigma_{d,1}$	$\sigma_{d,2}$	α_N	α_M	α_V	α_k	(8-3)	Check	(8-4)	Check
[-]	[-]	[N/mm²]	[N/mm²]	[-]	[-]	[-]	[-]	[-]		[-]	
Corner	1	47	-	0.4	0.86	0.75	0.5	0.8	0.8<1	-	
	2	-	23					-		1.3	1.3>1

The verification is not fulfilled for position 2!

Summer:

The verification for the loading case is similar to the loading case “Winter”. The results are resumed in the Table E.14 to Table E.16.

Table E.14 Forces and moments in the Fischer undercut anchor, fixing 1, Summer, $\sigma_{glob,60}$

Loading case	N_d	M_x		M_x		$M_{d,res}$	V_x	V_y	$V_{d,res}$	k	$\sigma_{glob,60}$
		FE	M_G	FE	M_G						
[-]	[N]	[Nmm]	[Nmm]	[Nmm]	[Nmm]	[Nmm]	[N]	[N]	[N]	[-]	[N/mm²]
0	0	185	0	0	5385		0	750		1	0
1	513	2565	0	2375	0		0	0		1	8.00
Σ	513	2750		7760		8233	0	750	750	-	8.00

Table E.15 The tensile stress components at the borehole, fixing 1, Summer

FZP-G-Z	N_d	$M_{d,res}$	$V_{d,res}$	$\sigma_{N,max}$	$\sigma_{M,max}$	$\sigma_{V,max}$
[-]	[N]	[Nmm]	[N]	[N/mm²]	[N/mm²]	[N/mm²]
Corner	513	8233	750	13.60	12.76	9.6

Table E.16 Verification of the connection “FZP-G-Z – Glass”, fixing 1, Summer

FZP-G-Z	Position	$\sigma_{d,1}$	$\sigma_{d,2}$	α_N	α_M	α_V	α_k	(8-3)	Check	(8-4)	Check
[-]	[-]	[N/mm²]	[N/mm²]	[-]	[-]	[-]	[-]	[-]		[-]	
Corner	1	47	-	0.4	0.86	0.75	0.5	0.85	0.85<1	-	
	2	-	23					-		1.4	1.4>1

The verification is not fulfilled for position 2!

Edge fixing: (Fixing 3 in Figure E.1)

Winter:

The verification procedure for the edge fixing is the same than for the corner fixing. The only difference consists in a different value of the k-factor. In fact, the values are given in the Table Table 8.5 and the Table 8.6.

For t_i = 10 mm and $t_i/t_e \geq 1.0$:

$$k = -0.14 \cdot \frac{t_e}{t_i} + 1.94 = -0.14 \cdot 1 + 1.94 = 1.80$$

The verification is condensed in the Table E.17 to Table E.19:

Table E.17 Forces and moments in the Fischer undercut anchor, fixing 3, Winter, $\sigma_{glob,60}$

Loading case	N_d	M_x		M_x		$M_{d,res}$	V_x	V_y	$V_{d,res}$	k	$\sigma_{glob,60}$
		FE	M_G	FE	M_G						
[-]	[N]	[Nmm]	[Nmm]	[Nmm]	[Nmm]	[Nmm]	[N]	[N]	[N]	[-]	[N/mm²]
0	0	0	0	0	0		0	0		1.8	0
1	1244	0	0	6017	0		0	0		1.8	20
Σ	1244	0		6017		6017	0	0	0	-	20

Table E.18 The tensile stress components at the borehole, fixing 3, Winter

FZP-G-Z	N_d	$M_{d,res}$	$V_{d,res}$	$\sigma_{N,max}$	$\sigma_{M,max}$	$\sigma_{V,max}$
[-]	[N]	[Nmm]	[N]	[N/mm²]	[N/mm²]	[N/mm²]
Edge	1244	6017	0	33	9.32	0

FZP-G-Z	Position	$\sigma_{d,1}$	$\sigma_{d,2}$	α_N	α_M	α_V	α_k	(8-3)	Check	(8-4)	Check
[-]	[-]	[N/mm²]	[N/mm²]	[-]	[-]	[-]	[-]	[-]		[-]	
Corner	1	47	-	0.4	0.86	0.75	0.5	1.60	1.60>1	-	
	2	-	23					-		1.80	1.80>1

The verification is not fulfilled for position 1 and 2!

Summer:

The verification procedure is identic to the climate loading case “Winter”.

Table E.19 Forces and moments in the Fischer undercut anchor, fixing 3, Summer, $\sigma_{glob,60}$

Loading case	N_d	M_x		M_x		$M_{d,res}$	V_x	V_y	$V_{d,res}$	k	$\sigma_{glob,60}$
		FE	M_G	FE	M_G						
[-]	[N]	[Nmm]	[Nmm]	[Nmm]	[Nmm]	[Nmm]	[N]	[N]	[N]	[-]	[N/mm²]
0	0	0	0	0	0		0	0		1.8	0
1	1224	0	0	105	0		0	0		1.8	20
Σ	1224	0		105		105	0	0	0	-	20

Table E.20 The tensile stress components at the borehole, fixing 3, Summer

FZP-G-Z	N_d	$M_{d,res}$	$V_{d,res}$	$\sigma_{N,max}$	$\sigma_{M,max}$	$\sigma_{V,max}$
[-]	[N]	[Nmm]	[N]	[N/mm²]	[N/mm²]	[N/mm²]
Edge	1224	105	0	32.56	0	0

FZP-G-Z	Position	$\sigma_{d,1}$	$\sigma_{d,2}$	α_N	α_M	α_V	α_k	(8-3)	Check	(8-4)	Check
[-]	[-]	[N/mm²]	[N/mm²]	[-]	[-]	[-]	[-]	[-]		[-]	
Corner	1	47	-	0.4	0.86	0.75	0.5	0.9	0.9<1	-	
	2	-	23					-		1.30	1.30>1

The verification is not fulfilled for position 2!

As the structural safety of the IGU is not proofed, it is proposed to increase the number of the Fischer undercut anchors from 6 to 8. Alternatively, a thicker inner glass pane can be applied.

In conclusion, the novel design concept allows a quick design of point fitted insulation glass with undercut anchors. A simple 2D FE-model of the point fitted IGU is sufficient for the design and there is no need for complex 3D FE calculation.